DISSERTATION

From High-Performance Detectors to Surface Emitting Rings: Integrating miniaturized Spectroscopic Technologies on a Chip

ausgeführt zum Zwecke der Erlangung des akademischen Grades
eines Doktors der technischen Wissenschaften

unter der Leitung von

Univ. Prof. Dr. Benedikt Schwarz
Institut für Festkörperelektronik

eingereicht an der

Technischen Universität Wien
Fakultät für Elektrotechnik und Informationstechnik

von

Dipl.-Ing. Georg Marschick, BSc

Mat.Nr. 01129923

Wien, im November 2024

Betreuer:	Univ. Prof. Dr. Benedikt Schwarz
Zweitbetreuer:	Univ. Prof. Dr. Gottfried Strasser
1. Gutachter:	Prof. Dr. Raffaele Colombelli
2. Gutachter:	Prof. Dr. Giacomo Scalari
Tag der Verteidigung:	20. Dezember 2024

Abstract

This thesis presents advancements in mid-infrared optoelectronic devices with both in-plane and out-of-plane light emitting properties. Quantum cascade lasers (QCL) have grown to a more and more established source of coherent mid-infrared (MIR) radiation since their first implementation in the mid-1990s. As a further development, the interband cascade laser (ICL) blends the principles of traditional interband diode lasers with the periodic structure of QCLs, exploiting intersubband transitions. ICLs leverage the extended upper laser level lifetime from diode lasers and the voltage-efficient multiple active region design of QCLs. Their inherent low power consumption, often utilizing only a few periods in the active region, renders them particularly appealing for compact and portable applications across the mid-infrared spectrum. This encompasses areas such as trace gas sensing, process monitoring, and medical diagnosis. Building upon previous research, this work introduces the next generation of vertical emitting ring-ICLs capable of low-dissipative continuous wave emission at room temperature, achieved through innovative mounting techniques and effective cooling strategies. Through the integration of second-order distributed feedback gratings and advanced fabrication techniques, the emitted light can be tailored for specific applications, demonstrating the versatility and practicality of these devices. The usability of these ring-laser devices is further demonstrated through noise measurements, unveiling their exceptional performance especially in areas where low noise behavior is crucial. Additionally, this thesis explores a novel approach to on-chip guiding of MIR radiation. Utilizing bi-functional quantum cascade material as a laser and a photodetector on the same chip, the focus is directed towards minimizing losses in Germanium-based plasmonic waveguides for on-chip beam combining. This concept enables the compact and cost-effective integration of previously table-top-sized optical systems onto areas smaller than a fingertip, with the added benefit of eliminating the need for manual alignment of optical components. Through simulation studies and experimental validation, novel solutions are proposed to mitigate losses and enhance device performance through the integration of Au-covered micro-mirror structures to efficiently redirect surface plasmon polaritons, facilitating low-loss on-chip routing over extended waveguide lengths. The research presented here contributes to the advancement of MIR optoelectronic technology and the on-chip integration of optical systems, offering insights into device design, fabrication techniques, and practical applications. The demonstrated capabilities of the developed devices pave the way for future innovations various fields ranging from telecommunications to environmental monitoring and healthcare.

Kurzfassung

Diese Arbeit präsentiert Fortschritte bei optoelektronischen Geräten im mittleren Infrarotbereich mit sowohl in der Ebene als auch außerhalb der Ebene emittierenden Eigenschaften. Quantenkaskadenlaser (QCL) haben sich seit ihrer ersten Implementierung Mitte der 1990er Jahre zu einer immer etablierteren Quelle kohärenter Mittelinfrarot (MIR)-Strahlung entwickelt. Als weitere Entwicklung verbindet der Interband-Kaskadenlaser (ICL) die Prinzipien herkömmlicher Interband-Diodenlaser mit der periodischen Struktur von QCLs und nutzt Inter-Subband-Übergänge aus. ICLs nutzen die verlängerte Lebensdauer des oberen Laserlevels von Diodenlasern und das spannungseffiziente Design mit mehreren, kaskadierten aktiven Zonen von QCLs. Ihr inhärenter geringer Stromverbrauch, bedingt durch ein energieeffizientes Design mit nur wenigen aktiven Halbleiterschichten, macht sie besonders attraktiv für kompakte und tragbare Anwendungen im gesamten Mittelinfrarotspektrum. Dies umfasst Bereiche wie die Spurengaserfassung, die industrielle Prozessüberwachung und medizinische Diagnostik. Basierend auf früheren Forschungsarbeiten, präsentiert diese Arbeit die nächste Generation von vertikal emittierenden Ring-ICLs, die in der Lage sind, bei Raumtemperatur emissionsarm und im Dauerbetrieb zu strahlen, was durch innovative Montagetechniken und effektive Kühlstrategien erreicht wird. Durch die Integration von Rückkopplungsgittern zweiter Ordnung und fortschrittlichen Fertigungstechniken kann das emittierte Licht für spezifische Anwendungen maßgeschneidert werden, was die Vielseitigkeit und Praktikabilität dieser Laser demonstriert. Weiters wurde das Rauschverhalten dieser Laserimplementierung untersucht und über breite Frequenzbereiche eine Limitierung die nur durch Schottkyrauschen hervorgerufen wird, festgestellt.

Zusätzlich untersucht diese Arbeit einen neuartigen Ansatz zur On-Chip-Führung von MIR-Strahlung. Unter Verwendung von bifunktionalem Quantenkaskadenmaterial als Laser und Fotodetektor auf demselben Chip liegt der Fokus auf der Minimierung von Verlusten in Germanium-basierten plasmonischen Wellenleitern für die On-Chip-Strahlkombination. Dieses Konzept ermöglicht eine kompakte und kostengünstige Integration von optischen Systemen, die zuvor Tischgröße hatten, auf Bereiche kleiner als ein Fingernagel, mit dem zusätzlichen Vorteil, dass eine Ausrichtung der optischen Komponenten zueinander überflüssig wird. Durch Simulationsstudien und experimentelle Validierung werden neuartige Lösungen vorgeschlagen, um Verluste zu verringern und die Geräteleistung durch die Integration von mit Gold bedeckten Mikrospiegelstrukturen zur effizienten Umleitung von Oberflächenplasmonen zu verbessern, was eine verlustarme Übertragung über Winkeländerungen und vergleichsweise lange Weglängen ermöglicht. Die hier vorgestellte Forschung trägt zum Fortschritt von optoelektronischen Implementierungen im mittleren Infrarotbereich und zur On-Chip-Integration optischer Systeme bei, indem Einblicke in Gerätedesign, Fertigungstechniken und praktische Anwendungen geboten werden. Die gezeigten Fähigkeiten der entwickelten Geräte ebnen den Weg für zukünftige Innovationen in der Hochgeschwindigkeits-Funkkommunikation und spektroskopischen Erfassung und adressieren damit kritische Herausforderungen in verschiedenen Bereichen von der Telekommunikation bis zur Umweltüberwachung und Gesundheitsversorgung.

Acknowledgements

First and foremost, I would like to thank my supervisors, Benedikt Schwarz and Gottfried Strasser, for their support and guidance, making it possible to complete this PhD. Further thanks go to Borislav Hinkov for his support and guidance during the early years of my PhD.

I am deeply grateful to the staff of Zentrum für Mikro- und Nanostrukturen (ZMNS), especially Werner Schrenk, whose expertise and knowledge were incredibly helpful during my work in both the cleanroom and the laboratory.

A huge THANK YOU goes to all my colleagues at FKE, who provided both technical and emotional support whenever needed—whether in the lab, the cleanroom, the office, or while riding bikes, having lunch, coffee, or beers together. You made this time special. Thank you!

A special thank you goes to the people at LENS, the European Laboratory for Non-Linear Spectroscopy in Sesto Fiorentino, who contributed greatly to publishing my second paper, without which I could not be here. Thank you!

I would also like to express my gratitude to the CAVS group of the Faculty of Technical Chemistry at TU Wien for their collaboration and support.

My friends outside TU deserve a huge thank you for being an anchor in my life, helping me escape certain stressful situations during my PhD journey.

Last but not least, I want to deeply thank my family, especially my dear partner, Federica, who, from the very beginning, went through this journey with me and was there for all the highs and lows. Thank you!

CONTENTS

CHAPTER 1

INTRODUCTION

1.1 Scope and Cohesion of this Thesis

This thesis presents significant advancements in the miniaturization and dense integration of mid-infrared (MIR) optoelectronic devices.[1] It focuses on both in-plane and out-of-plane light-emitting properties, highlighting the development and optimization of processing steps used to fabricate ring shaped, vertically emitting interband cascade laser (ICL) and a new concept of photonic integrated circuits with integrated plasmonic routing based on a bifunctional quantum cascade laser/detector (QCL/QCD/QCLD) material. These advancements are explored through innovative designs and integrated systems aimed at creating compact, high-performance devices. The introductory chapter of this thesis provides a foundational understanding of how a quantum cascade laser (QCL) and an ICL function, along with an exploration of their use cases and potential applications. In chapters 2 to 5 the listed publications are presented, offering a concise overview with state of the art literature, the contributing investigations and their findings. Chapter 6 offers a detailed account of the processing technologies and steps utilized, addressing the challenges and obstacles encountered to ensure the preservation of knowledge and facilitate the continuation of the research topics discussed herein. The appendix offers an overview of the used standard fabrication recipes. The cohesion of this thesis, which encompasses diverse research topics, is articulated in the following abstract.

The journey begins with the quantum cascade detector (QCD), which has shown promise due to its zero external bias operation and low dark current.[2] These characteristics make QCDs ideal for a variety of applications ranging from high sensitivity spectroscopy to high bitrate free-space optical communication.[3] The investigation aimed to overcome performance limitations at long wavelengths by comparing single and multi-period QCDs, optimizing their responsivity and noise behavior. This foundational work lays the groundwork for integrating QCDs into photonic integrated circuit (PIC), demonstrating their potential for advanced communication technologies. By achieving effective on-chip integration, this research paves the way for miniaturized and densely packed optical systems.[4]

The possibility to integrate the functionalities of both a QCL and a QCD within a single material structure, so called quantum cascade laser detector (QCLD) material, opens a new degree of freedom in device design.[5] Building upon this, the research extends to the development of a MIR device that might pose a crucial development step for applications such as biomedical analysis, chemical reaction monitoring, and high-bitrate free-space telecommunication. The miniaturization of these devices into complex MIR-PICs represents a significant technological advancement.[6] This is exemplified by the introduction of a monolithic on-chip beam combiner, integrating active quantum cascade devices with tailored passive plasmonic waveguides and novel on-chip micro-mirror optics. These advancements enable low-loss on-chip mode guiding and beam combining, essential for the next generation of sophisticated MIR-PICs, highlighting the potential for compact and efficient integrated systems like monolithic heterodyne detectors or Mach-Zehnder interferometers.

Compared to detection schemes in liquids, where the high density of analytes allows for sufficient interaction lengths even in short paths, on-chip analysis of gaseous specimens is more complex. The necessity for longer interaction lengths in gas analysis suggests the use of surface-emitting lasers to incorporate standard optics and measurement cells into the beam path effectively.[7] A key innovation in this thesis is the development of small-footprint, vertical emitting single-ring ICLs capable of low-dissipative continuous wave emission at room temperature. These devices, achieved through an innovative mounting technique on custom made aluminum nitride (AlN) submounts, offer compact and reliable solutions for CO_2 sensing applications. This research demonstrates the versatility and practicality of ring-laser devices for portable devices and the possibility to implement them into existing industrial infrastructure, emphasizing their potential for dense integration and miniaturization.

Further, the noise characteristics of ring ICLs are meticulously analyzed, addressing the constraints imposed by quantum effects on precision applications in the MIR spectral range. By providing a comprehensive characterization of bias-dependent intensity noise power spectral density (INPSD) and relative intensity noise (RIN),

the study achieves shot-noise-limited statistics for Fourier frequencies above 100 kHz. These findings offer a crucial understanding of the sensitivity and resolution of ring-ICL based MIR imaging and spectroscopic systems.
Together, these investigations form a cohesive body of work that advances the field of mid-infrared optoelectronic technology. By focusing on the dense integration of active (QCL, QCD) and passive devices into PICs and the miniaturization of ICLs, this thesis addresses critical challenges in the implementation of MIR optoelectronic devices into existing industrial infrastructure. The demonstrated capabilities of the developed devices not only enhance our understanding of MIR technologies but also pave the way for future innovations in high-speed wireless communication and spectroscopic sensing.

1.2 The Mid-Infrared Spectral Region

Since the dawn of civilization, humanity has been driven by an insatiable curiosity to unravel the mysteries of existence. From ancient philosophers pondering the elements to modern scientists probing the depths of the cosmos, the quest to understand what the world is made of and why things happen the way they do has been a fundamental pursuit of human inquiry. Discoveries of interactions between light and matter that were made centuries ago built the foundation of modern day mid-infrared wireless communication systems or spectroscopy measurements. According to Einstein and Planck, light is composed of photons, each carrying discrete packets of energy

$$E = h\nu = \hbar\omega = \frac{hc}{\lambda} \tag{1.1}$$

with Planck´s constant h, the reduced Planck‘s constant $\hbar = \frac{h}{2\pi}$, the frequency v, the angular frequency $\omega = 2\pi\nu$, and the photons wavelength λ.[8] Electromagnetic waves, encompassing a vast spectrum of frequencies and energies, govern a wide array of natural phenomena. Spanning from gamma rays with their high frequencies and harmful energies down to radio waves, with wavelengths of kilometers, able to transmit data around the globe and through outter space, the electromagnetic spectrum also illuminates our world. Light, the tiny part of the electromagnetic spectrum that is visible for the human eye, yet just covers a very short wavelength range (λ= 400 nm-700 nm) of the electromagnetic spectrum. In 1800, W. Herschel discovered rising temperatures in thermometers placed next to the visible, red spectral portion of light dispersed by a prism. This longer-wave spectral neighbor of red light, invisible to the human eye, is called infrared radiation.[9] The infrared region is typically defined as covering wavelengths ranging from 700 nm up to 1 mm.[10] In this thesis, the focus lies on the MIR region, which occupies a pivotal position within the infrared spectrum. Characterized by wavelengths ranging from approximately 3 to 30 micrometers, MIR radiation holds particular significance in the study of molecular structures, as it corresponds to the characteristic vibro-rotational frequencies of chemical bonds and functional groups.[11] These unique frequencies act as distinctive fingerprints for different molecules, enabling precise identification, which is why this region is also referred to as the "fingerprint region".[12] By exploiting the unique absorption and emission properties of molecules in the mid-infrared range, scientists have made groundbreaking discoveries across diverse fields, from pharmaceuticals and environmental science to forensics and materials engineering.[13] In strong contrast, the mid-wave infrared (MWIR) and long-wave infrared (LWIR) regions within the MIR region also feature atmospheric windows at specific wavelengths (3-5 µm and 8-14 µm). These windows allow infrared light to pass through the atmosphere, largely due to the absence of significant water absorption lines combined with insensitivity to scattering through fog, dust, rain or snow, enabling robust free-space transmission lines with high data throughput.[14]

Figure 1.1 shows a cut out of the infrared spectrum, emphasizing the strong presence of absorption lines of eight selected, representative molecules in the MIR as well as two atmospheric windows, characterized by the absence of H_2O absorption lines. To identify and quantify molecules at low concentrations with high precision, it is essential to have powerful and precise infrared light sources that can be engineered to emit at specific wavelengths with narrow linewidths.

1.3 From Crystals to Lasers

The following section should provide a fundamental understanding of electromagnetic waves and radiation to the reader. A conceptualization of why solid-state lasers operating in the mid-infrared spectral region are used and examined is made. We also set a foundation of our understanding of light-matter interactions, starting from the free electron model and progressing to the complex interactions of electrons and photons in quantum wells. The free electron model is the simplest approximation to describe the behavior of electrons in a material.[16] This model assumes that electrons move freely within a solid without being influenced by the atomic potential of the lattice. As proposed by Drude in 1900, electrons can be treated as classical particles that respond to electric and magnetic fields. The conductivity σ of a material is given by:

$$\sigma = \frac{ne^2\tau}{m_e}$$

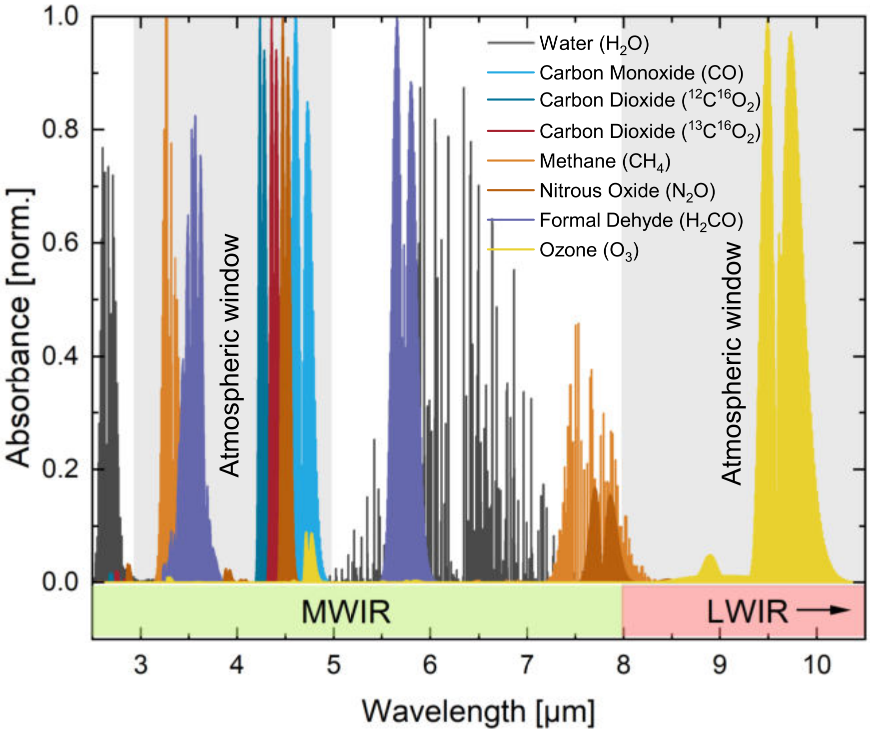

Figure 1.1: Normalized absorption spectra for destinctive chemical compounds. The MWIR and LWIR region are highlighted in the bottom of the figure. The atmospheric windows (grey shaded rectangles) describe areas without water absorption. The datasets were obtained from the HITRAN online database.[15]

where n is the electron density, e is the electron charge, τ is the mean free time between collisions, and m_e is the electron mass.[17] While the Drude model explains some electrical properties, it fails to account for the quantized nature of electrons and the band structure of solids. This limitation led to the development of quantum mechanical models. Quantum mechanics provides a more accurate description of electron behavior in solids. Electrons are treated as wavefunctions that obey the Schrödinger equation.[18] The time-independent Schrödinger equation is given by:

$$\hat{H}\psi(\mathbf{r}) = E\psi(\mathbf{r}) \tag{1.2}$$

$$\left(\frac{\mathbf{p}^2}{2m_0} + V(\mathbf{r})\right)\psi(\mathbf{r}) = E\psi(\mathbf{r}) \tag{1.3}$$

where $\hat{H}$ is the Hamiltonian operator of the crystal lattice, $\psi(\mathbf{r})$ is the wavefunction of the electron, E is the energy eigenvalue associated with the wavefunction, $\mathbf{p}$ the momentum operator and m_0 the free electron mass. In a solid, the potential experienced by an electron is periodic due to the regular arrangement of atoms in a crystal lattice. This periodic potential can be described as $V(\mathbf{r}) = V(\mathbf{r} + \mathbf{R})$, where $\mathbf{R}$ is a translation vector of the periodic lattice. Bloch's theorem states that electrons in a periodic potential, such as a crystal lattice, have wavefunctions that can be expressed as:

$$\psi(\mathbf{r}) = e^{i\mathbf{kr}} u_{\mathbf{k}}(\mathbf{r}), \tag{1.4}$$

a combination of a plane wave ($e^{i\mathbf{kr}}$) and a Bloch function $u_k(\mathbf{r})$ that shares the same periodicity as the lattice.[19] When we solve the Schrödinger equation for an electron in a periodic potential, we find that the allowed energy levels of the electron are not discrete as in an isolated atom, but form continuous ranges called energy bands. These energy bands arise because the periodic potential of the crystal lattice causes the electron wavefunctions to overlap and interact at the Brillouin-zone edge, leading to the splitting of energy levels into a band of closely spaced niveaus. Between these energy bands, there can exist ranges of energy where no electron states are allowed. These ranges are known as band gaps. The formation of energy bands and band gaps can be understood through the concept of Brillouin zones in reciprocal space, where the electron wavevector $\mathbf{k}$ determines the allowed energy states.

In essence, the periodic potential modifies the free electron energy dispersion relation, $E = \hbar^2 k^2 / 2m$, leading to a band structure that is characterized by allowed and forbidden energy regions. The electronic band structure of a material determines its electrical and optical properties: In conductors, the conduction band is partially filled with electrons, allowing them to move freely and conduct electricity. In insulators, a large band gap exists between the valence band (fully occupied) and the conduction band (empty), preventing electrical conduction. In semiconductors, the band gap is small enough that electronic, thermal or optical excitation can promote electrons from the valence band to the conduction band, enabling controlled conductivity. Vice versa, electrons from the conduction band can recombine with holes in the valence band by releasing the energy difference for example in form of emission of a photon.[20]

1.4 Materials

III-V semiconductors, as the name suggests, are compounds of elements from group III (such as Ga, Al, In) and group V (such as As, P, Sb) of the periodic table. They crystallize in the zincblende structure, which, similar to the diamond structure, consists of a face-centered cubic lattice with a two-atomic basis (one atom from group III and one atom from group V).

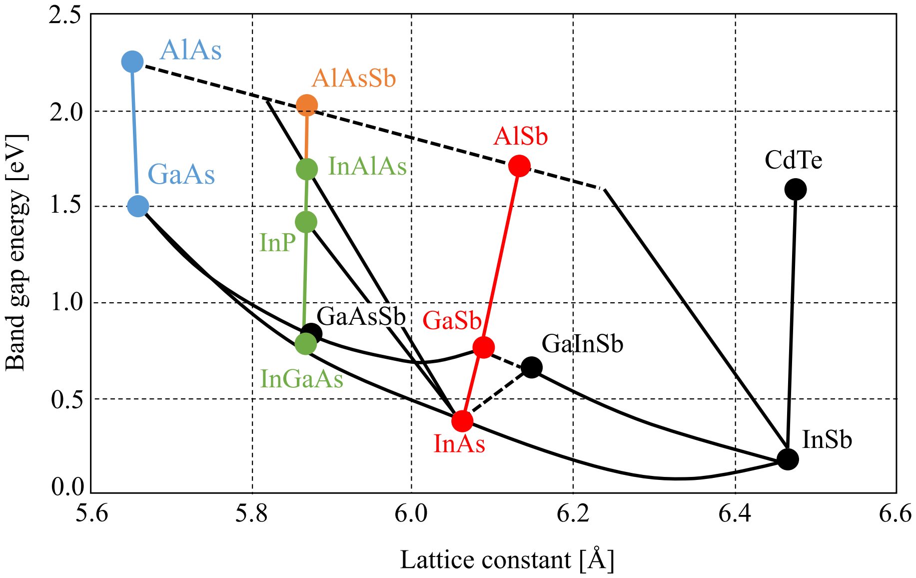

Figure 1.2: Band gap energy versus lattice constant of the most commonly used III-V semiconductors. Band gap energies of ternary components are depicted by the connection lines.[21]

Depending on the number of contributing elements, the alloys are called binary (e.g. GaAs, GaSb), ternary (InGaAs, InAlAs) or even quaternary (GaInAsSb) compounds. Figure 1.2 shows the band gap energy of the most important III-V semiconductors in comparison to their lattice constant at room temperature. Many III-V semiconductors have direct bandgaps, and they offer the ability to engineer electronic and optical properties through alloying and heterostructure formation. By exploiting the band discontinuity and the bandgap of different materials, band profiles can be specifically tailored in heterostructure-based components. With the three binary semiconductors GaSb, InAs, and AlSb, which have a similar lattice constant, this results in high flexibility.[21] Heterostructures are engineered through a layer-by-layer epitaxial deposition of the desired III-V semiconductors, typically achieved by metal-organic chemical vapor deposition (MOCVD)[22] or molecular beam epitaxy (MBE).[23]

1.5 Quantum Confinement and Band Structures

Understanding the formation of energy bands and band gaps is crucial for the design and function of semiconductor devices. Referring to section 1.3, we know that a periodic potential, as caused by the atomic-potential in a crystal lattice, leads to the formation of energy bands separated by areas of forbidden states.

In quantum wells the confinement of electrons in one dimension modifies the band structure further, leading to discrete energy levels within the wells. These quantum-confined states are integral to the operation of quantum cascade or interband cascade lasers, where electron transitions between these states result in the emission of light. In quantum wells, which are thin layers of, in the case of MIR optoelectronic devices mostly III-V semiconductor material sandwiched between barriers of a material with a larger band gap, the motion of electrons is confined in one dimension. The Schrödinger equation for an electron in a quantum well can be written as:

$$\left(-\frac{\hbar^2}{2m}\nabla^2 + V(z)\right)\psi(x,y,z) = E\psi(x,y,z) \tag{1.5}$$

where $V(z)$ represents the potential profile of the quantum well, which is typically a finite square well potential. This confinement leads to the quantization of energy levels within the well as the values of k_z are given by the classical expression of standing waves $k_z = n\pi/L$ with L being the quantum well width and n an integer (quantum) number. The solutions to this equation are discrete energy levels, and the corresponding wavefunctions are standing waves with energies

$$E(k) = E_c + \frac{\hbar^2\pi^2 n^2}{2mL^2} + \frac{\hbar^2}{2m}(k_x^2 + k_y^2). \tag{1.6}$$

Thus, for each n-value a distinctive subband emerges. When light interacts with a quantum well, electrons can be excited between these quantized energy levels, and conversely, they can relax from excited states to lower energy levels. By carefully designing the quantum well, the bandgaps and thus the transition energies can be precisely engineered. These transitions are referred to as intersubband transitions because they occur within the same energy band, typically the conduction band.[24]

1.6 Interband and Intersubband Transitions

In semiconductor lasers, transitions can occur between different types of energy states, leading to different kinds of transitions: interband and intersubband transitions.

As Figure 1.3 shows, interband transitions involve electrons moving from a state in the valence band to a state in the conduction band or vice versa. For interband processes, the transition energy is given by the sum of the energy of the confined states in conduction and valence band together with the bandgap energy. Since this bandgap energy is a material intrinsic property, interband transitions are limited by this lower boundary state. As the electron and hole distributions exhibit opposite curvatures in the dispersion relation $E(k)$, the gain spectrum of interband

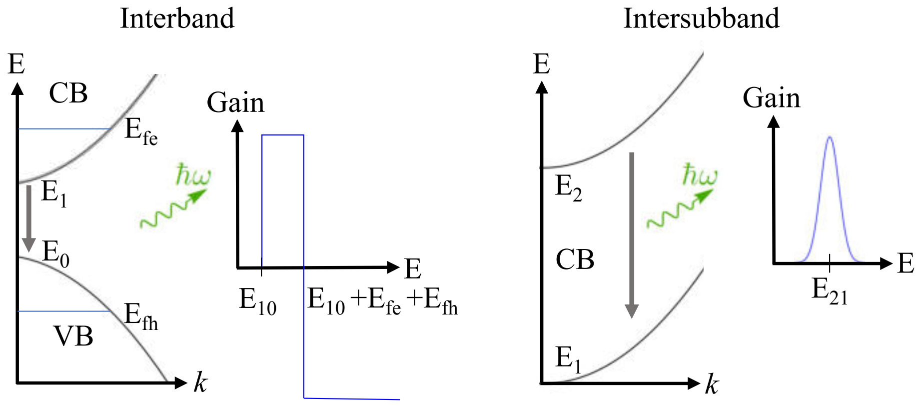

Figure 1.3: A schematic view of interband (left) and intersubband (right) transitions in quantum wells at zero temperature. In an interband transition, an electron in the conduction band recombines with a hole in the valence band. If this transition is radiative, the energy difference E_1-E_0=$\hbar\omega$ is emitted as a photon. Due to the opposite curvature of the conduction and valence band dispersion relations, and the separate Fermi levels E_{fe} and E_{fh}, the resulting gain spectrum is broadened. In contrast, for intersubband transitions, where both subbands have the same dispersion relation form, the gain peak is narrow Lorentzian-shaped around the transition energy $\hbar\omega$=E_2-E_1.[25] For simplicity, line broadening is neglected in the interband transition case, resulting in a rectangular representation.

transitions is broadened (see Fig. 1.3). Intersubband transitions occur within the same band, typically the conduction band, between different subbands formed by quantum confinement in low-dimensional structures like quantum wells. In comparison to interband transitions, intersubband transitions are not subjected to bandgap limitations but can be designed by proper engineering of the involved quantum wells as described in section 1.5. These transitions are typically found in QCLs. Intersubband transitions are subject to different selection rules compared to interband transitions. The most notable selection rule for intersubband transitions in the conduction band is visible through light emission polarized perpendicular to the plane of the quantum well layers (i.e., in the growth direction, TM-polarized). As can be seen in Figure 1.3, the optical transition appears within subbands of the same band, the dispersion relation shows the same curvature, leading to a narrow-Lorentzian shaped gain spectrum.[25] Efficient carrier leakage suppression through bandgap blocking and the elimination of nonradiative phonon relaxation, results in a higher radiative efficiency of the interband transition in ICLs compared to the intersubband transition in QCLs.[26, 27, 28]

1.7 Cascading

This section is mainly based on reference [29]. For any semiconductor laser to function effectively, the active region must generate sufficient gain to overcome the total losses, including mirror and waveguide losses. Gain media consisting of quantum well (QW) structures confines carriers within the active region, resulting in a quasi-two-dimensional density of states. In conventional diode lasers, where electrons and holes are injected from opposite sides of a pn-junction, multiple QWs are often used in a parallel fashion to increase gain. These QWs are separated by barriers thick enough to limit the coupling of individual wave functions, maintaining their two-dimensional characteristics, effectively creating a parallel connection of the QWs. The threshold voltage V_{Th} is similar to that of a single QW where the photon energy is determined by the band gap energy $E_g = \hbar\omega$ and an additional term ΔE describing a contribution of the differential gain and internal losses, resulting in

$$V_{th} = \frac{E_g + \Delta E}{e} \tag{1.7}$$

with e describing the electron charge. On the other hand, the threshold current increases with increasing number of QWs. An additional series resistance (ρ_s) must be considered, which can arise from contacts, transition layers between different regions of the device, the optical cladding, or the active region itself. The threshold power for a laser structure with a parallel QW design is given through

$$P_{\mathrm{th}}^{(\mathrm{parallel})} = (V_{\mathrm{th}} + \rho_s M J_{\mathrm{th}}) M J_{\mathrm{th}} = \frac{(E_g + \Delta E) M J_{\mathrm{th}}}{e} + \rho_s M^2 J_{\mathrm{th}}^2. \tag{1.8}$$

In the parallel configuration, the voltage threshold (V_{th}) remains consistent with that of a single QW, but the series resistance impact is magnified by the number of QWs (M), affecting the overall current flow. The second term of equation 1.8 shows that the parasitic influence of the series resistance ρ_s scales in a quadratic order with the number of stages and the current threshold density. On the other hand, cascading, as used in QCLs and ICLs allows a serial combination of a multitude of QWs, resulting in a threshold current density independent of the number of stages and a voltage drop that results as the sum of V_{Th} of all single stages. The threshold power for a series configuration in semiconductor lasers can be represented by the following equation:

$$P_{\mathrm{th}}^{(\mathrm{series})} = (M V_{\mathrm{th}} + \rho_s J_{\mathrm{th}}) J_{\mathrm{th}} = \frac{(E_g + \Delta E) M J_{\mathrm{th}}}{e} + \rho_s J_{\mathrm{th}}^2. \tag{1.9}$$

In this configuration, the voltage threshold is multiplied by the number of quantum wells, indicating a cumulative voltage increase across all wells. This configuration implies that each quantum well adds linearly to the overall voltage requirement, and the series resistance affects the entire current flow, enhancing the voltage drop further. The power loss due to the parasitic series resistance in the second term of the formula here only scales in a quadratic order with the current threshold density and does not include the number of stages. Thus, the main difference between the two configurations lies in the impact of the series resistance and the distribution of the threshold current. In the series configuration, the resistive losses do not depend on the number of QWs, whereas, in the parallel configuration, these losses increase quadratically, showing the advantages of the cascading approach.

1.8 MIR Sources and Detectors

1.8.1 Thermal Sources

The classic sources of infrared radiation are simple black body radiators which are simply bodies with ideal emission properties heated to a certain temperature. The discretisation of light into small packages of quantized energy as described in 1.1 was a result of the attempts to thoroughly describe the radiated emission spectrum depending on the temperature of such a black body radiator.[30] According to the results, the spectral power density of a black body radiator can be calculated by

$$B_\lambda(T) = \frac{2hc_0^2}{\lambda^5}\frac{1}{exp(\frac{hc_0}{\lambda k_B T}) - 1} \tag{1.10}$$

with c_0 being the speed of light and k_B embodying the Boltzmann constant. Figure 1.4 shows the spectral power density of black body radiators at different temperatures. Black body radiators are broadband emitting objects and the emission intensity can only be adjusted with changes in temperature. Emission maxima in the MIR region are emitted by bodies with relatively low temperature with an emission peak wavelength of λ=9.6 µm for bodies at room temperature. Thus, thermal emitters serving the MIR would have to be operated at room temperature or slightly above, making them indistinguishable of background thermal emission. Higher intensity in the MIR can only be reached by an increase in total temperature, again leading to an intensity peak shift out of the spectral region of interest. Commonly, the light source used in a Fourier transform infrared spectrometer (FTIR) is a heated silicon-carbide rod (glowbar), emitting at a temperature of around T=1600°C. The necessity of

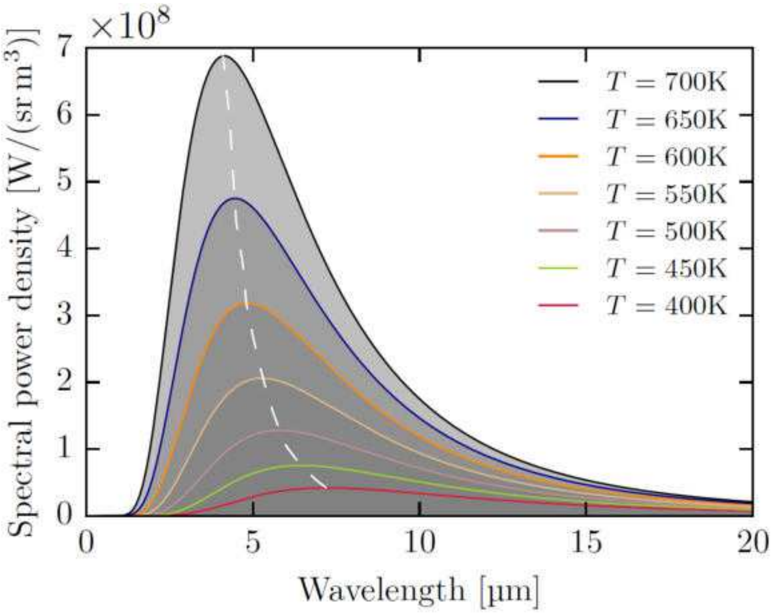

Figure 1.4: Spectral power density emitted by a black body radiator depending on its temperature. The white line shows that the emission maximum transits to shorter wavelengths with increasing temperature. Figure taken from [31]

interferometric, spectral filtering makes FTIR spectrometers bulky and difficult to transport. There are possibilities to engineer the surface of thermal emitters in such way that the spectral temperature curve deviates from Wien´s displacement law and shows higher emission at specific wavelengths, anyway, if narrowband emission is needed, coherent MIR sources might be the better option.[32, 33]

1.8.2 Lasers

Lasers, which stand for Light Amplification by Stimulated Emission of Radiation, are devices that produce coherent light through the process of stimulated emission. At a basic level, a laser requires at least three energy levels in an atom or molecule: one ground state, one excited state, and a metastable state.[34] This arrangement is necessary to achieve population inversion, where more particles occupy the excited state than the ground state, allowing for stimulated emission of photons. A simplified model, only showing two energy levels can be seen in Figure 1.5: excited state E_2 and ground state E_1. Electrons can be lifted up to higher energy levels by absorption of a photon. At the same time, when an electron in an atom or molecule transitions from the excited state to the ground state, it can reduce its energy via the emission of a photon. If this emitted photon interacts with another electron in the excited state, it can stimulate that electron to transition to the ground state and emit a second photon, coherent with the first.

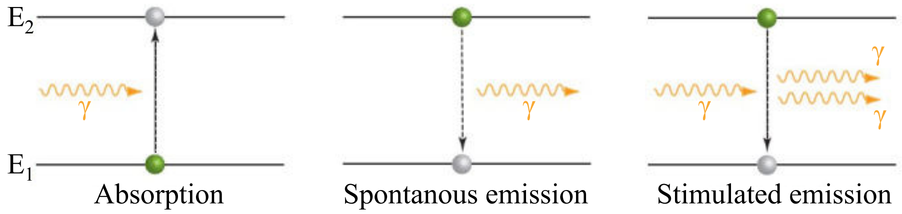

Figure 1.5: A schematic view of the most important electron-photon transition processes between two energy levels.

To achieve lasing, a population inversion is required, meaning that more electrons must occupy the excited state than the ground state. This condition is typically achieved through pumping mechanisms, which excites electrons to higher energy levels, creating the necessary population inversion. The pumping process can either be of optical (solid state lasers, gas lasers) or electrical (semiconductor lasers) origin. Another crucial component of a laser is the optical cavity or resonator, which provides feedback to the amplificated light. The optical cavity typically consists of two mirrors placed at either end of the lasing medium. One of the mirrors is partially reflective, allowing some portion of the light to escape as the laser output. Photons emitted within the lasing medium reflect back and forth between the mirrors, stimulating the emission of more photons and amplifying the light. This repeated reflection and amplification ensures that the light is coherent, meaning the photons are in phase and have the same wavelength and direction.[35]

Diode Lasers

Different from the light emitting diode (LED) the diode laser functions based on stimulated emission, thereby yielding highly coherent light emission. This distinction arises from the fundamental differences in their underlying mechanisms of light generation. While LEDs rely on spontaneous emission, where photons are emitted randomly in time and phase during electron-hole recombination, diode lasers exploit stimulated emission to enforce coherence among emitted photons. In a diode laser, the semiconductor gain medium is engineered to achieve population inversion, where more electrons occupy higher energy states than lower ones. When a photon passes through the gain medium, it can stimulate the emission of additional photons with identical phase, frequency, and direction. This process basically clones a photon with all its properties and leads to the coherent amplification of light within the laser cavity.[36]

Quantum Cascade Lasers

QCLs represent a significant advancement in semiconductor laser technology, particularly for applications requiring MIR and terahertz radiation. Since their first implementation in 1994,[37] QCLs have rapidly evolved from a laboratory demonstration to becoming one of the most widely used coherent light sources in the mid-infrared spectral region.[38] While the first QCL required cryogenic temperatures, pulsed room-temperature operation was achieved as early as 1996.[39] However, due to limitations in thermal management, continuous wave (CW) operation initially remained constrained to cryogenic temperatures up to 175 K.[40] The first CW operation at temperatures achievable with a thermoelectric cooler was demonstrated in 2001,[41] followed by CW room-temperature operation the following year.[42]

The room-temperature wall-plug efficiency, defined as the ratio of extracted optical power to injected electrical power, has steadily improved, reaching 22% in CW operation with an output power of 5.6 W[43] and exceeding 30% with an output power of 23 W in pulsed operation.[44] QCLs now span a broad spectral range, covering wavelengths from approximately 2.6 µm[45] to 25 µm[46] in the mid-infrared and frequencies from 1.2 to 5 THz in the terahertz band.[47, 48, 49] As materials epistructures and methods of thermal management developed with time, also the threshold current densities of the QCLs decreased from initially 15 kA/cm^2 of the device presented in reference [37], down to devices with threshold current densities below 1 kA/cm^2.[50] Unlike conventional diode lasers, which rely on interband transitions within a single material, QCLs utilize intersubband transitions within a multiple quantum well heterostructure to generate light. As depicted in Figure 1.6, in a QCL, electrons are injected into the conduction band of a precisely engineered quantum well structure, where the wells create discrete energy levels (subbands). As an electron transitions from a higher energy subband (E_3) to a lower one (E_2), it emits a photon. The energy difference E_3-E_2 between these subbands determines the wavelength $\hbar\omega$ of the emitted light. The cascading nature of QCLs is achieved by repeating this quantum well structure multiple times.

After emitting a photon in one section, the electron tunnels through a barrier into the next stage, where it can emit another photon by repeating the described process. This mechanism continues through many stages, allowing a single electron to generate multiple photons, significantly enhancing the laser's efficiency as described earlier. The optical gain in a QCL is the amplification of the light wave as it propagates through the active region of the laser. The gain depends on several factors, including the population inversion, which describes the difference in electron population between the upper and lower lasing states, the dipole matrix element, and

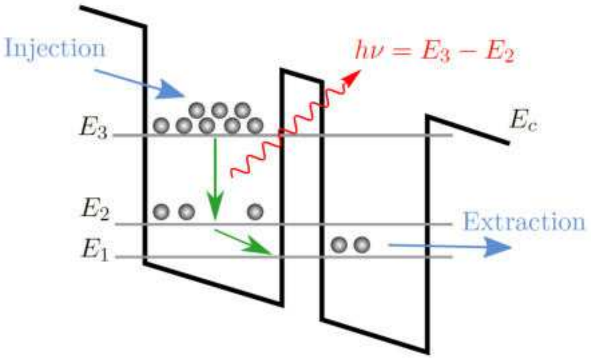

Figure 1.6: A schematic illustration of the conduction band diagram and energy levels of an intersubband laser. The tunable energy difference $h\nu$=E$_3$-E$_2$ determines the wavelength of the emitted photon. In quantum cascade lasers, multiple stages are connected in serie. Figure taken and adapted from [31] and [25]

the density of states. The gain coefficient g in a QCL can be expressed as

$$g = \tau_3 \left(1 - \frac{\tau_2}{\tau_3 2}\right) \frac{4\pi e z_{32}^2}{\lambda_0 \epsilon_0 n_{\text{eff}} L_p} \frac{1}{2\gamma_{32}}, \tag{1.11}$$

where e is the electron charge, λ_0 is the wavelength of the emitted light, z_{32}^2 is the dipole matrix element, L_p is the length of a single active region period plus injector, ϵ_0 is the permittivity of free space, n_{eff} is the effective refractive index of the medium, γ_{32} describes the full width half maximum (FWHM) value of the luminence spectrum. The transition time between the energy levels E$_3$ and E$_2$ and the level lifetimes are given through τ_{32}, τ_3 and τ_2 respectively.[51] A larger dipole matrix element leads to a stronger interaction between the electromagnetic field and the electrons, resulting in higher emission probability for photons. This increased probability enhances the optical gain of the laser. Thus, achieving high optical gain in QCLs requires not only creating a significant population inversion but also designing the quantum wells to have large dipole matrix elements. This combination ensures efficient light emission and amplification, which are critical for the laser's operation. The structure of a QCL is highly complex, involving precise fabrication of hundreds of layers epitaxially grown onto each other. Common material combinations for QCLs include InGaAs/InAlAs on an InP substrate or GaAs/AlGaAs on GaAs substrate. A single stage is comprised of an electron injector, the active region where the optical transition takes place and an extractor region, that works as the injector for the following stage. Cascading of this structure allows the "recycling" of

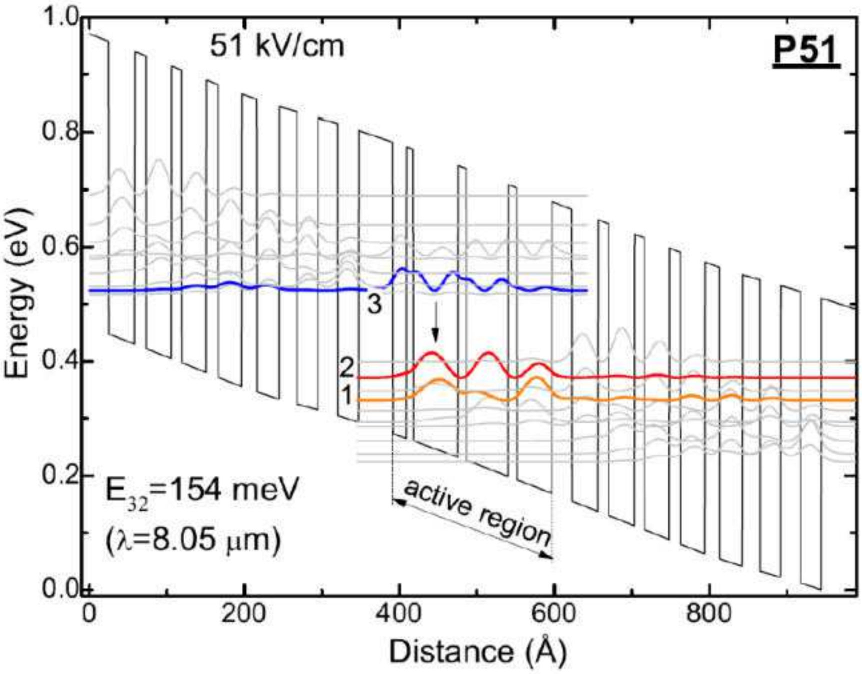

Figure 1.7: Simulated conduction band diagram of a representative QCL material. In this case, the transition energy between E_3 (blue wavefunction) and E_2 (red wavefunction) is given with 154 meV which corresponds to a photon wavelength of λ=8.05 µm. The transition itself is shown through the black arrow. Fast depopulation of the lower laser level E_2 is achieved through LO phonons over the energy level E_1 (orange wavefunction). Adapted from [52] and reprinted with permission from [53]

electrons as they lose energy in form of photons in every active region as they travel down the cascade. Through the creation of minibands by intelligent QW coupling in the injector region, a reservoir of electrons can be created and the availability of electrons is altered through appropriate doping of the involved materials. Figure 1.7 shows a simulated conduction band diagram of a representative QCL material. When an external bias is applied, electrons are delivered to the upper lasing level E_3 in the active region through the miniband that is formed through the superlattice of QWs on the left side of the active region area. The optical transition itself happens in the first active region QW, shown through the black arrow. To achieve a sufficient population inversion, the lower lasing level E_2 is quickly depopulated by the extraction wavefunction E_1 through resonant LO-phonon scattering.[54] Those two wavefunctions again are part of a miniband that at the same time acts as the extractor region as well as the injector region for the next cascade. The number of active stages in QCL devices typically ranges in a region between 20-40 with exceptions of devices with fewer than ten or up to 100 stages.[55, 56] QCLs, especially with growing number of stages, generate significant heat during operation, which must be effectively managed to maintain performance and prevent damage. This is typically achieved through the use of proper device mounting technologies on special heat sinks and careful thermal design of the device structure itself. To guide the emitted light, the active region of QCLs is incorporated into a waveguide structure, typically involving cladding layers that confine the light within the active region to maximize the gain. The waveguide must be designed to support the emitted MIR wavelengths, which requires careful consideration of the refractive index and thickness of the cladding materials.

Interband Cascade Lasers

Similar to QCLs, the origins of ICLs reach back to the mid 1990s, where interband tunneling fist was proposed as an effective approach to remove carriers from the lower lasing level of intersubband lasers.[26] From there on, refinements of the epi-layer structure lead to the first experimental implementation of an ICL in 1997.[57] Although the band structure design of ICLs was refined within a few years to closely resemble the structure used in modern ICLs, incorporating a hole injector[27] and a two-well type-II interface (the so-called W-quantum well),[58] operation possibilities at elevated temperatures were limited.[59] The first pulsed lasing operation at room temperature was reached in 2003,[60] while CW operation at room temperature was finally achieved in 2008. This device introduced the use of GaSb separate-confinement layers (SCLs) into the state of the art ICL design.[61] A major design advancement occurred in 2011, when the previously intrinsic imbalance of carrier densities in the active wells of ICLs was identified and addressed through heavy n-type doping of the electron injector regions.[62] This modification led to a significant reduction in threshold current densities down to values of 98 A/cm^2 in pulsed operation[63] and around 300 A/cm^2 in CW operation at room temperature.[64] CW operation at room temperature of ICLs based on the GaSb material system has been shown in a wavelength range between 2.7 µm[65] up to 6.1 µm,[66] exhibiting a performance sweet-spot at wavelengths around 3-4 µm. The origin of this property was identified recently, showing possibilities to mitigate the performance limitations for longer wavelengths.[67] InAs-based ICLs show pulsed emission wavelengths of up to 13 µm at a temperature of 120 K.[68] Output powers of ICLs reach values of 500 mW in CW operation and maximum wall-plug efficiencies of 18 %, which compares to the maximum 22 % of a QCL.[69]

ICLs combine the benefits of both interband and intersubband transition mechanisms, offering efficient light emission through an interband transition with reduced power consumption compared to QCLs. This can be attributed to the stronger na-

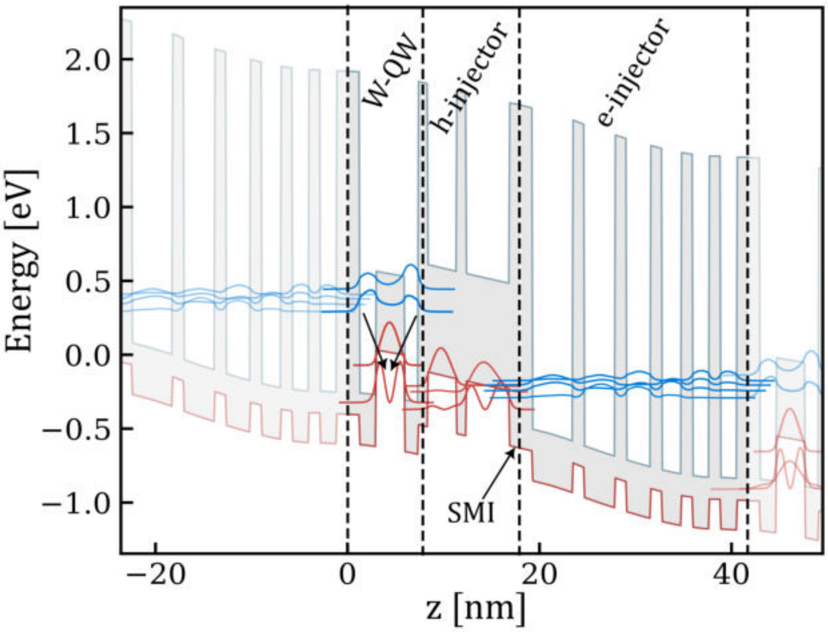

Figure 1.8: Simulated band diagram of a representative ICL material. The conduction band as well as the valence band profiles are plotted with electron injector minibands in blue and hole injector bands in red. A single period is highlighted consisting of the W-QW and the hole/electron injector regions separated by the semimetallic interface (SMI). Reprinted and modified with permission from [70].

ture of interband transitions due to the mentioned higher overlap integral between initial and final states. The structure of an ICL consists of alternating layers of different semiconductor materials, typically involving combinations like InAs/GaSb, GaInSb or InAs/AlSb. These layers form the quantum wells and barriers necessary for the cascading process. The quantum wells are carefully engineered to create discrete energy levels (subbands) within the conduction and valence bands. Figure 1.8 shows the band structure of a representative ICL material incorporating the before mentioned W-quantum well design (W-QW). The name originates from the appearance of the growth design, where a single GaInSb QW, that is used to confine holes, is sandwiched between two InAs QWs, that are needed to confine electrons. This creates a type-II QW arrangement in which the conduction band minimum and the valence band maximum appear in two different materials and the optical transition is happening via a interband tunneling process.[28, 71] The spatial wavefunction overlap for a type-I quantum well design (where electrons and holes are located in the same well) is commonly better than for a type-II transition, but the latter can effectively suppress Auger scattering (nonradiative relaxation) processes which, when combined with the possibility of cascading shows better overall performance figures.[72] The internal generation of holes and electrons is facilitated through the so called semimetallic interface (SMI) that separates the hole injector region from the electron injector region of the next cascade. There, when a bias is applied, the upper valence band edge of a GaSb QW surpasses the lower conduction band edge of an InAs QW that leads to the generation of equal hole and electron densities. Through the applied bias, the electrons are transported away from the SMI in direction of the electron injector while the holes are purged through the hole injector and confined in the hole QW.[62] The cascading nature of ICLs is achieved by repeating the quantum well structure multiple times. This multi-stage configuration allows for the re-use of carriers which reduces the threshold current and increases the efficiency of the laser. As mentioned, the dipole matrix element of interband transitions is way higher as of intersubband transitions. One contribution to this are the lifetimes of the carriers in the upper laser level. While upper state lifetimes of ICLs are in the range of nanoseconds, the intersubband lifetimes as in QCLs are with picoseconds shorter by two orders of magnitude.[73] Thus, ICLs show higher modal gain per stage and compared to QCLs, usually only employ 5-15 stages.[74, 75] Each stage of the ICL contributes to the overall light output, and the cumulative effect results in higher output power and efficiency compared to single-stage devices. The efficiency of an ICL is further enhanced by the use of a waveguide structure that confines the light within the active region, similar to the mechanism in QCL devices. This typically involves cladding layers that have a lower refractive index than the active region, ensuring that the light remains confined and experiences multiple passes through the gain medium.

1.8.3 MIR Detectors

Infrared detectors are crucial for sensing light emitted by coherent sources or black-body radiators. The primary detection mechanisms can be divided into three groups: thermal detectors measuring radiation through a change in temperature, interband detectors and intersubband detectors, that are both photonic detectors utilizing the photoelectric effect.

Thermal Detectors

Thermal detectors are sensitive to the absorbed radiation power, which increases the temperature of the isolated detector element. This temperature change can be translated into a measureable voltage through the thermoelectric effect, [76] or a change in resistance through the bolometric effect.[77] As the temperature change in bolometers is always connected to the thermal capacity of the absorber material, these detectors exhibit a rather slow response time. Another sensitive IR-detector is the so called Golay-cell, that uses the thermal expansion of an absorber material to move a membrane for optical readout.[78] Another family member of thermal detectors is the pyroelectric detector. Pyroelectricity refers to temperature dependent electrical polarisation of a material. Thus, impingind radiation creates a readable temporary voltage by changind the materials polarisation. A well known pyroelectric detector based on deuterated triglycine sulfate (DTGS) is commonly used in FTIRs. [79]

Interband Detectors

In contrast, photonic detectors operate based on photon-induced electronic excitations, with the excited electrons being measured via an electronic readout scheme. Direct band gap detectors utilize the fundamental transition of electrons from the valence band to the conduction band.[80] The group of interband detectors can be divided into photoconductive and photovoltaic detectors according to the underlaying physical working principle. While photoconductive detectors express detection through a change of the materials conductivity, photovoltaic detectors generate current flow without applying an external voltage. The development of interband detectors has evolved significantly over the decades, starting with the early use of materials like Indium Antimonide (InSb) and mercury cadmium telluride (MCT). InSb detectors were among the first widely used infrared detectors, with high sensitivity in the 3–5 µm range, making them ideal for thermal imaging and sensing applications. Following the success of InSb, MCT detectors became popular due to their tunable bandgap, which allowed for the detection of infrared radiation across a broader range, from the mid- to long-wave infrared regions. MCTs, available in photoconductive and photovoltaic configurations, remain a standard material for high-performance infrared detectors.[81] In Schottky detectors, incident photons excite electrons in a metal to higher energy states. These electrons must then overcome a potential barrier (the Schottky barrier) at the metal-semiconductor junction to be detected as a measurable current.[82] In recent years, type II-bandgap detectors, such as the interband cascade detector (ICD) or the interband cascade infrared photodetector (ICIP) have emerged as a promising technology for infrared detection.[83] Similar to ICLs, these detectors leverage the unique band structure of type-II heterostructures. In the literature, the terms ICIP and ICD are often used interchangeably. Different to the ICDs using the classic W-quantum well structure as an absorption region,[84] there are designs taking advantage of a type-II superlattice structure, increasing their photon absorption efficiency, first demonstrated in 2010.[83] ICDs

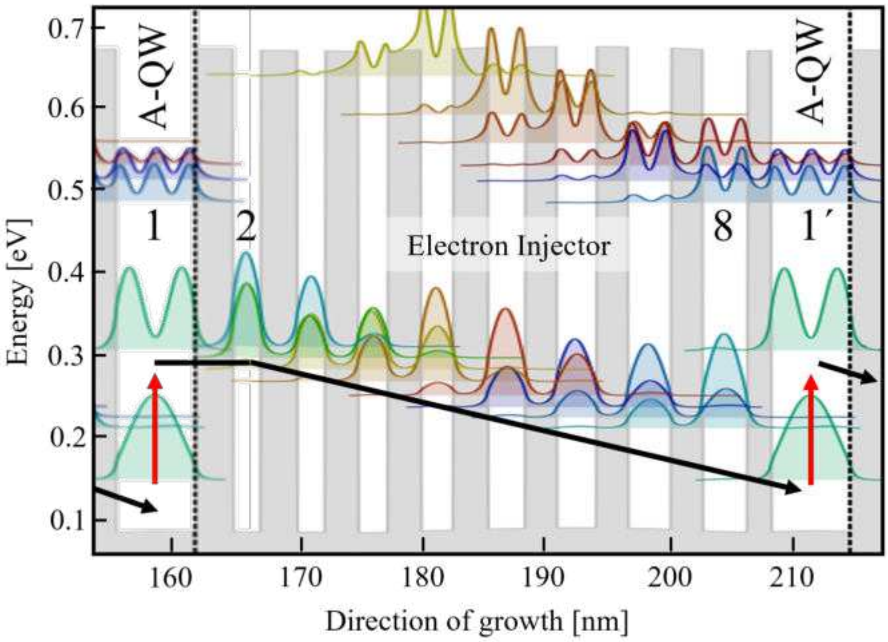

Figure 1.9: Simulated band diagram of a representative QCD material. The vertical dotted lines indicate the layers of one single period, which is repeated several times. The black arrows show the current path while the optical transitions are highlighted by the red arrows.[89]

show extraordinary noise characteristics at room temperature operation rendering them the perfect candidates for high speed data transmission applications.[85, 86]

Intersubband Detectors

Quantum well infrared photodetectors (QWIPs) operate by utilizing quantum wells, where electrons are confined in a semiconductor material. When photons with sufficient energy strike the detector, they excite electrons from a lower energy state within the quantum well to a higher energy state. These excited electrons must then overcome the barrier (formed by the quantum well's confining layers) to contribute to the photocurrent.[87] In the last years, QCDs have been developed, which, like QCLs, operate on a cascading scheme.[88] Unlike QWIPs, each excited electron in QCDs is recycled and guided to the lowest energy level of the next active quantum well.[2] Figure 1.9 shows a schematic band structure of one stage of a representative QCD material. The bandstructure of a QCD is similar to the bandstructure of QCLs without external bias. Through the cascaded structure of the electron injector, the lower energy level in the active quantum well is highly populated with electrons. If a photon with an adequate energy $\hbar\omega$ impinges in the active quantum well (A-QW), it elevates an electron from the lower level into an excited state. From there, the

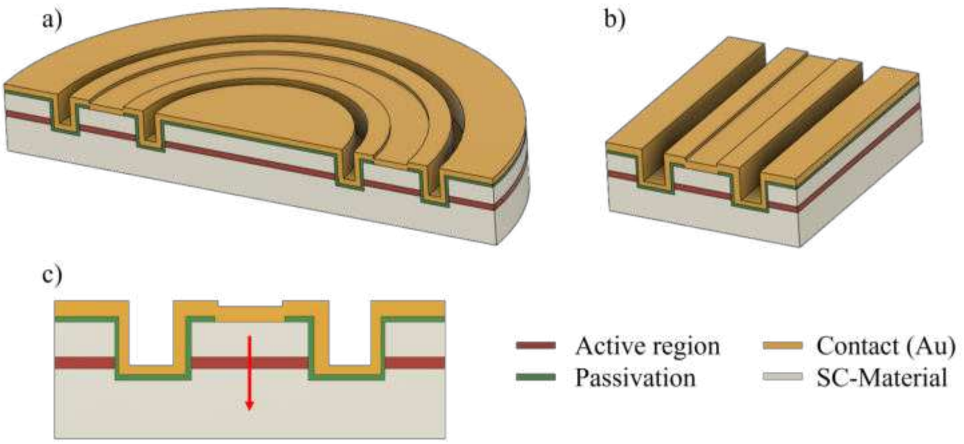

Figure 1.10: Illustrations of a 180 ° cutout of a ring shaped waveguide (a) and a Fabry-Perot (linear) (b) waveguide in ridge configuration. (c) Lateral mode confinement is achieved through waveguide definition (removal and deposition of material) and the resulting lateral change in reflective index. The current path is represented through the red arrow.

electron is extracted via resonant tunneling into QW 2 and cascades down to QW 8 via LO-phonon scattering and finally again populates the lower level of QW 1´ which is the active quantum well of the next stage. This procedure is repeated if another photon impinges. QCDs have become increasingly important in on-chip sensing applications due to their sensitivity, rapid response time, and ability to operate at room temperature. QCDs are particularly valuable in compact, integrated photonic circuits where space is limited, enabling advanced sensing capabilities in a miniature form factor as they can be realized with the same materials as QCLs.[90] This makes them ideal for on-chip applications.

1.9 Optical Waveguides, Cavities and Mode selection

Optical waveguides and resonators are fundamental components in the design and operation of semiconductor lasers. The waveguide is designed to ensure proper confinement of the mode in the active region to maximize gain. This is realized by sandwiching the high reflective index active region material with a cladding material with a lower refractive index. The resonator is crucial to provide the necessary feedback mechanism to achieve lasing. All waveguides described in this thesis were fabricated in the ridge configuration as seen in Figure 1.10 To enhance the mechanical stability of the structures, waveguides are usually processed with surrounding trenches instead of in free-standing geometry. As the red arrow in

Figure 1.10(c) shows, the current path is defined through an opening of the isolating SiN passivation layer.

1.9.1 Fabry-Perot Cavities

Fabry-Perot cavities are integral components in many semiconductor lasers, providing the necessary feedback mechanism for lasing action. These cavities consist of two parallel mirrors, typically formed by cleaving the facets of the semiconductor material, thereby creating a resonant optical cavity.[91] The quality of these facets, which act as optical mirrors, is crucial for the performance of the cavity. An alternative method to form these facets is through deep etching. Although this method can result in lower mirror quality, it enables the creation of mirror facets in situations where cleaving the sample is not feasible. Light reflecting back and forth between these mirrors constructively interferes at specific wavelengths, known as the resonance frequencies, leading to amplification of the optical signal. The reflectivity for a plane wave between two materials with different refractive indices at normal incidence is given by

$$R = \left(\frac{n - n_0}{n + n_0}\right)^2, \tag{1.12}$$

in this case with n being the refractive index of the semiconductor material and with n_0 being the refractive index of air. For a typical semiconductor material with refractive index of around n=3.2 and air as the surrounding material, a facet reflectivity of $R = 27\,\%$ is calculated. This means, that $73\,\%$ of an incoming plane wave is coupled out. Covering one facet with a high reflectivity material to supress outcoupling, increases the outcoupled power on the other facet. This is a standard method to increase the output power of semiconductor lasers. The resonance frequencies ν_m of a Fabry-Perot cavity are given by the condition for constructive interference:

$$\nu_m = \frac{mc}{2n_{eff}L} \tag{1.13}$$

where m is an integer (the mode number), c is the speed of light in a vacuum, n_{eff} is the effective phase index of the material inside the cavity, and L is the length of the cavity.[92]

In a typical Fabry-Perot cavity, multiple longitudinal modes can oscillate simultaneously, leading to multimode operation. This occurs because the cavity supports several resonance frequencies within the gain bandwidth of the semiconductor material. The large number of longitudinal modes can for example be utilized to generate frequency comb emission. Frequency combs are generated using a broadband gain material together with a locking mechanism, such as injection locking or mode locking, to produce a series of equally spaced phase-locked modes.[93, 94, 95] In an ordinary multi-mode Fabry-Perot laser, the modes are usually not coupled and are not exactly equidistant due to the wavelength dependence of the group refractive index, which is a measure of how the phase velocity of light within a medium changes with its wavelength, influencing the propagation of optical pulses through the material. Therefore, a multimode laser alone is not sufficient to create a frequency comb. Although engineering of the group velocity dispersion can enhance stability and coherence in some frequency combs, it is the nonlinear mechanisms that establish phase-locking between modes that are essential for comb formation.[96] To achieve single-mode operation, several techniques can be employed. Shortening the cavity length increases the free spectral range (FSR), which can help ensure that only one mode falls within the gain bandwidth of the laser. External cavity lasers can also achieve single-mode operation by coupling the semiconductor laser output to an external cavity with a wavelength-selective element, such as a diffraction grating, narrowing the linewidth and selecting a specific wavelength. Using distributed feedback (DFB) structures, which integrate gratings into the cavity to provide wavelength-selective feedback, can favor a single longitudinal mode over others. This method will be further explained in section 1.9.3.

1.9.2 Ring Resonators

Circular (ring-shaped) cavities (see Figure 1.10(a)) in semiconductor lasers are highly effective resonators that utilize the principles of total internal reflection to confine light. The first implementation of a circular cavity was realized as a microdisc laser instead of the established ring resonators described in this thesis.[97] Circular cavities allow for the formation of whispering gallery modes (WGM), where light waves travel along the circumference of the ring, reflecting internally with minimal loss.[98] The absence of mirror facets as in Fabry-Perot cavities, which were identified as a restraining factor for device performance, is particularly advantageous for achieving high Q-factors (quality factors), leading to efficient lasing with low threshold currents.[97]

The resonance frequencies ν_m in a circular cavity are given by the condition that the round-trip phase accumulation must be an integer multiple of 2π:

$$\nu_m = \frac{mc}{2\pi r n_{eff}} \tag{1.14}$$

where m is an integer (mode number), c is the speed of light in a vacuum, r is the radius of the ring, and n_{eff} is the effective phase index of the material inside the cavity.

Whispering gallery modes in circular cavities are characterized by their ability to confine light efficiently around the periphery of the ring. These modes are named after the acoustic phenomenon observed in circular whispering galleries, where sound waves can travel along the curved surface with minimal loss.[99] Similarly, in optical WGMs, light is confined due to continuous total internal reflection at the curved boundary of the cavity.[100] Figure 1.11 shows two mode simulations of ring cavities with a radius of 120 µm (a) and 50 µm (b). It can be seen that the mode is not centered in the waveguide but pressed towards the outer radius of the ring. This effect decreases with increasing ring radius and vanishes at linear waveguides, which can be seen as circular waveguides with an infinitely large ring radius.[102] Circular-shaped cavities can operate in either multimode or single-mode configurations. In multimode operation, multiple longitudinal and transverse modes are supported simultaneously, each with different resonance conditions. This can lead to complex interference patterns and less coherent output, which may be useful in some applications but can also reduce the overall stability and coherence of the laser output.[103]

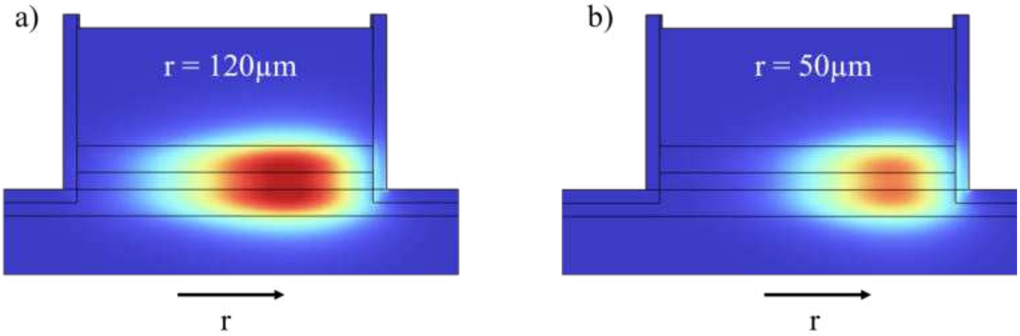

Figure 1.11: COMSOL mode simulations of ICL ring waveguides with center radii of a) 120 µm and b) 50 µm. Concentration of the mode along the outside waveguide wall is strongly visible.[101]

Achieving single-mode operation in circular cavities involves careful design to ensure that only one mode is supported within the gain bandwidth. Higher-order lateral modes can be effectively suppressed by reducing the waveguide width, as this introduces higher propagation losses for these modes. This strategy ensures that only the fundamental mode is efficiently supported, improving the overall mode purity and performance of the waveguide.[104] However, the absence of reflecting facets in circular cavities poses challenges in extracting the light. As mentioned, in traditional

Fabry-Perot cavities, the cleaved facet reflect a portion of light to create optical feedback and outcouple the rest. In contrast, circular cavities require alternative methods to couple the light out efficiently. If the outer sidewall of the ring waveguide is not covered with metal, light will be radially scattered, making it difficult to collimate the entire emitted optical power. To manage this, techniques such as evanescent coupling to a nearby waveguide are often employed.[105] Moreover, the unique geometry of circular cavities can be leveraged for vertical emission. By incorporating a second-order DFB grating or by etching a pattern into the top surface of the ring, it is possible to diffract the confined light out of the plane of the wafer, achieving vertical emission.[106, 107] This vertical output is highly desirable for applications requiring direct coupling to external optics and compared to linear surface emitters, offers a radial-symmetric farfield, sharing symmetry with most discrete optical elements such as lenses and mirrors.[108] Despite the engineering challenges, vertical emission from circular cavities offers a pathway to highly efficient, compact, and versatile laser sources for a wide range of photonic applications.[109]

1.9.3 Mode Selection with Distributed Feedback Gratings

As mentioned, semiconductor lasers doe not inherently operate in single mode emission. The gain medium within the active region offers a finite bandwidth for amplification, allowing multiple waveguide modes within this wavelength range to achieve lasing threshold, and sometimes, multimode emission is even desired. For most of the application forms mentioned in section 1.10, single-mode operation of the laser source is imperative, where the laser oscillates in the fundamental transverse, lateral, and longitudinal modes. To ensure only one mode achieves lasing, the losses for other waveguide modes must be selectively increased. This can be accomplished through simple geometric modifications, meaning reduction of the cavity size,[110] or more complex structures such as coupled cavities,[111] external cavities[112] or gratings in different forms. The subsequent section will focus on the mode selection and vertical outcoupling through the implementation of second order DFB gratings into the laser waveguide.

DFB gratings are essential components in fabrication of semiconductor lasers. They are employed to achieve single-mode operation by providing wavelength-selective feedback directly within the laser cavity. The DFB structure is typically integrated into the laser waveguide and consists of a periodic variation of the refractive index or the gain/loss profile along the length of the waveguide. This is usually achieved by either depositing a metal or dielectric grating structure on the waveguide, or, more common, to etch periodic slits into the waveguide surface.[113]

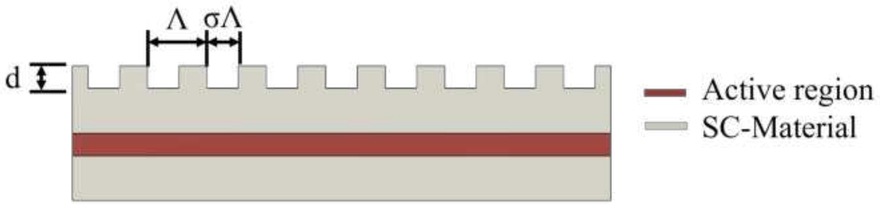

Figure 1.12: Illustration of a linear ridge laser cavity with a DFB grating implemented atop the waveguide structure. The demensions of the grating etch depth d, the grating period Λ and the grating duty cycle σ are shown.

Figure 1.12 illustrates a schematic of an etched DFB grating, highlighting three critical design parameters: the grating period Λ, the grating etch depth d, and the grating duty cycle σ. The grating duty cycle is defined as the ratio between the etched groove width and the grating period Λ. This periodic structure establishes a Bragg scattering condition, leading to interference between the forward and backward propagating wave for only certain wavelengths. The Bragg condition is given by:

$$\lambda_B = \frac{2n_{\text{eff}}\Lambda}{m}, \tag{1.15}$$

where λ_B is the Bragg wavelength, n_{eff} is the effective phase index of the waveguide mode, Λ is the grating period, and m is the diffraction grating order. The strength of the coupling between the two counter-propagating waves is the coupling constant

$$\kappa = \frac{\pi \Delta n}{\lambda_0} + j\frac{1}{2}\Delta\alpha, \tag{1.16}$$

giving a measure of the feedback per unit length (cm^{-1}).[114] Depending on the variation of the refractive index Δn and the modal gain $\Delta\alpha$ in equation 1.16, the coupling can be distinguished into two extrema: When κ is real and the variation of $\Delta\alpha$ is zero, the modes are purely index coupled and form a stop-band centered at the Bragg frequency $\omega_B = c_0/\lambda_B$, similar to a Bragg mirror, nearly fully reflecting and destructively interfering at this frequency. Thus, index coupled waveguides are not able to lase at the Bragg wavelength, but show the lowest lasing tresholds for the two modes at the short- and long wavelength stop-band edge. The other extreme case of coupling is pure gain coupling, when κ is imaginary and the variation of refractive index Δn is zero. Here, a mode with antinodes in the grating region with higher gain will be excited and no stop band is formed leading to the lowest lasing threshold for a mode with frequency ω_B. In reality, as variations in refractive index lead to variations in gain, a mix of the mentioned cases is the dominating coupling scheme, lifting the mode degeneracy of an index coupled DFB grating, enabling stable single mode emission.[115, 31]

Thus, by precisely designing the grating period Λ, a DFB laser can be tailored to emit at a specific single wavelength, ensuring high spectral purity and stability. In addition to mode selection, DFB gratings can also be engineered to facilitate vertical emission, which is particularly advantageous for integrating lasers into planar photonic circuits and for applications requiring direct emission perpendicular to the substrate. Vertical emission can be achieved by incorporating second-order DFB gratings (m=2). As a second order grating also incorporates the first order diffraction, mode selection and vertical emission can be targeted at once. Higher order diffraction gratings can under certain circumstances even facilitate horizontal emission of the laser mode on an elevated emission plane above the laser.[116] A detailled description on distributed feedback gratings and a thorough explaination of the corresponding theories can be found in [31]. For lasers operating in the MIR, following equation 1.15, the feature size of the grating slits is in the range of a few hundreds of nanometers. Thus, fabrication of DFB gratings in QCLs and ICLs involve precise lithographic techniques to create the periodic structures with high accuracy. As the limits of optical lithography procedures taking use of the so called i-line (wavelength of 365 nm) are reached at feature sizes of around 0.6-0.8 µm, these structures are usually defined through electron-beam lithography. The grating duty cycle and grating depth must be carefully controlled to achieve the desired feedback strength and emission properties. Overall, DFB gratings play a critical role in enabling single-mode operation and vertical emission in semiconductor lasers, enhancing their functionality and integration capabilities for advanced photonic applications. The ability to precisely control the emission wavelength and even the emission direction through DFB gratings offers a tremendous enhancement in device versatility.

1.10 Use Cases and Potential

1.10.1 Spectroscopic Applications

The MWIR and LWIR spectral regions offer a widespread variety of applications. In the realm of MIR spectroscopy, materials are commonly categorized into three states of matter: solids, liquids, and gases. Each state presents unique challenges and opportunities for spectroscopic analysis, primarily due to differences in molecular mobility and intermolecular interactions. According to the Beer-Lambert Law, the absorbance of a specimen

$$A = \epsilon \; c \; l \tag{1.17}$$

is linearly connected to the analytes concentration c and the distance l the light has to travel. The constant ϵ represents the molar absorptivity of the specimen under test.[117] This unfolds obvious challenges that arise with measuring different species in different phase conditions. While solids are mostly opaque, gases often need longer interaction paths in order to sufficiently interact with the analyzing lightwave compared to liquids. Complementary to x-ray diffraction methods, MIR spectroscopy can be used to examine solid structures and deliver additional information about structural features as phase composition or the identification of single compounds in solid materials. Significant usecases are widespread: The determination of phase composition for example is an important factor to ensure proper mechanical stability and hydration behavior of cementitious structures.[118, 119, 120] Soil is a complex mixture of minerals, organic matter and micro-organisms. In times of industrialized agriculture, soil fertility is one of the most important factors concerning crop yield. In this matter, MIR spectroscopy allows a precise analysis of the soils constituents and thus paves the way for precision fertilization. As a side effect of increased soil fertility, the environmental impact can be decreased as overfertilisation is prevented.[121, 122, 123] As also many pharmaceutical molecules show interactions with MIR radiation, spectroscopic methods are often used to characterize pharmaceutical samples, able to destinguish even polymorphisms in substances.[124] Another popular application is the exact determination of color pigments used in paintings through MIR spectroscopy.[125]

Applications of MIR spectroscopy in liquids are diverse and impactful. For instance, in the pharmaceutical industry, it enables the characterization of various liquid formulations, facilitating the identification of active ingredients and potential impurities.[126] Significant progress towards the ‘holy grail’ of MIR spectroscopy in healthcare, a handheld, multi-analyte detection device, has been made using tunable ICL and QCL devices. One promising application is non-invasive glucose measurement, which demonstrates the potential of these technologies for real-time health monitoring.[127, 128] Moreover, MIR spectroscopy proves instrumental in monitoring chemical reactions and assessing reaction kinetics in liquid-phase processes, aiding in the optimization of synthetic routes and quality control in manufacturing even in real time.[129, 130] Environmental monitoring benefits from MIR spectroscopy as well, particularly in the analysis of water quality. By detecting specific chemical signatures associated with pollutants or contaminants, this technique facilitates rapid and sensitive screening of water samples, contributing to the preservation of aquatic ecosystems and safeguarding public health.[131] In the realm of food science and agriculture, MIR spectroscopy finds applications in assessing the nutritional content, authenticity, and quality of liquid food products. Whether analyzing the composition of beverages, oils, or dairy products, MIR spectroscopy offers a non-destructive and efficient means of quality assurance.[132, 133] With increasing atmospheric pollution caused by the vast exploitation of our planets resources and the use of fossil fuels, the importance of atmospheric, environmental and process monitoring is growing.[134, 135] The main isotope of atmospheric CO_2, with an abundance of around 98%, is $^{12}C^{16}O_2$. In contrast, the radioactive isotope $^{14}C^{16}O_2$ is only present at the ppb (parts per billion) level. IR spectroscopic measurements of our atmosphere not only allow for precise determinations of CO_2 levels but also provide a method for tracing the origins of this significant greenhouse gas by monitoring the levels of $^{14}C^{16}O_2$: While CO_2 from natural sources always contains traces of $^{14}C^{16}O_2$, the carbon in fossil fuels is entirely depleted of ^{14}C due to its half-life of around 5,700 years.[136, 137] Of course, MIR spectroscopy of gases is also widely used in healthcare. Human breath is a complex mixture of gases and volatile organic compounds (VOC). Many VOCs are important biomarkers indicating various metabolic processes and some can be indicating the emergence of different diseases. Real time MIR breath analysis thus can be used to monitor and diagnose various health conditions as well as the effectiveness of treatments.[138, 139] MIR gas sensing is an application that is not solely happening on planet earth. NASAs Mars exploration rover Curiosity beared two MIR laser sources within its so called "Sample Analysis at Mars instrument suite". A tunable diode laser at λ=2.78 µm, able to scan isotope lines of H_2O and CO_2, as well as a tuneable ICL at λ=3.27 µm used for methane detection.[140]

1.10.2 Free Space Optical Communication

In strong contrast to sensing applications, where strong interactions between radiation and matter is desired, data transmission via free space optical (FSO) communication requires stable, undisturbed links. As atmospheric conditions such as rain, fog, dust, smoke or other aerosoles are consantly influencing FSO links, transmission wavelengths that are insensitive to such perturbations are seeked.[141] The MIR spectral region offers two atmospheric windows, the high-frequency window between approximately λ=3-5 µm and the LWIR window between around λ=8-12 µm.[142] The LWIR window, with its O_3 absorption cutout between λ=9.5-10 µm, easily outperforms the MIR window in terms of adverse weather and turbulent atmospheric conditions.[14, 143] For long time, adequate LWIR sources and detectors were missing but with the upcoming and further commercialisation of QCL devices, this gap finally was closed. Stable data transmission links in metropolitan areas with typically high aerosol pollution were shown and through the possibility of ultra fast modulation of QCLs, error-free data transmissions of up to 10 Gbit/s could be reached, setting new benchmarks on the way to 6G datatransmission with theoretical limits in the Tbit/s range.[144, 145]

CHAPTER 2

HIGH-RESPONSIVITY OPERATION OF QUANTUM CASCADE DETECTORS AT 9 μm

2.1 Motivation, Background and State-of-the-Art

QCDs, first demonstrated in 2002, support high-speed and room-temperature operation,[88] with low dark-current detection due to their unbiased operation, which is crucial for low-noise applications.[146] Most existing literature concerning quantum cascade detectors focuses on wavelengths below 7.5 µm, with few exceptions covering the atmospheric window at 9 µm,[147] and extending up to wavelengths of 19 µm in the infrared and beyond, able to detect teraherz ratiation.[148] Traditional telecommunication in the near-IR spectral range at 1.5 µm is effective for fiber-based long-range data transmission. However, in free-space geometries, it faces limitations in bandwidth and transmission, especially under turbulent atmospheric conditions. An often-used approach in mid-infrared FSO systems involves wavelength conversion techniques, where classical telecom transceivers operate at 1.5 µm and are then converted to MIR wavelengths ($\sim$3-4 µm) using difference frequency generation (DFG). This method has achieved impressive data rates, such as single-channel 10 Gb/s in-phase and quadrature (IQ) modulated transmissions[149] and up to 300 Gb/s with wavelength- and mode-division multiplexing.[150] Despite these successes, the high power consumption and hardware complexity associated with nonlinear wavelength conversion hinder its practical deployment. A promising alternative lies in the development of direct-emission semiconductor lasers and photodetectors, although challenges such as material limitations, low efficiency, thermal noise, and fabrication complexity currently limit their practicality. The state-of-the-art in QCDs operating in the long-wave infrared (LWIR) region, particularly within the 9 µm atmospheric window, is marked by both advancements and challenges. Recently, as the use of QC-devices is growing in FSO links, advances in LWIR QCD operation were made with high bit-rate optical transmission lines with QCDs operating at roomtemperature.[151, 152, 145] With ongoing advancements, these devices hold the potential to provide more efficient and simplified solutions for LWIR FSO applications. LWIR QC-based systems as shown here, offer significant advantages in these situations. The realization of monolithic devices, integrating active and passive components like lasers, detectors, and waveguides on a single chip, makes them suitable for sensing and telecommunication applications.[153, 5] Even more important for compact heterodyne detection is their linearity and high saturation intensity.[133] LWIR free-space optical links promise small device footprints, low power consumption, and high modulation speeds with stable connections even under harsh weather conditions, including fog and rain.[154, 155] Additionally, QCLs offer benefits such as high direct modulation capabilities, reaching frequencies up to tens of GHz.[156] Literature suggests that systems operating in the LWIR atmospheric window (8–12 µm) are suitable candidates for such applications,[157] though, as mentioned, performance limitations of LWIR QC devices at longer wavelengths require further advancements. QCDs are evaluated using several key figures of merit. First, the responsivity (R) measures the detector's efficiency by quantifying the generated photocurrent relative to the incident optical power, which is usually expressed in A/W. On the other hand there is the noise equivalent power (NEP), which represents the minimum optical power required to produce a detector signal equal to the detector's noise, indicating sensitivity. Connected to it, the Detectivity (D), expressed in Jones (cm$\sqrt{Hz}$/W), normalizes the NEP to the detector area and measures signal detection amidst noise. Last but not least, the bandwidth determines the speed of response, essential for high-speeds required in optical communication. These parameters are critical in assessing the performance of QCDs in practical applications. The number of periods in a QCD directly impacts its figures of merit. Responsivity typically decreases with an increasing number of periods, while NEP and thus Detectivity improve with more periods as the device resistance increases, thereby reducing Johnson noise. A detailed description of the underlying mechanisms and their interplay can be found in Reference [158]. To understand the influence of the number of periods on the mentioned figures of merits in a real scenario, devices with similar characteristics and sensitivity for the same wavelengths have to be compared. We conducted initial spectral response measurements between 8 µm and 11 µm using a commercial external cavity QCL to highlight the differences between a classic QCD with 15 periods and the extreme case of a QCD that only entails a single period, both working at the same wavelength.[159] The exploration of QCDs is a significant focus of my research, motivated by their potential to revolutionize LWIR free-space optical communication systems. QCDs are particularly notable for their operation at zero external bias and low dark current and highly suitable for applications requiring linear detection and high saturation intensities. These characteristics are essential for effective heterodyne detection, a technique that promises enhanced performance in optical communication by leveraging the superposition of signals for improved signal-to-noise ratios and greater data throughput.[160]

2.2 Contribution to the Field

In the following first-author publication, an approach to mitigate performance limitations for QCDs at longer wavelengths is presented. This comparative study aims to optimize responsivity and noise behavior, which are critical parameters for the practical deployment of QCDs in communication systems. Specifically, InGaAs/InAlAs/InP ridge QCDs designed for operation at 9.124 µm were analyzed, revealing significant differences in responsivity between the single-period and 15-period devices. This detailed device analysis, supported by optical waveguide simulations, underscores the importance of optimizing the design parameters to achieve superior performance in real-world applications. We present the first room-temperature InGaAs/InAlAs ridge QCDs covering the LWIR range.
The insights gained from this study lay the groundwork for the second paper, which extends the investigation into the integration of QCDs within photonic integrated circuits (PICs). The development of mid-infrared (MIR) devices is crucial for a wide range of applications, including biomedical analysis, chemical reaction monitoring, and high-bitrate free-space telecommunication. The miniaturization of these devices into complex MIR-PICs represents a significant technological advancement, yet it is constrained by existing material and technological limitations. In summary, the investigation of QCDs and their integration into MIR-PICs represents a step towards advancing optical communication and sensing technologies. The findings from these studies not only enhance our understanding of QCD performance but also provide a blueprint for future developments in integrated photonic devices.

2.3 Publication

© 2022 publication Optica Publishing Group, Reprinted, with permission, from G. Marschick, M. David, E. Arigliani, N. Opačak, B. Schwarz, M. Giparakis, A. Delga, M. Lagree, T. Poletti, V. Trinite, A. Evirgen, B. Gerard, G. Ramer, R. Maulini, J. Butet, S. Blaser, A. M. Andrews, G. Strasser, and B. Hinkov, "High-responsivity operation of quantum cascade detectors at 9 µm,"
Opt. Express 30, 40188-40195 (2022), https://doi.org/10.1364/OE.470615 Published by Optica Publishing Group under the terms of the Creative Commons Attribution 4.0 License.

Research Article Vol. 30, No. 22 / 24 Oct 2022 / *Optics Express* 40188

Optics EXPRESS

High-responsivity operation of quantum cascade detectors at 9 μm

G. MARSCHICK,[1,5] M. DAVID,[1] E. ARIGLIANI,[1] N. OPAČAK,[1] B. SCHWARZ,[1] M. GIPARAKIS,[1] A. DELGA,[2] M. LAGREE,[2] T. POLETTI,[2] V. TRINITE,[2] A. EVIRGEN,[2] B. GERARD,[2] G. RAMER,[3] R. MAULINI,[4] J. BUTET,[4] S. BLASER,[4] A. M. ANDREWS,[1] G. STRASSER,[1] AND B. HINKOV[1,6]

[1] *Institute of Solid State Electronics and Center for Micro- and Nanostructures, Technische Universität Wien, Vienna, Austria*
[2] *III-VLab, a joint Thales, Nokia and CEA-LETI laboratory, Palaiseau, France*
[3] *Institute of Chemical Technologies and Analytics, Technische Universität Wien, Vienna, Austria*
[4] *Alpes Lasers SA, St-Blaise, Switzerland*
[5] *georg.marschick@tuwien.ac.at*
[6] *borislav.hinkov@tuwien.ac.at*

Abstract: Quantum cascade detectors (QCDs) are devices operating at zero external bias with a low dark-current. They show linear detection and high saturation intensities, making them suitable candidates for heterodyne detection in long-wave infrared (LWIR) free space optical communication systems. We present an approach to mitigate the performance limitation at long wavelengths, by a comparison of similar single and multi-period QCDs for optimizing their responsivity and noise behaviour. Our InGaAs/InAlAs/InP ridge QCDs are designed for operation at $\lambda = 9.124\,\mu$m. Optical waveguide simulations support the accurate optical characterization. A detailed device analysis reveals room-temperature responsivities of 111 mA/W for the 15-period and 411 mA/W for the single-period device.

1. Introduction

The mid-infrared spectral region is the portion of the electromagnetic spectrum, that is highly suitable for spectroscopy of gases and liquids by addressing their fundamental bending and stretching vibrations [1,2]. It also hosts multiple atmospheric transmission windows, extending to the long-wavelength infrared (LWIR). Especially, the low susceptibility towards atmospheric turbulences and small attenuation in the LWIR [3], together with the fast modulation capabilities of intersubband devices [4,5], make this spectral range highly promising for unlocking novel telecom applications [5,6]. One crucial component in telecommunication receiver systems are suitable high-performance detectors. While HgCdTe-based interband photodetectors (MCTs) are very sensitive, moderate bandwidth (low-GHz range) detectors, they have low saturation thresholds, limiting their application in heterodyne detection. MCTs are in particular not suitable for monolithic integration due to their incompatible material system. In contrast, photoconductive quantum well infrared photodetectors (QWIPs) [7,8], show high responsivities and improved high frequency behaviour (»10 GHz) [9], due to short intrinsic carrier lifetimes. One major drawback of QWIPs is their pervasive dark current, originating from biased detector operation [10]. Quantum cascade detectors (QCDs), demonstrated in 2002, support high-speed and room temperature operation [11,12]. Based on QC laser (QCL) structures relying on intersubband transitions, they allow unbiased, i.e. low dark-current, detection, opening pathways for low-noise

#470615 https://doi.org/10.1364/OE.470615
Journal © 2022 Received 14 Jul 2022; revised 13 Sep 2022; accepted 21 Sep 2022; published 14 Oct 2022

applications [13]. Even more important for compact heterodyne detection is their linearity and high saturation intensity [2]. The realization of monolithic devices, integrating active and passive components like lasers, detectors and waveguides on one chip, makes them suitable for sensing and telecommunication applications [14–16]. Extending the telecom-bandwidth to mid-infrared frequencies mitigates bandwidth and availability limitations in current fifth generation (e.g. Long-Term Evolution (LTE)) communication systems, arising from demanding high-speed breakthrough technologies like unmanned mobility, industry 4.0, e-health [17,18] and satellite communication [19]. Moreover, mid-infrared free space optical links have small device footprints, low power consumption and high modulation speeds [20,21] with high connection stability and reliability even under harsh weather conditions including fog and rain. Literature shows that systems operating in the 8-12 μm atmospheric window are suitable candidates for such systems [22], but limited due to device performance at longer wavelengths and need further improvements. QCL devices covering this wavelength range were already successfully used as atmospherically robust transmitter units [23–26]. The first 9 μm QCDs operating at room temperature took advantage of the GaAs/AlGaAs material system [5]. We present room-temperature InGaAs/InAlAs ridge QCDs at this wavelength and show an experimental comparison between similar single and multi-period QCDs in our study. The reduction of the number of periods, in order to increase the device responsivity and its impact on the noise behaviour, is an important parameter to optimize QCDs for implementation into monolithic heterodyne detectors.

2. Device design and fabrication

In this work, we demonstrate two different QCDs designed for the target wavelength of 9.124 μm: 1) a 15-period device with high-specific-detectivity, and 2) a high-responsivity single-period device. The facet-illuminated ridge devices are optimized for low-noise, high-responsivity operation. This geometry is required for the development of a monolithic photonic integrated circuit (PIC) device [27,28]. For monolithical integration of active and passive components, as for example needed for a heterodyne detection system, ridge geometry can be directly implemented. Laser, waveguide, and detector can be fabricated aligned to each other on a single chip, preventing difficult alignment procedures between components. A trade off between the optical active area and the effective electric area has to be found. Small electrical areas lead to high device resistivities and thus improve the signal to noise ratio (SNR) while large optical areas increase the device response. Mesa structures, illuminated from the top-side, show the same size of electrical and optical area while the optical area can be increased through different structures, like photonic crystal cavities or plasmonic lenses [29,30]. Ridge devices, on the other hand, can be fabricated narrow and short, reducing the electrical active area. By incoupling light from the side facet, optimal absorption lengths are ensured even though the optical active area is small compared to mesa-geometries [31,32]. Further, light polarized in growth direction can be directly detected without additional gratings [33], compared to, for example, surface detecting devices [34]. One of the most commonly used material systems in mid-IR and terahertz photonics is InGaAs/InAlAs, lattice matched to InP substrate. We used the same material system in this work grown by molecular beam epitaxy (MBE). The alternating stacking of InGaAs and InAlAs creates a series of quantum wells, forming energy bands through the coupling of the individual energy states. One period is typically referred to as the part of the active region that contains the optical active quantum well together with the extractor/injector sections transporting the electrons from one active region period to the next. The extraction mechanism is a reason why QCDs are highly suitable candidates for data transmission: the lifetime of the typically involved LO phonons is < 1 ps, making QCDs fast devices with very high saturation thresholds [35]. QCDs are typically realized with 5 to 50 periods in their active region, with exceptions like single period devices [36] as in this work. The simulated band structures were obtained via a self-consistent calculation scheme of the eight-band $k \cdot p$ model and the Poisson equation [37,38]. As the former yields the subbands spatial distribution based on the band structure, the latter finds the corresponding Fermi levels with consideration of the dopant densities. The Hartree potentials are calculated as the electrostatic potential of the electron charge densities. Figure 1 shows the simulated band structure of the single period device at room temperature and at zero-bias operation. The optical transition occurring in the active well is indicated by the red arrow, while the current flow through the device is indicated by the black arrows. The active zone is embedded in a waveguide and composed as follows (**InAlAs** layers in bold, Si-doped layers underlined, in nanometers): **2.5**, 7.2, **2.5**, 6.6, **2.5**, 6.6, **3.5** (2 x 10^{17} cm^{-3}), 9.4 (8 x 10^{17} cm^{-3}), **4.5**, 3.3, **4.1**, 3.5, **4.1**, 4.1, **3.4**, 4.4, **3.4**, 5, **3**, 6.5, **3** (3 x 10^{17} cm^{-3}). The layer sequence of the active region stack, including the injector/extractor structure of the 15 period device in nanometers is **4.5**, 3.2, **4.3**, 3.3, **3.9**, 3.5 (1 x 10^{17} cm^{-3}), **3.9**, 3.8, **4.1**, 4.4, **3.7**, **3.7**, 4.7, 5.1, **3.7**, 5.3, **2.8** (1 x 10^{17} cm^{-3}), 9.4 (2 x 10^{17} cm^{-3}), with **InAlAs** barrier layers in bold and Si-doped layers underlined. In Fig. 2, a cutout showing one period (between the dashed lines) of the simulated bandstructure of the multiperiod design, is depicted. This stack is repeated 15 times and embedded in a top, and bottom charge balancing region, easing the formation of ohmic contacts. In both designs, the series resistances of the bulk InGaAs/InP interfaces were reduced by the implementation of a contact chirped superlattice structure. Figure 1 and 2 allow a quantitative explanation of how the number of periods used in a design, will finally influence the detector performance and its figures of merit. The responsivity R of a QCD, the figure of merit describing the produced photocurrent per incoupled optical power, is proportional to 1/N, with N being the number of periods [10]. On the other hand, a higher number of periods will increase the device resistance, improving its noise behaviour. This trade-off is the typical challenge in QCD design. The devices used in this work were fabricated as 200-μm-long and 14-μm-wide ridges, with a height of approximately 7 μm. After patterning the ridges with UV lithography and reactive ion etching (RIE), the surface was passivated with SiN using plasma enhanced chemical vapor deposition (PECVD). The devices were electrically contacted through a sputtered layer of titanium as an adhesion promoter, and gold. After cleaving to produce clean facets, the device was soldered to a copper base plate and bonded to a printed circuit board. Figure 3 shows a SEM picture of the cleaved facet of a 15-period detector ridge with indicated layers. The active region can be seen as the rectangle in a slightly brighter grey tone compared to the surrounding cladding layers. The SiN passivation

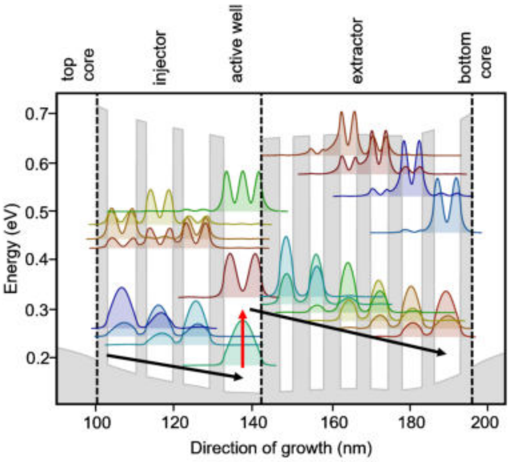

Fig. 1. Band structure of the single period design. The current path is visualized by the black arrows while the optical transition is pointed out by the red arrow.

layer can be identified as a dark, nearly black line between the substrate and the gold contact layer. The quality of the cleaved facet is a crucial parameter, determining the effectivity of incoupling the light.

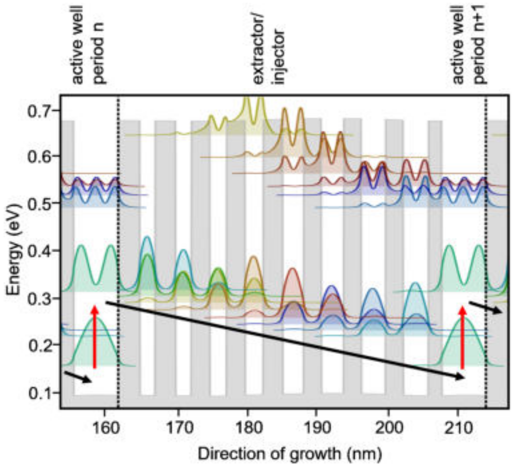

Fig. 2. Band structure of the 15-period design. The vertical dotted lines indicate the layers of one single period, which is repeated 15 times. The black arrows show the current path while the optical transitions are highlighted by the red arrows.

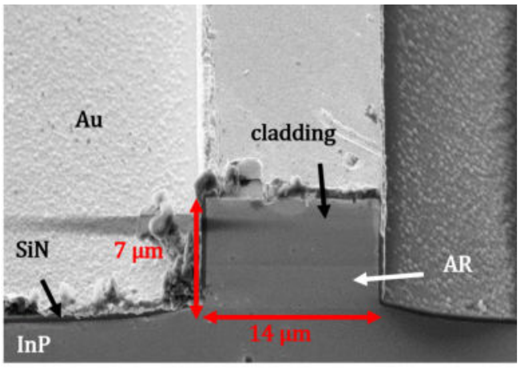

Fig. 3. Scanning electron microscope picture of the facet of a 15-period device. The individual layers are indicated.

3. Characterization

Both samples were characterized optically and electrically. I-V curves were measured with a Keithley 2601B source-meter for different device temperatures under dark conditions in order to extract the differential resistance at zero bias R_0. For the plotted I-V curves we refer the reader to Figures S1 in the supplementary material. The extracted zero bias resistance $R_0 = dV/dI$ was plotted on a logarithmic scale as function of the inverse measurement temperature. The slope of the resulting curve in the arrhenius plot, shown in Fig. 4 describes the activation energy of the quantum well structure, and thus its transition energy. We extracted activation energies of $E_{A15-per} = 111.3$ meV for the 15-period device and $E_{Asingle} = 126.1$ meV for the single period

Optics EXPRESS

device, respectively. The low room-temperature resistances of 18 Ω and 264 Ω of the single period device and the 15-period device, respectively, can be explained by the low transition energy at a wavelength of 9.124 μm. Using a single period design lowers the resistance by simply reducing the number of subsequent barriers. The spectral characterization of the devices was conducted with an external-cavity QCL in pulsed operation, able to cover a wavelength range from $8-12$ μm. Absolute responsivity measurements were done with an Alpes Lasers QCL in continuous wave operation at a wavelength of 9.28 μm. After the laser beam shape measurement and power calibration with the help of an automatized X-Y stage and an optical powermeter, the spectral responsivity curves were recorded at room temperature using a transimpedance- and a lock-in amplifier and scaled to the absolute values measured at 9.28 μm. To examine the free-space detector coupling and calculate the incoupled optical power with high precision, FEM simulations were performed. Figure 5 illustrates the spatial distribution of the optical mode intensity for the two QCD designs extracted with the simulation software COMSOL Multiphysics. The detector ridge structures were modeled according to the waveguide design. The effective mode area (A_{eff}) was calculated from the simulations as shown in Eq. (1),

$$A_{eff} = \frac{\left[\int_{-\infty}^{\infty} |E|^2 dA\right]^2}{\int_{-\infty}^{\infty} |E|^4 dA}, \tag{1}$$

where E is the electric field amplitude. The mode areas calculated at a wavelength of $\lambda = 9.124$ μm are 36.06 μm^2 and 41.15 μm^2 for the single period and 15-period device, respectively. Despite having only one active period, the single period device shows a similar optical active area as the mode is confined in the thicker waveguide claddings for this design. The substrate is not a relevant factor for light coupling, due to its high doping density ($10^{17}\ cm^{-3}$) and the strong impact of free-carrier absorption [39]. The simulations of the optical areas offer an accurate normalization factor for the incoupled power with relatively high precision. The optical coupling coefficient is assumed to be unity. This further means that our results represent rather conservative values as the incoupled power might be lower. Figure 6 shows the spectral responsivity curves of both detector designs at room temperature. We can see that the responsivity peak at $\lambda_{R_P} = 9.42$ μm of the single period device is slightly off the targeted wavelength of $\lambda_T = 9.124$ μm while the 15-period devices responsivity peaks exactly at λ_T. With a laser power of $P_{Laser} = 13.5$ mW measured after the ZnSe lens, used to focus the beam, the calculated incoupled power to the 15-period device was $P_{in-15} = 8.61$ μW and $P_{in-1} = 5.85$ μW to the single-period device. Peak responsivities of $R_P = 0.411$ A/W and $R_P = 0.111$ A/W were extracted from the single period device and the 15-period device, respectively. At λ_T, the single period device shows a room temperature responsivity of $R_{\lambda_T} = 0.279$ A/W. The reached peak responsivities correspond to external quantum efficiencies of 5.4% and 1.5% for the single-period and the 15-period device respectively. The extraction efficiency was assumed to be unity in this calculation. The measured properties, responsivity and zero bias differential resistance, were used to obtain the specific Johnson detectivity, a figure of merit describing the Johnson noise behavior of the detector device. Specific detectivities of $D^*_{J-1} = 6.33{*}10^7$ Jones for the singe-period device's very low and $D^*_{J-15} = 6.54{*}10^7$ Jones for the 15-period device were calculated. As in the case of monolithic waveguide integration the signal does not scale with the detector area (direct end-fire coupling), the noise equivalent power (NEP), which is not normalized on the detector area, is a more meaningful quantity. The corresponding noise equivalent powers at room temperature are $NEP_1 = 83.6$ pW/$\sqrt{Hz}$ and $NEP_{15} = 80.9$ pW/$\sqrt{Hz}$ for the single period and the 15-period device, respectively.

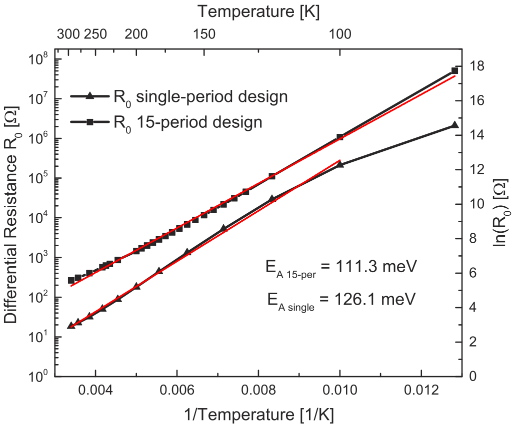

Fig. 4. Arrhenius plot: natural logarithm of the differential zero bias resistance plotted as a function of the reciprocal temperature. The slope of the curves is proportional to the activation energy E_A.

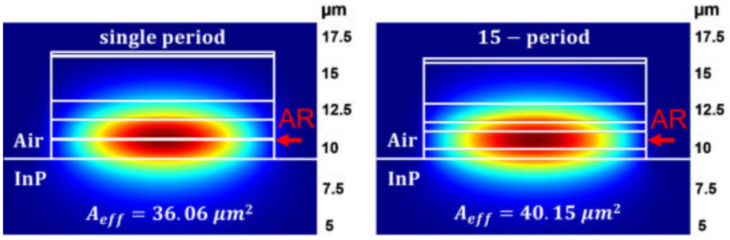

Fig. 5. Simulation of the spatial distribution of the optical mode intensitiy inside the waveguide. The active regions are highlighted by the red arrows.

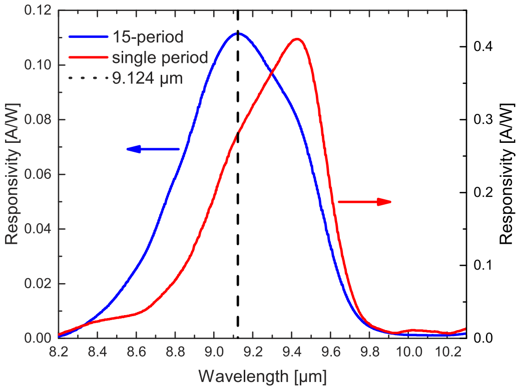

Fig. 6. Spectral responsivity curves acquired at room temperature. The 15-period device is shown in blue, the single period device is shown in red. The black dashed line marks the target wavelength of 9.124 μm.

4. Conclusion

Concluding our work, we designed, fabricated and characterized two different types of quantum cascade detectors, targeting a wavelength of 9.124 μm. As expected, the single period device shows a higher peak responsivity of $R_P = 0.411$ A/W compared to the 15-period device with $R_P = 0.111$ A/W. Due to the single-period devices very low resistance, it shows a slightly higher noise equivalent power of $NEP_1 = 83.6\,\text{pW}/\sqrt{Hz}$ compared to the 15-period device with $NEP_{15} = 80.9\,\text{pW}/\sqrt{Hz}$, at room temperature. Device characterization, particularly the normalization of incoupled power and the alignment of the ridge devices, is quite challenging for this geometry. Due to the low resistances of the devices, the electrical measurements required careful data analysis and interpretation. We see that the reduction of the number of periods effectively increases the device responsivity, with the drawback of a decrease in device resistance. Future challenges include the simulation and design of a single-period structure with a higher zero-bias resistance at room temperature in order to improve its noise behaviour and thus its usability in photonic integrated circuits.

Funding. Horizon 2020 Framework Programme (828893); Austrian Science Fund (M2485-N34); Air Force Office of Scientific Research (FA8655-22-1-7170); Österreichische Forschungsförderungsgesellschaft (883941).

Acknowledgments. The authors want to acknowledge frutiful scientific discussions with W. Schrenk and E. Gornik.

Disclosures. The authors declare no conflicts of interest.

Data availability. Data underlying the results presented in this paper are not publicly available at this time but may be obtained from the authors upon reasonable request.

Supplemental document. See Supplement 1 for supporting content.

References

1. A. Harrer, R. Szedlak, B. Schwarz, H. Moser, T. Zederbauer, D. MacFarland, H. Detz, A. M. Andrews, W. Schrenk, B. Lendl, and G. Strasser, "Mid-infrared surface transmitting and detecting quantum cascade device for gas-sensing," Sci. Rep. **6**(1), 21795 (2016).
2. A. Dabrowska, M. David, S. Freitag, A. M. Andrews, G. Strasser, B. Hinkov, A. Schwaighofer, and B. Lendl, "Broadband laser-based mid-infrared spectroscopy employing a quantum cascade detector for milk protein analysis," Sens. Actuators, B **350**, 130873 (2022).
3. C. Tomasi and F. Tampieri, "Size distribution models of small water droplets in mist and their volume extinction coefficients at visible and infrared wavelengths," Atmos. Environ. (1967) **10**(11), 1005–1013 (1976).
4. B. Hinkov, A. Hugi, M. Beck, and J. Faist, "Rf-modulation of mid-infrared distributed feedback quantum cascade lasers," Opt. Express **24**(4), 3294–3312 (2016).
5. H. Dely, T. Bonazzi, O. Spitz, E. Rodriguez, D. Gacemi, Y. Todorov, K. Pantzas, G. Beaudoin, I. Sagnes, L. Li, A. G. Davies, E. H. Linfield, F. Grillot, A. Vasanelli, and C. Sirtori, "10 gbit/s free space data transmission at 9 μm wavelength with unipolar quantum optoelectronics," Laser Photonics Rev. **16**(2), 2100414 (2022).
6. A. Soibel, M. W. Wright, W. H. Farr, S. A. Keo, C. J. Hill, R. Q. Yang, and H. C. Liu, "Midinfrared interband cascade laser for free space optical communication," IEEE Photonics Technol. Lett. **22**(2), 121–123 (2010).
7. B. Levine, K. Choi, C. Bethea, J. Walker, and R. Malik, "New 10 μm infrared detector using intersubband absorption in resonant tunneling GaAlAs superlattices," Appl. Phys. Lett. **50**(16), 1092–1094 (1987).
8. D. Palaferri, Y. Todorov, A. Bigioli, A. Mottaghizadeh, D. Gacemi, A. Calabrese, A. Vasanelli, L. Li, A. G. Davies, E. H. Linfield, F. Kapsalidis, M. Beck, J. Faist, and C. Sirtori, "Room-temperature nine-μm-wavelength photodetectors and GHz-frequency heterodyne receivers," Nature **556**(7699), 85–88 (2018).
9. H. Liu, J. Li, M. Buchanan, and Z. Wasilewski, "High-frequency quantum-well infrared photodetectors measured by microwave-rectification technique," IEEE J. Quantum Electron. **32**(6), 1024–1028 (1996).
10. M. Graf, N. Hoyler, M. Giovannini, T. Aellen, J. Faist, and D. Hofstetter, "Mid-infrared quantum cascade detectors on inp," in *Infrared and Photoelectronic Imagers and Detector Devices II*, vol. 6294 (International Society for Optics and Photonics, 2006), p. 62940P.
11. D. Hofstetter, M. Beck, and J. Faist, "Quantum-cascade-laser structures as photodetectors," Appl. Phys. Lett. **81**(15), 2683–2685 (2002).
12. H. Schneider, C. Schönbein, G. Bihlmann, P. Van Son, and H. Sigg, "High-speed infrared detection by uncooled photovoltaic quantum well infrared photodetectors," Appl. Phys. Lett. **70**(12), 1602–1604 (1997).
13. J. Faist, M. Beck, T. Aellen, and E. Gini, "Quantum-cascade lasers based on a bound-to-continuum transition," Appl. Phys. Lett. **78**(2), 147–149 (2001).
14. M. David, A. Dabrowska, M. Sistani, I. Doganlar, E. Hinkelmann, H. Detz, W. Weber, B. Lendl, G. Strasser, and B. Hinkov, "Octave-spanning low-loss mid-IR waveguides based on semiconductor-loaded plasmonics," Opt. Express **29**(26), 43567–43579 (2021).

15. B. Schwarz, P. Reininger, D. Ristanić, H. Detz, A. M. Andrews, W. Schrenk, and G. Strasser, "Monolithically integrated mid-infrared lab-on-a-chip using plasmonics and quantum cascade structures," Nat. Commun. **5**(1), 4085 (2014).
16. B. Hinkov, F. Pilat, L. Lux, P. L. Souza, M. David, A. Schwaighofer, D. Ristanić, B. Schwarz, H. Detz, A. M. Andrews, B. Lendl, and G. Strasser, "A mid-infrared lab-on-a-chip for dynamic reaction monitoring," Nat. Commun. **13**(1), 4753 (2022).
17. Z. Zhang, Y. Xiao, Z. Ma, M. Xiao, Z. Ding, X. Lei, G. K. Karagiannidis, and P. Fan, "6G wireless networks: Vision, requirements, architecture, and key technologies," IEEE Veh. Technol. Mag. **14**(3), 28–41 (2019).
18. M. Giordani, M. Polese, M. Mezzavilla, S. Rangan, and M. Zorzi, "Toward 6G networks: Use cases and technologies," IEEE Commun. Mag. **58**(3), 55–61 (2020).
19. N. Witternigg, M. Schönhuber, E. Leitgeb, and T. Plank, "Feasibility assessment of optical technologies for reliable high capacity feeder links," Acta Astronaut. **89**, 254–260 (2013).
20. X. Pang, O. Ozolins, L. Zhang, R. Schatz, A. Udalcovs, X. Yu, G. Jacobsen, S. Popov, J. Chen, and S. Lourdudoss, "Free-space communications enabled by quantum cascade lasers," Phys. Status Solidi A **218**(3), 2000407 (2021).
21. B. Hinkov, A. Bismuto, Y. Bonetti, M. Beck, S. Blaser, and J. Faist, "Singlemode quantum cascade lasers with power dissipation below 1 W," Electron. Lett. **48**(11), 646–647 (2012).
22. T. Plank, E. Leitgeb, P. Pezzei, and Z. Ghassemlooy, "Wavelength-selection for high data rate free space optics (FSO) in next generation wireless communications," in *2012 17th European Conference on Networks and Optical Communications*, (2012), pp. 1–5.
23. S. Blaser, D. Hofstetter, M. Beck, and J. Faist, "Free-space optical data link using peltier-cooled quantum cascade laser," Electron. Lett. **37**(12), 778–780 (2001).
24. M. Taslakov, V. Simeonov, and H. Van den Bergh, "Line-of-sight data transmission system based on mid IR quantum cascade laser," in *Free-Space Laser Communication Technologies XX*, vol. 6877 (International Society for Optics and Photonics, 2008), p. 68770F.
25. J. Mikołajczyk, D. Szabra, A. Prokopiuk, K. Achtenberg, J. Wojtas, and Z. Bielecki, "Optical wireless communications operated at long-wave infrared radiation," Int. J. Electron. Telecommun. **66**(2), 383–387 (2020).
26. M. Garlinska, A. Pregowska, I. Gutowska, M. Osial, and J. Szczepanski, "Experimental study of the free space optics communication system operating in the 8–12 μm spectral range," Electronics **10**(8), 875 (2021).
27. B. Schwarz, P. Reininger, H. Detz, T. Zederbauer, A. M. Andrews, W. Schrenk, and G. Strasser, "Monolithically integrated mid-infrared quantum cascade laser and detector," Sensors **13**(2), 2196–2205 (2013).
28. Y. Zou, K. Vijayraghavan, P. Wray, S. Chakravarty, M. A. Belkin, and R. T. Chen, "Monolithically integrated quantum cascade lasers, detectors and dielectric waveguides at 9.5 μm for far-infrared lab-on-chip chemical sensing," in *CLEO: Science and Innovations*, (Optical Society of America, 2015), pp. STu4I–2.
29. A. Harrer, B. Schwarz, R. Gansch, P. Reininger, H. Detz, T. Zederbauer, A. M. Andrews, W. Schrenk, and G. Strasser, "Plasmonic lens enhanced mid-infrared quantum cascade detector," Appl. Phys. Lett. **105**(17), 171112 (2014).
30. P. Reininger, B. Schwarz, R. Gansch, H. Detz, D. MacFarland, T. Zederbauer, A. Andrews, W. Schrenk, and G. Strasser, "Quantum cascade detector utilizing the diagonal-transition scheme for high quality cavities," Opt. Express **23**(5), 6283–6291 (2015).
31. A. Jollivet, B. Hinkov, S. Pirotta, H. Hoang, S. Derelle, J. Jaeck, M. Tchernycheva, R. Colombelli, A. Bousseksou, M. Hugues, N. Le Biavan, J. Tamayo-Arriola, M. Montes Bajo, L. Rigutti, A. Hierro, G. Strasser, J.-M. Chauveau, and F. H. Julien, "Short infrared wavelength quantum cascade detectors based on m-plane ZnO/ZnMgO quantum wells," Appl. Phys. Lett. **113**(25), 251104 (2018).
32. S. Sakr, P. Crozat, D. Gacemi, Y. Kotsar, A. Pesach, P. Quach, N. Isac, M. Tchernycheva, L. Vivien, G. Bahir, E. Monroy, and F. H. Julien, "GaN/AlGaN waveguide quantum cascade photodetectors at lambda approximate to 1.55 μm with enhanced responsivity and similar to 40 GHz frequency bandwidth," Appl. Phys. Lett. **102**(1), 011135 (2013).
33. M. Helm, "The basic physics of intersubband transitions," in *Semiconductors and semimetals*, vol. 62 (Elsevier, 1999), pp. 1–99.
34. M. Giparakis, H. Knötig, H. Detz, M. Beiser, W. Schrenk, B. Schwarz, G. Strasser, and A. M. Andrews, "2.7 μm quantum cascade detector: Above band gap energy intersubband detection," Appl. Phys. Lett. **120**(7), 071104 (2022).
35. A. Delga, "Quantum cascade detectors: A review," in *Mid-infrared Optoelectronics*, (Woodhead Publishing, 2020), Woodhead Publishing Series in Electronic and Optical Materials, pp. 337–377.
36. B. Schwarz, P. Reininger, A. Harrer, D. MacFarland, H. Detz, A. M. Andrews, W. Schrenk, and G. Strasser, "The limit of quantum cascade detectors: A single period device," Appl. Phys. Lett. **111**(6), 061107 (2017).
37. P. Enders and M. Woerner, "Exact block diagonalization of the eight-band hamiltonian matrix for tetrahedral semiconductors and its application to strained quantum wells," Semicond. Sci. Technol. **11**(7), 983–988 (1996).
38. B. A. Foreman, "Elimination of spurious solutions from eight-band $\mathbf{k} \cdot \mathbf{p}$ theory," Phys. Rev. B **56**(20), R12748 (1997).
39. M. A. Panah, L. Han, K. Norrman, N. Pryds, A. Nadtochiy, A. Zhukov, A. Lavrinenko, and E. Semenova, "Mid-IR optical properties of silicon doped InP," Opt. Mater. Express **7**(7), 2260–2271 (2017).

CHAPTER 3

MICRO-MIRROR AIDED MID-INFRARED PLASMONIC BEAM COMBINER MONOLITHICALLY INTEGRATED WITH QUANTUM CASCADE LASERS AND DETECTORS

3.1 Motivation, Background and State-of-the-Art

While PICs have already been developed and commercialized for use in the visible and near-infrared spectra, their counterparts in the MIR, especially in the LWIR range, are still in the early stages of development.[161] One of the primary reasons is the lack of suitable materials with low optical losses in the MIR range. Conventional materials used in visible and near-IR PICs, such as silicon, have significantly higher losses in the mid- and long wavelength IR, hindering efficient light guiding and manipulation.[162] Additionally, developing components like waveguides, modulators, and detectors optimized for MIR wavelengths is often more complex due missing compatibility of integration in standard optoelectronic semiconductor fabrication schemes or CMOS processes.[163, 164] However, there is a growing interest in addressing these challenges because the MIR and LWIR spectra are critical for applications in sensing and telecommunications as mentioned in section 1.10. Researchers are exploring new materials like chalcogenide glasses,[165, 166], CdTe,[167] HgCdTe[168] or group IV semiconductors like germanium[169, 170] and Si[171, 172, 173, 174] which exhibit lower losses in the MIR region, to develop waveguides and other photonic components.[175]

Plasmonics offers a promising solution to the challenges faced in developing MIR and LWIR PICs, particularly in terms of material losses and device integration. Surface plasmon polaritons (SPP) are electromagnetic waves that travel along the boundary between a metal and a dielectric, generated by the interaction of light with collective electron oscillations at the metal surface, bypassing the limitations of conventional dielectric waveguides.[176] Metals like gold and silver, which are commonly used in plasmonic systems, exhibit strong plasmonic resonances in the mid- and long wave IR, allowing efficient propagation of light at these wavelengths. Another advantage to the mentioned dielectric waveguides is the easy implementation of plasmonic waveguides with other photonic components.[177, 178, 179] On-chip guiding and routing of plasmons, especially the possibility to incorporate changes in routing direction of MIR and LWIR light also presents exciting possibilities for the miniaturisation of complex systems to the chip-level.[180] This can be facilitated through so called dielectric loading, which essentially describes plasmon confinement through a deposited dielectric waveguide ridge atop the plasmonic active metal layer. The effective mode index is increased and thus the plasmons are better confined.[181] Extending the wavelengths to the LWIR, we again encounter the problems of high absorptions of dielectric materials needed to increase the confinement.[182] Solutions were shown by David et al., implementing waveguides of polyethylene (PE),[183] with its large transparency region between 2-200 µm.[184] Besides the complex fabrication processes of PE,[185] especially the implementation into existing workflows in semiconductor and optoelectronic processing, the PE waveguides can be fabricated in a way that the mode confinement is high enough to allow guiding around 90° corners.[183] This is a crucial achievement towards plasmonic LWIR PICs. However, achieving low-loss propagation similar to that in straight plasmonic or dielectric waveguide elements is challenging because the higher degree of confinement needed to guide the mode. A way to circumvent the need of strong mode confinement for achieveing 90°-bends is the implementation of reflection planes, which act as micro mirrors, redirecting the plasmons.[186] A material that shows good transparancy throughout the mid- and long wavelength IR region is Germanium.[187, 188] It is frequently used in standard semiconductor and optoelectronic fabrication processes and its deposition or etching can be easily implemented in standardized workflows. Thin Ge-ridges acting as the dielectric loading waveguides atop a plasmonic active Au-layer confine the plasmon laterally and thus allow proper guiding. A combination with the previously mentioned micro-mirror structures allows routing capabilities comparably to the high-confinement PE waveguides but combined with much simpler fabrication complexity.[189] The mentioned compatibility with standard fabrication processes, facilitates the integration into components with existing semiconductor technologies such as QCLs and QCDs.[5] By leveraging plasmonic structures, it is possible to design more efficient PICs with perpendicular coupling capabilities in the MIR and LWIR ranges, enabling the development of fully integrated structures as e.g. on-chip beam combiners that combine active plasmonic components with semiconductor electronics.[129, 190]

3.2 Contribution to the field

In the second publication, we introduce a novel concept for realizing low-loss on-chip mode guiding and beam combining capabilities, which are essential for the development of sophisticated MIR-PICs. The core of this study is the implementation of a monolithic on-chip beam combiner, achieved through the integration of active quantum cascade devices with tailored passive plasmonic waveguides and innovative on-chip micro-mirror optics. These integrated gold-coated micro-mirrors enhance directional control and beam merging capabilities while minimizing energy dissipation, addressing a critical challenge in plasmonic device design.

This new device exemplifies a foundational component in the development of advanced and complex PICs, paving the way for applications such as on-chip heterodyne detectors and Mach-Zehnder interferometers. The comparative analysis with simpler routing concepts further highlights the advantages of the proposed design. By addressing the limitations of current technology, this work contributes to the ongoing evolution of PICs, underscoring the potential of micro-mirror-enhanced plasmonic waveguides as critical enablers for the next generation of MIR-PIC devices.

3.3 Publication

Submitted to Nanophotonics in November 2024. Reprinted, with permission, from G. Marschick, M. David, X. Gsodam, N. Opačak, D. Koukola, E. Arigliani, A. Evirgen, N. Vaissiere, V. Trinite, S. Pes, S. Isceri, H. Detz, W. Schrenk, A. M. Andrews, B. Lendl, B. Schwarz, G. Strasser, and B. Hinkov "Micro-mirror aided mid-infrared plasmonic beam combiner monolithically integrated with quantum cascade lasers and detectors"

Micro-mirror aided mid-infrared plasmonic beam combiner monolithically integrated with quantum cascade lasers and detectors

Georg Marschick,[1, a)] Mauro David,[1, a)] Xaver Gsodam,[1] Nikola Opačak,[1] Dominik Koukola,[1] Elena Arigliani,[1] Axel Evirgen,[2] Virginie Trinité,[2] Salvatore Pes,[2] Stefania Isceri,[1] Hermann Detz,[3, 4] Werner Schrenk,[1] Aaron M. Andrews,[1] Bernhard Lendl,[5] Benedikt Schwarz,[1] Gottfried Strasser,[1] and Borislav Hinkov[1, 6]

[1)] *TU Wien, Institute of Solid State Electronics & Center for Micro- and Nanostructures, Vienna, Austria*
[2)] *III-V Lab, a joint Thales, Nokia and CEA-LETI laboratory, Palaiseau, France*
[3)] *CEITEC, Brno University of Technology, Brno, Czech Republic*
[4)] *current address: University of Applied Sciences Technikum Wien, Department of Applied Mathematics & Physics, Vienna, Austria*
[5)] *TU Wien, Institute of Chemical Technologies and Analytics, Vienna, Austria*
[6)] *Silicon Austria Labs, Villach, Austria*

(*Electronic mail: borislav.hinkov@tuwien.ac.at; borislav.hinkov@silicon-austria.com)

(Dated: 12 November 2024)

The development of novel mid-infrared (MIR) devices and systems is crucial for addressing applications in biomedical analysis, chemical reaction-monitoring, or high-bitrate free-space telecommunication. Combining multiple functional elements on one chip into complex miniaturized photonic integrated circuits (PICs), is the next step in these developments, yet limited by existing material and technology constraints.

In this work, we introduce a new concept for realizing fully monolithic MIR-PICs based on low-loss on-chip plasmonic guiding and beam combining. The core of our study demonstrates a monolithic beam combiner by integration of active quantum cascade (QC) devices at ∼8 µm (laser & detector) with tailored passive waveguides based on weakly-coupled Ge/Au plasmonics and on-chip micro-mirror optics. The on-chip gold-coated micro-mirrors enhance the directional control and beam combining capabilities of the plasmon waveguides while minimizing energy dissipation typically associated with tight plasmon confinement. We discuss the MIR-PIC beam combiner design, micro-fabrication, and characterization and compare it to the routing concept of simple plasmonic Ge/Au y-couplers exploiting strong-confinement.

I. INTRODUCTION

Energy-efficient electronics (E3) is a long standing research field established with the first transistor[1] and followed by decades of development of micro- and nano-scale electronic devices. Their continuous increase in functional density and energy efficiency led to highly integrated central processing units (CPUs) with more than 130 billion individual transistors.[2] In contrast, energy-efficient photonics (E^2P, also "Green Photonics") is still in a much earlier stage of development and photonic integrated circuits (PICs), i.e. fully chip-scale photonic devices, have not yet reached a similar level of maturity and integrated functionality as their electronic counterparts. In addition, PIC development is currently still strongly focused on near-infrared (NIR) devices for telecom applications[3–7]. This leaves out the important mid-infrared (MIR) spectral range, which hosts many fundamental molecular absorptions[8–15] and simultaneously covers multiple atmospheric transparency windows suitable for telecommunication applications[16–18]. However, the bulky nature of the existing MIR systems poses several limitations including thermal challenges for mobile applications and prevents miniaturized setups as needed in in-situ spectroscopy.[19,20]

MIR-PICs offer a solution to these challenges. They are intrinsically more robust, cost-effective and show a drastically reduced power consumption (1-2 orders of magnitude) as compared to lab-scale MIR instrumentation such as the well-established Fourier Transform Infrared (FTIR) spectrometers. In addition, MIR-PICs unlock unprecedented capabilities based on combining chip-scale active components like quantum cascade lasers (QCL)[21–23] and detectors (QCD)[24,25] with passive components such as waveguides and modulators. They include beam-directing (with much better control than single-element QCLs[26]), shaping and modulating and thus hold immense potential for cost-efficient sensors and free-space telecom devices.[27,28] Passive MIR waveguides are pivotal parts of such novel PIC architectures. Traditionally, dielectric waveguides based on total internal reflection and utilizing epitaxially-grown layer structures are employed, resulting in low-loss characteristics.[29,30] But their typically strong mode confinement makes them less suitable for on-chip sensing and spectroscopic applications.[31–33]

In contrast to that, recent advances in MIR plasmonic waveguides, such as dielectric-loaded or semiconductor-loaded surface plasmon polariton (DL/SLSPP) structures, offer a promising alternative.[19,34–36] They can be tailored by thin (∼100s of nanometer) dielectric/semiconductor layer stripes to adjust the vertical mode extension for over 95% of the mode being efficiently propagated in the surrounding medium.[37] The drawback of this configuration is the low modal index which results in very poor mode guiding capabilities along bent waveguide structures on the chip surface. In contrast, thick dielectric/semiconductor ridges (∼micrometer-scale) on top of the plasmonic metal layer significantly reduce the

---

[a)] These authors equally contributed to this work.

modal overlap with the surrounding medium, while simultaneously enabling effective routing capabilities, which is a crucial characteristic for realizing complex MIR-PIC geometries. However, finding suitable dielectric or semiconductor materials transparent up to wavelengths of λ=12 µm that are also compatible with state-of-the-art MIR photonic processing technology is a challenging task.[38,39] While it is true that plasmonic waveguides exhibit higher losses compared to dielectric waveguides, their flexibility in integrating both sensing and guiding sections, due to better mode profile matching, offers significant advantages for compact and multifunctional designs. Recently, we demonstrated the implementation of the polymeric material linear low-density Polyethylene (PE) on Au in the thick-ridge geometry, achieving the first proof of efficient MIR plasmonic mode-guiding along the chip surface.[40] However, the integration of PE polymer layers with QCL and QCD ridge structures is challenging due to their sensitivity to ambient conditions during fabrication which significantly complicates their integration into monolithic MIR-PICs.
In this work, we study two different integrated plasmonic designs for enabling MIR on-chip guiding and show their successful integration with QCLs and QCDs. We introduce a new MIR approach with plasmonic waveguiding to achieve versatile routing capabilities while preserving low-loss propagation by the integration of monolithic micro-mirror optics. As a proof-of-concept of a complex MIR-PIC, we demonstrate a fully monolithic QC-based integrated MIR beam combiner. This device architecture represents an alternative approach to our previously demonstrated interband cascade (IC)-based device[41] and opens the path for longer wavelength applications of more advanced devices like heterodyne receivers.

II. EXPERIMENTAL SECTION

A. Design and Simulation

In order to evaluate the optical characteristics of SLSPP waveguides (WGs) based on Ge-layers on Au, we conducted finite element method (FEM) based simulations analyzing the resulting effective mode confinement. A careful study yields two distinct geometries, each offering unique advantages, illustrated in Figure 1. It shows the cross-section view sketches of both geometries in (a) and (b) together with the simulation results of the corresponding TM-polarized modes in (c) and (d): the first geometry (Fig. 1(a)) provides weak vertical mode confinement, making it suitable for sensing applications due to its large modal overlap with the surrounding medium (Fig. 1(c)) and low losses, while the second geometry offers sub-wavelength mode confinement (Fig. 1(b) and 1(d)) and potentially good guiding/routing capabilities. The former is achieved by a thin and wide Ge waveguide layer, while the latter is best featured by a thick and narrow Ge waveguide ridge. TM is the polarization for direct light coupling from QC devices and, therefore, relevant in this case. To carefully predict and optimize the geometrical factors to minimize the optical losses prior to device fabrication, the Wave Optics Module within the COMSOL Multiphysics was utilized.

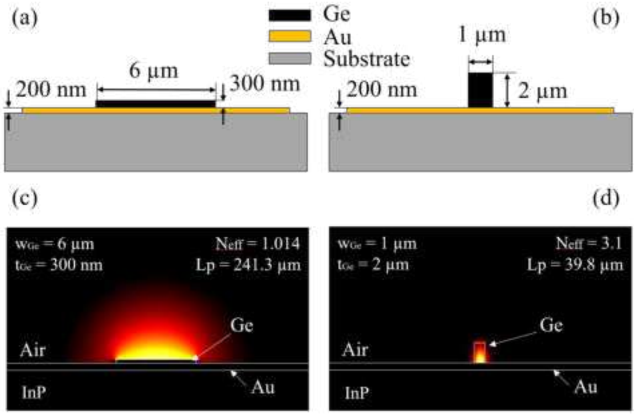

FIG. 1. Cross sections of the proposed SLSPP waveguides: (a) schematic illustration and (c) simulation of a Ge-based plasmonic waveguide (thin configuration) with a weakly confined mode. (b) schematic illustration and (d) simulation of a Ge ridge SLSPP waveguide with a highly confined mode (thick configuration).

To obtain precise predictions of the waveguide losses, we conducted simulations using material parameters extracted from ellipsometry and atomic force microscopy (AFM) measurements of fabricated layers using the same fabrication protocol as for the final integrated WGs. The higher losses presented here surpass those in previous studies using sputtered Au[35,42] due to the increased roughness of the evaporated gold layer beneath the Ge stripe in this case[43]. In the configuration employing the thick Ge-WG with optimized dimensions of 1x2 µm (width x thickness), the SPP mode is effectively confined within the Ge-ridge due to the high material refractive index in the long-wave IR (LWIR) of approximately n = 3.8. The pronounced confinement and resulting large effective mode index of $N_{eff} = 3.1$ consequently facilitates efficient routing of the SPP modes along the chip-surface, potentially even around sharp bending angles[44] . However, this confinement comes at the cost of substantial interaction between the SPP mode and the bottom plasmonic Au layer, leading to remarkably high ohmic losses of 0.11 dB/µm even in a simple linear WG ridge ($\lambda \sim 8.2$ µm). Despite the general possibility of adjusting this design to provide good mode guiding in non-straight geometries, the overall losses are very high, calling for the investigation of alternative solutions for guiding. In contrast, the geometry featuring the thin Ge-SLSPP WG (width x thickness: 6 µm x 300 nm) exhibits significantly lower losses, approximately 0.016 dB/mm for a straight WG. Additionally, the larger mode supported by the thin Ge/Au architecture, facilitates efficient coupling of the optical mode between the plasmonic and the laser/detector waveguides. The effective refractive index of the mode in this configuration is close to unity ($N_{eff} = 1.014$), suggesting weak confinement to the WG. Therefore, very poor mode guiding capabilities along WG-bends can be expected, which proves the initially mentioned impracticality of this geometry for complex MIR PICs. However, here we propose an innovative solution that enables on-chip mode-guiding while maintaining the advantages of the thin Ge SLSPP configuration. This approach reduces the losses and simplifies the fabrication compared to the challenges posed by the geometry with thick Ge. Building on the plasmonic reflection planes for 90° plasmon redirection demonstrated by Markey et al.[45], our approach introduces a novel strategy that integrates monolithic micro-optical structures with both active and passive components at the chip scale. As illustrated in the mode propagation simulation in Fig. 2(a), a circular bent thin Ge SLSSP WG couples barely any light along its curvature. Instead, the introduction of an additional vertical gold-coated mirror structure, very efficiently couples the vast majority of the light even for an angle of 90° between the two arms of the plasmonic waveguide (see Fig. 2(b)). The geometrical parameters of the mirror structures show a significant impact on the reflection losses in the simulations as shown in Figure 3. The achievable maximum mirror height of 8 µm, limited by the deep etch of the QCL/QCD structure itself, yields acceptable losses. For the lateral mirror dimension, simulations indicate low losses for values above 25 µm. The gap between the SPP-WG and the Au-coated mirror structure shows less significant impact on the mirror losses and gap widths below 1 µm, as seen in Figure 4 are easily feasible with appropriate lithography alignment. The simulation results in Figure 3 were achieved by varying one parameter while the others were kept constant at 0.5 µm gap-width, 8 µm mirror height and 28.5 µm mirror width. Considering these results, the expected losses due to a single Au-covered mirror with technologically feasible parameters are estimated to be 2.2 dB. Comparing the thin (300 nm) Ge WG geometry (0.016 dB/µm) with two additional integrated Gold mirrors (4.4 dB) to the thick (2 µm) Ge WG design (0.11 dB/µm), the former becomes already more advantageous for relatively short total WG lengths exceeding 47 µm.

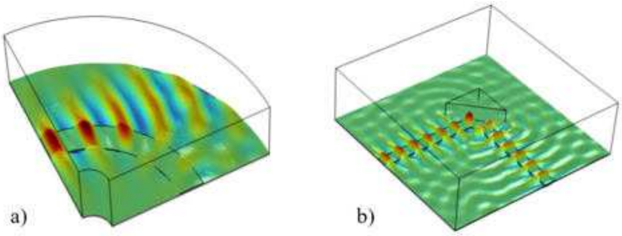

FIG. 2. Simulation of the electric field component in z-direction for two distinct cases: Thin Ge-WG configuration with (a) a 90° curved waveguide and (b) two perpendicular waveguide sections (90° angle) employing an additional gold-covered micro-mirror.

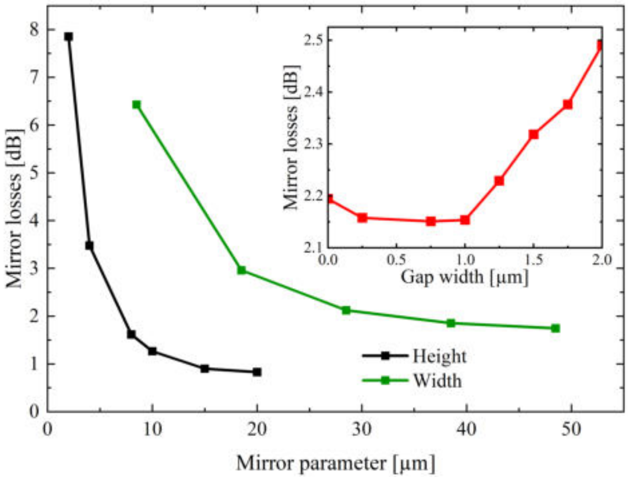

FIG. 3. Simulated losses of a Au-coated micro-mirror with differing mirror parameters: SLSPP WG-mirror gap (red), mirror width (green), mirror height (black).

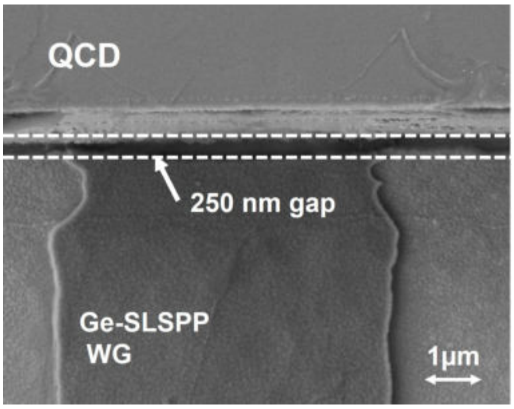

FIG. 4. Fabricated gap between SLSPP-WG and on chip QCD through standard lithography and optical marker alignmend with high precision. The gap-width here, highlighted through the two white dashed lines, is 250 nm.

B. Device Fabrication

The realization and integration of those additional micro-mirror structures requires, besides establishing the process itself, careful alignment with the fabrication steps of the other on-chip components, such as the QCL and QCD. The fabrication procedure is schematically shown in Figure 5. It starts with the deposition of a 1 µm-thick layer of SiN, acting as a hardmask (HM), onto the epitaxial active region structure via plasma-enhanced chemical vapor deposition (PECVD). Subsequently, the SiN is patterned utilizing standard photolithography (PL), integrating structures for the corresponding QCL, QCD, and micro-mirrors. This step is finalized through CHF_3 reactive-ion etching (RIE) of the SiN hardmask. Residual resist is removed using Acetone and Isopropanol, followed by a RIE deep etch in a Cl_2-Ar chemistry to transfer the pattern from the SiN hardmask into the semiconductor material. Surface passivation and protection are achieved through a 250 nm-thick layer of SiN (PECVD). Top contact openings on top of the QCL/QCD ridges are created through another PL and RIE process. A subsequent PL step precedes sputtering of 10 nm of Titanium (Ti) and 300 nm of Gold (Au) onto the sample for the top contacts, with undesired Au be-

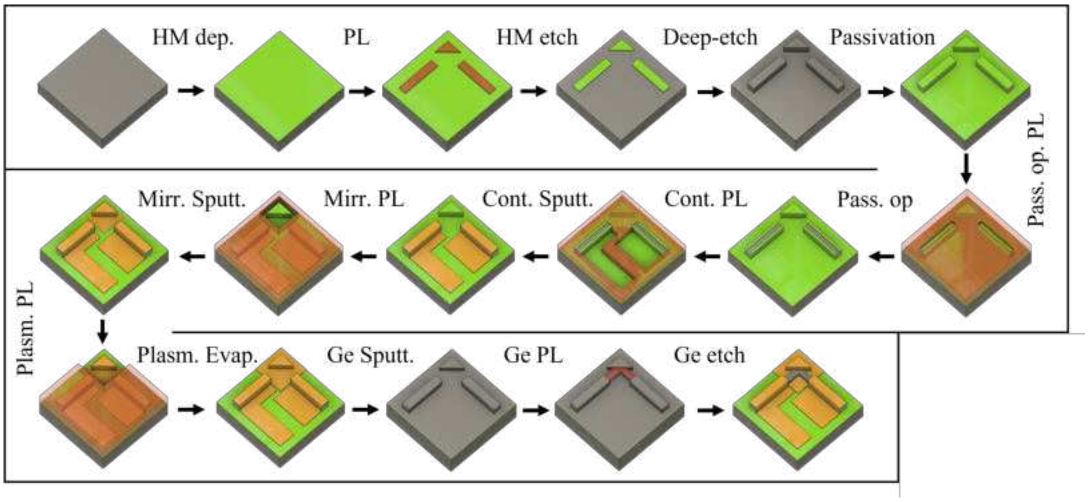

FIG. 5. Process flow of the monolithic integrated laser-micro-mirror-detector structures at the example of a 90° configuration. The shown process steps are described in the main text. Abbreviations: hardmask (HM), photolithography (PL), passivation opening (Pass. op.), contact (Cont.), micro-mirror (Mirr.), sputtering (Sputt.), evaporation (Evap.), plasmonic-Au-layer (Plasm.)

ing removed in a lift-off process. To cover the sidewalls of the mirror structures with gold and without covering the laser/detector facets, a two-step PL-deposition process is necessary. First, we perform a PL for metallization of the mirror structures, ensuring that the laser and detector facets are protected with photoresist. The mirror structures are coated with 10 nm of Ti and 30 nm of Au via a sputtering process to ensure adequate sidewall coverage for efficient reflection of the plasmonic mode. This is followed by a second PL step to prepare for the subsequent anisotropic evaporation process of the plasmonic Au-layer (Ti: 10 nm / Au: 350 nm), which is optimized for metal deposition close to the facets without contaminating them, as an evaporation process more efficiently avoids coverage of vertical surfaces. After a lift-off process, 300 nm of Ge are sputtered, WGs are masked by PL, and WG definition is accomplished via oxygen-free SF_6 etching in an inductively coupled plasma (ICP) RIE step. In the final step, the back facets of the QCLs are cleaved, and the devices are mounted on copper submounts and wire-bonded to printed circuit boards, rendering them ready for measurement. The processed structures are shown in Fig. 6 including straight WGs in (a), 90° bends with a single mirror in (b) and quasi-s-bends with a center micro-mirror combiner in (c) with a combining angle of 100°. This configuration is the fundamental part of the spectral beam combiner. Figure 6 (d) shows for comparison a y-coupler geometry where the thick Ge on Au configuration is used.

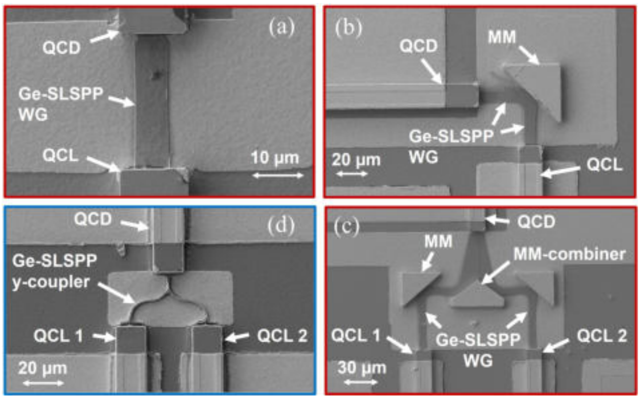

FIG. 6. Scanning Electron Microscope (SEM) pictures of the different on-chip structures. The red-framed pictures show the thin Ge-WGs with micro-mirrors (MM), while the blued-framed one shows the thick Ge-WG with y-coupler geometry.
Monolithic integrated: (a) QCL, QCD and thin straight Ge-SLSPP waveguide, (b) 90° arrangement of QCL and QCD with Ge-SLSPP waveguide and Au-coated micro-mirror, (c) spectral beam-combiner configuration consisting of two QCLs, a Ge-SLSPP waveguide guided by two 90° single mirrors and a center micro-mirror combiner with a combining angle of 100°, and a QCD, (d) spectral beam-combiner configuration consisting of two QCLs and a thick Ge-SLSPP y-coupler waveguide.

C. Optical characterization

In the previously presented simulations, defect-free device fabrication is assumed. Consequently, only optical losses arising from material properties and waveguide design are examined. However, in real devices, three sources contribute to optical losses associated with the waveguides: coupling losses (between the QCL/QCD and waveguide), waveguide losses due to attenuation of the electromagnetic field within the waveguide material, and scattering losses resulting from defects and imperfections during the fabrication process. To characterize the losses of the Ge-SLSPP waveguides, we employ a methodology similar to the effective cutback technique commonly utilized for waveguide characterization.[46] Instead of cleaving the chip, we fabricated waveguides of varying lengths on the same chip and measured each one individually. This method relies on the assumption that the optical properties are consistent across all waveguides, allowing us to obtain results comparable to the standard cutback technique. We used a calibration sample without a waveguide to normalize the measurements. The used on-chip QCL was operated in pulsed mode (1 kHz, 1 µs pulse width) using an HP 8114A pulse generator. Signals from both the on-chip QCD and an external MCT aligned to the device back-facet were recorded simultaneously via a Tektronix TDS 2024C oscilloscope. Probing needles connected the pulse generator and oscilloscope to the top and bottom contacts of the QCL and QCD for measurements. The sample stage, including the copper sample holder, was maintained at 17°C using an integrated Peltier cooler to ensure consistent conditions during testing. Various waveguide lengths were tested as part of the configurations.

III. RESULTS AND DISCUSSION

A. Optical characterization

The summary of all measured losses for the different configurations from Fig. 6(a-c) is presented in Fig. 7 with the main values extracted in Tab. I. As anticipated from the simulation data shown in Fig. 1(d), the losses of the thick Ge configuration are very high, even preventing proper experimental analysis of these devices. We attribute the inability to measure even the short (<50 µm) thick Ge/Au plasmonic waveguide samples to the significant additional fabrication and coupling losses obtained as a consequence of the geometry. Therefore, we focus the further analysis on the thin-Ge plus micro-mirror samples, which not only show promising performance, but also enable effective measurements across various configurations.

The blue diamonds in Fig. 7 represent the mean values for the linear waveguide devices at various lengths (see Fig. 6(a)), serving as the reference without mode redirection. A linear fit (black dotted line) reveals waveguide losses of α_{wg}= 0.018 dB/µm, while coupling losses (α_c = 7.2 dB) are extracted from the line's zero offset. As the QCL devices were not wavelength-locked, slight wavelength variations (8-8.3 µm) were considered in the simulations, reflected by the widening purple cone. Colored data points show results for different integrated gold micro-mirror designs. To quantify mirror losses, total losses (α_{tot}) were adjusted by subtracting coupling and waveguide losses. The discrepancy observed between the simulated (0.016 dB/µm) and actual (0.018 dB/µm) WG losses can again be reasonably attributed to imperfections in the waveguides and the underlying plasmonic Au layer. Mirror losses (α_M) were then calculated, with experimental results showing approximately 5 dB higher losses than simulations for the single-mirror design. This discrepancy is likely due to fabrication imperfections, such as surface roughness, edge diffraction, and coating imperfections, all of which can increase scattering, absorption, and reduce reflectivity. Additionally, although SEM images suggest that the reflective surfaces are mostly vertical, slight deviations from perfect verticality could also contribute to the increased losses.

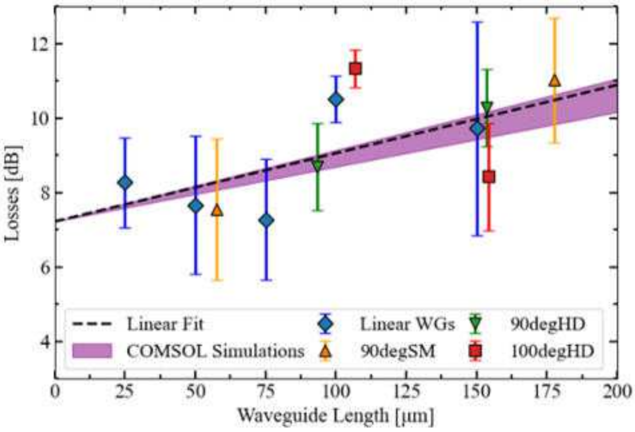

FIG. 7. Experimental results showing $\alpha_{tot} - \overline{\alpha_M}$ for different WG configurations. The color-coded data points correspond to the different designs depicted in Figure 6(a-c). Each data point encompasses at least three measurements from separate samples. The black dotted line is a linear fit of the linear WG configuration (blue datapoints) showing the waveguide losses α_{wg}. The purple cone illustrates the simulation region resulting from a wavelength range variation between λ = 8-8.3 µm of the individual on-chip QCLs that are used for the measurements on every single chip. The crossing point of the linear fit with the y-axis for zero WG length corresponds to the SLSPP WG coupling losses (α_c).

After demonstrating the effectiveness of the micro-mirror design, a critical component is the single s-bend or double s-bend, i.e. y-coupler. The later structure enables the combination of optical signals from two inputs into a single output (or vice versa), making it a fundamental building block for efficient signal routing. To optimize signal coupling, we designed and realized two combiner configurations: one with a 90-degree combining angle and the second one with a 100-degree angle and a tapered structure. A comparison of the simulated (left column) and measured losses (right column) for the various geometries—including the micro-mirror, double micro-mirror (100° and 90°), and the waveguide can be found in Table I. The measured losses show that the double micro-mirror structure with a 100° combining angle (Fig. 6c) exhibits twice the losses of a single mirror, while the 90° configuration shows nearly three times the losses. This is because the slightly larger angle allows for a smoother light transition between waveguides, reducing scattering and improving signal combination efficiency. Therefore the 100-degree design is more effective than the 90-degree one. Overall, these results demonstrate that adjusting the mirror angle can significantly improve the efficiency of the combiner. This proves that, through careful design, on-chip routing can be optimized to suit specific applications or requirements, offering flexibility in how light is managed and routed within the photonic circuit.

TABLE I. Comparison of the simulated (left column) and measured losses (right column) for the different analyzed geometries, i.e. micro-mirror, double micro-mirror (100° & 90°) and the waveguide. (* Double mirrors were not simulated but assumed to show twice the mirror losses of a single mirror.)

Losses	Simulation	Measurement
Micro-mirror	2.2 dB	7.9 dB
Double micro-mirror (100°)	4.4 dB*	14.8 dB
Double micro-mirror (90°)	4.4 dB*	20.1 dB
Coupling	-	7.2 dB
Waveguide	0.016 dB/µm	0.018 dB/µm

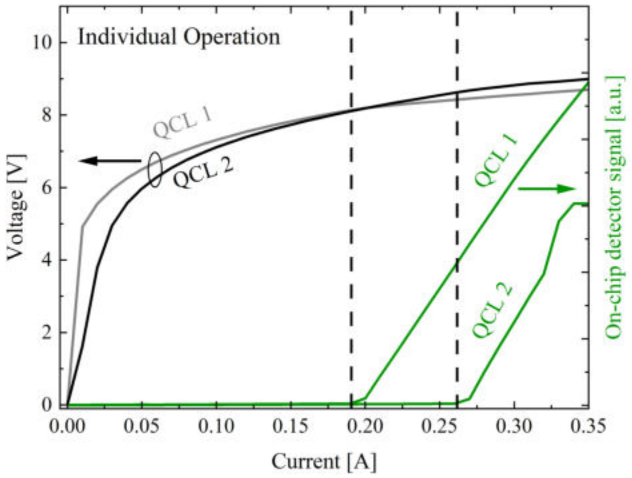

FIG. 8. Individual CW light-current-voltage (LIV) characterization of QCL 1 and QCL 2 in the 90° beam combiner configuration (similar to Fig. 6 (c), but center mirror with 90° combining angle) measured with the on-chip QCD (green traces). The threshold currents are emphasized by the dotted lines.

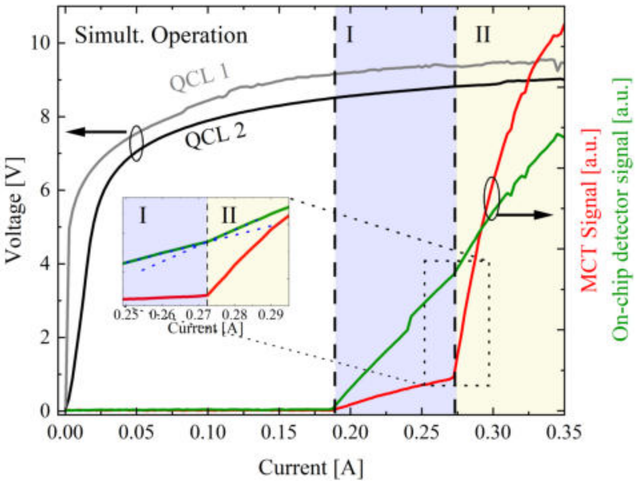

FIG. 9. CW-LIV characterization of the monolithic beam combiner, showing the measured optical signals on the on-chip QCD (green trace) and the external MCT detector (red trace) for both QCLs being driven in parallel.

B. Monolithic mid-infrared Beam Combiner

In this section, we present a proof-of-concept demonstration of a monolithic mid-infrared beam combiner utilizing micro-mirror-aided plasmonic guiding. The goal of these measurements is to validate the ability of our integrated design to combine light from two distinct lasers into a single on-chip detector. The significance of our findings is illustrated in Figures 8 and 9, which present an operational analysis of a dedicated sample using our beam combiner configuration with a 90° center mirror (design shown in Figure 6 (c)). Here, the 90° center mirror structure was selected for the superior laser performance. The sample was cooled to a temperature of T = -194°C within a cryostat to facilitate continuous-wave (CW) operation of the QCLs. Figure 8 shows light-current-voltage (LIV) data of both QCLs in individual operation detected via the on-chip QCD. Figure 9 shows the concurrent operation of both QCLs and confirms the simultaneous detection of both optical signals through the on-chip QCD. The lasing behavior can be categorized into two distinct regimes: Regime I (blue area) represents lasing of QCL 1 only. Due to the SiN/Au coating on the backside facet of QCL 1, the weak signal detected on the external MCT likely originates from emission through the substrate. In Regime II (yellow area), QCL 1 and QCL 2 are in the lasing regime simultaneously. Here, the back-facet of QCL 2 is uncovered, allowing its laser emission to be more efficiently out-coupled and detected with the MCT. A change in the slope of the on-chip detector photocurrent at QCL 2's threshold current highlights this transition, as shown in the inset graph. The threshold current of QCL 2 is slightly higher during simultaneous lasing, likely due to thermal effects induced by QCL 1's operation. These experiments demonstrate the significant role of the on-chip beam combiner in advancing MIR-PIC technology and show its potential in enabling the development of more complex PIC systems. For example, the integration of our beam combiner could facilitate sophisticated functionalities such as multi-channel signal processing and enhanced sensor applications, ultimately paving the way for innovative solutions in telecommunications, environmental monitoring, and biomedical diagnostics. This work lays a solid foundation for future research and development, demonstrating the impact of our on-chip beam combiners design in realizing the next generation of MIR photonic system.

IV. CONCLUSIONS AND OUTLOOK

In this work, we present the first integration of Au-covered monolithic micro-mirrors, thin Ge-based plasmonic waveguides, and QCL/QCD structures on a single epilayer chip. Through a combination of numerical simulations and experimental validation, we demonstrate the feasibility of using thin Ge/Au-based SPP waveguides integrated with Au-covered micro-mirrors for on-chip signal routing. While our approach does not surpass dielectric waveguides in performance, it demonstrates the feasibility of effectively achieving on-chip signal routing in monolithic MIR PICs. This integration lays the foundation for more advanced applications, such as high-speed heterodyne detection and on-chip Mach-Zehnder interferometry, with potential for miniaturized transceivers, and sensing systems in healthcare and environmental monitoring.[44,47,48]

A. Supplemental Material

1. *Cutback Technique and Measurement Approach*

To characterize optical losses, we used a method similar to the standard cutback technique. In traditional cutback, waveguides (WGs) are progressively shortened and measured at each length, allowing WG and coupling losses to be derived from a linear fit of the total measured losses as a function of inverse device length. In this study, we fabricated multiple WGs of varying lengths on the same chip and characterized them individually. This method, assuming consistent optical properties across WGs, yields comparable results to the standard cutback technique[35]. A calibration sample without a Ge-WG was fabricated to normalize the measurements. The sample, featuring a directly butt-coupled QCD and external QCL, had an air gap of approximately 2 µm. The losses attributed to the micro-mirrors (α_M) were calculated by subtracting the coupling losses (α_c = 7.2 dB) and the waveguide losses (α_{wg} = 0.018 dB/µm) from the total measured losses (α_{tot}) of the structures employing mirrors. Figure 7 in the manuscript shows the mean values of linear WG devices for various lengths, with blue diamonds representing the reference configuration without additional mode redirection. A linear fit to the data (black dotted line) reveals waveguide losses (α_{wg}) of 0.018 dB/µm, while coupling losses (α_c) were determined to be 7.2 dB from the zero offset of the line. Variations in emitted wavelengths from the QCL devices (between 8 and 8.3 µm) due to the absence of wavelength locking were accounted for in the simulations, as seen by the widening purple cone in the plot. Colored data points correspond to designs incorporating integrated gold micro-mirrors for mode redirection. To quantitatively assess and compare losses from different micro-mirror designs, the total measured losses (α_{tot}) were adjusted by subtracting coupling and waveguide losses. The resulting mirror losses were calculated as follows:

$$\overline{\alpha_M} = \frac{1}{n}\sum_{i=1}^{n} \alpha_{tot_n} - \alpha_{wg} - \alpha_c$$

where n is the number of measured devices. Figure 7 illustrates $\alpha_{tot} - \overline{\alpha_M}$ alongside the standard deviation of α_{tot} at corresponding waveguide lengths. Different waveguide lengths for single and double mirror configurations stem from various design versions. Experimental results show that the mirror losses for the single-mirror configuration are about 5 dB higher than in simulations, likely due to fabrication imperfections such as non-fully vertical reflection planes of the gold layer, leading to increased reflection losses.

ACKNOWLEDGMENTS

We acknowledge received funding from the EU Horizon 2020 Framework Program (No. 828893 project "cFlow") and the Austrian Research Promotion Agency (FFG, No. 883941 project "Greensensing"). B.H. acknowledges funding by the Austrian Science Fund FWF (M2485-N34). S.I. and A.M.A acknowledge the support of the European Office of Aerospace Research and Development / Air Force Office of Scientific Research (EOARD/AFOSR No. FA8655-22-1-7170 and FA8655-23-1-7070), and the FFG project "Green Sensing" (No. 883941). CzechNanoLab project LM2018110 funded by MEYS CR is gratefully acknowledged for the financial support of the measurements at CEITEC Nano Research Infrastructure. We want to thank Alicja Dabrowska, Niklas Brandacher, Sandro Dal Cin, Florian Pilat and Andreas Linzer for expert technical assistance.

DATA AVAILABILITY STATEMENT

The data presented in this study is available from the corresponding author upon reasonable request.

LITERATURE

[1] J. Bardeen and W. H. Brattain, "Transistor, a semiconductor triode," Physical Review **74**, 230–231 (1948).

[2] "Apple m2 ultra," https://www.apple.com/newsroom/2023/06/apple-introduces-m2-ultra/ (2023).

[3] M. Asghari and A. V. Krishnamoorthy, "Energy-efficient communication," Nature photonics **5**, 268–270 (2011).

[4] F. Testa, A. Bianchi, S. Stracca, and R. Sabella, "Silicon photonics iii - systems and applications," (2016) pp. 421–446.

[5] H. Tuorila, J. Viheriälä, M. Cherchi, A. T. Aho, T. Aalto, and M. Guina, "Low loss gainnas/gaas gain waveguides with u-bend geometry for single-facet coupling in hybrid photonic integration," Applied Physics Letters **113** (2018), 10.1063/1.5042813.

[6] Z. Zhou, X. Ou, Y. Fang, E. Alkhazraji, R. Xu, Y. Wan, and J. E. Bowers, "Prospects and applications of on-chip lasers," eLight **3** (2023), 10.1186/s43593-022-00027-x.

[7] H. Thiel, L. Jehle, R. J. Chapman, S. Frick, H. Conradi, M. Kleinert, H. Suchomel, M. Kamp, S. Höfling, C. Schneider, N. Keil, and G. Weihs, "Time-bin entanglement at telecom wavelengths from a hybrid photonic integrated circuit," Scientific Reports **14** (2024), 10.1038/s41598-024-60758-4.

[8] H. Fabian and W. Mäntele, "Infrared spectroscopy of proteins," In book: Handbook of Vibrational Spectroscopy (2006), https://doi.org/10.1002/0470027320.s8201.

[9] B. Hinkov, F. Fuchs, Q. K. Yang, J. M. Kaster, W. Bronner, R. Aidam, K. Köhler, and J. Wagner, "Time-resolved spectral characteristics of external-cavity quantum cascade lasers and their application to stand-off detection of explosives," Applied Physics B: Lasers and Optics **100**, 253–260 (2010).

[10] B. Tuzson, M. Mangold, H. Looser, A. Manninen, and L. Emmenegger, "Compact multipass optical cell for laser spectroscopy." Optics letters **38**, 257–9 (2013).

[11] P. Patimisco, G. Scamarcio, F. K. Tittel, and V. Spagnolo, "Quartz-enhanced photoacoustic spectroscopy: A review," Sensors **14**, 6165–6206 (2014).

[12] T. Schädle and B. Mizaikoff, “Mid-infrared waveguides: A perspective,” Applied Spectroscopy **70**, 1625–1638 (2016).

[13] P. Karioja, T. Alajoki, M. Cherchi, J. Ollila, M. Harjanne, N. Heinilehto, S. Suomalainen, J. Viheriälä, N. Zia, M. Guina, R. Buczyński, R. Kasztelanic, I. Kujawa, T. Salo, S. Virtanen, P. Kluczyński, H. Sagberg, M. Ratajczyk, and P. Kalinowski, “Multi-wavelength mid-ir light source for gas sensing,” (SPIE, 2017) p. 101100P.

[14] A. Schwaighofer and B. Lendl, “Quantum cascade laser-based infrared transmission spectroscopy of proteins in solution,” Vibrational Spectroscopy in Protein Research , 59–88 (2020).

[15] M. Vlk, A. Datta, S. Alberti, H. D. Yallew, V. Mittal, G. S. Murugan, and J. Jágerská, “Extraordinary evanescent field confinement waveguide sensor for mid-infrared trace gas spectroscopy,” (2021).

[16] N. Corrias, T. Gabbrielli, P. D. Natale, L. Consolino, and F. Cappelli, “Analog fm free-space optical communication based on a mid-infrared quantum cascade laser frequency comb,” Optics Express **30**, 10217–10228 (2022).

[17] P. Didier, H. Dely, T. Bonazzi, O. Spitz, E. Awwad, Étienne Rodriguez, A. Vasanelli, C. Sirtori, and F. Grillot, “High-capacity free-space optical link in the midinfrared thermal atmospheric windows using unipolar quantum devices,” Advanced Photonics **4** (2022), 10.1117/1.ap.4.5.056004.

[18] H. Dely, M. Joharifar, X. Pang, D. Gacemi, T. Salgals, R. Schatz, Y.-T. Sun, T. Bonazzi, E. Rodriguez, Y. Todorov, A. Vasanelli, A. Udalcovs, S. Spolitis, V. Bobrovs, O. Ozolins, S. Popov, and C. Sirtori, “High bitrate data transmission in the 8-14 µm atmospheric window using an external stark-effect modulator with digital equalization,” Optics Express **31**, 7259–7264 (2023).

[19] B. Hinkov, F. Pilat, L. Lux, P. L. Souza, M. David, A. Schwaighofer, D. Ristanić, B. Schwarz, H. Detz, A. M. Andrews, B. Lendl, and G. Strasser, “A mid-infrared lab-on-a-chip for dynamic reaction monitoring,” Nature Communications **13**, 4753 (2022).

[20] F. Pilat, B. Schwarz, B. Baumgartner, D. Ristanić, H. Detz, A. M. Andrews, B. Lendl, G. Strasser, and B. Hinkov, “Beyond karl fischer titration: a monolithic quantum cascade sensor for monitoring residual water concentration in solvents,” Lab on a Chip **23**, 1816–1824 (2023).

[21] B. Schwarz, C. A. Wang, L. Missaggia, T. S. Mansuripur, P. Chevalier, M. K. Connors, D. McNulty, J. Cederberg, G. Strasser, and F. Capasso, “Watt-level continuous-wave emission from a bifunctional quantum cascade laser/detector,” ACS photonics **4**, 1225–1231 (2017).

[22] Q. Lu, Y. Bai, N. Bandyopadhyay, S. Slivken, and M. Razeghi, “2.4 w room temperature continuous wave operation of distributed feedback quantum cascade lasers,” Applied physics letters **98** (2011).

[23] B. Hinkov, A. Bismuto, Y. Bonetti, M. Beck, S. Blaser, and J. Faist, “Singlemode quantum cascade lasers with power dissipation below 1 w,” Electronics Letters **48**, 646–647 (2012).

[24] G. Marschick, M. David, E. Arigliani, N. Opačak, B. Schwarz, M. Giparakis, A. Delga, M. Lagree, T. Poletti, V. Trinite, *et al.*, “High-responsivity operation of quantum cascade detectors at 9 μm,” Optics Express **30**, 40188–40195 (2022).

[25] A. Delga, “Quantum cascade detectors: A review,” Mid-infrared Optoelectronics , 337–377 (2020).

[26] B. Hinkov, F. Fuchs, W. Bronner, K. Köhler, and J. Wagner, “Current- and temperature-induced beam steering in 7.8-µm emitting quantum cascade lasers,” IEEE Journal of Quantum Electronics **44**, 1124–1128 (2008).

[27] M. J. Heck, “Highly integrated optical phased arrays: photonic integrated circuits for optical beam shaping and beam steering,” Nanophotonics **6**, 93–107 (2017).

[28] W. Guo, P. R. Binetti, C. Althouse, M. L. Mašanović, H. P. Ambrosius, L. A. Johansson, and L. A. Coldren, “Two-dimensional optical beam steering with inp-based photonic integrated circuits,” IEEE Journal of Selected Topics in Quantum Electronics **19**, 6100212–6100212 (2013).

[29] S. Jung, D. Palaferri, K. Zhang, F. Xie, Y. Okuno, C. Pinzone, K. Lascola, and M. A. Belkin, “Homogeneous photonic integration of mid-infrared quantum cascade lasers with low-loss passive waveguides on an inp platform,” Optica **6**, 1023 (2019).

[30] R. Wang, P. Täschler, Z. Wang, E. Gini, M. Beck, and J. Faist, “Monolithic integration of mid-infrared quantum cascade lasers and frequency combs with passive waveguides,” ACS Photonics **9**, 426–431 (2022).

[31] E. Chatzianagnostou, A. Manolis, G. Dabos, D. Ketzaki, A. Miliou, N. Pleros, L. Markey, J.-C. Weeber, A. Dereux, B. Chmielak, *et al.*, “Scaling the sensitivity of integrated plasmo-photonic interferometric sensors,” ACS Photonics **6**, 1664–1673 (2019).

[32] J. Homola, “Surface plasmon resonance sensors for detection of chemical and biological species,” Chemical reviews **108**, 462–493 (2008).

[33] R. Slavík and J. Homola, “Ultrahigh resolution long range surface plasmon-based sensor,” Sensors and Actuators B: Chemical **123**, 10–12 (2007).

[34] B. Schwarz, P. Reininger, D. Ristanić, H. Detz, A. M. Andrews, W. Schrenk, and G. Strasser, “Monolithically integrated mid-infrared lab-on-a-chip using plasmonics and quantum cascade structures.” Nature Communications **5**, 4085 (2014).

[35] M. David, A. Dabrowska, M. Sistani, I. Doganlar, E. Hinkelmann, H. Detz, W. Weber, B. Lendl, G. Strasser, and B. Hinkov, “Octave-spanning low-loss mid-ir waveguides based on semiconductor-loaded plasmonics,” Optics Express **29**, 43567–43579 (2021).

[36] M. David, D. Disnan, E. Arigliani, A. Lardschneider, G. Marschick, H. T. Hoang, H. Detz, B. Lendl, U. Schmid, G. Strasser, *et al.*, “Advanced mid-infrared plasmonic waveguides for on-chip integrated photonics,” Photonics Research **11**, 1694–1702 (2023).

[37] A. Krasavin and A. Zayats, “Passive photonic elements based on dielectric-loaded surface plasmon polariton waveguides,” Applied physics letters **90** (2007).

[38] Y. Zhong, S. D. Malagari, T. Hamilton, and D. Wasserman, “Review of mid-infrared plasmonic materials,” Journal of Nanophotonics **9**, 093791–093791 (2015).

[39] T. Schädle and B. Mizaikoff, “Mid-infrared waveguides: a perspective,” Applied Spectroscopy **70**, 1625–1638 (2016).

[40] M. David, D. Disnan, A. Lardschneider, D. Wacht, H. T. Hoang, G. Ramer, H. Detz, B. Lendl, U. Schmid, G. Strasser, *et al.*, “Structure and mid-infrared optical properties of spin-coated polyethylene films developed for integrated photonics applications,” Optical Materials Express **12**, 2168–2180 (2022).

[41] S. D. Cin, A. Windischhofer, F. Pilat, M. Leskowschek, V. F. Pecile, M. David, M. Beiser, R. Weih, J. Koeth, G. Marschick, B. Hinkov, G. Strasser, O. H. Heckl, and B. Schwarz, “An interband cascade laser based heterodyne detector with integrated optical amplifier and local oscillator,” Nanophotonics **13**, 1759–1764 (2024).

[42] M. David, I. Doganlar, D. Nazzari, E. Arigliani, D. Wacht, M. Sistani, H. Detz, G. Ramer, B. Lendl, W. Weber, G. Strasser, and B. Hinkov, “Surface protection and activation of mid-ir plasmonic waveguides for spectroscopy of liquids,” Journal of Lightwave Technology **in press** (2023), 10.1109/JLT.2023.3321034.

[43] X. Gsodam, “Mid-infrared plasmonic waveguide design and characterization for a chip-scale heterodyne receiver,” Master Thesis **TU Wien** (2023).

[44] M. David, *Plasmonics for Mid-infrared Photonic Integrated Circuits*, Ph.D. thesis, Technische Universität Wien (2023).

[45] L. Markey, C. Vernoux, K. Hammani, J. Arocas, J.-C. Weeber, and A. Dereux, “A long-range plasmonic optical waveguide corner mirror chip,” Micro and Nano Engineering **7**, 100049 (2020).

[46] P. Berini, R. Charbonneau, N. Lahoud, and G. Mattiussi, “Characterization of long-range surface-plasmon-polariton waveguides,” Journal of Applied Physics **98** (2005).

[47] A. Orieux and E. Diamanti, “Recent advances on integrated quantum communications,” Journal of Optics **18** (2016), 10.1088/2040-8978/18/8/083002.

[48] C. Chen and J. Wang, “Optical biosensors: An exhaustive and comprehensive review,” Analyst **145**, 1605–1628 (2020).

CHAPTER 4

COMPACT VERTICAL EMITTING RING INTERBAND CASCADE LASERS FOR ISOTOPE-RESOLVED CO_2 SENSING

4.1 Motivation, Background and State-of-the-Art

In recent years, significant advancements in ICL design have addressed key performance challenges such as efficiency, scalability, and broader application potential. Compared to QCLs, ICLs have gained recognition for their low threshold current densities and minimal power consumption, making them particularly well-suited for mobile applications. For instance, ICLs have achieved threshold current densities below 100 A/cm^2 in pulsed mode at room temperature for wavelengths around 3.6 µm, making them ideal for compact, battery-powered, portable trace gas sensing systems.[63, 191] ICLs have already been successfully employed to detect various gases such as sulfur dioxide,[192] formaldehyde,[193] methane and ethane.[194] The growing need for CO_2 sensors is driven by increasing environmental concerns, industrial monitoring requirements, and the demand for air quality control in both public and private spaces.[195] Accurate detection and monitoring of CO_2 levels, including the ability to distinguish between isotopes like $^{12}CO_2$ and $^{13}CO_2$, are critical for addressing climate change, carbon cycle studies, and improving energy efficiency. Isotope distinction is particularly important in environmental research and industrial applications, where understanding the sources and sinks of CO_2 is essential.[196, 197] ICLs, with their highly efficient operation in the mid-infrared region where CO_2 and its isotopes have strong absorption lines, are ideal candidates for these sensing applications. Their low power consumption, compact size, and ability to operate at room temperature make ICLs particularly well-suited for portable and miniaturized CO_2 sensors, offering precise, real-time monitoring and isotope distinction in a variety of environments. Miniaturization remains a key driving factor in the development of ICLs, as it is often associated with enhanced energy efficiency and resource savings. However, the integration of ICLs into existing fabrication processes, especially their compatibility with CMOS production, is still ongoing and has yet to reach full industry readiness.[198, 171] Recently, PICs with interband cascade devices as active components have been realized, demonstrating the concept's maturity.[199] The development of surface-emitting ring ICLs builds on foundational research in both QCL and ICL technologies. Ring-shaped cavities, initially explored in QCLs, have shown benefits such as supporting specific mode distributions, reducing threshold current densities, and improving beam properties.[53, 200] These advancements have been applied to ICLs to enhance the MIR performance of ring-ICL structures.[104] Unlike conventional edge-emitting devices, which require emission from a cleaved facet, ring ICLs could benefit from on-chip testing capabilities during production, significantly improving quality control and advancing industry readiness. Additionally, the position of the cleaved edge relative to the grating in traditional designs strongly impacts device performance.[107] As an alternative, surface-emitting lasers eliminate the need for cleaved edges and offer the advantage of integrating multiple devices into two-dimensional arrays or even in concentric configurations, emitting along the same optical axis.[201, 202] These innovations have propelled ICL technology forward, improving integration with optoelectronic systems. Recent advancements in substrate-emitting designs have further enhanced the potential of ring-ICLs, offering more efficient light extraction and superior thermal management through epi-down bonding, both of which are crucial for the stability and long-term reliability of MIR lasers.

4.2 Contribution to the field

The investigation of ICLs with ring waveguides forms a critical part of my research, motivated by their unique capabilities and potential applications in spectroscopy and precision measurement. ICLs are particularly advantageous for MIR applications due to their efficient interband transitions in type-II band alignment geometry, allowing operation over a broad spectral range from less than 3 µm to over 6 µm. Our research specifically explores the miniaturization of these devices which is pivotal for enhancing their performance in various practical applications. In the third paper, we present the development of a compact, substrate-emitting ring ICL with low power consumption, designed for seamless integration into CO_2 sensing applications. These devices demonstrate excellent performance characteristics, including low threshold currents, small footprints, and stable single-mode emission, making them highly suitable for rapid, isotope-resolved CO_2 detection in battery-driven, handheld, and portable devices.

The ring ICLs developed in this study utilize epi-down bonding with sub-micron accuracy, enabling robust integration into industrial environments and ensuring reliability and scalability for mass production. Comprehensive experimental results validate the efficacy of this approach, with detailed spectral analysis and demonstration of CO_2 sensing capabilities. The compact, low-dissipation, and reliable nature of these devices positions them as ideal candidates for a wide range of industrial applications, including environmental monitoring, process control, and atmospheric research, where efficient and portable CO_2 sensors are essential.

4.3 Publication

Reprinted, with permission, from G. Marschick, S. Isceri, R. Szedlak, H. Moser, P. Waclawek, E. Arigliani, B. Hinkov, R. Weih, W. Schrenk, G. Strasser, A. M. Andrews, B. Lendl, and B. Schwarz "Compact vertical emitting ring interband cascade lasers for isotope-resolved CO_2 sensing."

APL Photonics 1 October 2024; 9 (10): 100806. https://doi.org/10.1063/5.0221189

APL Photonics ARTICLE pubs.aip.org/aip/app

Compact vertical emitting ring interband cascade lasers for isotope-resolved CO_2 sensing

Cite as: APL Photon. **9**, 100806 (2024); doi: 10.1063/5.0221189
Submitted: 30 May 2024 • Accepted: 4 October 2024 •

Georg Marschick,[1] Stefania Isceri,[1] Rolf Szedlak,[1] Harald Moser,[2] Johannes P. Waclawek,[2] Elena Arigliani,[1] Robert Weih,[3] Werner Schrenk,[1] Gottfried Strasser,[1] Borislav Hinkov,[4] Aaron Maxwell Andrews,[1] Bernhard Lendl,[2] and Benedikt Schwarz[1,a)]

AFFILIATIONS

[1] Institute of Solid State Electronics and Center for Micro- and Nanostructures, TU Wien, Gußhausstraße 25, 1040 Vienna, Austria
[2] Institute of Chemical Technologies and Analytics, TU Wien, Getreidemarkt 9, 1060 Vienna, Austria
[3] Nanoplus Nanosystems and Technologies GmbH, Oberer Kirschberg 4, 97218 Gerbrunn, Germany
[4] Silicon Austria Labs, Europastraße 12, 9500 Villach, Austria

Note: This paper is part of the APL Photonics Special Topic on Mid-IR Photonics.

[a)] **Author to whom correspondence should be addressed:** benedikt.schwarz@tuwien.ac.at

ABSTRACT

We present a compact vertically emitting ring interband cascade laser (ICL) with low power consumption and the possibility for seamless integration into various CO_2 sensing applications. Our devices exhibit desirable performance characteristics in battery-driven handheld devices, including room temperature (20 °C) threshold currents as low as 15 mA, small footprints, and stable single-mode emission, suitable for rapid isotope-resolved CO_2 detection. Through epi-down bonding with sub-micron accuracy, we achieved robust integration of substrate-emitting ring ICLs, ensuring reliability and scalability that would be required for mass production. We present comprehensive experimental results validating the efficacy of our approach, including spectral analysis and CO_2 sensing capabilities with limits of detection of 24 and 13 ppmv utilizing the $^{12}CO_2$ P(60) and $^{13}CO_2$ R(10) transitions in the ν_3 fundamental band, respectively. The demonstrated devices hold great promise for a wide range of industrial applications, including environmental monitoring, process control, and atmospheric research, where compact low-power sensors are essential.

I. INTRODUCTION AND MOTIVATION

The mid-infrared (mid-IR) spectral region, spanning wavelengths from 2.5 to 25 μm, encompasses fundamental molecular vibrational and rotational absorption bands, enabling precise detection and characterization of molecules with unique absorption fingerprints.[1] Accordingly, mid-IR technologies are indispensable in gas sensing[2–4] and liquid spectroscopy,[5,6] covering a broad spectrum of applications ranging from industrial process control and environmental monitoring to medical and health analysis.[7–9] Among the diverse array of mid-IR laser sources, interband cascade lasers (ICLs) have emerged as prominent candidates due to their exceptional performance characteristics.[10] Unlike traditional diode lasers, which depend on interband transitions within a single material, ICLs, akin to quantum cascade lasers (QCLs), utilize cascading processes across multiple quantum wells. These cascaded interband transitions enable efficient light emission, and the proper design of the quantum-well structures allows precise control over the emission wavelength, facilitating access to key absorption lines of target molecules within the mid-IR spectrum. Their unique design allows low threshold currents, high quantum efficiency, and continuous wave (CW) operation at room temperature, making them well-suited for a wide range of advanced technological applications.[11] In addition, ICLs exhibit excellent wavelength stability and spectral purity, essential attributes for sensitive and selective detection of trace gases and pollutants.[12]

Vertically emitting lasers with a ring-shaped design have demonstrated clear benefits compared to their straight, edge-emitting counterparts.[13] They enable on-chip testing without cleaving to obtain their performance. Furthermore, surface emitters generally exhibit superior far-field profiles compared to edge-emitting lasers.[14,15] The latter often present asymmetrical far-field shapes due to their asymmetrical emitting area. This disparity can limit their applicability in certain scenarios. In contrast, ring ICLs offer a compelling alternative with their rotationally symmetric geometry. This unique feature endows ring ICLs with a uniform and concentric far-field pattern, making them exceptionally well-suited for a wide range of applications where consistent beam characteristics are crucial. In recent years, substrate-emitting ring ICLs have undergone significant advancements, marking critical milestones in their development. The year 2017 saw the first demonstration of single-mode, pulsed-operation devices, vertically emitting through their substrate up to temperatures of 35 °C, which showcased the potential of ring ICLs in the efficient generation of coherent mid-infrared light.[16] This was followed by a pivotal breakthrough in 2020, when CW operation up to temperatures of 38 °C was achieved, highlighting the lasers' capability for stable and sustained emission, essential for many practical applications.[17] Recently, the low-noise nature of ring ICLs has been investigated, showing shot-noise-limited operation for Fourier frequencies above 100 kHz, making them ideal candidates for various spectroscopic applications.[18] Building on these foundational achievements, our latest efforts focus on further refining and enhancing the performance of vertically emitting ring ICLs. Miniaturization stands as a cornerstone in the evolution of semiconductor devices, including ICLs, owing to its profound implications across multiple fronts.[19] First, reducing the footprint of ring ICLs translates directly into enhanced portability and compatibility, facilitating their integration into a myriad of systems and applications where space is at a premium, such as portable electronics, wearable devices, and miniature sensors.[20] Moreover, miniaturization often correlates with improved energy efficiency as reduced device dimensions typically entail lower power consumption. This translates into tangible benefits, particularly in battery-powered or resource-constrained environments.[21,22] By reducing the size of ring ICLs and integrating them more densely, we can achieve substantial reductions in manufacturing costs. This is largely due to the more efficient use of materials and the ability to produce larger quantities of devices per wafer. The implementation of wafer-level on-chip testing, such as light–current–voltage (LIV) and spectral characterization through needle probing, further contributes to cost efficiency. This approach allows early identification of high-performing devices, ensuring that only the best candidates proceed to the final stages of production. Consequently, this enhances yield and lowers production expenses. Epi-down bonding on tailored aluminum nitride submounts significantly enhances the industry readiness of our devices. This bonding technique improves thermal management by providing superior heat dissipation, which is critical for maintaining stable continuous wave operation and extending device longevity.[23] As the customization of the submounts increases the possibilities of seamless integration into a wide range of industrial and scientific setups, epi-down bonding enhances the devices' versatility and broadens their potential field of applications.[24] To demonstrate the practical applicability of our devices, we performed isotope-resolved CO_2 absorption measurements through the second harmonic ($2f$) wavelength modulation spectroscopy (WMS) method. By leveraging the precise emission wavelength of 4.36 μm (~2290 cm^{-1}) in continuous wave operation, we effectively distinguished between the absorption spectra of $^{12}CO_2$ and $^{13}CO_2$. Our devices exhibited high spectral resolution and sensitivity, enabling the accurate detection of these isotopes' distinct absorption peaks down to concentrations as low as 10 ppm. This capability underscores the utility of our devices in environmental monitoring and industrial applications where precise gas detection is critical.

II. RESULTS AND DISCUSSION

A. Materials and processing

1. Interband cascade laser

The ICL material is epitaxially grown using molecular beam epitaxy (MBE) on a low-doped GaSb substrate, facilitating efficient light emission through the substrate. The active region features a seven-stage design based on a classical W-type quantum well (QW) structure, comprising two InAs QWs separated by a single GaInSb barrier per stage: 2.22 nm InAs/2.5 nm S–In(0.4)Ga(0.6)Sb/1.8 nm InAs. This active region is flanked by two 500 nm thick GaSb separate-confinement layers (SCLs) with a doping concentration of 1×10^{17} cm^{-3}, which ensure a high modal gain through effective vertical mode confinement at the center of the active region. The entire structure is further encapsulated between InAs/AlSb superlattice claddings. The lower cladding, with a thickness of 3.5 μm, is specifically designed to prevent vertical mode leakage into the high-refractive-index substrate, while the upper cladding has a thickness of 2 μm. This meticulously engineered epitaxial structure ensures high performance and reliability during CW operation at a wavelength of 4.36 μm.

The processing of the ring laser structures followed standard III–V semiconductor cleanroom processes. The design incorporated eight rings with different center radii (20, 40, 50, 60, 80, 90, 100, and 120 μm) and waveguide widths of 5.5 μm into a single laser module. A total of 24 laser modules (192 individual lasers) were integrated onto a single 1×1 cm^2 sample for processing. Each laser module measures 800×1300 μm^2. Starting with the definition of the ring structures, a silicon nitride (SiN) hardmask was deposited onto the samples via a plasma enhanced chemical vapor deposition (PECVD) process. All photolithography processes involved in the manufacturing were conducted with a Heidelberg MLA150 maskless laser lithography system, with manual marker alignment between the single lithography steps. Following the definition of the ring structures, the hardmask was initially etched using CHF_3 reactive ion etching (RIE), followed by semiconductor deep-etching employing Cl_2–Ar chemistry, and concluded with a wet etching step in diluted hydrochloric acid. The residual hardmask was removed with isotropic SF_6 RIE. For vertical outcoupling of the light and single mode emission, a second order distributed feedback grating (DFB) was integrated on top of the ring-shaped waveguide. Due to the small feature size of the grating (~600 nm), e-beam lithography was used for definition after deposition of a second SiN hardmask. The grating was then etched, again with Cl_2–Ar, around 1 μm deep into the waveguide cladding. After hardmask removal, a 250 nm thick SiN passivation layer was deposited via PECVD and opened along the centerline of the waveguide with CHF_3 RIE chemistry. Metallization of the ring lasers was realized through photolithography and sputtering of 10 nm Ti acting as an adhesion promoter, 100 nm Pt as a diffusion barrier, and finally, 300 nm Au as the contact. The relatively thick Pt layer is crucial to inhibit diffusion of Au atoms into the epilayers at elevated temperatures, especially during the sub-micron

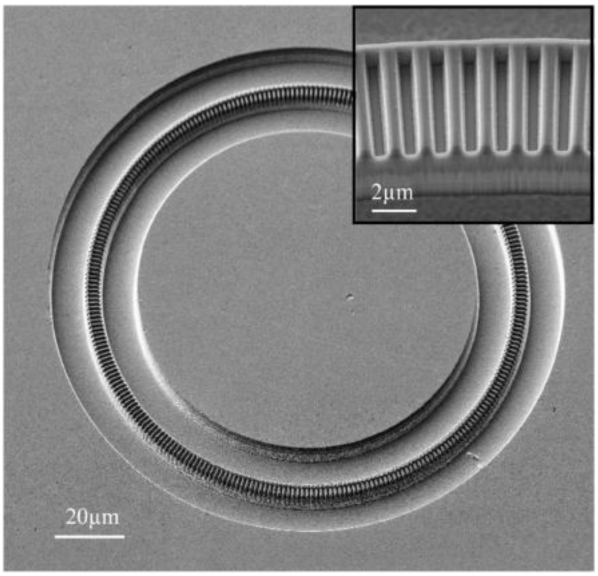

FIG. 1. Scanning electron microscopy image of a ring ICL with a center radius of 60 μm prior to flip-chip bonding. The inset shows a segment of the ring with the etched DFB grating. For better visualization, the grating is shown directly after etching, before the passivation and contact sputtering.

accuracy bonding process at 220 °C. As a last step, the sample was polished to a thickness of 180 μm and the backside was contacted with a Ge–Au–Ni–Au bottom contact to create an ohmic contact with the low-doped GaSb substrate. Figure 1 shows a scanning electron microscopy image of a ring ICL with a radius of 60 μm. The inset depicts a detailed view of the fabricated second order DFB grating atop the waveguide.

2. Aluminum nitride submounts

The choice of aluminum nitride (AlN) for the submounts offers several advantages. With its high intrinsic thermal conductivity of up to 285 W/m K, it effectively dissipates heat generated during the laser operation, preventing thermal accumulation and enhancing device reliability.[25] In addition, AlN's excellent electrical insulation properties minimize electrical crosstalk and interference, ensuring stable laser performance. Its low thermal expansion coefficient ensures durable bond-stability. The combination of these properties makes AlN an optimal material for supporting high-power and high-efficiency optoelectronic devices. The submounts are designed to hold a single laser module consisting of eight lasers. Each of these lasers is contacted through a separate Au bonding pad. Processing AlN submounts involves several challenges, primarily due to the material's transparency to ultraviolet (UV) light, which complicates standard lithography techniques. To address this issue, a thin layer of gold (Au), ~20 nm thick, was deposited onto the AlN surface. This Au layer serves as an opaque coating, enabling effective photolithography by blocking UV light and allowing accurate patterning. After depositing the Au layer, photolithography was performed to define the areas where contacts were to be deposited. The patterns were developed, and the Au opacity layer was selectively etched away from these areas. Following this, Ti–Au contacts were sputtered and a lift-off process ensured that contacts remained only in areas without resist, which are the areas where the opacity layer was previously etched away. At this stage, next to the deposited contacts, the sample still had the Au layer in the regions where it was not etched away, keeping it completely opaque for the following photolithography step to define the bonding pads for electroplating. After electroplating of ~ 5 μm thick Au-bond pads, the submounts underwent a final short potassium iodide (KI–I_2) Au-etch to remove any remaining Au from the initial opacity layer, ensuring that the surfaces were clean and free of contaminants or short-circuits between the contacts. The completed AlN submounts, now equipped with robust Au bonding pads, were ready for the subsequent bonding process with the cleaved ring ICL modules. This bonding process was realized through a Finetech Fineplacer lambda sub-micron flip chip die bonder. The laser modules (800 × 1300 μm^2) were aligned to the AlN submounts and bonded at a temperature of 220 °C with a force of 15 N. The benefits of the utilized AlN submount and the epi-down mounting are directly visible in the achieved low thermal resistance area products as low as $R_{th}A = 4.6$ K cm^2/kW for a device with a center radius of 80 μm. This is notably lower compared to devices with similar growth parameters, especially those with similar cladding thicknesses.[26]

B. Footprint reduction

The miniaturization and optimization of semiconductor lasers play a pivotal role in advancing various technological domains, from telecommunications[27] to sensing in medical diagnostics.[28] In this study, we aim to substantially reduce the footprint of ring ICLs in order to facilitate mass production and cost-effectiveness. Leveraging a multifaceted approach, we employ COMSOL Multiphysics simulations alongside experimental fabrication to explore the minimal dimensions achievable for these ring ICLs. Through systematic characterization of fabricated devices with varying ring radii, we validate our simulations and unveil insights into the relationship between device size and performance metrics, such as the threshold current density. In addition, we introduce a novel submount and bonding scheme, tailored to enable on-chip testing and seamless integration into industrial environments, thereby enhancing the practical viability of these miniaturized ring ICLs. This endeavor not only contributes to the fundamental understanding of semiconductor laser physics but also paves the way for their widespread application in diverse fields.

We comprehensively investigated the modes of the ring interband cascade lasers using COMSOL. We designed second order DFB gratings aiming at the target wavelength of 4.36 μm, with 50% duty-cycle and an etch depth equal to 1 μm, consistent with the fabricated devices. Consequently, an eigenfrequency analysis was performed in a transformed coordinate system to incorporate intrinsic bending losses and absorption losses, which served as an estimation of the mode confinement. The eigenmodes in circular cavities have to satisfy the phase condition given by $m\,\lambda/n_{eff} = L_{eff}$, where n_{eff} is the effective refractive index of the waveguide, $L_{eff} = 2\pi r_{eff}$, and r_{eff} is the effective mode radius. We simulated 5.5 μm wide waveguides, with central radius varying between 50 and 120 μm. The refractive index of the III–V semiconductors, the SiN isolation, and the Au contact

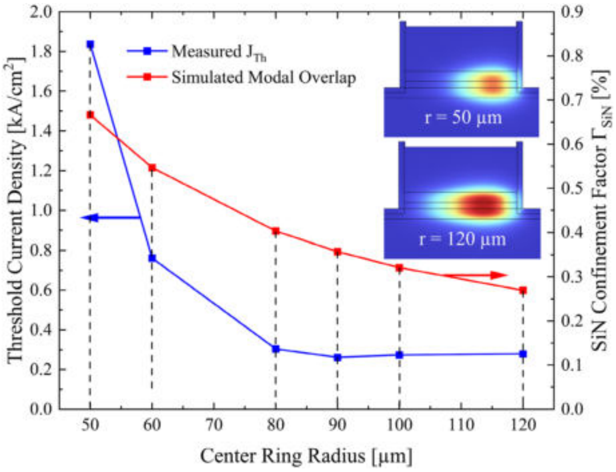

FIG. 2. Simulated confinement factor in SiN (red) and measured threshold current density (blue) in pulsed operation vs the center radius of the ring ICLs. The inset shows COMSOL simulations of the whispering gallery mode for radii of 50 and 120 μm.

were calculated using the Lorentz–Drude model and the Sellmeier dispersion relation.

With decreasing radius, the ring curvature increases and the whispering gallery mode is pushed further toward the outside wall of the ring laser (see the inset of Fig. 2).[29] Hence, the confinement factor in the SiN passivation layer increases, which introduces additional losses. The losses in the SiN isolation α_{SiN} are calculated as follows:

$$\alpha_{SiN} = \Gamma_{SiN} \times 4 \times \pi \times \frac{f_0}{c_0} \times \Im(n_{SiN(\lambda)}), \tag{1}$$

where f_0 describes the mode eigenfrequency, c_0 describes the speed of light in vacuum, and Γ_{SiN} describes the confinement factor of the optical mode in the SiN isolation layer.[30] $\Im(n_{SiN(\lambda)})$ is the imaginary part of the refractive index of SiN at the wavelength of interest λ, which was taken from Ferré *et al.*[31]

Figure 2 shows the simulated confinement factor in the SiN and the measured threshold current density vs the center ring radius of six representative devices.

Simulation and experiment show an increase in the confinement factor and the threshold current density for radii smaller than 80 μm. While lasing was observed in only a limited number of rings with a radius of 50 μm, no rings with smaller radii exhibited lasing. For rings with radii of 80 μm and larger, the threshold current density stays relatively constant, while the confinement factor keeps decreasing. This indicates that the abrupt increase in the threshold current density for smaller rings cannot be completely attributed to the losses in the SiN alone. Hence, we assume that additional losses at the semiconductor–SiN interface contribute to the elevated thresholds for smaller rings. Since the whispering gallery mode is pushed more outward for smaller rings, the optical mode in smaller rings has a stronger interaction with this interface. Losses there may come from interface roughness introduced during the RIE process.[32] The difference in the volatility of the involved etch-products may trigger such interface degradation.[33] As this interface roughness is also transferred to the metallization, ohmic losses in the imperfect conductor increase.[34,35] A further origin of interface roughness and absorption at the semiconductor–passivation interface is processing residuals, such as highly absorbing Si-containing and polymeric micro-residuals originating from the CHF_3 RIE process during the SiN passivation opening.[36,37] For this particular type of laser source, the critical parameter for miniaturization is a radius of 80 μm. The laser dimensions can be decreased to this extent without any compromise in performance. A deeper understanding of the effects of the interface losses and the ability to control them may result in further reductions in the minimum size of similar lasers.

C. Toward automated testing and industrial implementation

Automated testing and seamless integration into industrial environments are paramount considerations in the development and deployment of advanced semiconductor technologies, including ring ICLs. One of the key advancements in our approach lies in the implementation of epi-down bonding on custom-made AlN submounts. This technique not only enhances the thermal dissipation and thus allows CW operation of the lasers but also facilitates seamless integration into industrial systems, where reliability and performance are crucial. Our substrate-emitting ring ICLs enable on-chip testing as shown in Fig. 3(a). On-chip testing is performed at room temperature after the fabrication of the epi-up devices, but prior to cleaving and the epi-down bonding process of the semiconductor chip. This facilitates performance and quality control, as well as the selection of devices with the most suitable characteristics for a given application. Figure 3(b) depicts the results of the on-chip testing. This pulsed (f = 5 kHz, t = 100 ns, 0.05% duty cycle) LIV characterization is realized through needle probing at the wafer level. All the manufactured ring sizes were tested. Lasing was observed in rings with radii of 50 μm and larger, which are consequently depicted in Fig. 3(b). A microscope image of the corresponding lasers is given in the inset of Fig. 3(b). The measured threshold current density is continuously increasing with decreasing ring radius due to the increasing losses experienced by the whispering gallery mode (see Fig. 2). The thresholds vary from 0.27 kA/cm^2 for lasers with a radius larger than and equal to 80 μm to 0.75 and 1.9 kA/cm^2 for lasers with 60 and 50 μm radii, respectively. This is a significant reduction compared to previously reported ring ICLs at 3.7–3.8 μm with room-temperature threshold current densities of 0.75 kA/cm^2 in pulsed[16] and 0.6 kA/cm^2 in CW operation.[17] These ring ICLs have a typical radius of 200–400 μm. The ring thresholds reported in this paper are comparable to straight, broad-area lasers at similar wavelengths of 4.35 and 4.5 μm, with thresholds of 0.48 and 0.28 kA/cm^2 at 300 K, respectively. Lower threshold current densities of 0.25 kA/cm^2 have been achieved at 4.6 μm. In addition, a narrow ridge device lasing at 4.6 μm with a ridge width of 10 μm—nearly twice the width of the devices presented in this work—exhibited threshold current densities of around 0.4 kA/cm^2.[38,39] It is important to note that additional challenges, such as sidewall leakage and optical scattering losses, directly influence the threshold performance of narrow-ridge devices.[40,41]

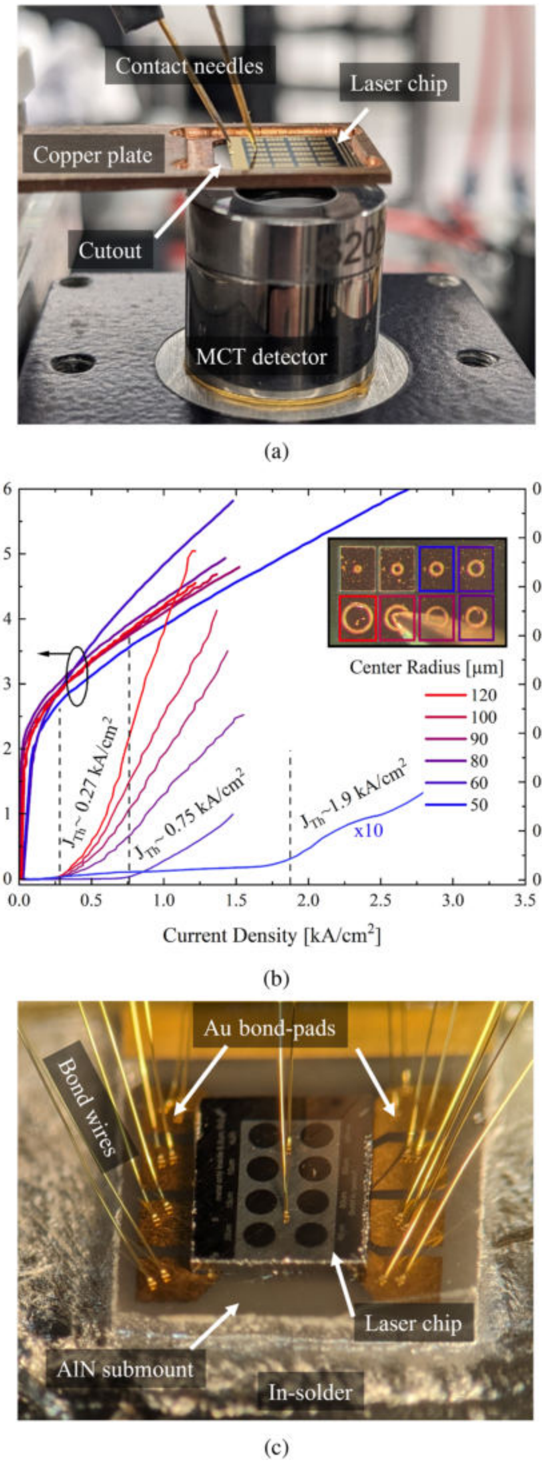

(a)

(b)

(c)

FIG. 3. (a) Pulsed on-chip testing of unmounted laser devices. (b) Pulsed LIV characterization results of ring ICLs with best current density performance and different radii. The inset shows a microscope image of one laser module under test. (c) Mounted ring ICL chip with bonding pads.

The rigorous and scalable screening process enables testing of a multitude of lasers in a short time and helps identify and optimize devices with superior performance metrics, ensuring efficiency of the integrated lasers after the bonding process.

Figure 3(c) illustrates the flip-chip bonded and contacted laser chip on the AlN submount. The latter contains eight individual bonding pads, one for each ring laser on the ICL chip. The shared bottom contact features circular openings located directly above each ring ICL for efficient light extraction.

D. Far-field

Figure 4 shows the far-field of an epi-down bonded ring ICL with a radius of 80 μm. The light is emitted through the substrate and recorded with an MCT detector on an x–y translational stage at a distance of 6 cm in a lens-less configuration. The captured beam profile features a ring-shaped intensity pattern with an opening angle of ±10° and a central intensity minimum. The radial symmetry of the circular intensity pattern aligns well with standard optical elements, such as lenses and mirrors. This symmetry allows more efficient collimation and focusing compared to non-circular surface emitters. The bigger effective surface area of circular waveguides compared with the facets of laser ridges results in a broad aperture resulting in narrowly divergent beams. For certain applications, the non-Gaussian beam profile with a central intensity minimum may be disadvantageous. However, with appropriate grating engineering, the beam can be shaped to achieve maximum intensity at the center.[42,43] The larger opening angle compared to previous devices, as published in Ref. 17, can be attributed to the smaller footprint of the ring laser and the associated increased beam divergence. Inhomogeneities in the emission pattern are attributed to processing imperfections.

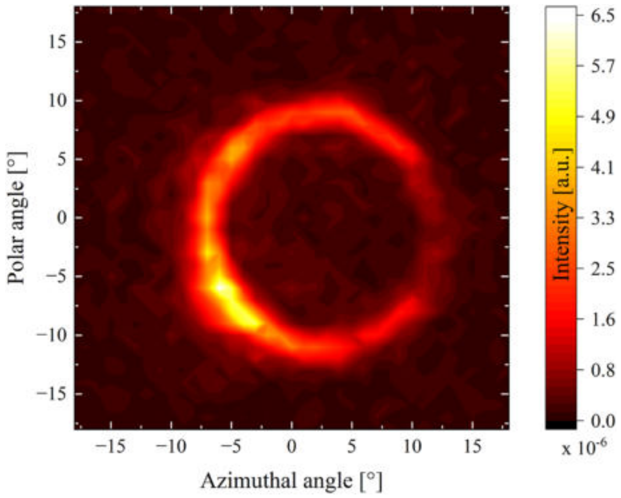

FIG. 4. Circular far-field intensity pattern of a ring ICL with a radius of 80 μm and an opening angle of ±10°. The angular resolution is limited to 1° due to the detector size. Graphical pixel interpolation was used to smoothen the data.

E. Continuous-wave operation

Flip-chip bonding of the ring ICL chip onto the AlN submount results in improved heat dissipation and enables CW operation. However, despite this enhanced thermal management, the threshold current density (J_{th}) increases when transitioning from pulsed operation to CW operation due to the continuous injection of current, which leads to heat accumulation in the device. While the AlN submount helps mitigate some thermal effects, the inherent nature of CW operation results in a higher thermal load compared to pulsed mode, particularly in ICLs where the superlattice cladding layers contribute to higher thermal resistance compared to QCLs. Anyway, CW-operation offers several advantages in various applications, particularly in gas spectroscopy.[44] First, it ensures a steady and uninterrupted output, facilitating stable and precise measurements over extended periods. This continuous emission enables consistent interaction with the gas sample, resulting in an enhanced signal-to-noise ratio and improved spectral resolution.[45] In addition, CW lasers typically exhibit narrower linewidths compared to pulsed lasers, leading to finer spectral features and more accurate spectral analysis. In gas spectroscopy, where the identification and quantification of trace gases are crucial, the continuous emission of CW lasers enables real-time monitoring and detection of gas concentrations with high sensitivity and accuracy.[46]

Figure 5 depicts the CW-LIV characteristics and the corresponding spectra at several driving currents of a ring ICL with a radius of 80 μm.

The total spectral coverage of this ring laser amounts to 4 cm^{-1} around the central wavenumber of 2290 cm^{-1} with a tuning coefficient of 0.27 cm^{-1}/mA. In continuous wave operation, this laser exhibits a measured total optical output power of around 200 μW and a threshold current of 22 mA. Larger rings have demonstrated measured output powers reaching up to 600 μW. Output power measurements were conducted with a carefully aligned calibrated integrating sphere to ensure proper collection of all emitted power. Anyway, the given values must be seen as a lower limit as a 100% collection efficiency might not have been reached. The highest measured submount temperature allowing stable CW operation was 25 °C. The lowest recorded threshold current amounts to 15 mA in a ring ICL with a radius of 80 μm, resulting in a total power dissipation of 68 mW at threshold. To the authors' knowledge, this is the lowest achieved threshold current for vertical-emitting ICLs.

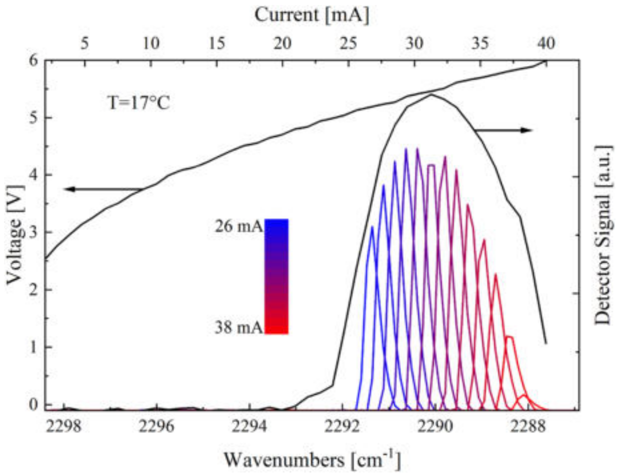

FIG. 5. LIV characteristics and emission spectrum of a typical device measured at a temperature of 17 °C (black curves). This device's CW threshold current density of $J_{\text{th-CW}}$ = 800 A/cm^2 is higher compared to its pulsed threshold current density of $J_{\text{th-pulsed}}$ = 430 A/cm^2 due to thermal effects. The color coded spectral emission lines show the direct correlation between the driving current (top x-axis) and emission wavenumber (bottom x-axis).

F. CO_2 isotope measurements

The isotopic substitution of a single carbon atom in CO_2 results in slight changes in the vibrational frequencies of molecular bonds, leading to distinct absorption peaks in the MIR spectrum, allowing spectral discrimination between $^{12}CO_2$ and $^{13}CO_2$. The operating wavelength of our ring ICLs, set at around 2900 cm^{-1} (4.36 μm) in continuous wave operation, is particularly chosen as in this spectral region, the absorption spectra of both isotopes overlap, providing enhanced sensitivity and specificity for CO_2 sensing. The primary goal of this work was not to achieve ultra-high sensitivity but rather to demonstrate the feasibility and capabilities of vertically emitting ring ICLs for isotope-resolved CO_2 detection. This proof-of-concept experiment showcases the potential of these compact lasers for CO_2 sensing, paving the way for further developments in sensor technology. The isotopic analysis of CO_2 is of great importance in various fields, such as geochemistry, atmospheric chemistry, and medical diagnostics. In geochemistry, studying the carbon isotopic ratios in volcanic gases helps predict volcanic activity by tracking changes in the source regions.[47] In atmospheric chemistry, analyzing the isotopic compositions provides critical insights into the biosphere–atmosphere carbon exchange and the influence of CO_2 on global warming.[48] In the medical field, carbon isotope analysis in exhaled breath offers a non-invasive approach for diagnosing conditions such as *Helicobacter pylori* infections and liver disorders.[49–51]

In our work, we utilized 2f-scanned-wavelength WMS for CO_2 isotope measurements. WMS involves modulating the laser with a high-frequency modulation superimposed on the fixed injection current. This modulation generates harmonic components in the detector signal, which can be isolated for analysis. The scanned-wavelength WMS strategy combines this fast modulation with a slow modulation of the injection current to achieve effective signal filtering. The slow modulation was realized in the form of a sawtooth ramp signal. The detected modulated absorption signal is then processed to demodulate the second harmonic, providing enhanced sensitivity and detection limits.[52,53] For the CO_2 isotope measurements, a ring ICL, operated at 15 °C, with a radius of 90 μm is utilized. Driving this laser with a 0.5 Hz current ramp from 35.9 to 41.9 mA facilitated a maximum spectral bandwidth of ~ 1.5 cm^{-1}. The fast modulation was executed at a frequency of 5 kHz with an amplitude of 0.5 mA. The emitted laser light was collimated using a parabolic mirror and guided through a 10 cm long gas cell and then focused using another parabolic mirror onto an MCT detector. The CO_2 WMS experiment was conducted within a nitrogen-flushed enclosure to ensure a controlled and inert atmosphere, mitigating potential interference from ambient gases. Different CO_2 concentration levels within a range from 10 to 500 ppmv were prepared by diluting a certified 1000 ppmv CO_2:N_2 calibration mixture with 5.0 N_2 (99.999%). The subsequent gas concentration analysis focused on the P(60) $^{12}CO_2$ peak at 2291.542 cm^{-1} and the R(10) $^{13}CO_2$ peak at 2291.68 cm^{-1}. These are the two strongest peaks in the above-mentioned spectral range of the laser. The corresponding WMS spectra are depicted in Fig. 6(a). The absorption signal for $^{13}CO_2$ is higher than that for $^{12}CO_2$ due to the stronger intrinsic line intensity of the $^{13}CO_2$ transition. While $^{12}CO_2$ is more abundant in natural CO_2, the R(10) transition of $^{13}CO_2$ has a higher absorption cross section compared to the P(60) transition of $^{12}CO_2$. Each concentration step was measured three times, and the resulting peak-to-peak signal for both absorption lines was averaged, fit by linear regression, and plotted as a function of the concentration, as shown in Fig. 6(b). A good linearity between signal amplitudes and CO_2 concentrations was observed. The R^2-value of both regression curves is larger than 0.99. The corresponding limit of detection (LOD) was ascertained at three times the standard deviation (3σ) of the intercept divided by the slope of the calibration curve. The LOD for natural CO_2 is 24 ppmv when measured using the $^{12}CO_2$ peak and 13 ppmv when measured using the $^{13}CO_2$ peak. Adjusting for natural abundance, the absolute LODs are 23.5 ppmv for $^{12}CO_2$ and 144 ppbv for $^{13}CO_2$. Our sensor reaches these sensitivities using a 10 cm absorption path length, which differs in sensitivity compared to other systems. Tuzson *et al.* achieved a precision of 0.12 ppm using a 56 m absorption path,[54] while Croizékasy *et al.* reported a precision of 0.05 ppm with a 5 m path length.[55] Kasyutich *et al.* demonstrated a precision of 36–60 ppb over a 50 cm path length, although this was measured at a 1-sigma confidence level.[56] When comparing performance based on ppm-m values, our system (2 ppm-m) outperforms Tuzson's (5 ppm-m) but falls short of the more sensitive systems by Croizé (0.25 ppm-m) and Kasyutich (0.025 ppm-m), indicating their higher overall sensitivity and performance.

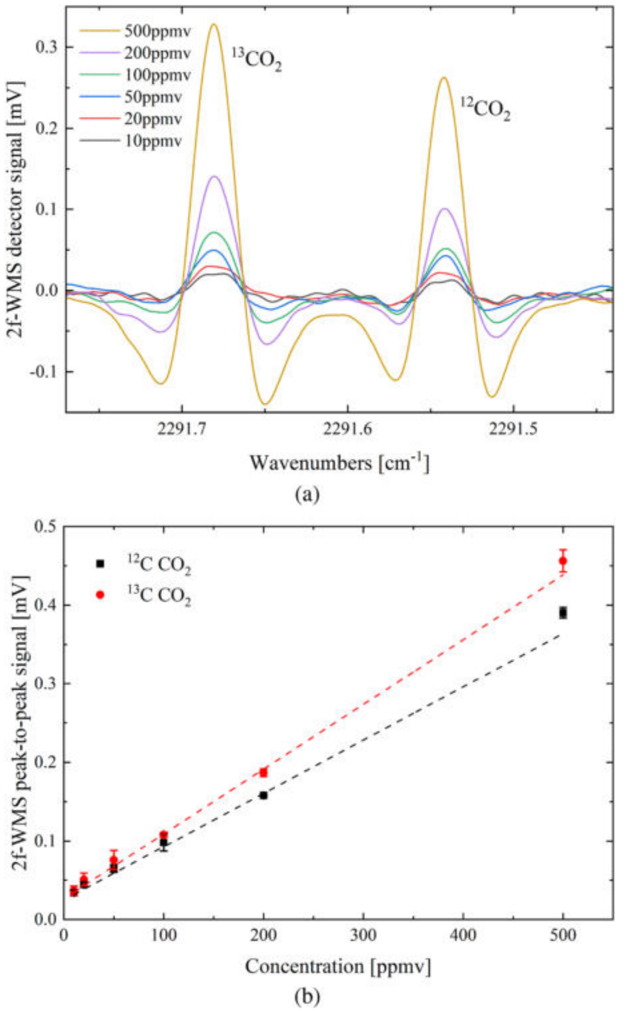

FIG. 6. (a) WMS signal for CO_2 concentrations ranging from 10 to 500 ppmv. (b) Peak-to-peak WMS signal as a function of CO_2 concentration for both isotopes.

III. CONCLUSION

Our investigation into substrate emitting ring ICLs at the central wavelength of 4.36 μm, ideal for CO_2 sensing, has yielded significant insights vital for their mass adoption in industrial and medical settings. Through comprehensive theoretical and experimental analyses, we have determined that the minimum size of these ring lasers can be reduced to 80 μm without compromising performance. For smaller radii, we observed a notable increase in the threshold current density, attributed, in part, to the increase in the whispering gallery mode confinement factor in the SiN isolation, alongside additional losses at the interface. Furthermore, our design considerations facilitate automated testing and seamless integration into industrial workflows. The utilization of an AlN submount has proved instrumental in enabling effective heat dissipation and CW operation. Notably, our proof-of-principle demonstration involved isotope-resolved CO_2 measurements using the $2f$-WMS method, yielding a linear correlation between the WMS signal and gas concentrations ranging from 10 to 500 ppmv. We achieved a limit of detection for natural CO_2 of 24 and 13 ppmv utilizing the P(60) $^{12}CO_2$ and R(10) $^{13}CO_2$ absorption lines, respectively, underscoring the efficacy of our approach in precise CO_2 sensing applications.

ACKNOWLEDGMENTS

The authors acknowledge the financial support from the European Union's research and innovation program Horizon 2020 (ERC project Monocomb No. 853014), the FFG - Austrian Research Promotion Agency Green Sensing Project (FFG No. 883941), and the FFG - Austrian Research Promotion Agency and the European Union as part of the Eurostars project "Vaporshine" (FFG No. 904813). Eurostars is part of the European Partnership on Innovative SMEs. The partnership is co-funded by the European Union through Horizon Europe. Furthermore, this project was funded by the Austrian Science Fund (FWF) EVEREST Project (FWF No. I 5772) and the European Office of Aerospace Research and Development/Air Force Office of Scientific Research (EOARD/AFOSR Nos. FA8655-22-1-7170 and FA8655-23-1-7070). The authors gratefully acknowledge the Center for Micro- and Nanostructures (ZMNS) of TU Wien for providing the cleanroom facilities.

AUTHOR DECLARATIONS

Conflict of Interest

The authors have no conflicts to disclose.

Author Contributions

Georg Marschick: Conceptualization (equal); Data curation (lead); Formal analysis (lead); Investigation (lead); Methodology (equal); Software (equal); Validation (equal); Visualization (equal); Writing – original draft (lead); Writing – review & editing (equal). **Stefania Isceri**: Formal analysis (equal); Investigation (equal); Methodology (equal); Software (equal); Writing – review & editing (equal). **Rolf Szedlak**: Conceptualization (equal); Investigation (equal); Methodology (equal); Supervision (equal); Writing – original draft (equal); Writing – review & editing (equal). **Harald Moser**: Data curation (equal); Investigation (equal); Methodology (equal). **Johannes P. Waclawek**: Data curation (equal); Investigation (equal); Methodology (equal). **Elena Arigliani**: Investigation (equal); Writing – review & editing (equal). **Robert Weih**: Resources (equal); Writing – review & editing (equal). **Werner Schrenk**: Investigation (equal); Methodology (equal); Resources (equal); Validation (equal); Writing – review & editing (equal). **Gottfried Strasser**: Funding acquisition (equal); Project administration (equal); Resources (equal); Writing – review & editing (equal). **Borislav Hinkov**: Formal analysis (equal); Resources (equal); Writing – review & editing (equal). **Aaron Maxwell Andrews**: Funding acquisition (equal); Resources (equal); Writing – review & editing (equal). **Bernhard Lendl**: Resources (equal). **Benedikt Schwarz**: Conceptualization (equal); Formal analysis (equal); Funding acquisition (equal); Investigation (equal); Project administration (equal); Resources (equal); Supervision (equal); Validation (equal); Visualization (equal); Writing – review & editing (equal).

DATA AVAILABILITY

The data that support the findings of this study are available from the corresponding author upon reasonable request.

REFERENCES

[1] B. H. Stuart, *Infrared Spectroscopy: Fundamentals and Applications* (John Wiley & Sons, 2004).

[2] R. Szedlak, A. Harrer, M. Holzbauer, B. Schwarz, J. P. Waclawek, D. MacFarland, T. Zederbauer, H. Detz, A. M. Andrews, W. Schrenk, B. Lendl, and G. Strasser, "Remote sensing with commutable monolithic laser and detector," ACS Photonics **3**, 1794–1798 (2016).

[3] J. Hodgkinson and R. P. Tatam, "Optical gas sensing: A review," Meas. Sci. Technol. **24**, 012004 (2012).

[4] H. D. Yallew, M. Vlk, A. Datta, S. Alberti, R. A. Zakoldaev, J. Høvik, A. Aksnes, and J. Jágerská, "Sub-ppm methane detection with mid-infrared slot waveguides," ACS Photonics **10**, 4282–4289 (2023).

[5] B. Hinkov, F. Pilat, L. Lux, P. L. Souza, M. David, A. Schwaighofer, D. Ristanić, B. Schwarz, H. Detz, A. M. Andrews *et al.*, "A mid-infrared lab-on-a-chip for dynamic reaction monitoring," Nat. Commun. **13**, 4753 (2022).

[6] A. Dabrowska, S. Lindner, A. Schwaighofer, and B. Lendl, "Mid-IR dispersion spectroscopy—A new avenue for liquid phase analysis," Spectrochim. Acta, Part A **286**, 122014 (2023).

[7] B. Pejcic, M. Myers, and A. Ross, "Mid-infrared sensing of organic pollutants in aqueous environments," Sensors **9**, 6232–6253 (2009).

[8] M. Siciliani de Cumis, S. Viciani, S. Borri, P. Patimisco, A. Sampaolo, G. Scamarcio, P. De Natale, F. D'Amato, and V. Spagnolo, "Widely-tunable mid-infrared fiber-coupled quartz-enhanced photoacoustic sensor for environmental monitoring," Opt. Express **22**, 28222–28231 (2014).

[9] K. V. Sreekanth, Y. Alapan, M. ElKabbash, E. Ilker, M. Hinczewski, U. A. Gurkan, A. De Luca, and G. Strangi, "Extreme sensitivity biosensing platform based on hyperbolic metamaterials," Nat. Mater. **15**, 621–627 (2016).

[10] R. Q. Yang, "Infrared laser based on intersubband transitions in quantum wells," Superlattices Microstruct. **17**, 77–83 (1995).

[11] I. Vurgaftman, R. Weih, M. Kamp, J. Meyer, C. Canedy, C. Kim, M. Kim, W. Bewley, C. Merritt, J. Abell, and S. Höfling, "Interband cascade lasers," J. Phys. D: Appl. Phys. **48**, 123001 (2015).

[12] J. R. Meyer, W. W. Bewley, C. L. Canedy, C. S. Kim, M. Kim, C. D. Merritt, and I. Vurgaftman, "The interband cascade laser," Photonics **7**, 75 (2020).

[13] E. Mujagić, C. Schwarzer, Y. Yao, J. Chen, C. Gmachl, and G. Strasser, "Two-dimensional broadband distributed-feedback quantum cascade laser arrays," Appl. Phys. Lett. **98**, 141101 (2011).

[14] K. Iga, F. Koyama, and S. Kinoshita, "Surface emitting semiconductor lasers," IEEE J. Quantum Electron. **24**, 1845–1855 (1988).

[15] E. Mujagić, L. K. Hoffmann, S. Schartner, M. Nobile, W. Schrenk, M. P. Semtsiv, M. Wienold, W. T. Masselink, and G. Strasser, "Low divergence single-mode surface emitting quantum cascade ring lasers," Appl. Phys. Lett. **93**, 161101 (2008).

[16] M. Holzhauer, R. Szedlak, H. Detz, R. Weih, S. Höfling, W. Schrenk, J. Koeth, and G. Strasser, "Substrate-emitting ring interband cascade lasers," Appl. Phys. Lett. **111**, 1 (2017).

[17] H. Knötig, B. Hinkov, R. Weih, S. Höfling, J. Koeth, and G. Strasser, "Continuous-wave operation of vertically emitting ring interband cascade lasers at room temperature," Appl. Phys. Lett. **116**, 131101 (2020).

[18] G. Marschick, J. Pelini, T. Gabbrielli, F. Cappelli, R. Weih, H. Knotig, J. Koeth, S. Hofling, P. De Natale, G. Strasser *et al.*, "Mid-infrared ring interband cascade laser: Operation at the standard quantum limit," ACS Photonics **11**, 395 (2024).

[19] S.-S. Kim, C. Young, and B. Mizaikoff, "Miniaturized mid-infrared sensor technologies," Anal. Bioanal. Chem. **390**, 231–237 (2008).

[20] R. W. Waynant, I. K. Ilev, and I. Gannot, "Mid-infrared laser applications in medicine and biology," Philos. Trans. R. Soc., A **359**, 635–644 (2001).

[21] C.-Z. Ning, "Semiconductor nanolasers and the size-energy-efficiency challenge: A review," Adv. Photonics **1**, 014002 (2019).

[22] D. Stark, F. Kapsalidis, S. Markmann, M. Bertrand, B. Marzban, E. Gini, M. Beck, and J. Faist, "Quantum cascade surface emitting lasers," Laser Photonics Rev. **18**, 2300663 (2024).

[23] A. Tsekoun, R. Go, M. Pushkarsky, M. Razeghi, and C. K. N. Patel, "Improved performance of quantum cascade lasers via manufacturable quality epitaxial side down mounting process utilizing aluminum nitride heatsinks," Proc. SPIE **6127**, 612702 (2006).

[24] X. Liu, L. C. Hughes, M. H. Rasmussen, M. H. Hu, V. A. Bhagavatula, R. W. Davis, C. G. Caneau, R. Bhat, and C.-E. Zah, "Packaging and performance of high power semiconductor lasers of high heat flux up to 2000 W/cm^2," in *Proceedings Electronic Components and Technology, 2005 ECTC'05* (IEEE, 2005), pp. 251–258.

[25] G. A. Slack, R. A. Tanzilli, R. Pohl, and J. Vandersande, "The intrinsic thermal conductivity of AIN," J. Phys. Chem. Solids **48**, 641–647 (1987).

[26] R. Weih, M. Kamp, and S. Höfling, "Interband cascade lasers with room temperature threshold current densities below 100 A/cm^2," Appl. Phys. Lett. **102**, 231123 (2013).

[27] H. Dely, T. Bonazzi, O. Spitz, E. Rodriguez, D. Gacemi, Y. Todorov, K. Pantzas, G. Beaudoin, I. Sagnes, L. Li *et al.*, "10 Gbit s^{-1} free space data transmission at 9 μm wavelength with unipolar quantum optoelectronics," Laser Photonics Rev. **16**, 2100414 (2022).

[28] S.-S. Kim and B. Mizaikoff, "Miniaturized optical sensors for medical diagnostics," in *Handbook of Spectroscopy: Second, Enlarged Edition* (John Wiley & Sons, Ltd, 2014), pp. 1557–1584.

[29] R. Szedlak, M. Holzbauer, D. MacFarland, T. Zederbauer, H. Detz, A. M. Andrews, C. Schwarzer, W. Schrenk, and G. Strasser, "The influence of whispering gallery modes on the far field of ring lasers," Sci. Rep. **5**, 16668 (2015).

[30] T. Visser, H. Blok, B. Demeulenaere, and D. Lenstra, "Confinement factors and gain in optical amplifiers," IEEE J. Quantum Electron. **33**, 1763–1766 (1997).

[31] S. Ferré, A. Peinado, E. Garcia-Caurel, V. Trinité, M. Carras, and R. Ferreira, "Comparative study of SiO_2, $\mathrm{Si}_3\mathrm{N}_4$ and TiO_2 thin films as passivation layers for quantum cascade lasers," Opt. Express **24**, 24032–24044 (2016).

[32] F. Toor, D. L. Sivco, H. E. Liu, and C. F. Gmachl, "Effect of waveguide sidewall roughness on the threshold current density and slope efficiency of quantum cascade lasers," Appl. Phys. Lett. **93**, 031104 (2008).

[33] S. Pearton, U. Chakrabarti, W. Hobson, and A. Kinsella, "Reactive ion etching of GaAs, AlGaAs, and GaSb in Cl_2 and SiCl_4," J. Vac. Sci. Technol. B **8**, 607–617 (1990).

[34] E. Hammerstad and O. Jensen, "Accurate models for microstrip computer-aided design," in *1980 IEEE MTT-S International Microwave Symposium Digest* (IEEE, 1980), pp. 407–409.

[35] W. Frei, *Modeling Metallic Objects in Wave Electromagnetics Problems* (Comsol Blog, 2015).

[36] P. Dutta, H. Bhat, and V. Kumar, "The physics and technology of gallium antimonide: An emerging optoelectronic material," J. Appl. Phys. **81**, 5821 (1997).

[37] C. Gatzert, A. Blakers, P. N. Deenapanray, D. Macdonald, and F. Auret, "Investigation of reactive ion etching of dielectrics and Si in $\mathrm{CHF}_3/\mathrm{O}_2$ or $\mathrm{CHF}_3/\mathrm{Ar}$ for photovoltaic applications," J. Vac. Sci. Technol. A **24**, 1857–1865 (2006).

[38] L. Li, Y. Jiang, H. Ye, R. Q. Yang, T. D. Mishima, M. B. Santos, and M. B. Johnson, "Low-threshold InAs-based interband cascade lasers operating at high temperatures," Appl. Phys. Lett. **106**, 251102 (2015).

[39] K. Zhang, Y. Lin, W. Zheng, R. Q. Yang, H. Lu, and Y.-F. Chen, "Low threshold inas-based interband cascade lasers grown by MBE," J. Cryst. Growth **586**, 126618 (2022).

[40] W. Bewley, C. Canedy, C. S. Kim, M. Kim, J. R. Lindle, J. Abell, I. Vurgaftman, and J. Meyer, "Ridge-width dependence of midinfrared interband cascade laser characteristics," Opt. Eng. **49**, 111116 (2010).

[41] J. A. Massengale, Y. Shen, R. Q. Yang, S. D. Hawkins, and A. J. Muhowski, "Low threshold, long wavelength interband cascade lasers with high voltage efficiencies," IEEE J. Quantum Electron. **59**, 2000507 (2023).

[42] R. Szedlak, T. Hisch, B. Schwarz, M. Holzbauer, D. MacFarland, T. Zederbauer, H. Detz, A. M. Andrews, W. Schrenk, S. Rotter, and G. Strasser, "Ring quantum cascade lasers with twisted wavefronts," Sci. Rep. **8**, 7998 (2018).

[43] C. Schwarzer, R. Szedlak, S. Il Ahn, T. Zederbauer, H. Detz, A. Maxwell Andrews, W. Schrenk, and G. Strasser, "Linearly polarized light from substrate emitting ring cavity quantum cascade lasers," Appl. Phys. Lett. **103**, 081101 (2013).

[44] S. Höfling, R. Weih, A. Bauer, M. Kamp, and A. Forchel, "Room temperature continuous wave interband cascade lasers for gas sensing," SPIE Proc. **8432**, 84320N (2012).

[45] F. K. Tittel, Y. Bakhirkin, A. A. Kosterev, and G. Wysocki, "Recent advances in trace gas detection using quantum and interband cascade lasers," Rev. Laser Eng. **34**, 275–282 (2006).

[46] J. Li, U. Parchatka, R. Königstedt, and H. Fischer, "Real-time measurements of atmospheric CO using a continuous-wave room temperature quantum cascade laser based spectrometer," Opt. Express **20**, 7590–7601 (2012).

[47] A. Castrillo, G. Casa, M. van Burgel, D. Tedesco, and L. Gianfrani, "First field determination of the $^{13}\mathrm{C}/^{12}\mathrm{C}$ isotope ratio in volcanic CO_2 by diode-laser spectrometry," Opt. Express **12**, 6515–6523 (2004).

[48] H. Graven, R. F. Keeling, and J. Rogelj, "Changes to carbon isotopes in atmospheric CO_2 over the industrial era and into the future," Global Biogeochem. Cycles **34**, e2019GB006170, https://doi.org/10.1029/2019gb006170 (2020).

[49] D. E. Cooper, R. U. Martinelli, C. B. Carlisle, H. Riris, D. B. Bour, and R. Menna, "Measurement of $^{12}\mathrm{CO}_2$:$^{13}\mathrm{CO}_2$ ratios for medical diagnostics with 1.6 μm distributed-feedback semiconductor diode lasers," Appl. Opt. **32**, 6727–6731 (1993).

[50] R. M. Zagari, P. Pozzato, C. Martuzzi, L. Fuccio, G. Martinelli, E. Roda, and F. Bazzoli, "^{13}C-urea breath test to assess *Helicobacter pylori* bacterial load," Helicobacter **10**, 615–619 (2005).

[51] L. Bonfrate, I. Grattagliano, G. Palasciano, and P. Portincasa, "Dynamic carbon 13 breath tests for the study of liver function and gastric emptying," Gastroenterol. Rep. **3**, 12–21 (2015).

[52] D. S. Bomse, A. C. Stanton, and J. A. Silver, "Frequency modulation and wavelength modulation spectroscopies: Comparison of experimental methods using a lead-salt diode laser," Appl. Opt. **31**, 718–731 (1992).

[53] P. Kluczynski, J. Gustafsson, Å. M. Lindberg, and O. Axner, "Wavelength modulation absorption spectrometry—An extensive scrutiny of the generation of signals," Spectrochim. Acta, Part B **56**, 1277–1354 (2001).

[54] B. Tuzson, M. J. Zeeman, M. S. Zahniser, and L. Emmenegger, "Quantum cascade laser based spectrometer for *in situ* stable carbon dioxide isotope measurements," Infrared Phys. Technol. **51**, 198–206 (2008).

[55] L. Croizé, D. Mondelain, C. Camy-Peyret, C. Janssen, M. Lopez, M. Delmotte, and M. Schmidt, "Isotopic composition and concentration measurements of atmospheric CO_2 with a diode laser making use of correlations between non-equivalent absorption cells," Appl. Phys. B **101**, 411–421 (2010).

[56] V. L. Kasyutich and P. A. Martin, "A CO_2 sensor based upon a continuous-wave thermoelectrically-cooled quantum cascade laser," Sens. Actuators, B **157**, 635–640 (2011).

CHAPTER 5

MID-INFRARED RING INTERBAND CASCADE LASER: OPERATION AT THE STANDARD QUANTUM LIMIT

5.1 Motivation, Background and State-of-the-Art

Semiconductor lasers exhibit intensity noise due to several underlying processes related to how they operate. One primary source is spontaneous emission, a random process that occurs alongside the desired stimulated emission in the laser. Although semiconductor lasers rely on stimulated emission to produce coherent light, a small fraction of spontaneously emitted photons gets coupled into the laser's optical mode. This randomness in photon generation leads to fluctuations in the intensity of the laser's output.[203] Another contributing factor is the fluctuation in the number of carriers (electrons and holes) within the laser's active region. The laser's intensity depends on the population of these carriers because they drive the process of light amplification. However, carriers are injected and recombine in a somewhat random manner, leading to variations in the number of photons generated per unit of time. This process results in intensity noise, as the laser's output power will fluctuate slightly due to the dynamic nature of carrier recombination and photon generation.[204] Usually, the intensity noise of semiconductor lasers is given through the so called relative intensity noise (RIN), which is defined as the noise power in the intensity of the laser light per unit frequency (INPSD), normalized to the square of the average output power.[35] RIN is a crucial factor in determining the performance limits of lasers, particularly in sensitive measurement systems where signal stability is essential.[205]

The development of MIR emitters, capable of shot-noise-limited, or even sub-shot-noise emission, opens up possibilities for creating imaging and spectroscopic systems with enhanced sensitivity and resolution.[206] Non-classical light, like squeezed states, reduces quantum noise in specific properties, making it useful for high-precision quantum measurements and quantum-communications.[207] Shot-noise-limited lasers are essential in these setups because they provide a noise floor that allows the detection of quantum effects. By minimizing their own noise, these lasers ensure the precision needed to observe and utilize the benefits of non-classical light.[208] While the frequency noise of QCLs and ICLs has been intensively studied,[209, 210] the intensity noise behavior, especially of ICLs is only presented in a few studies, which exclusively focus on linear devices with Fabry-Perot or DFB cavities.[211, 212, 213, 214] In the state of the art, studies have demonstrated the advantages of ring-cavity designs in MIR lasers for beam collimation, frequency modulation, and power scaling.[53, 104, 108] However, the noise performance, specifically the RIN in such structures, has not been thoroughly explored. This paper addresses that gap by investigating the noise characteristics of substrate-emitting ring ICLs, focusing on their operation near the standard quantum limit. In comparison to existing literature, the ring lasers demonstrate shot-noise-limited behavior with the lowest RIN, comparable to lasers operated at cryogenic temperatures.[212] The influence of the ring cavity on noise performance has not been comprehensively studied, but it is reasonable to assume that the circular waveguide structure, free of reflecting facets susceptible to external optical feedback, plays a role in improving the laser's noise characteristics.

5.2 Contribution to the field

The fourth paper investigates the noise characteristics of vertical emitting ring ICLs, which are crucial for precision applications in the MIR spectral range. Quantum effects often impose significant constraints on the sensitivity and resolution of MIR imaging and spectroscopic systems, as well as the bit-error rate in optical free-space communication. Understanding and mitigating these noise characteristics are vital for optimizing device performance. This study provides a comprehensive characterization of continuous-wave, 3.8 µm-emitting ring ICLs operating at room temperature. Through an in-depth analysis of bias-dependent INPSD and RIN, we have achieved shot-noise-limited statistics for Fourier frequencies above 100 kHz. These

results are particularly significant for precision applications such as interferometry and advanced spectroscopy, which benefit from the high sensitivity enabled by shot-noise-limited sources. Additionally, these findings hold promise for novel quantum optics schemes, including the testing of specific light states below the shot-noise level, such as squeezed states. This research, combined with the findings on the previous work presented in chapter 4 is closely linked by the overarching goal of enhancing the functionality and performance of ICLs for advanced applications. The development of miniaturized ring ICLs for CO_2 spectroscopy lays the foundation for exploring their noise characteristics. By addressing both the practical application and fundamental noise properties of these devices, this research provides a comprehensive understanding of ring ICLs and their potential to advance MIR technologies.
Together, these investigations contribute to the broader field of PICs and highlight the importance of ICLs in developing sophisticated sensing and communication systems. The findings from these studies not only enhance our knowledge of ICL performance but also pave the way for future innovations in integrated photonic devices.

5.3 Publication

Reprinted, with permission, from G. Marschick, J. Pelini, T. Gabbrielli, F. Cappelli, R. Weih, H. Knötig, J. Koeth, S. Höfling, P. de Natale, G. Strasser, S. Borri, and B. Hinkov "Mid-infrared Ring Interband Cascade Laser: Operation at the Standard Quantum Limit"
ACS Photonics 2023, 11, 2, 395–403, https://doi.org/10.1021/acsphotonics.3c01159

ACS Photonics

pubs.acs.org/journal/apchd5

Article

Mid-infrared Ring Interband Cascade Laser: Operation at the Standard Quantum Limit

Georg Marschick,○ Jacopo Pelini,○ Tecla Gabbrielli, Francesco Cappelli,* Robert Weih, Hedwig Knötig, Johannes Koeth, Sven Höfling, Paolo De Natale, Gottfried Strasser, Simone Borri, and Borislav Hinkov*

Cite This: ACS Photonics 2024, 11, 395−403

Read Online

ACCESS | Metrics & More | Article Recommendations | Supporting Information

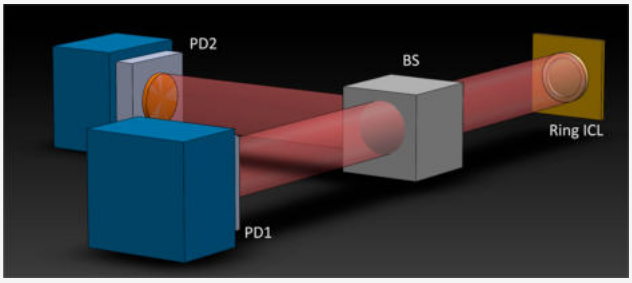

ABSTRACT: Many precision applications in the mid-infrared spectral range have strong constraints based on quantum effects that are expressed in particular noise characteristics. They limit, e.g., sensitivity and resolution of mid-infrared imaging and spectroscopic systems as well as the bit-error rate in optical free-space communication. Interband cascade lasers (ICLs) are a class of mid-infrared lasers exploiting interband transitions in type-II band alignment geometry. They are currently gaining significant importance for mid-infrared applications from < 3 to > 6 μm wavelength, enabled by novel types of high-performance ICLs such as ring-cavity devices. Their noise behavior is an important feature that still needs to be thoroughly analyzed, including its potential reduction with respect to the shot-noise limit. In this work, we provide a comprehensive characterization of λ = 3.8 μm-emitting, continuous-wave ring ICLs operating at room temperature. It is based on an in-depth study of their main physical intensity noise features such as their bias-dependent intensity noise power spectral density and relative intensity noise. We obtained shot-noise-limited statistics for Fourier frequencies above 100 kHz. This is an important result for precision applications, e.g., interferometry or advanced spectroscopy, which benefit from exploiting the advantage of using such a shot-noise-limited source, enhancing the setup sensitivity. Moreover, it is an important feature for novel quantum optics schemes, including testing specific light states below the shot-noise level, such as squeezed states.

KEYWORDS: *mid-infrared, optoelectronics, interband cascade laser, balanced detection, intensity noise, shot-noise, quantum limit*

INTRODUCTION

Interband cascade lasers (ICLs) are semiconductor-based, coherent mid-IR light sources, first demonstrated by Yang et al. in 1995.[1] They are the interband counterpart to quantum cascade lasers (QCLs), which instead rely on intersubband transitions,[2] and have been the dominant mid-IR lasers since their realization in 1994.[3] These sources have immediately attracted wide interest in view of the many potential applications, with a focus on molecular species detection in solid,[4,5] liquid,[6,7] and gas phases.[8,9] This has sparked, e.g., important works in greenhouse gas detection of methane, carbon dioxide, or nitrous oxide, including the detection of the most elusive gas isotopes,[10] in high-sensitivity gas measurements down to the ppq level[11,12] even in real-world applications, or in broadband (>10 cm^{-1}), high-resolution (MHz-range) spectroscopy techniques like dual-comb spectroscopy.[13] Moreover, other important mid-IR applications are currently getting significant attention, such as spectral imaging[4,5,14] and, in more recent years, optical free-space communication.[15−17]

This large interest acted as a strong driving force for the technological development of these sources. ICLs differ from QCLs, for example, by their much lower power consumption and their operation at shorter wavelengths, even below 3 μm. Due to these and other peculiarities, ICLs are nowadays in many fields competitive with their QCL counterparts, matching the requests for high optical output power,[18,19] wide spectral tunability,[20] comb emission,[21] compact dimensions and integrability,[20] spectral control and (ultra)narrow line width,[22−24] and low noise emission.[25]

ICLs are the result of combining the strong interband transitions and long recombination lifetimes inherent to traditional diode lasers[26] with the voltage-efficient cascading design of QCLs[3] into an active region (AR) using type-II band alignment. This allows for maintaining the QCL-like flexibility in designing the emission wavelength of ICLs through band-structure engineering while simultaneously strongly reducing their number of AR periods. As mentioned, the result is significantly lower power consumption, e.g., at a laser

Received: August 14, 2023
Revised: December 26, 2023
Accepted: December 27, 2023
Published: January 18, 2024

https://doi.org/10.1021/acsphotonics.3c01159

threshold[27] of around 170 mW,[23] to compare to even specifically optimized low dissipation QCLs with threshold dissipation values between 350 and 850 mW.[28−30] This advantage is particularly important for portable ICL-based sensors[31] or for future space deployment. In novel ring-ICLs, ring-shaped ridge cavities are used together with vertical light emission, merging multiple advantages into a single device. First, the ring-cavity shares radial symmetry with most discrete optical elements such as lenses and mirrors, which is beneficial for light collimation or focusing. Second, the large effective surface area of circular waveguides offers a large aperture, providing small divergent emission beams with angles below ±10° and thus simpler collimation.[23] Third, previous work in QCLs has revealed that ring geometries, due to their different mode distribution within the cavity as compared to straight ridges, offer specific, electronically controllable frequency-modulation (FM) states,[32] which are useful features for high-speed spectroscopy.[33] Fourth, compared to other vertical surface-emitting lasers, such as vertical-cavity surface-emitting lasers (VCSELs),[34,35] with their limited output power due to small gain volumes, the output power of ring ICLs can be scaled up by simply increasing the ring diameter or the waveguide width. In this case, obeying certain design guidelines prevents higher-order lateral modes.[23]

For controlling line width, single-mode emission capabilities, and vertical light outcoupling in ring ICLs, distributed feedback (DFB) gratings etched into the laser waveguide which periodically modulate the complex refractive index of the waveguide can be used.[36,37] Design and fabrication of the DFB grating are some of the most important steps in order to achieve a well-functioning device. While the grating period width Λ is determined by the Bragg condition $n_{\mathrm{eff}} \times \Lambda = m \times \frac{\lambda}{2}$, with n_{eff} being the effective refractive index, m describing the grating order, and λ being the design emission wavelength, the precise influence of the grating etch depth as well as the grating duty cycle is either obtained by optical simulations or determined experimentally. DFB gratings have already been successfully integrated into ICLs using various waveguide geometries.[22,23,38] Especially in the case of vertically emitting devices, a second-order DFB grating is needed. The optical feedback necessary for single-mode operation and vertical light coupling is introduced through the second-order Bragg scattering (order $m = 2$) which simultaneously rotates the Poynting vector by ±90° and selects one single emission wavelength.[23,38] This opens the pathway to implement 2D multiwavelength concentric array geometries,[39] an important step toward broadband chip-scale spectrometers.

Despite all the achievements of ICLs, their intensity noise together with its potential reduction in ring ICLs still needs to be thoroughly characterized. Fundamentally, intensity noise in semiconductor lasers like ICLs originates from their various internal electronic and optical processes such as spontaneous emission and random carrier generation/recombination.[25] Understanding its characteristics is important for increasing the sensitivity and resolution of imaging or spectroscopic systems[25,40] and for telecommunication concepts with reduced bit-error rates.[41] Furthermore, it is of particular relevance in the future development of quantum optics schemes, such as homodyne detection, where a shot-noise-limited source is highly desirable, as a local oscillator, to test light states below the shot-noise level (e.g., squeezed states).[42,43]

In the current work, we follow this need and investigate for the first time the relative intensity noise (RIN) of a single-mode-emitting ring-ICL. The device operates in continuous-wave (CW) mode at room temperature with an emission wavelength of $\lambda = 3.8\ \mu$m. As previously discussed, ring devices have beneficial features for spectroscopic applications as compared to similar ridge devices.[23,32,39] In our study, we first analyze the light-current−voltage (LIV) and single-mode emission characteristics of a typical custom-made second-order DFB ring ICL. Then, a balanced-detection setup, consisting of a 50/50 beam splitter and two identical photovoltaic detectors, is employed to characterize the intensity noise power spectral density (INPSD) of the ring ICL and compare it to the directly measured shot-noise level. We further analyze the RIN of the ICL under different laser driving conditions to understand the optimal low-intensity-noise working regime of the tested device geometry.

DEVICE STRUCTURE AND WORKING PRINCIPLE

The quantum structure of the device investigated in this work is grown by solid-source molecular beam epitaxy (MBE) on an n-GaSb (100) substrate. The w-shaped AR with 6 periods follows the layer sequence 2.50 nm AlSb/1.92 nm InAs/2.40 nm $\mathrm{In_{0.35}Ga_{0.65}Sb}$/1.49 nm InAs/1.0 nm AlSb for a target emission wavelength of 3.8 μm. It is sandwiched between two 200 nm thick GaSb separate confinement layers as well as a 3.5 and 2.0 μm InAs/AlSb lower and upper cladding, respectively. Since within the superlattice-like structure of the active region, most interfaces involve a change of both group III and group V materials, careful optimizations of interface roughness and strain balance were carried out using so-called group V soak times during the growth. Figure 1a shows the band structure including simulated wave functions of the AR design for an applied external field of 69 kV/cm. The epitaxial ICL structure is processed into ring-shaped cavities with a diameter of ~800 μm and a ridge width of 6 μm (circumference: approximately 2.5 mm) using state-of-the-art cleanroom fabrication techniques. Special attention is given to the below-1 micrometer feature size of the implemented second-order DFB grating for vertical and single-mode light coupling, which was patterned through electron-beam lithography and as a next step etched around 1100 nm deep into the already existing waveguide with Cl2−Ar reactive ion etching. The structure of the device characterized in this work is similar to the device characterized in ref 23 with the mentioned main differences of a wider waveguide (6 μm instead of 5 μm) and a different DFB grating period to address shorter wavelengths. The measured device is a typical representative of the processed ring ICLs; thus, the results shown in this work are expected to be a benchmark for the noise behavior of devices with similar epi-structure and dimensions. Figure 1b displays a microscope image of a typical finalized ring-ICL device, including scanning electron microscopy (SEM) images of the DFB grating implemented on the laser waveguide and a focused ion beam (FIB) cut through the ridge of the ring device revealing its high-quality cross-section profile.

Substrate-side emission is the preferred geometry for such devices, which allows covering the entire topside of the rings including the DFB grating structure with gold and the use of flip-chip bonding on copper submounts with indium solder. This results in significantly improved heat extraction from the device AR and is important for a high-performance CW

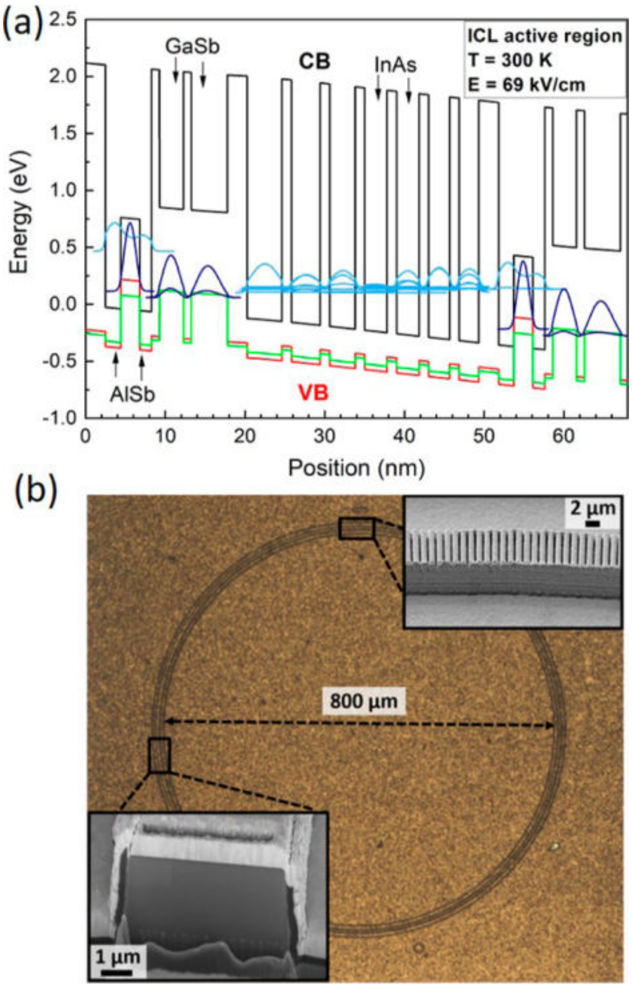

Figure 1. (a) Band structure of the ring ICL including the simulated wave functions for an applied field of 69 kV/cm. (b) Microscope image of the fabricated ring ICL. The insets show: (top right) a detailed view of the ring waveguide with the implemented 2nd-order DFB grating for vertical light coupling and single-mode emission and (bottom left) a SEM image of an FIB cut through the ridge of the ring device.

operation. More details on the AR design and device fabrication can be found elsewhere.[23]

DEVICE CHARACTERIZATION

LIV Curve and Emission Spectrum Characterization. First, a typical ring ICL is characterized in order to determine its optimal working point when operated at a fixed temperature of 16 °C in CW mode [The temperature of 16 °C for the characterization was chosen to simultaneously satisfy: (1) a high enough optical output power of the laser (for which a lower temperature is beneficial) together with (2) laser operation that does not need a more sophisticated setup including, e.g., purging of the laser with dry air/nitrogen to prevent water condensation at the laser facet from ambient humidity.]. In our setup, the ring ICL is driven by an integrated modular controller (ppqSense s.r.l., QubeCL10) including temperature stabilization by using a thermo-electric cooler. Its laser driving unit is characterized by a low bias current noise density, typically around 300 pA/$\sqrt{\text{Hz}}$, for reducing its effect on the intensity noise of the operated device.

As shown by the LIV curve in Figure 2a, the tested ring ICL exhibits a lasing threshold of around 50 mA when operated at 16 °C, while it reaches its maximum optical output power of approximately 1.6 mW at 160 mA. Regarding the measured optical spectra shown in Figure 2b, the laser maintains a well-defined single-mode emission at around 3.79 μm within its whole working range, reaching a side-mode suppression ratio (SMSR) of up to 30 dB. As expected, the emission peak moves to longer wavelengths with increasing laser bias current, going from λ = 3.788 μm at 60 mA to λ = 3.793 μm at 160 mA. By

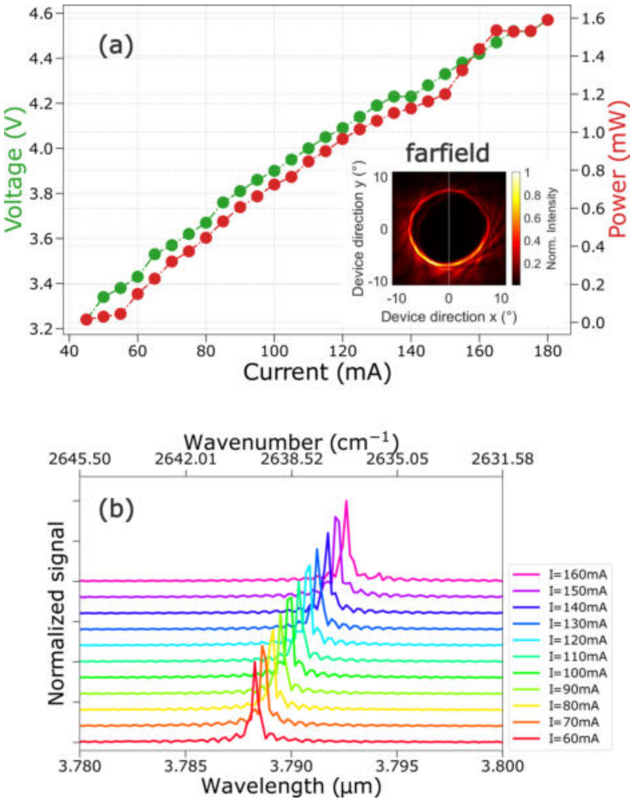

Figure 2. Ring-ICL characterization at a fixed temperature of 16 °C. (a) LIV curve of the ring ICL analyzed between ~40 and 180 mA. The measured optical power is shown in red and the associated voltage in green. Inset: far-field measured with a HgCdTe-detector on a *xy*-stage and at a distance of 20 cm to the ring-ICL device. (b) Corresponding, individually normalized, bias-dependent emission spectra of the ring ICL measured with an optical spectrum analyzer (FTIR 721, Bristol), which has a resolution of 6 GHz (i.e., 0.2 cm^{-1}). The y-scale is linear, and the tick span is 0.5 au. The emission spectra show an SMSR up to 30 dB as compared to the flat part of the spectrum away from the peaks. It is worth noting that the traces have been normalized to their respective maximum peak and an offset is added in the *y*-direction to allow a good visibility of all the spectra within a single graph [In brief, the SMSR was computed by dividing the peak value by the mean level of the spectrum calculated far from the peaks (around 3.85 μm), which is limited by the instrumental background, and has then been translated to the dB scale. The maximum SMSR value, i.e., approximately 30 dB, refers to the maximum peak signal recorded in the whole series of FTIR acquisitions (i.e., for bias currents of 140−160 mA). Since the peak maximum value changes for each acquisition at different operating currents, in Figure 2, the acquired traces have been normalized to their individual peak value to allow a clear view of the emitted spectra as a function of the applied bias current within a single plot.].

analyzing the laser peak emission wavelength as a function of bias current, we obtain a current-tuning coefficient of $\mathcal{T} = (903 \pm 2)$ MHz/mA. More details regarding this analysis are presented in Appendix A in the Supporting Information.

While the optical emission power of this specific ring ICL is limited, especially when compared to typical mid-IR QCLs or ICLs, both of which can reach emission powers of tens to hundreds of milliwatts,[27,44−46] our ring device is able to operate at very low consumed electrical power (at maximum bias: ∼160 mA at ∼4.5 V). This demonstrates its suitability for in-field applications where energy resources are limited to battery operation or even solar energy only.[47,48] Moreover, an optical emission power of about 1 mW is often sufficient for sensing applications,[26] as long as the target wavelength is precisely hit. Indeed, depending on the detector sensitivity, hundreds of microwatts of optical power can be sufficient for transmission spectroscopy applications also,[49] as well as novel chip-level applications using compact photonic integrated circuits.[50,51] We therefore focused our work on the spectral stability and purity of the laser emission for achieving low-noise characteristics instead of trying to improve "traditional" figures of merit such as the optical emission power or wall-plug efficiency. Thus, the high spectral purity and stability of our ring ICL can be considered suitable for different state-of-the-art applications, including cavity-enhanced spectroscopy experiments,[52−55] free-space optical communication,[56] and metrological measurements.[57]

To finalize the basic optical characterization of the ring ICL, we report, in the inset of Figure 2, the acquired far-field profile of the device, measured with an MCT detector mounted on a translational xy-stage which was placed at a distance of 20 cm from the ring ICL. The ring-shaped geometry with its typical dark central part and a narrow circular beam hosting the device power can clearly be observed.

Intensity Noise Characterization Using Balanced Detection. In order to understand the intensity noise features of the presented ring ICL, we analyzed its INPSD using a balanced-detection experiment. In this setup, sketched in Figure 3,[43] the light under investigation is split into two identical beams via a 50/50 beam splitter and acquired via two commercial HgCdTe photovoltaic detectors (D1 and D2) equipped with a 5 MHz-bandwidth preamplifier (VIGO Photonics S.A., amplifier: PIP-UC-LS, detector: PV-4TE-4-1 × 1). The used MCT detectors are optimized for having a high saturation level, that is, about 12 mW. They have been chosen for minimizing the "optical attenuation" required for performing the measurements since the introduction of additional optical attenuation alters the original ratio between the observed intensity noise and the related computed shot noise. The saturation level is so high because they are large-area detectors; therefore, they cannot have a fast response.

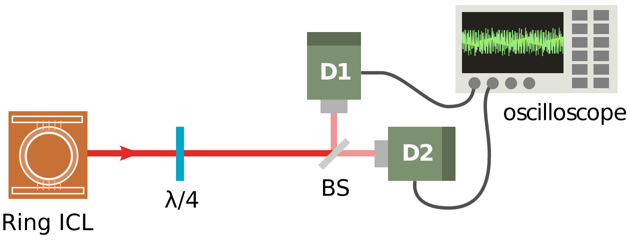

Figure 3. Schematic representation of the experimental setup used for balanced detection. The figure is readapted from ref 43.

The electronic architecture of the detectors consists of two amplifier stages: a 6 kΩ preamplifier transimpedance stage, where the dc-output is collected, and a second stage for which coupling (i.e., ac or dc) and gain can be chosen via a PC software (VIGO Photonics S.A., Smart Manager). In our case, the ac-coupled second stage is used to amplify the ac-voltage noise amplitude by a factor of 62 V/V [we fixed the gain to 20 via the Smart Manager control platform, but we also measured a minimum amplification amount between the 1st-stage output voltage and the 2nd-stage output voltage equal to 3.1 V/V when the ac gain is set to 1. The two factors (3.1 × 20 in our case) need to be multiplied to retrieve the actual voltage amplification factor.]. The detectors are maintained at a fixed temperature of 200 K by a four-stage Peltier cooling system using a thermometric cooler controller (VIGO Photonics S.A., PTCC-01-BAS). The signals are analyzed in the time domain. In particular, a 12 bit oscilloscope (Tektronix, MSO64) is used to acquire the two detectors' output signals in a 20 ms time window and at a fixed sampling rate of 31.25 Ms/s. In our measurements, the oscilloscope bandwidth is limited to 20 MHz. Finally, a Python script is used to compute the sum and the difference of the acquired signal and to convert them from the time to the frequency domain, computing the INPSD of the difference and of the sum.[43] Since at each point, the polarization is tangential to the beam (i.e., circular), a $\lambda/4$ wave plate is placed just after the device to retrieve a linear polarization (a $\lambda/2$ wave plate is also needed to equally balance the two split arms.). The emitted laser beam from the chip is uncollimated; therefore, we placed an additional 50 mm lens in front of each detector to collect all the light within its 1 × 1 mm^2 collection area.

For evaluating the performance of the assembled balanced-detection system, we performed a preliminary characterization of the used photodetectors. One key parameter in our measurements is the detector responsivity, defined as the detector output signal (voltage or current) as a function of the incident optical power. In particular, in order to perform a balanced detection in which the common noise of both arms is suppressed at the shot-noise level, it is necessary to use two photovoltaic detectors with a responsivity that is as similar as possible. Otherwise, the detection is unbalanced in favor of one of the two arms, even when investigating two initially identical incident optical signals on D1 and D2. Thus, when performing the balanced-detection experiments in the linear responsivity regime of two detectors, the INPSD computed from the difference of the photocurrent output signals is expected to be at the shot-noise level and, therefore, proportional to the incident power impinging on the beam splitter.[43] This is true in the limit given by the maximum common mode rejection ratio (CMRR) achievable with our setup, i.e., the maximum excess of noise with respect to the shot-noise level that can be canceled with our differential measurement.[43] Instead, the sum of the two photocurrent ac output signals corresponds to the measurement of the whole intensity noise associated with the radiation impinging on the balanced detector. It is linked to the intensity noise of the laser minus a possible attenuation factor (due to the losses experienced by the propagating beam and the detector efficiency), plus an extra contribution due to the coupling of the tested radiation with the vacuum field caused by the losses[43] [from a quantum optics point of view, "coupling the radiation with the vacuum field" means that via optical attenuation (e.g., attenuation due to optical elements such as lenses, isolators, and beam splitters, quantum efficiency of the used detectors, and absorption of the laser waveguide), the radiation is attenuated and the statistics of the photon flux is altered toward a Poissonian distribution. In quantum optics, the attenuations are modeled with beam splitters, where one input port is used for the signal, while the other has no field except the vacuum. This is why it is said that the losses couple the radiation to the vacuum.]. Under the condition of balanced detection performed in the linear responsivity regime and assuming the noise level does not exceed the maximum CMRR, it is sufficient to directly compare the retrieved INPSD of sum and difference for judging whether the light collected from the source under investigation is shot-noise-limited. This means that its photons are Poissonian-like distributed, as expected for a coherent light source.[42] Based on these considerations, we carefully selected two photodetectors with a very similar responsivity at $\lambda = 3.79\ \mu$m of $R_1 = (0.704 \pm 0.007)$ A/W and $R_2 = (0.659 \pm 0.008)$ A/W, respectively. Furthermore, when the differential measurement is performed, a CMRR of up to 25 dB is achievable in the tested bandwidth. More details of this analysis are available in Appendix C in the Supporting Information.

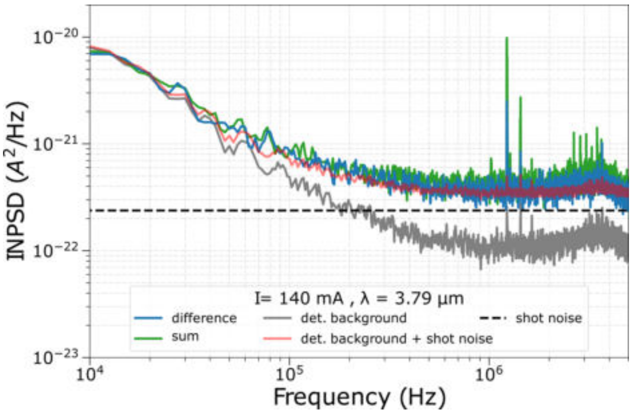

Figure 4. Ring-ICL INPSD analysis performed at a fixed temperature of 16 °C and at a laser bias current of 140 mA. The INPSD sum and difference signal traces are colored green and blue, respectively. The dashed black line represents the theoretical shot-noise level, obtained from the dc outputs of the detectors, while the detector background is shown in gray. The red line shows the sum of the shot-noise level and detector background noise. In the INPSD of the detector background and of the laser, some spurious noise peaks at slightly above 1 MHz are present. They are due to technical noise originating from different sources including intrinsic electronic noise of the current driver, mass-loop noise due to its power supply, and the supply used for the detectors. This technical noise can be reduced, e.g., by using battery operation. It is important to note that even though these peaks are present, still a shot-noise-limited intensity noise for the tested ICL is demonstrated, with the exception of those few particular frequencies.

Figure 4 shows the INPSD of the ring ICL analyzed at 140 mA, which corresponds to a condition in which the laser is affected neither by noise contributions from spontaneous emission events close to the laser threshold nor by any saturation effects close to the device rollover, as shown in Figure 2. The output power under these driving conditions is around 1.2 mW. Therefore, the detectors, each receiving around 0.6 mW, are not saturated (the optical losses due to the optical tools, e.g., mirrors, wave plates, and lenses are around 2%). As evidenced in Figure 4, the INPSD of the difference signal (blue trace) corresponds to a direct measurement of the shot-noise level: indeed, the INPSD of the difference signal overlaps with the red trace, which shows the sum of the background noise (gray trace) and the theoretically computed shot-noise power spectral density (PSD) (dashed black line). To retrieve this latter quantity, we measure the dc output of the two photovoltaic detectors and calculate the shot-noise PSD as $\mathrm{PSD_{SN}} = 2e(V_1 + V_2)/R$, where e is the electron charge, $V_{1\text{ and }2}$ are the voltages measured at the two first-stage transimpedance dc-outputs of both detectors, and R is the transimpedance resistance value. Instead, the detector background noise was measured by blocking the laser emission via an opaque obstacle placed close to the laser (far from the detector). The signal from the detectors was therefore acquired without the contribution of laser emission. The red trace is then displayed as the sum of the gray and dashed black trace to take into account the effect of the background with respect to the calculated shot-noise level. It is important to note that, despite a non-negligible contribution of the background in the measured shot noise, the INPSD of the difference signal lies well above the sole detector background level, reaching a so-called clearance, defined as the ratio between the INPSD of the difference signal and the detector background, of up to 6 dB at a Fourier frequency of about 1 MHz.[43] This result confirms the possibility of performing shot-noise-limited detection with the assembled setup, e.g., the setup can be successfully applied in a homodyne detection scheme using the tested ring ICL as a local oscillator.[43] With this purpose, the optimal working conditions are those which guarantee exploitation of clearance as high as possible to minimize the effect of the background on the measurement and thus potentially increase the possibility of exploring subshot-noise signal levels in balanced detection.[42,43] In our case, the best working conditions are therefore the use of the ring ICL at a driving current of 140 mA where it emits a power of > 1 mW which allows reaching the best clearance (i.e., 6 dB) with the assembled setup. In view of possible nonclassical application, one major limitation arises from the limited quantum efficiency of the detectors (i.e., the number of generated electrons in a detector as a function of the number of impinging photons). As shown in Appendix B of the Supporting Information, this quantity lies at around 22–23% at the investigated wavelength. Still, the results presented here give a good starting point for the development of future quantum technology systems based on the light source tested in this work. Next, we will seek to implement commercial detectors, optimized for working in the 4 μm window, with higher quantum efficiency, to potentially address quantum optics applications, where losses directly correspond to a degradation of the nonclassicality of a tested nonclassical signal (e.g., a squeezed state of light characterized by subshot-noise-level amplitude noise). This is done by mixing it with the vacuum state of the electromagnetic field for a percentage corresponding to the amount of the losses.[42,43]

Coming back to the characterization of the tested ICL, it clearly benefits from a shot-noise-limited intensity noise within the tested detector efficiency. Indeed, the obtained data show an INPSD of the sum signal (green trace, Figure 4) that is superimposed with the INPSD of the difference trace in blue for the entire investigated Fourier frequency domain. In Appendix C of the Supporting Information, we also demonstrate that this interesting behavior is similar for different laser drive currents, at a fixed laser temperature.

The shot-noise-limited operation represents an important feature in ring ICLs for applications requiring a well-suppressed-intensity-noise light source, such as in quantum homodyne detection,[42,43] high-sensitivity interferometry,[58,59] and spectroscopy.[60] With this purpose, it is worth noting that at lower frequencies (up to 100 kHz), all traces are background-noise-limited. Therefore, in view of future applications, the optimum working range for our balanced-detection setup is in the frequency range between 100 kHz and 5 MHz, where there is a rollover due to the limited bandwidth of the detectors.

Finally, Figure 5 depicts the RIN of the ring ICL at different bias currents for a fixed temperature of 16 °C. The RIN is defined as the INPSD of the sum signal normalized to the square of the sum of the photocurrents measured by the two photodetectors. As expected, the RIN decreases with increasing laser bias current for measurements between I = 80 mA and I = 140 mA.

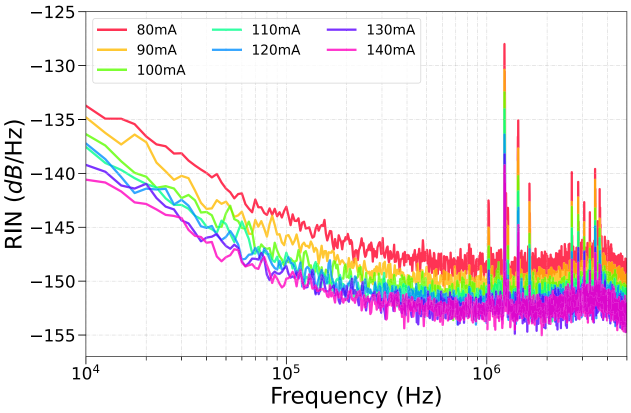

Figure 5. RIN of the ring ICL measured for different bias currents at a fixed temperature of 16 °C. As already discussed in Figure 4, the here-reported RIN also shows some spurious noise peaks due to the presence of excess technical noise, originating from the laser driving unit.

Compared to previous studies where the reported RIN levels for ICLs cover a range from −110 dB/Hz[61] up to −130 dB/Hz,[25] our device shows better intensity noise performance in terms of RINs which decreases down to −153 dB/Hz at a current of 140 mA. This is similar to the values found in reference 62[62] where the tested ICL has an RIN which decreases down to −160 dB/Hz, however, at a temperature of 30 K. Fundamental differences of our devices compared to the devices from the literature include single-mode emission through the implemented second-order DFB grating and a ring-cavity geometry, which inherently supports a different internal mode structure as compared to standard Fabry−Pérot ridge devices.

CONCLUSIONS

In conclusion, we investigated the noise characteristics of a second-order DFB ring ICL emitting at λ = 3.79 μm at a fixed temperature of 16 °C. The INPSD level found at a driving current of I = 140 mA, i.e., far from the laser threshold and from the laser rollover, with a balanced-detection setup, demonstrates shot-noise-limited operation between 100 kHz and 5 MHz. In the setup, we employed two HgCdTe photovoltaic detectors with similar responsivity, which are moreover linear over the whole range of investigated laser bias currents. Subshot-noise detection is shown to be potentially possible with such a configuration. For this purpose, the detector quantum efficiency should be improved, in order to enhance the chance of unveiling subclassical emission, by limiting losses.

We further investigated the RIN of our experimental configuration, obtaining decreasing RIN values with increasing laser bias currents. Moreover, in contrast to previous RIN studies performed with ICLs operated at room temperature[25,61] where RIN levels up to −130 dB/Hz are reported, we show that our ring-DFB laser exhibits orders of magnitude of lower values for all the tested bias currents reaching a level down to −153 dB/Hz, approximately, which is in line with the values observed with ICLs operated at lower temperatures (100 and 30 K).[62]

In the future, better detection technology with significantly higher quantum efficiencies (currently ∼22%) is needed, to explore the subclassical regime and quantum optics applications.

ASSOCIATED CONTENT

Data Availability Statement

The data that support the findings of this study are available from the corresponding author upon reasonable request.

Supporting Information

The Supporting Information is available free of charge at https://pubs.acs.org/doi/10.1021/acsphotonics.3c01159.

Characterization of the tuning coefficient, detector responsivities, detector CMRR, and INPSD at different laser currents (PDF)

AUTHOR INFORMATION

Corresponding Authors

Francesco Cappelli − *CNR-INO—Istituto Nazionale di Ottica, Florence 50019, Italy; LENS—European Laboratory for Non-Linear Spectroscopy, Florence 50019, Italy*;
Email: francesco.cappelli@ino.cnr.it
Borislav Hinkov − *TU Wien—Institute of Solid State Electronics & Center for Micro- and Nanostructures, Vienna 1040, Austria*; Present Address: Silicon Austria Laboratories (SAL), Europastraβe 12,Villach 9524, Austria; orcid.org/0000-0003-2564-5449;
Email: borislav.hinkov@tuwien.ac.at

Authors

Georg Marschick − *TU Wien—Institute of Solid State Electronics & Center for Micro- and Nanostructures, Vienna 1040, Austria*
Jacopo Pelini − *University of Naples Federico II, Napoli 80138, Italy; CNR-INO—Istituto Nazionale di Ottica, Firenze, FI 50125, Italy*
Tecla Gabbrielli − *CNR-INO—Istituto Nazionale di Ottica, Florence 50019, Italy; LENS—European Laboratory for Non-Linear Spectroscopy, Florence 50019, Italy*
Robert Weih − *nanoplus Nanosystems and Technologies GmbH, Gerbrunn 97218, Germany*
Hedwig Knötig − *TU Wien—Institute of Solid State Electronics & Center for Micro- and Nanostructures, Vienna 1040, Austria*
Johannes Koeth − *nanoplus Nanosystems and Technologies GmbH, Gerbrunn 97218, Germany*

Sven Höfling − *Julius-Maximilians-Universität Würzburg—Physikalisches Institut, Lehrstuhl für Technische Physik, Würzburg 97074, Germany;* orcid.org/0000-0003-0034-4682

Paolo De Natale − *CNR-INO—Istituto Nazionale di Ottica, Firenze, FI 50125, Italy; CNR-INO—Istituto Nazionale di Ottica, Florence 50019, Italy; LENS—European Laboratory for Non-Linear Spectroscopy, Florence 50019, Italy; INFN—Istituto Nazionale di Fisica Nucleare, Florence 50019, Italy;* orcid.org/0000-0002-3308-8569

Gottfried Strasser − *TU Wien—Institute of Solid State Electronics & Center for Micro- and Nanostructures, Vienna 1040, Austria*

Simone Borri − *CNR-INO—Istituto Nazionale di Ottica, Florence 50019, Italy; LENS—European Laboratory for Non-Linear Spectroscopy, Florence 50019, Italy; INFN—Istituto Nazionale di Fisica Nucleare, Florence 50019, Italy*

Complete contact information is available at:
https://pubs.acs.org/10.1021/acsphotonics.3c01159

Author Contributions

○The authors contributed equally to this work.

Funding

The authors acknowledge financial support by the European Union's Next Generation EU Programme with the I-PHOQS Infrastructure [IR0000016, ID D2B8D520, CUP B53C22001750006] "Integrated infrastructure initiative in Photonic and Quantum Sciences", by the European Union's Research and Innovation Programmes Horizon 2020 and Horizon Europe with the cFlow Project [G.A. n. 828893] "Coherent ultrafast long wave infrared communications" and the MUQUABIS Project [G.A. n. 101070546] "Multiscale quantum bioimaging and spectroscopy", by the European Union's QuantERA II [G.A. n. 101017733]—QATACOMB Project "Quantum correlations in terahertz QCL combs", by Fondazione CR Firenze through the SALUS project, and by the Italian ESFRI Roadmap (Extreme Light Infrastructure—ELI Project). The authors are grateful for financial support from the Austrian Research Promotion Agency (FFG) through the ATMO-SENSE project [G.A. n. 1516332] "Novel portable, ultrasensitive, fast and rugged trace gas sensor for atmospheric research based on photothermal interferometry" and the NanoWaterSense project [G.A. n. 873057] "Mid-IR Sensor for Trace Water Detection in Organic Solvents, Oils, and Petrochemical Products". Financial support by the State of Bavaria is greatly acknowledged.

Notes

The authors declare no competing financial interest.

■ ACKNOWLEDGMENTS

The authors gratefully thank M. Schinnerl for expert technical assistance in FIB cutting and SEM characterization of the devices. Fruitful discussions with W. Schrenk and E. Gornik are greatly acknowledged. The authors gratefully acknowledge Iacopo Galli (CNR-INO) and Pablo Cancio Pastor (CNR-INO) for their support in the circuital characterization of the detectors used in this work.

■ REFERENCES

(1) Yang, R. Q. Infrared laser based on intersubband transitions in quantum wells. *Superlattices Microstruct.* **1995**, *17*, 77−83.

(2) Faist, J. *Quantum Cascade Lasers*; Oxford University Press, 2013; p 318.

(3) Faist, J.; Capasso, F.; Sivco, D. L.; Sirtori, C.; Hutchinson, A. L.; Cho, A. Y. Quantum Cascade Laser. *Science* **1994**, *264*, 553−556.

(4) Fuchs, F.; Hinkov, B.; Hugger, S.; Kaster, J. M.; Aidam, R.; Bronner, W.; Köhler, K.; Yang, Q.; Rademacher, S.; Degreif, K.; Schnürer, F.; Schweikert, W. Imaging stand-off detection of explosives using tunable MIR quantum cascade lasers. *Proc. SPIE* **2010**, *7608*, 760809.

(5) Amrania, H.; Woodley-Barker, L.; Goddard, K.; Rosales, B.; Shousha, S.; Thomas, G.; McFarlane, T.; Sroya, M.; Wilhelm-Benartzi, C.; Cocks, K.; Coombes, R. C.; Phillips, C. C. Mid-infrared imaging in breast cancer tissue: an objective measure of grading breast cancer biopsies. *Convergent Sci. Phys. Oncol.* **2018**, *4*, 025001.

(6) Mizaikoff, B. Waveguide-enhanced mid-infrared chem/bio sensors. *Chem. Soc. Rev.* **2013**, *42*, 8683−8699.

(7) Dabrowska, A.; David, M.; Freitag, S.; Andrews, A. M.; Strasser, G.; Hinkov, B.; Schwaighofer, A.; Lendl, B. Broadband laser-based mid-infrared spectroscopy employing a quantum cascade detector for milk protein analysis. *Sens. Actuators, B* **2022**, *350*, 130873.

(8) Griffiths, P. R.; de Haseth, J. A. Introduction to Vibrational Spectroscopy. *Fourier Transform Infrared Spectrom*; John Wiley & Sons, 2007; pp 1−18.

(9) Kosterev, A.; Wysocki, G.; Bakhirkin, Y.; So, S.; Lewicki, R.; Fraser, M.; Tittel, F.; Curl, R. F. Application of quantum cascade lasers to trace gas analysis. *Appl. Phys. B: Lasers Opt.* **2008**, *90*, 165−176.

(10) Tuzson, B.; Mangold, M.; Looser, H.; Manninen, A.; Emmenegger, L. Compact multipass optical cell for laser spectroscopy. *Opt. Lett.* **2013**, *38*, 257−259.

(11) Galli, I.; Bartalini, S.; Ballerini, R.; Barucci, M.; Cancio, P.; De Pas, M.; Giusfredi, G.; Mazzotti, D.; Akikusa, N.; De Natale, P. Spectroscopic Detection of Radiocarbon Dioxide at Parts-per-quadrillion Sensitivity. *Optica* **2016**, *3*, 385−388.

(12) Delli Santi, M. G.; Bartalini, S.; Cancio, P.; Galli, I.; Giusfredi, G.; Haraldsson, C.; Mazzotti, D.; Pesonen, A.; De Natale, P. Biogenic Fraction Determination in Fuel Blends by Laser?Based 14 CO 2 Detection. *Adv. Photonics Res.* **2021**, *2*, 2000069.

(13) Villares, G.; Hugi, A.; Blaser, S.; Faist, J. Dual-comb spectroscopy based on quantum-cascade-laser frequency combs. *Nat. Commun.* **2014**, *5*, 5192.

(14) Razeghi, M. InAs/GaSb type II superlattices: A developing material system for third generation of IR imaging. *Mid-infrared Optoelectronics Materials, Devices, and Applications*, 2020; Vol. 9, pp 379−413.

(15) Dely, H.; Bonazzi, T.; Spitz, O.; Rodriguez, E.; Gacemi, D.; Todorov, Y.; Pantzas, K.; Beaudoin, G.; Sagnes, I.; Li, L.; Davies, A. G.; Linfield, E. H.; Grillot, F.; Vasanelli, A.; Sirtori, C. 10 Gbit s^{-1} Free Space Data Transmission at 9 μm Wavelength With Unipolar Quantum Optoelectronics. *Laser Photonics Rev.* **2022**, *16*, 2100414.

(16) Pang, X.; Schatz, R.; Joharifar, M.; Udalcovs, A.; Bobrovs, V.; Zhang, L.; Yu, X.; Sun, Y. T.; Maisons, G.; Carras, M.; Popov, S.; Lourdudoss, S.; Ozolins, O. Direct Modulation and Free-Space Transmissions of up to 6 Gbps Multilevel Signals With a 4.65 μm Quantum Cascade Laser at Room Temperature. *J. Lightwave Technol.* **2022**, *40*, 2370−2377.

(17) Flannigan, L.; Yoell, L.; Xu, C. Q. Mid-wave and long-wave infrared transmitters and detectors for optical satellite communications - A review. *J. Opt.* **2022**, *24*, 043002.

(18) Vurgaftman, I.; Bewley, W.; Canedy, C.; Kim, C.; Kim, M.; Merritt, C.; Abell, J.; Lindle, J.; Meyer, J. Rebalancing of internally generated carriers for mid-infrared interband cascade lasers with very low power consumption. *Nat. Commun.* **2011**, *2*, 585.

(19) Knötig, H.; Nauschütz, J.; Opačak, N.; Höfling, S.; Koeth, J.; Weih, R.; Schwarz, B. Mitigating Valence Intersubband Absorption in Interband Cascade Lasers. *Laser Photonics Rev.* **2022**, *16*, 2200156.

(20) Shim, E.; Gil-Molina, A.; Westreich, O.; Dikmelik, Y.; Lascola, K.; Gaeta, A. L.; Lipson, M. Tunable single-mode chip-scale mid-infrared laser. *Commun. Phys.* **2021**, *4*, 268.

(21) Sterczewski, L. A.; Bagheri, M.; Frez, C.; Canedy, C. L.; Vurgaftman, I.; Meyer, J. R. Mid-infrared dual-comb spectroscopy with room-temperature bi-functional interband cascade lasers and detectors. *Appl. Phys. Lett.* **2020**, *116*, 141102.

(22) Weih, R.; Nähle, L.; Höfling, S.; Koeth, J.; Kamp, M. Single mode interband cascade lasers based on lateral metal gratings. *Appl. Phys. Lett.* **2014**, *105*, 071111.

(23) Knötig, H.; Hinkov, B.; Weih, R.; Höfling, S.; Koeth, J.; Strasser, G. Continuous-wave operation of vertically emitting ring interband cascade lasers at room temperature. *Appl. Phys. Lett.* **2020**, *116*, 131101.

(24) Borri, S.; Siciliani de Cumis, M.; Viciani, S.; D'Amato, F.; De Natale, P. Unveiling quantum-limited operation of interband cascade lasers. *APL Photonics* **2020**, *5*, 036101.

(25) Deng, Y.; Zhao, B.-B.; Gu, Y.-T.; Wang, C. Relative intensity noise of a continuous-wave interband cascade laser at room temperature. *Opt. Lett.* **2019**, *44*, 1375−1378.

(26) Vurgaftman, I.; Weih, R.; Kamp, M.; Meyer, J.; Canedy, C.; Kim, C.; Kim, M.; Bewley, W.; Merritt, C.; Abell, J.; et al. Interband cascade lasers. *J. Phys. D: Appl. Phys.* **2015**, *48*, 123001.

(27) Vurgaftman, I.; Bewley, W. W.; Canedy, C. L.; Kim, C. S.; Kim, M.; Merritt, C. D.; Abell, J.; Meyer, J. R. Interband cascade lasers with low threshold powers and high output powers. *IEEE J. Sel. Top. Quantum Electron.* **2013**, *19*, 1200210.

(28) Hinkov, B.; Bismuto, A.; Bonetti, Y.; Beck, M.; Blaser, S.; Faist, J. Singlemode quantum cascade lasers with power dissipation below 1 W. *Electron. Lett.* **2012**, *48*, 646.

(29) Xie, F.; Caneau, C.; LeBlanc, H. P.; Visovsky, N. J.; Coleman, S.; Hughes, L. C.; Zah, C.-e. Room Temperature CW Operation of Mid-IR Distributed Feedback Quantum Cascade Lasers for CO2 and NO Gas Sensing. *IEEE J. Sel. Top. Quantum Electron.* **2012**, *18*, 1605−1612.

(30) Bismuto, A.; Blaser, S.; Terazzi, R.; Gresch, T.; Muller, A. High performance, low dissipation quantum cascade lasers across the mid-IR range. *Opt. Express* **2015**, *23*, 5477.

(31) Weih, R.; Kamp, M.; Höfling, S. Interband cascade lasers with room temperature threshold current densities below 100 A/cm2. *Appl. Phys. Lett.* **2013**, *102*, 231123.

(32) Hinkov, B.; Hayden, J.; Szedlak, R.; Martin-Mateos, P.; Jerez, B.; Acedo, P.; Strasser, G.; Lendl, B. High frequency modulation and (quasi) single-sideband emission of mid-infrared ring and ridge quantum cascade lasers. *Opt. Express* **2019**, *27*, 14716−14724.

(33) Hangauer, A.; Spinner, G.; Nikodem, M.; Wysocki, G. Chirped laser dispersion spectroscopy using a directly modulated quantum cascade laser. *Appl. Phys. Lett.* **2013**, *103*, 191107.

(34) Bewley, W. W.; Canedy, C. L.; Kim, C. S.; Merritt, C. D.; Warren, M. V.; Vurgaftman, I.; Meyer, J. R.; Kim, M. Room-temperature mid-infrared interband cascade vertical-cavity surface-emitting lasers. *Appl. Phys. Lett.* **2016**, *109*, 151108.

(35) Veerabathran, G. K.; Sprengel, S.; Andrejew, A.; Amann, M.-C. Room-temperature vertical-cavity surface-emitting lasers at 4 μm with gasb-based type-ii quantum wells. *Appl. Phys. Lett.* **2017**, *110*, 071104.

(36) Joannopoulos, J. D.; Johnson, S. G.; Winn, J. N.; Meade, R. D. *Photonic Crystals: Molding the Flow of Light*; Princet. Univ. Press, 2008; p 286.

(37) Suess, M. J.; Peretti, R.; Liang, Y.; Wolf, J. M.; Bonzon, C.; Hinkov, B.; Nida, S.; Jouy, P.; Metaferia, W.; Lourdudoss, S.; Beck, M.; Faist, J. Advanced fabrication of single-mode and multi-wavelength MIR-QCLs. *Photonics* **2016**, *3*, 26.

(38) Holzbauer, M.; Szedlak, R.; Detz, H.; Weih, R.; Höfling, S.; Schrenk, W.; Koeth, J.; Strasser, G. Substrate-emitting ring interband cascade lasers. *Appl. Phys. Lett.* **2017**, *111*, 171101.

(39) Marschick, G.; Knötig, H.; Weih, R.; Koeth, J.; Strasser, G.; Hinkov, B. Concentric double-ring interband cascade lasers for bi-color emission in continuous wave mode. *Proc. SPIE* **2023**, *12440*, PC1244009.

(40) Hodgkinson, J.; Tatam, R. P. Optical gas sensing: a review. *Meas. Sci. Technol.* **2013**, *24*, 012004.

(41) Tyson, R. K. Bit-error rate for free-space adaptive optics laser communications. *J. Opt. Soc. Am. A* **2002**, *19*, 753−758.

(42) Loudon, R. *The Quantum Theory of Light*; Oxford Academic, 2000.

(43) Gabbrielli, T.; Cappelli, F.; Bruno, N.; Corrias, N.; Borri, S.; De Natale, P.; Zavatta, A. Mid-infrared homodyne balanced detector for quantum light characterization. *Opt. Express* **2021**, *29*, 14536−14547.

(44) Kim, M.; Bewley, W. W.; Canedy, C. L.; Kim, C. S.; Merritt, C. D.; Abell, J.; Vurgaftman, I.; Meyer, J. R. High-power continuous-wave interband cascade lasers with 10 active stages. *Opt. Express* **2015**, *23*, 9664−9672.

(45) Razeghi, M.; Slivken, S.; Bai, Y.; Gokden, B.; Ramezani Darvish, S. High power quantum cascade lasers. *New J. Phys.* **2009**, *11*, 125017.

(46) Bewley, W.; Kim, C.; Canedy, C.; Merritt, C.; Vurgaftman, I.; Abell, J.; Meyer, J.; Kim, M. High-power, high-brightness continuous-wave interband cascade lasers with tapered ridges. *Appl. Phys. Lett.* **2013**, *103*, 111111.

(47) Wang, Z.; Wang, Q.; Ching, J. Y.-L.; Wu, J. C.-Y.; Zhang, G.; Ren, W. A portable low-power qepas-based co2 isotope sensor using a fiber-coupled interband cascade laser. *Sens. Actuators, B* **2017**, *246*, 710−715.

(48) Christensen, L. E.; Mansour, K.; Yang, R. Q. Thermoelectrically cooled interband cascade laser for field measurements. *Opt. Eng.* **2010**, *49*, 111119.

(49) Galli, I.; Bartalini, S.; Cancio, P.; Cappelli, F.; Giusfredi, G.; Mazzotti, D.; Akikusa, N.; Yamanishi, M.; De Natale, P. Mid-infrared frequency comb for broadband high precision and sensitivity molecular spectroscopy. *Opt. Lett.* **2014**, *39*, 5050−5053.

(50) Hinkov, B.; Pilat, F.; Lux, L.; Souza, P. L.; David, M.; Schwaighofer, A.; Ristanić, D.; Schwarz, B.; Detz, H.; Andrews, A. M.; Lendl, B.; Strasser, G. A mid-infrared lab-on-a-chip for dynamic reaction monitoring. *Nat. Commun.* **2022**, *13*, 4753.

(51) Pilat, F.; Schwarz, B.; Baumgartner, B.; Ristanić, D.; Detz, H.; Andrews, A. M.; Lendl, B.; Strasser, G.; Hinkov, B. Beyond Karl Fischer titration: a monolithic quantum cascade sensor for monitoring residual water concentration in solvents. *Lab Chip* **2023**, *23*, 1816−1824.

(52) Mhanna, M.; Zhang, G.; Kunnummal, N.; Farooq, A. Cavity-enhanced measurements of benzene for environmental monitoring. *IEEE Sens. J.* **2021**, *21*, 3849−3859.

(53) He, Q.; Zheng, C.; Lou, M.; Ye, W.; Wang, Y.; Tittel, F. K. Dual-feedback mid-infrared cavity-enhanced absorption spectroscopy for h 2 co detection using a radio-frequency electrically-modulated interband cascade laser. *Opt. Express* **2018**, *26*, 15436−15444.

(54) Richard, L.; Ventrillard, I.; Chau, G.; Jaulin, K.; Kerstel, E.; Romanini, D. Optical-feedback cavity-enhanced absorption spectroscopy with an interband cascade laser: application to so2 trace analysis. *Appl. Phys. B: Lasers Opt.* **2016**, *122*, 247.

(55) Manfred, K.; Ritchie, G.; Lang, N.; Röpcke, J.; Van Helden, J. Optical feedback cavity-enhanced absorption spectroscopy with a 3.24 μm interband cascade laser. *Appl. Phys. Lett.* **2015**, *106*, 221106.

(56) Soibel, A.; Wright, M.; Farr, W.; Keo, S.; Hill, C.; Yang, R. Q.; Liu, H. High-speed operation of interband cascade lasers. *Electron. Lett.* **2009**, *45*, 264−265.

(57) Maddaloni, P.; Bellini, M.; De Natale, P. *Laser-based Measurements for Time and Frequency Domain Applications: A Handbook*; CRC Press, 2013.

(58) Plick, W. N.; Dowling, J. P.; Agarwal, G. S. Coherent-light-boosted, sub-shot noise, quantum interferometry. *New J. Phys.* **2010**, *12*, 083014.

(59) Abbott, B.; Abbott, R.; Adhikari, R.; Ajith, P.; Allen, B.; Allen, G.; Amin, R.; Anderson, S.; Anderson, W.; Arain, M.; et al. Ligo: the laser interferometer gravitational-wave observatory. *Rep. Prog. Phys.* **2009**, *72*, 076901.

(60) Truong, G.-W.; Anstie, J. D.; May, E. F.; Stace, T. M.; Luiten, A. N. Absolute absorption line-shape measurements at the shot-noise limit. *Phys. Rev. A: At., Mol., Opt. Phys.* **2012**, *86*, 030501.

(61) Didier, P.; Spitz, O.; Cerutti, L.; Diaz-Thomas, D.; Baranov, A.; Carras, M.; Grillot, F. Relative intensity noise and intrinsic properties

of rf mounted interband cascade laser. *Appl. Phys. Lett.* **2021**, *119*, 171107.

(62) Folkes, P. A. Interband cascade laser photon noise. *J. Phys. D: Appl. Phys.* **2008**, *41*, 245109.

CHAPTER 6

PROCESSING TECHNOLOGIES

This chapter should give the reader a detailed overview on the processing technologies and techniques used to fabricate the devices that were described in the publications. Furthermore it should help to preserve processing knowledge for future refinements in device fabrication. A list of all standard-recipes and techniques used in the fabrication processes is given in the appendix. The single processing steps are always referring to this list. Deviations from the standard-recipe are given in the description.

6.1 Processing of Ring Interband Cascade Lasers

Similar to the devices used for the publication that can be found in chapter 5 (Mid-infrared Ring Interband Cascade Laser: Operation at the Standard Quantum Limit), the micro-ring devices used for the publication in chapter 4 (Compact vertical emitting ring interband cascade lasers for isotope-resolved CO_2 sensing) were processed as explained in the following section.
Referring to Figure 6.1, the single steps and the process recipes used are explained here.

1. Starting from the plain substrate,

2. in the first process step a silicon nitride (SiN) hardmask for the ICL deep etch is deposited. The etch depth needed to process ICL devices depends on the growth structure of the epistructure. This growth structure can be found in the growth sheets usually provided by the grower. In this thesis,

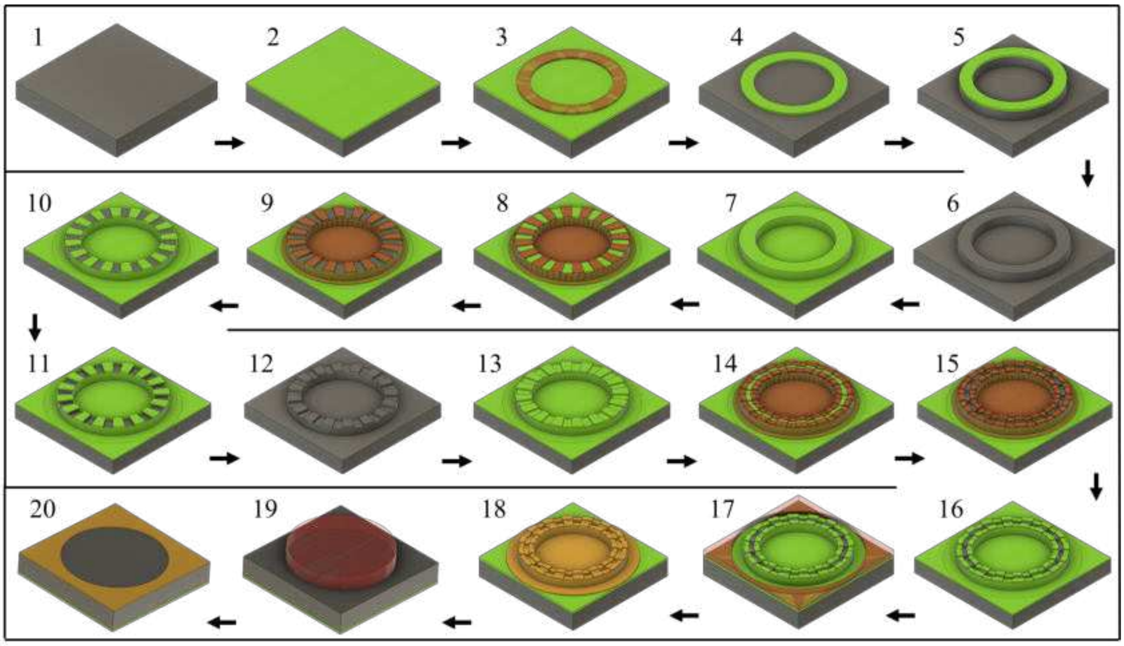

Figure 6.1: A schematic view of all processing steps used to fabricate ring-ICLs. The single processing steps are explained in the text.

ICL devices were always etched down slightly into the separate-confinement layer (SCL) layer below the active region which in typical devices accounts to roughly 3.1 µm. The active region should be visible in scanning electron microscopy as Figure 6.3a) shows. Due to the selectivity of the CL_2-Ar reactive ion etching (RIE) etch process for ICLs described in subsection A.1.4, the hardmask must account to a thickness of at least one sixth of the desired etch depth. To gain some extra security, a 900 nm thick SiN layer was deposited with a 72 min NH_3-free plasma enhanced chemical vapor deposition (PECVD) process described in subsection A.1.3.

3. The first lithography as described in subsection A.1.1 (AZ5214JP Positive Process, Laserwriter, Recipe 1) was done to define the ring structures on the hardmask.

4. The hardmask was then patterned with a 16 min 30 s CHF_3 RIE etch (Anisotropic CHF3 etching of SiN (Name: SiN RIE mode)). As the high HF power of this recipe also causes physical etching of the semiconductor when the SiN is removed, the etch time should be chosen properly and the process should be supervised by the reflexion setup as shown in Figure 6.12. It is important to remove the resist layer after hardmask definition with a short O_2 plasma step followed with acetone and isopropanol before deep-etching.

5. The sample is now ready for the Cl_2-Ar ICL deep etch process. To etch the structure just below the active region into the lower SCL, an etch depth of around 3.1 µm is needed, which accounts to an etch time of roughly 15 min and 15 s.

6. After the deep etch, the remaining SiN hardmask is removed through a SF_6 SiN etch. Resulting from the etch selectivity and the thickness of the initial hardmask, around 400 nm of SiN remain atop the etched ring structures. The high etch rate of the SF_6 etch results in a short step time of around 150 s. After the SiN removal, an optional wet-etch step in diluted hydrochloric acid ($HCl:H_2O$ 1:1) was done to remove potential residuals from the RIE etch and to smoothen the waveguide sidewalls.

7. To integrate the second order DFB grating atop the waveguide, another SiN hardmask is needed. As the etch depth of the grating is around 1 µm, a SiN thickness of 450 nm (36 min NH_3-free @ 280 °C) is sufficient.

8. As the feature size of the grating $\Lambda = \lambda/2n_{eff}$, with λ=4.3 µm and $n_{eff} \sim 3.3$ - 3.4, is in the sub-micrometer range, optical i-line lithography is not able to resolve the features. Thus, electon beam lithography as described in section A.1.2 is used to pattern the grating.

9. After developing the grating lithography, the SiN hardmask can be patterned with CHF_3 RIE chemistry (7 min 20 s)

10. This is followed by removal of the resist through O_2 plasma, acetone and isopropanol.

11. Now the sample is ready for the grating deep etch. In ICL devices the grating is etched about 1 µm deep into the cladding of the waveguide to achieve proper mode coupling. The grating etch is performed with Cl_2-Ar ICL RIE etching for 7 min 30 s followed by another 10 s $HCl:H_2O$ (1:1) dip to remove etch residuals.

12. The remaining SiN hardmask is removed with a SiN SF_6 RIE etch.

13. Now the waveguide is passivated with a 250 nm thick layer of SiN (20 min NH_3-free PECVD deposition @ 280 °C) in order to be able to create a defined current path through the waveguide strucutre. Further, this passivation inhibits the creation of oxide layers and thus the formation of surface leakage currents. Last but not least it also improves the mechanical stability of the waveguide. To eliminate the Si-H absorption peak at λ=4.5 µm thats inherent in SiN

deposited from hydrogen-containing precursers (see sections 6.4.4 and A.1.3), it is advisable to deposit the passivation layer with reactive sputtering.

14. To achieve uniform current distribution along the waveguide, the passivation layer is opened along the centerline of the ring. This lithography step has to be done with high precision and the sidewalls must be thouroughly covered by resist. Inadequate resist coverage will lead to holes in the passivation and thus to short circuiting of the structure. Thus, this lithography step is done with high-viscous maP1275 resist. In this case, to effectively remove the resist also in the trenches of the grating, the used dose is 600 mJ/cm^2 and the exposure is done twice followed by 20 s development.

15. & 16. The passivation opening is realized through 5 min CHF_3 RIE etching and the resist is removed through plasma etching, acetone and isopropanol.

17. To implement the last fabrication step of the ring processing, a photolithography for the top contact metallisation is realised with nLof2070 resist.

18. The top contact is realised by sputtering of 10 nm Ti, 100 nm Pt and 400 nm Au.

19. After thinning the sample to approximately 180 µm and polishing the substrate with a final grit size of 0.5 µm, the backside should exhibit a mirror-like finish, making it ready for the lithography of the backside contact, which is carried out using an AZ5214 positive process.

20. To finalize the process, the backside Ge-Au-Ni-Au contact is sputtered with thicknesses of 15-30-15-200 nm respectively and the residual photoresist is removed with acetone and isopropanol.

6.2 Processing of monolithic on-chip QCLD structures with micro-mirror aided plasmonic beam guiding

The devices used for the publication that can be found in chapter 3 (Micro-mirror aided mid-infrared plasmonic beam combiner monolithically integrated with quantum cascade lasers and detectors), were processed as the following section describes. As the processing steps here include many standard process steps for fabrication of QCL, QCD or QCLD material based on InP. The recipes can be adapted to a multitude of fabrication routines. The QCD devices characterized in the publication presented in chapter 2 were also processed used the same standard processes, with the difference of lithographies only done on the mask aligner as the laser writer was not yet available at this time. As the detectors, due to the lack of multiple structures, were way simpler to process compared to the monolithic beam combiner, this did not present an issue. Fabrication of the monolithic beam combiners on the other hand would have been nearly impossible, or at least would have to be done in a different manner without the use of the high precision laser writer.

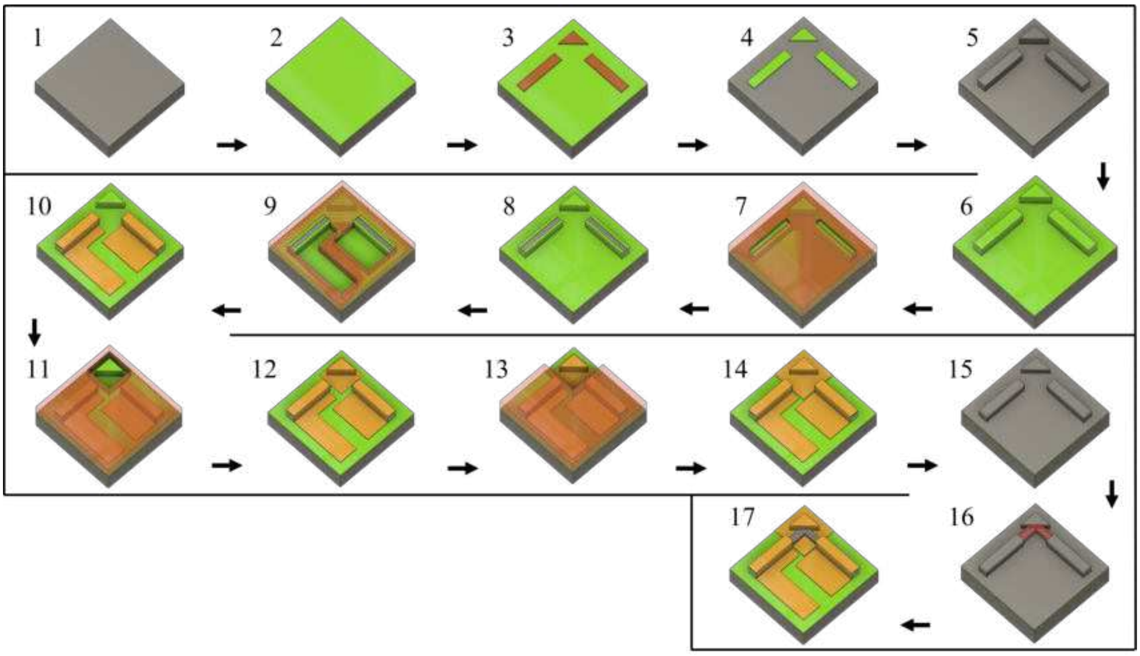

Figure 6.2: A schematic view of all processing steps used to fabricate the on chip beam-combiner structure with Au-coated mirrors to redirect the SPPs.

Referring to Figure 6.2, the single steps and the process recipes used are explained here.

1. Starting from the plain substrate,

2. In the first process step, a SiN hardmask for the QCL and micro-mirror deep etch is deposited. The etch depth needed to process QCL devices depends on the growth structure of the epistructure, which can be found in the growth sheets usually provided by the grower. In this thesis, QCL devices are always thoroughly etched down through the active region. The final etch depth in QCL material is less critical compared to ICL material as long as the active region is fully etched through. The active region should be visible in scanning electron microscopy, as shown in Figure 6.3b). Due to the selectivity of the Cl_2-Ar RIE etch process for QCLs (InGaAs/InAlAs Cl_2-Ar etch) described in subsection A.1.4, the hardmask must be at least one twelfth of the desired etch depth. To provide additional security for a desired etch depth of 8 µm, a 1000 nm thick SiN layer is deposited using an 80 min NH_3-free PECVD process, described in subsection A.1.3.

3. The first lithography step, as described in subsection A.1.1 (AZ5214JP Positive Process, Laserwriter, Recipe 1), is performed to define the waveguide structures for the lasers, detectors, and micro mirrors on the hardmask.

4. The hardmask is then patterned using a 16 min 30 s CHF_3 RIE etch (Anisotropic CHF_3 etching of SiN, Name: SiN RIE mode). As the high HF power of this recipe can also cause physical etching of the semiconductor when the SiN is removed, the etch time is carefully chosen, and the process is supervised using the reflection setup, as shown in Figure 6.12. It is important to remove the resist layer after hardmask definition with a short O_2 plasma step followed by acetone and isopropanol before deep-etching. The sample is now ready for the Cl_2-Ar QCL deep etch process.

5. To etch through the active region into the substrate, an etch depth of at least 8 µm is needed, which corresponds to an etch time of approximately 7 min and 20 s. If precise depths are necessary, using a reference sample before the actual "hot" sample is recommended. After the deep etch, the remaining SiN hardmask is removed using an SF_6 SiN etch. The high etch rate of the SF_6 etch results in a short etch time of around 300 s. After the SiN removal, an optional wet-etch step in a mixture of $HCl:H_3PO_4:C_2H_4O_2$ (1:1:2) is performed to remove potential residues from the RIE etch and to smooth the waveguide sidewalls.

6. The structures are now passivated with a 300 nm thick layer of SiN, which is achieved through a 33 min NH_3-free PECVD process.

7. To achieve uniform current distribution along the waveguide, the passivation layer is opened along the centerline of the laser and detector ridge. This lithography step requires high precision, and the sidewalls must be thoroughly covered by resist. Inadequate resist coverage will lead to holes in the passivation layer, potentially causing short circuits in the structure. The mirror structures remain covered with resist to maintain the passivation layer there. This lithography step is performed with high-viscosity maP1275 resist, exposed with a dose of 350 mJ/cm^2 and developed for 12 s.

8. The passivation layer atop the laser and detector ridges, as well as areas for the bottom contacts of lasers and detectors, are opened using a 4 min CHF_3 RIE etch (Anisotropic CHF_3 etching of SiN, Name: SiN RIE mode), followed by resist removal through plasma ashing (10 min at 600 W) and cleaning with acetone/isopropanol.

9. The lithography step defining the top contacts is now performed using a standard nLof2070 process.

10. Top contacts are realized through sputtering 10 nm of Ti and 300 nm of Au, followed by a lift-off process in acetone and cleaning with isopropanol.

11. The mirrors are then covered with Ti/Au to efficiently reflect the incoming plasmons. It is recommended to realize this step with sputtering. Evaporation with a tilted and rotating substrate to ensure appropriate sidewall coverage of the mirrors is possible but not recommended as the risk of contaminating the etched facets of the detector and laser building blocks is high. Thorough lithography alignment and proper resist profiles are essential in this step. The best results are achieved using nLof 2070 resist for this step.

12. The mirror is coated by sputtering a 10 nm Ti adhesion layer and a 50 nm Au reflection layer, followed by a lift-off process.

13. This second photolithography step is essential for applying a thicker and more precise Au layer to serve as the plasmonic layer without covering unwanted areas, such as the vertical surfaces (e.g., facets of the detectors and lasers). This step requires the highest precision in alignment, as excessive gaps between the facets and the plasmonic Au layer can impair device performance. This step is also carried out using nLof 2070 resist. At this point, the separated bottom contacts of the lasers and detectors are also defined.

14. Before the actual deposition, the surface of the substrate is ion-milled through Ar-plasma in the evaporation chamber. Deposition of 10 nm Ti and 300 nm Au, serving as the plasmonic layer and the bottom contacts, is carried out. Anisotropic evaporation is used here because it allows for directional deposition, meaning the metal primarily deposits on horizontal surfaces and does not coat vertical surfaces (like the facets). This is important because it minimizes the risk of short-circuiting or other electrical issues that could arise if metal were deposited on unintended areas. After deposition, the areas are defined through a lift-off process.

15. Since the Ge waveguides have a relatively small feature size, with widths of 6 µm, embedded in small areas between already existing detector, laser, and mirror structures, the concept of etch-definition yields better results compared to deposition of only the desired structures. Thus, the whole sample is covered with 300 nm of Ge through sputtering.

16. To pattern the resist structure that defines the waveguide by covering the Ge layer from the Ge etch, a two-step exposure lithography process with AZ5214 JP is implemented. First, the resist is removed everywhere on the sample except for rectangular areas of the size of the waveguide structures. The second exposure then precisely defines the waveguide structures. This is necessary to ensure that resist accumulating in edges and corners can be effectively developed without overdeveloping the sensitive, thin waveguide cover structures. The first exposure is carried out with a dose of 250 mJ/cm^2 and 20 s development, while the second exposure is done with 150 mJ/cm^2 and developed for 15 s.

17. The Ge is etched away using SF$_6$-ICP etching in the RIE for approximately 1 min. The etch process is supervised via the reflection measurement monitor (see Figure 6.13).

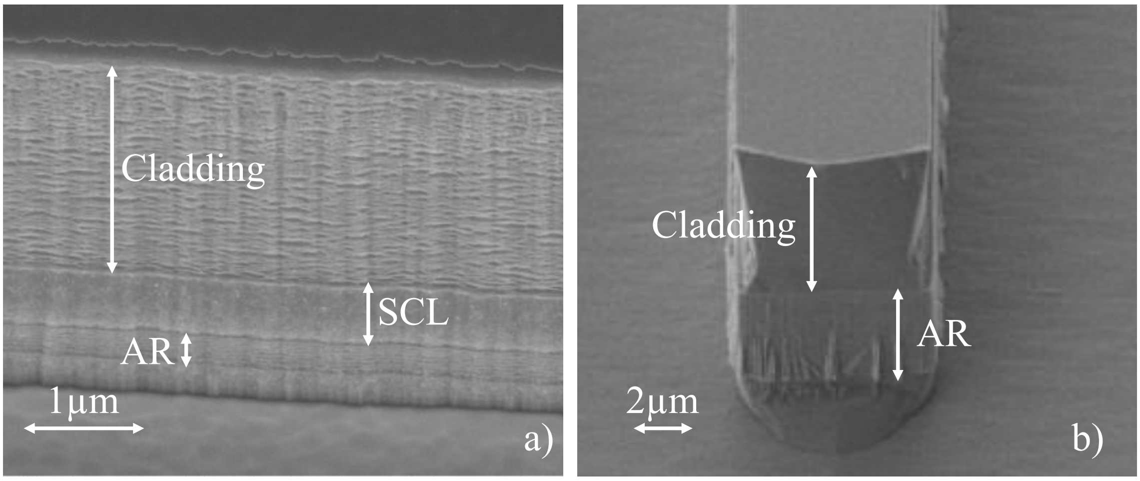

Figure 6.3: Comparison between successful ICL (left) and QCL (right) deep etch processes after wet-etch smoothing. It can be seen that the active region of an ICL is comprised of way fewer periods and the single layers are visible.

6.3 Processing of AlN laser submounts and bonding strategies

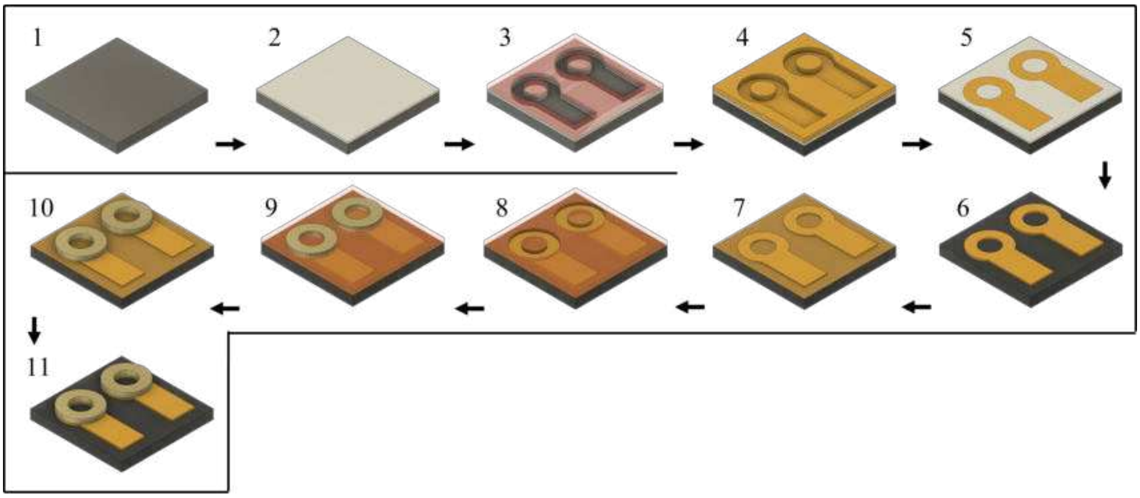

Figure 6.4: A schematic view of all processing steps used to fabricate customized AlN submounts for bonding ICL ring lasers.

Referring to Figure 6.4, the single steps and the process recipes used for them are explained in this section.

1. Starting from the plain AlN substrate,
2. In the first process step, a thin layer of aluminum or gold, approximately 20 nm thick, is deposited onto the AlN surface. This layer acts as an opaque coating,

which is necessary due to the transparency of AlN to ultraviolet (UV) light, which would otherwise complicate standard photolithography techniques.

3. With the sample now rendered opaque, reliable lithography is ensured. Lithography was performed using an image reversal TI35 process on the mask aligner; however, similar or potentially better results could also be achieved using the laser writer. The areas designated for contact deposition were then developed. In the case of an aluminum (Al) opacity layer, the developer AZ351B, which is based on sodium hydroxide, will also remove the thin Al layer from these regions. Alternatively, if gold (Au) is used as the opacity layer, a brief dip in KI-I_2 gold etch effectively removes the Au layer.

4. Now, the areas where the contacts are to be deposited are freed of the resist and the opacity layer is removed. Thus, the sample is ready for the contact deposition. A 10 nm layer of Ti and a 300 nm layer of Au are sputtered to ensure a stable contact on the AlN substrate.

5. After the deposition process, the contacts are formed through a lift-off process, and the remaining Al or Au opacity layer is removed either through etching with developer (Al) or KI-I_2 (Au).

6. This leaves the AlN submount with only the single contacts deposited on its surface. As the thicker Au for the bonding pad is deposited through an electroplating process, the sample must be prepared accordingly.

7. To ensure proper and uniform metal deposition with a consistent deposition rate across the sample, the single contacts must be connected and at the same potential. This is achieved by sputtering a thin (50 nm) conductive layer of Au over the entire sample. This layer also acts as an opacity layer for the subsequent lithography, which defines the areas for electroplating.

8. As the sample is again opaque, another image reversal TI35 lithography is performed to define the areas for the bonding pads. Before submerging the sample into the electroplating solution, it should be baked at approximately 70°C for about 10 minutes to remove excess solvents that could otherwise contaminate the electroplating solution.

9. Electroplating is carried out with an approximate current flow of 1.5 mA at a voltage of 0.55 V for roughly one hour. This resulted in a deposited Au thickness of 6 µm.

10. After electroplating, the resist is stripped using warm acetone and isopropanol.
11. As a final step, a short etching process using KI-I_2 to remove any remaining Au from the opacity layer is performed. This step ensures that the surfaces are clean, free of unwanted Au, and without any potential short-circuits between the contacts.

6.4 Processing Challenges and Mitigation Strategies

In this section, some challenges encountered during the fabrication processes of different optoelectronic devices will be discussed. By analyzing various diagnostic tools, such as scanning electron microscope (SEM) images, surface profiles from a Dektak stylus profiler, and optical microscope images, I will highlight some specific problems observed and, where applicable, offer suggestions to mitigate these issues. Furthermore, basic principles of the single processes will be explained to provide context for the discussion, ensuring a clearer understanding of the mechanisms behind the encountered defects and their solutions.

6.4.1 Lithography

Lithography serves as the foundation in the micro- and nano-fabrication process, where the quality of each individual lithographic step directly impacts the overall performance and reliability of the final device. The three families of photoresists (PR) are positive (e.g. maP1275), negative (e.g. Nlof2070) and image reversal (IR) resists (e.g. AZ5214JP, TI35IR). While in a positive resist exposure to light causes the exposed areas to become more soluble in the developer solution, in a negative resist exposed areas become less soluble through crosslinking. Image reversal resists classically behave as positive resists but through proper process steps a image reversal step can be achieved. There the initial exposure creates a latent image in the resist. Subsequent baking and exposure steps define whether the final image will be positive or negative. A thorough explanation of resist chemistry and a detailed description of the influence of doses and times can be found in the technical datasheets of the resists and in existing literature.[215] Photoresists are available in different viscosities and exhibit different reaction parameters for specific applications. For example, highly viscous resists are able to be spun thicker and are useful if sidewalls of existing structures have to be covered compared to low-viscous resists.

Varying resist behavior and aging

Since photoresists are susceptible to aging and environmental factors due to their hydrophilic nature, their properties change over time, affecting their performance. Thus, the standard lithography recipes provided in A.1.1 should be treated as flexible guidelines, adaptable to variations in resist behavior and process conditions. Figure 6.5 illustrates this point, presenting two microscopic images of the waveguide definition lithography for ICL double-ring structures fabricated on the same substrate.

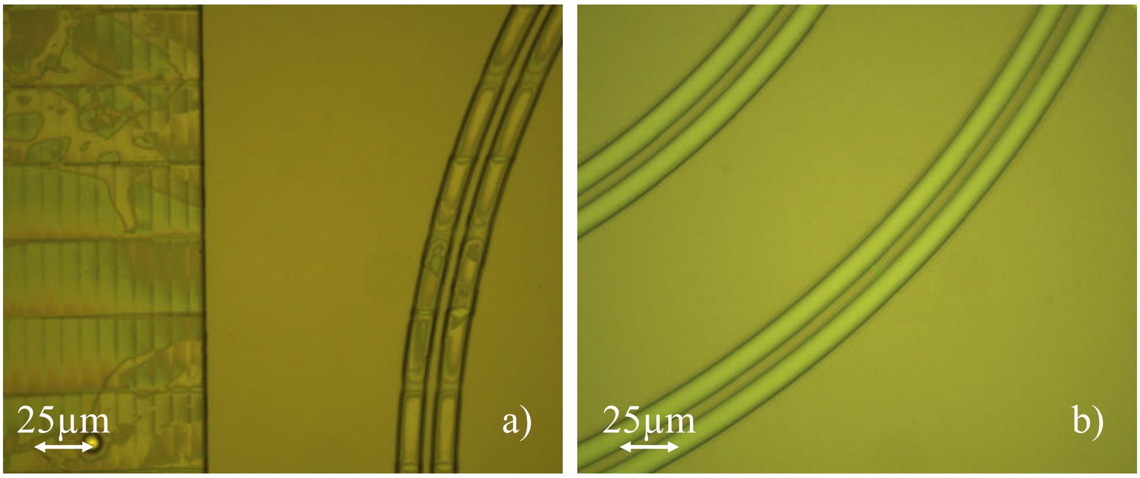

Figure 6.5: Microscope pictures of a) a clearly underexposed and b) a nicely developed lithography for ICL double ring structures.

Both lithography processes employed the same standard recipe, utilizing AZ5214JP resist on an MLA laser writer, with only minor adjustments in defoc parameter and exposure dose. In Figure 6.5a), areas of underexposure are evident, where insufficient overlap between adjacent laser-written lines is visible as vertical streaks. This underexposure, likely caused by improper focus and dose selection at that moment, highlights the sensitivity of the process to real time resist properties. Through fine-tuning, including a slight increase in the defocus parameter and an adjustment to the exposure dose parameters typically outside the standard recipe the lithography quality significantly improved. As demonstrated in Figure 6.5b), these modifications enabled a well defined pattern, demonstrating that resist aging or environmental variations can be compensated for by real time adjustments in process parameters. Another critical factor affecting the success of lithography processes is the adhesion of the photoresist to the substrate. It was observed that SiN hardmask layers, when deposited on the substrate several days prior to the lithography step, significantly degrade the lithography quality, even after thorough substrate cleaning before resist application. Although this issue was not studied in detail, it was effectively mitigated by removing the SiN layer using SF_6 RIE etching and redepositing it immediately before the lithography process. This simple approach successfully restored the resist adhesion and resolved the lithography issues.

Resist residuals

Another issue related to improper lithography execution is the presence of resist residues, often minimal, that can severely affect the adhesion of subsequent metal layers. These residuals are frequently less apparent than in the example shown in

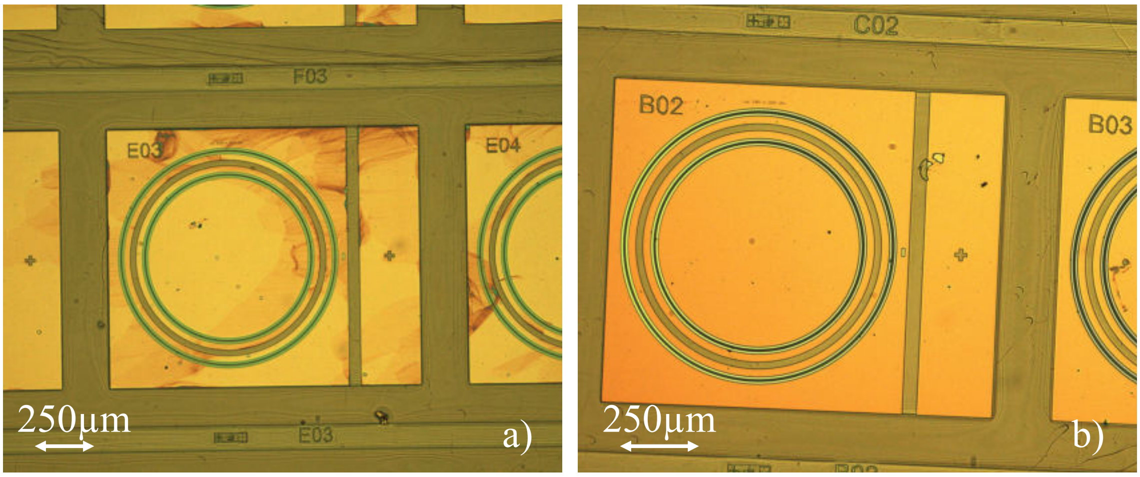

Figure 6.6: Microscope pictures of a) resist residuals after development and b) developed and clean sample after O_2 plasma ashing

Figure 6.6a), making their detection difficult. If left undiscovered, resist residues beneath the metallization layer can lead to thermal and structural failures, often resulting in complete loss of the samples. Ensuring proper development times, followed by an oxygen plasma treatment, can effectively remove developed resist in standard lithography processes. However, achieving complete resist removal from deep trenches or other geometrically complex structures, where resist can accumulate during the spin-coating process, can be more challenging. In such cases, multiple lithography steps may be required to ensure proper development and removal as can be seen in Figure 6.7. For example, the lithography process that defines the linear

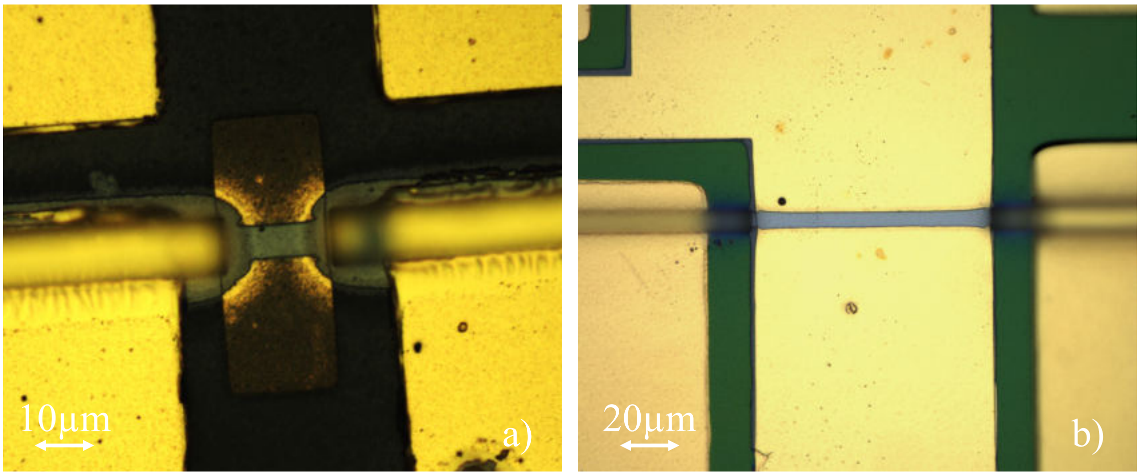

Figure 6.7: Microscope images showing: a) Residual resist accumulation at the edges of the laser and detector ridges, resulted in incomplete etching of the Ge layer (visible as grey areas around the ridges). b) Outcome after a two-step lithography process, where the edges of the laser and detector ridges are completely free of Ge contamination, demonstrating successful resist removal and proper patterning

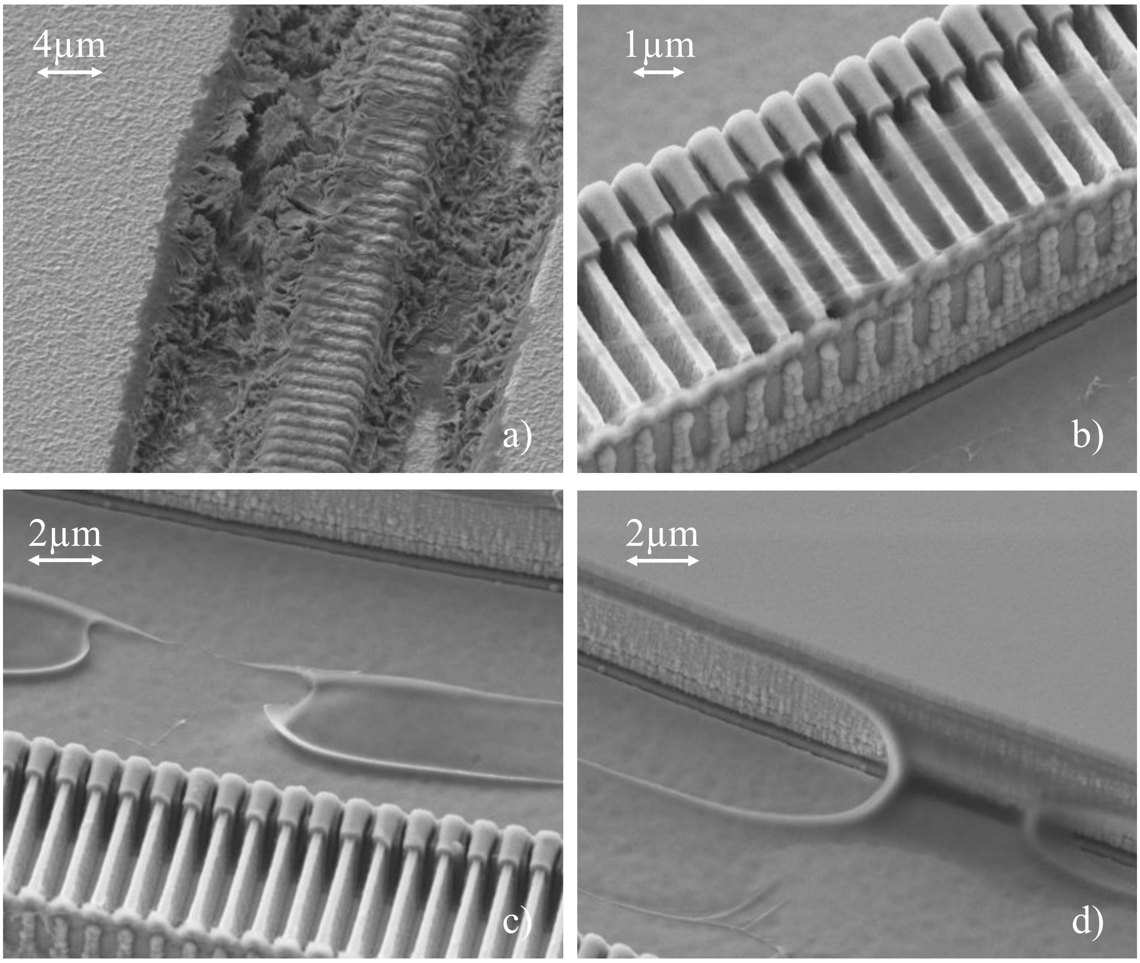

Figure 6.8: SEM images of resist residuals in different forms of appearance.

Ge-SPP waveguides was carried out in two stages. The first step involved a longer exposure and development to effectively remove resist from areas where it tends to accumulate, such as edges and corners. This step ensures that the resist is cleared from areas that are not needed, creating a clean rectangular region where the waveguide will later be patterned. The second lithography step then focuses on defining the thin and precise waveguide itself. By separating these steps, the exposure and development times can be tailored for optimal results, ensuring a high-quality outcome for the waveguide structure. To provide a clearer understanding of how resist residues can be identified using a SEM, Figure 6.8 displays four different forms in which these residues can appear. These subtle residues are often missed when using an optical microscope, as they can manifest in ways that are difficult to detect visually. The SEM's higher resolution and contrast allow for precise detection of resist remnants, which can critically affect subsequent processing steps if not properly addressed. In general its advised to regularly check the sample with the help of a SEM to properly follow the processing advancement and detect defect origins like the mentioned resist residuals before the next processing step.

6.4.2 Electron beam lithography

E-beam lithography is a high-resolution patterning technique used in microfabrication to define intricate nanostructures on a substrate, where optical lithography is limited by the diffraction limit. It employs a focused beam of electrons to draw custom patterns directly onto a resist-coated sample. To align existing structures, such as rings or other features, with the e-beam lithography coordinate system, distinctive alignment markers with known coordinates must be implemented during prior fabrication steps to ensure precise alignment. The resist is typically based on polymethyl methacrylate (PMMA), a polymer sensitive to the high-energy electron beam, which causes a break down of the polymer, leading to changes in solubility in specific developers. Precise control of the electron beam's focus is crucial to achieving accurate patterning. When the working distance plane, which corrects the sample tilt to maintain a stable working distance of the e-beam, is not set correctly, issues such as defocusing can occur. This results in blurred or distorted patterns, decreased resolution, and unintended exposure of areas outside the intended regions. Figure 6.9 shows two SEM images of grating hardmasks after development and mask opening with CHF_3 RIE chemistry as well as two optical microscope images to facilitate the identification of how a proper developed and etched grating hardmask should look like. The left image shows the hardmask barely untouched as the resist was not properly exposed and thus not developed uniformly. Only small parts were developed and thus etched away. Through proper setting of the working distance plane through a three-point alignment, the sample tilt can be effectively compensated and uniform exposure is ensured as seen in Figure 6.9b).

6.4.3 Reactive Ion etching

After lithography, RIE is the second most important step in processing optoelectronic devices. The quality of the resulting device is strongly depending on the quality of the single etching processes necessary for example for the hard mask patterning, the deep-etch or the definition of waveguides. Typical problems, besides the wrong calculation of etch time resulting in too shallow or too deep etch profiles, are the co-deposition of residuals or non-optimal power, pressure and gas flow settings. A short explanation of the impact of the different setting properties should be given here. RIE combines chemical and physical etching mechanisms to achieve high precision and anisotropic profiles. The etch rate and profile can be precisely

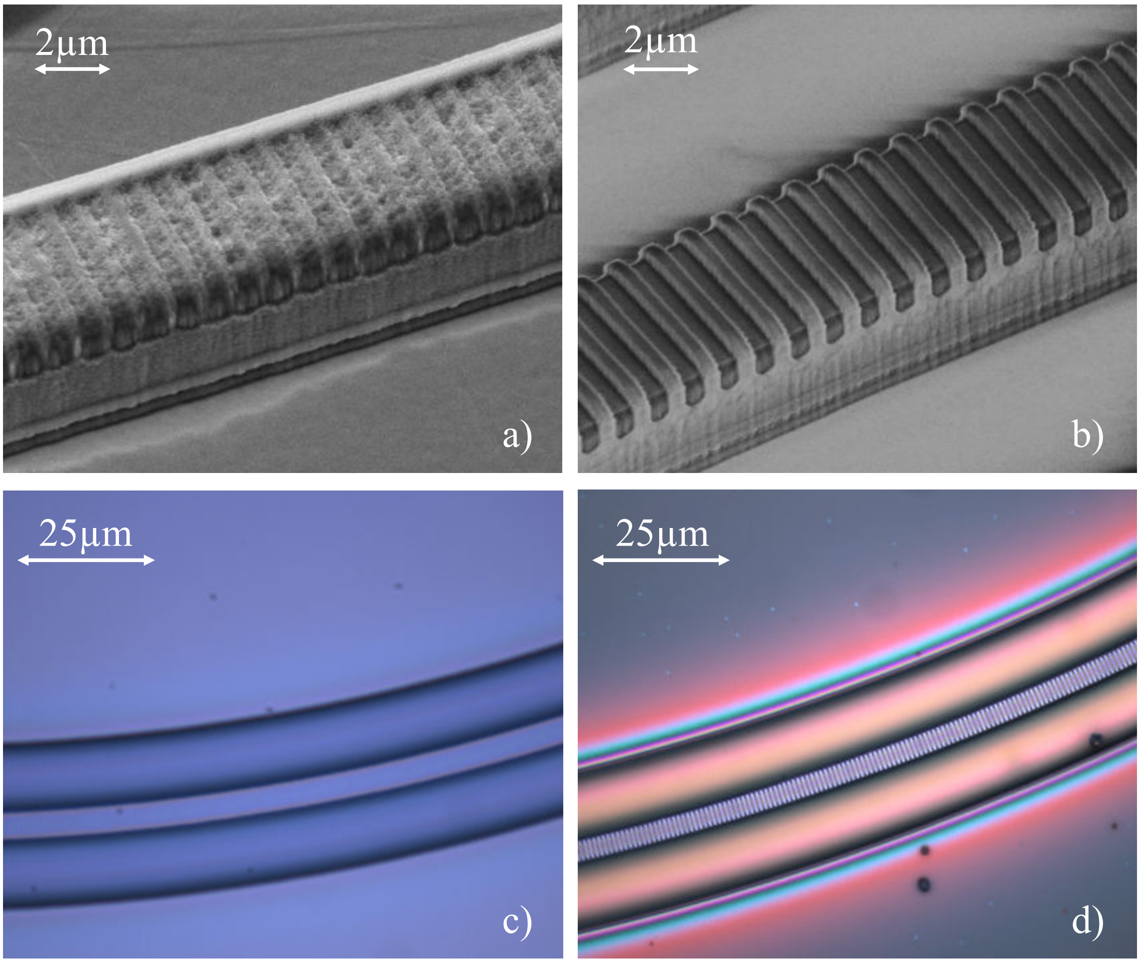

Figure 6.9: a & c) Improperly exposed and thus not etched DFB grating hardmask in electron and optical microscopy respectively. b & d) nicely exposed, developed and etched grating hardmask ready for RIE-etching (SEM and microscope).

controlled by adjusting parameters such as gas flow rates, chamber pressure, RF power, ICP power, and substrate temperature as briefly described in the following paragraph.[216]

- Pressure: Lower chamber pressure generally results in more anisotropic etching profiles due to increased ion bombardment energy and directionality. Higher pressure can lead to more isotropic etching due to more frequent gas-phase collisions.
- Temperature: The substrate temperature affects the chemical reaction rates on the surface. Higher temperatures can enhance the etch rate by increasing the volatility of etch by-products and improving the chemical reaction kinetics. However, too high temperatures may cause undesirable thermal effects on the substrate and photoresist.
- HF Power: The RF power applied to the substrate influences the ion energy.

Higher RF power increases the ion bombardment energy, leading to higher etch rates and more anisotropic etch profiles. However, excessive RF power can damage the substrate or cause excessive sputtering.

- ICP Power: inductively coupled plasma (ICP) power controls the plasma density. Higher ICP power increases the density of reactive species in the plasma, enhancing the etch rate. It also contributes to more uniform etching over large areas. Balancing ICP power with RF power is crucial to achieving desired etch profiles.
- Gas Flows: The type and flow rates of etching gases (e.g., CHF_3, SF_6, Cl_2) determine the chemical etching mechanisms. Adjusting gas flows can tailor the etch selectivity between different materials and influence the etch anisotropy. For instance, higher CHF_3 flow can increase sidewall passivation, resulting in more anisotropic etch profiles.

Chamber preconditioning

Chamber preconditioning in ICP-RIE etching is a critical step to ensure consistent and reliable etching results. It involves running a "dummy" etch using the same chemistry and conditions intended for the actual process. This step serves several purposes: it removes any residual gases, contaminants, or polymeric deposits from previous etches, stabilizes the plasma environment, and ensures uniform surface conditions throughout the chamber. Preconditioning helps to eliminate variation in etch rates, selectivity, and sidewall profiles, especially in sensitive applications involving III-V materials, especially in RIE chambers that are used to etch different materials with changing chemistries.[217] Proper chamber conditioning is especially important for deep etching processes. Before the actual deep etch, a two-minute precondition etch with only the specific carrier wafer (without sample) is recommended to ensure proper etch dynamics.

Polymeric residuals at CHF_3 etching of SiN

For SiN, fluorine-based chemistries, such as trifluoromethane (CHF_3) or sulfur hexafluoride (SF_6) are used. When SiN is exposed to SF_6 plasma, the fluorine radicals react with silicon to form volatile SiF_4, which is easily removed from the etching site. This process allows for precise and anisotropic etching with high etch rates with high selectivity to III-V semiconductors, thus its useful for the removal of residual SiN hardmasks after deep etch processes. RIE using trifluoromethane (CHF_3) is a widely employed technique for etching SiN in semiconductor fabrication. CHF_3 is preferred for its ability to provide a balance between etching and passivation, which

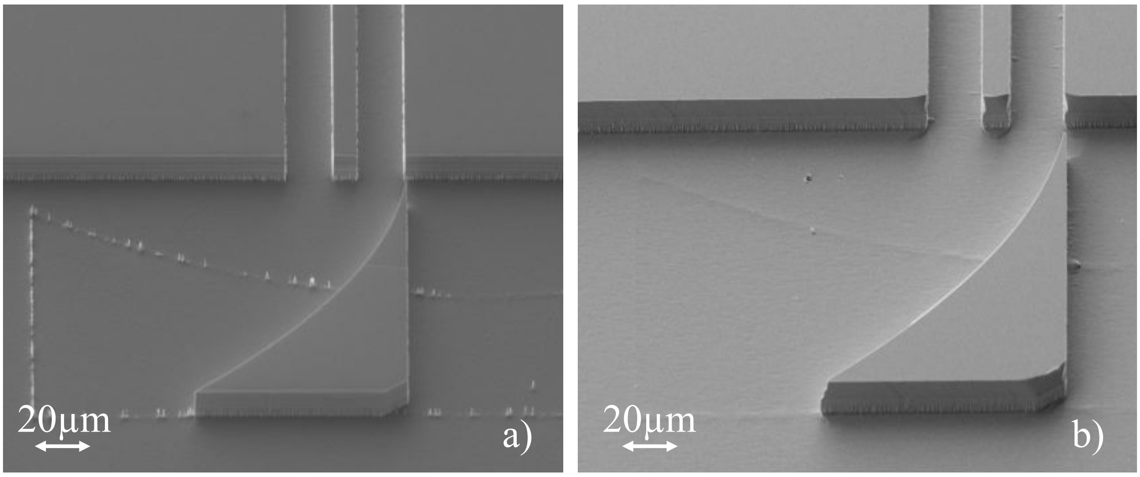

Figure 6.10: a) Pillar structures caused by micromasking through polymeric residuals of CHF_3-eching following the outline of the previous hardmask. b) Removed pillar structures and smoothed surface through a wet etch.

is crucial for achieving anisotropic etching profiles. In the presence of CHF_3 plasma, the fluorine radicals actively etch silicon nitride, forming volatile byproducts such as SiF_4. Simultaneously, the carbon content in CHF_3 contributes to the deposition of a thin polymer layer on the sidewalls of the features being etched, enhancing anisotropy by protecting the sidewalls from lateral etching.[218, 219] CHF_3-based RIE is especially useful in applications where high aspect ratio features and vertical sidewalls are needed. This is for example the case in hardmask patterning or passivation opening.

In all processes described in this thesis, hardmasks were patterned, and passivations were opened using CHF_3 chemistry. SF_6 chemistry was used for a short, last "cleanup" process when opening the passivation on grating structures to make sure the SiN is removed entirely from structures with smaller geometries as for example the grating slits. Another use for SF_6 etching was the removal of the remaining hardmask after the III-V deep-etch. The deposition of polymers when using CHF_3 for hardmask opening can lead to microshadowing of areas close to the etch-border at the following deep etch process.[220] This can be nicely seen in Figure 6.10. In this example, the SiN hardmask was already opened with CHF_3 RIE chemistry before realizing an error in the mask. Thus the whole hardmask was removed with SF_6 RIE chemistry and applied freshly. After a new lithography with the corrected mask geometry, the fresh hardmask was again opened with CHF_3 chemistry and the deep etch was performed. As can be seen in Figure 6.10a), the polymeric residuals of the CHF_3 etch cause microshadowing following the outline of the removed hardmask as they are not removed with it through the SF_6 plasma etch. These residuals are not

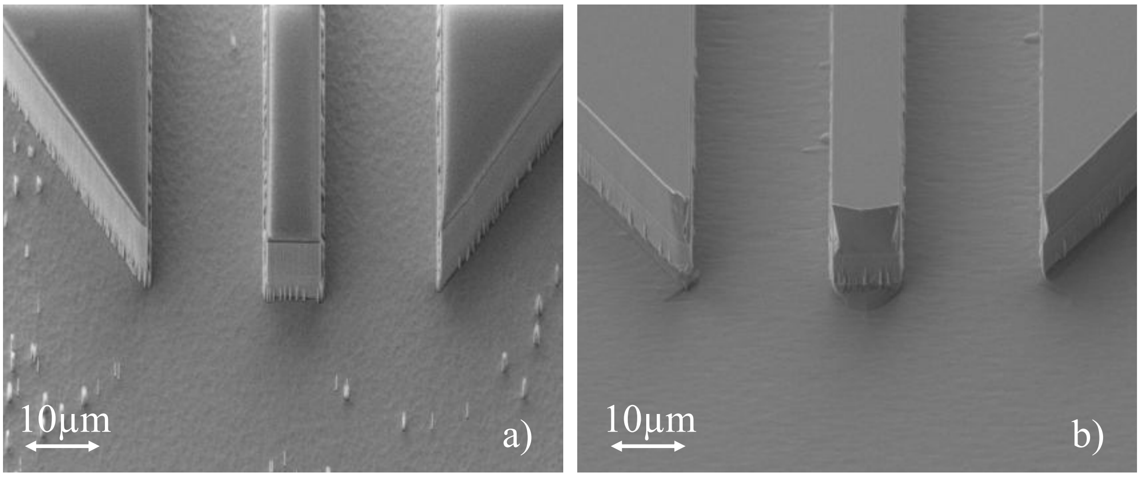

Figure 6.11: a) Pillar structures along the structures sidewalls and spread around the substrate. b) Wet-etch smoothened substrate with remaining pillar residuals at the active region of the structures.

visible in the microscope and thus are very likely to not be detected until the final deep-etch is performed. This micromasking causes pillar like structures which can limit the performance of the device. As seen in Figure 6.10b), these pillar structures can be removed with swiping the sample surface softly with a cotton swab in water followed by a $HCl:H_3PO_4:C_2H_4O_2$ (1:1:2) wet etch for 10 seconds. Figure 6.11 shows two SEM images where similar pillars are visible along the freshly deep-etched structures as well. As can be seen in subfigure a), these pillars touch the active region of the QCL material and thus might introduce roughness losses on the laser sidewall. A change of wet-etch chemistry or a two step wet-etch with chemistry that shows a higher etch rate for the active region material could solve that issue. Anyway, wet etching has to be done carefully as the etch profile is isotropic and thus also attacks the existing structures as can be seen on the sidewall profiles in Figure 6.11b). While the hardmask opening is always done with CHF_3-O_2 RIE chemistry, the behavior of microshadowing was so far only discovered at the following deep etch of QCL/QCD (InP-based) material with Cl_2-Ar RIE chemistry. The origin of this phenomenon is not fully understood yet but might be a result of the fabrication difficulties coming with the processing of InP-based optoelectronic materials. InP-based materials tend to require more energy to achieve effective ion sputtering during etching, which can result in non-uniform etching if polymeric residues from the CHF_3-O_2 step are left behind.[221] These residues can act as localized masks, leading to the formation of the needle-like artefacts observed.[222, 223] Thus, investigating the quality of hardmaks patterned with SF_6 is recommended.

Reflection measurements during RIE measurements

In situ etch depth measurements using laser reflectometry are a crucial technique during RIE processes, providing real-time feedback on the etch progress. This method involves directing a monochromatic laser beam (λ=635 nm) at the surface of the sample and monitoring the intensity of the reflected light. As the etching proceeds, the depth d of the etched layer changes, causing variations in the interference pattern of the reflected light. By analyzing the periodic oscillations in the reflectance signal, precise measurements of the etch depth can be obtained. The period of the oscillations is directly related to the etch rate and the material's refractive index n. For instance, each complete oscillation corresponds to an etch depth increment of

$$\frac{\lambda}{2n}. \tag{6.1}$$

This technique allows for continuous monitoring and immediate adjustments to the RIE parameters, ensuring consistent etch rates and precise etch depths. Of course, when etching epi structures which are basically a stack of different materials, the period lengths are difficult to refine as the refractive indices of the stacked materials are slightly different. To help the reader in interpreting different reflection patterns, some examples are given here. Reflectivity values during reflection measurements differ significantly between materials due to variations in optical properties and differences in the etch process characteristics.

Reflection pattern of SiN etching

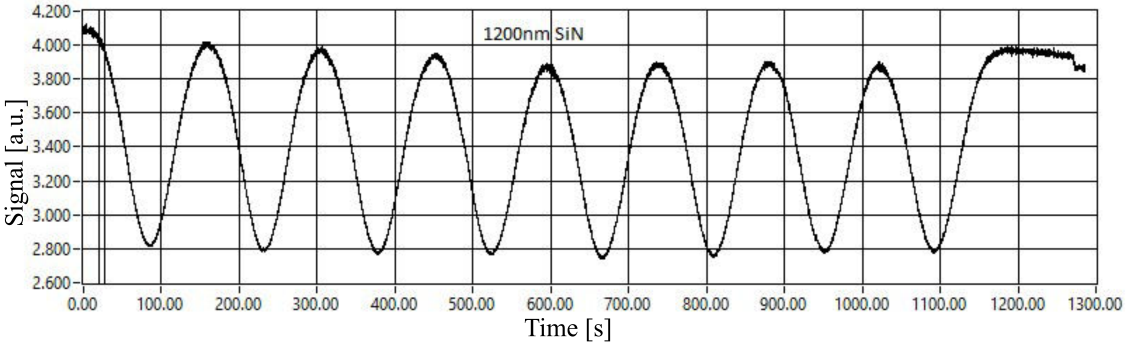

Figure 6.12: Signal of the reflexion system installed on the RIE system showing etching of 1200 nm of SiN with anisotropic CHF_3 etching. The periodicity of the signal is typical for materials transparent at the lasers wavelength.

As seen in Figure 6.12, a 1200 nm thick SiN hardmask was etched within less than 1200 s with CHF_3 RIE chemistry. The wavelength of the laser is λ=635 nm and the refractive index of SiN at that wavelength is around n=2. Following equation 6.1, one period of the reflected signal corresponds to an etch depth of 158.75 nm. The total of 8 periods thus amounts to an etch depth of 1270 nm SiN. The completed etch is visible through vanishing of the oscillation.

Reflection pattern of Ge etching

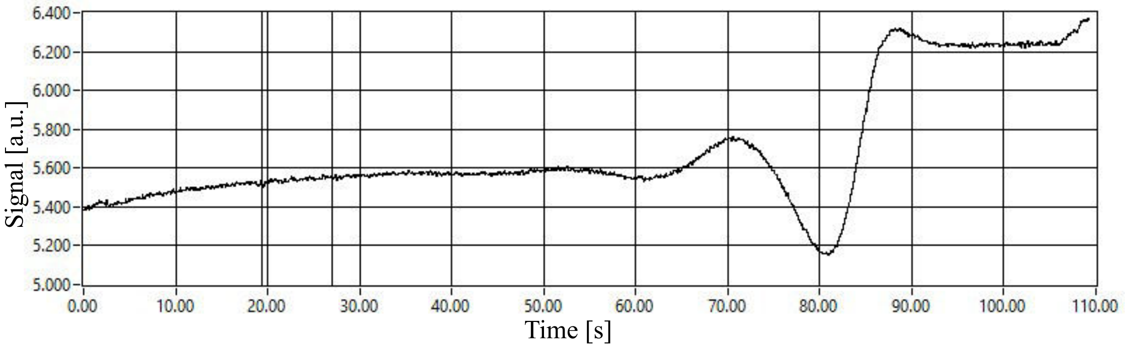

Figure 6.13: Signal of the reflection system installed on the RIE system showing etching of 300 nm of Ge with SF_6 ICP etching. As Ge is opaque at λ=635 nm, no oscillations are visible during the etch.

Germanium is opaque at the lasers wavelength, so there is no reflection from the Ge-substrate interface and thus also no interference pattern. As seen in Figure 6.13, when the germanium etch is finished, the signal intensity increases due to the higher reflectivity of the subjacent Au-layer. Here, the reflection measurement can be used to distinguish the finalization of the etching process very effectively.

Reflection pattern of ICL etching

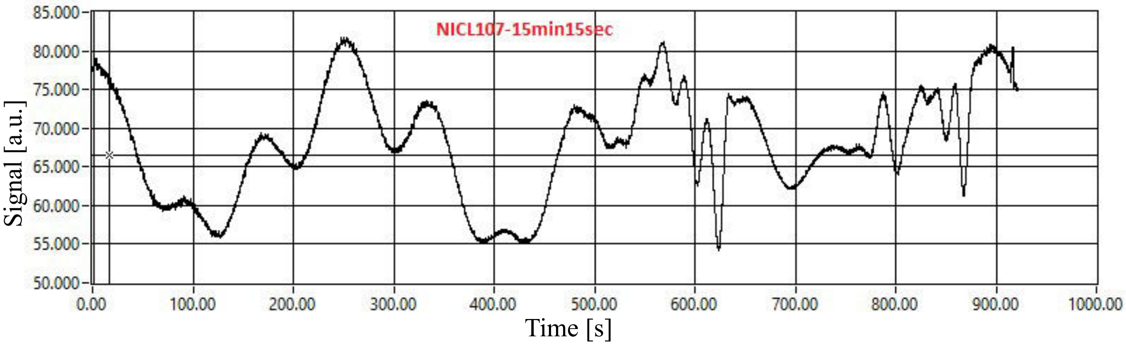

Figure 6.14: Signal of the reflection system installed on the RIE system showing etching of 3.15 µm of ICL material with Cl_2-Ar ICL RIE etching.

Figure 6.14 shows the reflection signal of an ICL deep etch with Cl_2-Ar RIE chemistry. For multilayer structures, such as those in ICLs with alternating layers of

InAs, GaInSb, and other materials, the reflectance signal will be a complex superposition of oscillations corresponding to each layer. Advanced signal processing techniques may be required to resolve the signal and accurately determine the layer structure. Thus, the etch rate and depth is more difficult to supervise but desired etch processes can be reproduced through monitoring of the signal.

Reflection pattern of QCL etching

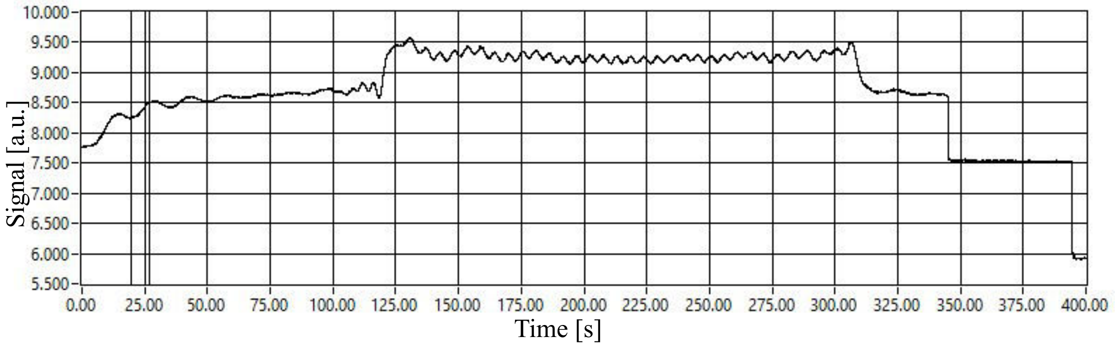

Figure 6.15: Signal of the reflexion system installed on the RIE system showing etching of 7.6 µm of QCL material with Cl_2-Ar InGaAs/InAlAs RIE etching.

Similar to the reflection signal in ICLs, the multilayer structures in QCL/QCDs create a superposition of reflections from multiple layers involved and thus is not easy to decode without additional software. Figure 6.15 shows a typical representation of a laser reflection signal of a QCL etch. The signal between the ordinate values 125 and 300 correspond to the etching of the active region.

6.4.4 Deposition methods of SiN

SiN is a versatile material widely used in semiconductor processing due to its excellent dielectric properties, high thermal stability, and chemical resistance. It serves as an effective insulating layer, masking material, and passivation layer in microfabrication processes. PECVD involves the decomposition of precursor gases in a plasma, which enhances the reaction rates at lower temperatures compared to traditional CVD processes. SiN deposition can be achieved using either NH_3-based or NH_3-free chemistries. In NH_3-based PECVD, silane (SiH_4) and ammonia (NH_3) are commonly used as precursor gases, resulting in high-quality SiN films. Alternatively, NH_3-free PECVD processes utilize SiH_4 and nitrogen (N_2) or nitrous oxide (N_2O) as precursors, providing a viable option for applications sensitive to hydrogen incorporation by reducing the amount of N-H bonds. Thus, for isolation or passivation deposition it is recommended to use the NH_3 free process. As can be

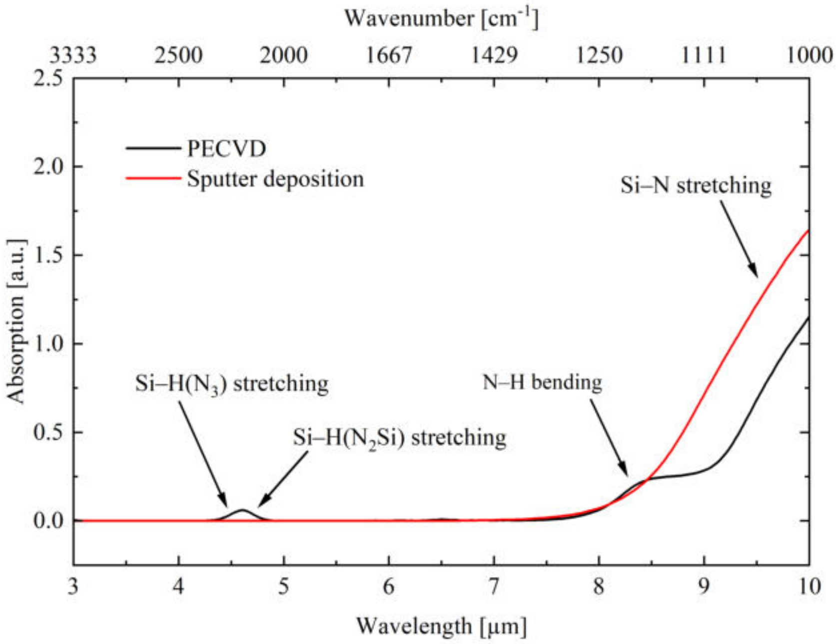

Figure 6.16: MIR absorption spectra of PECVD SiN (black) and reactive sputtered SiN (red) with distinctive absorption features, measured with ellipsometry. Data provided by S. Isceri.

seen in Figure 6.16, in any case, existing Si-H bonds will create an absorption peak around wavelengths of λ =4.5 µm.[224] This has to be taken into account during process planning. If the desired wavelength covers this region, reactive sputtering of Si in nitrogen atmosphere, which does not include hydrogen, is recommended. At longer wavelengths, the nitrogen based N-H bending and Si-N stretching absorption features begin to dominate the absorption spectra. Figure 6.16 shows that for wavelengths longer than approximately 8.5 µm, the reactive sputtered SiN shows higher absorption compared to the PECVD SiN, probably caused by a surplus of nitrogen during the deposition. These findings are in accordance to the finding of Frigg et al.[225] All SiN layers used in fabrication of devices described in this thesis were deposited using PECVD techniques as the hydrogen free sputter process was not developed fully yet.

6.4.5 Deposition of metals

The deposition of metals on the sample surface is one of the main processing steps during the fabrication of optoelectronic devices. Different metals can cover multiple usecases on optoelectronic devices from contacts with adhesion layers and diffusion barriers over waveguides to plasmonic transport layers and reflection planes. In this thesis, top contacts were made using titanium as the adhesion layer, an optional platinum layer as a diffusion barrier (necessary when fabricating ICL devices) and gold as the contact itself. Bottom contacts of low doped GaSb substrates were realized through a Ge-Au-Ni-Au deposition scheme to achieve ohmic contacts.[226, 227, 228] Bottom contacts on InP substrates (QCL, QCD) were realized through a standard Ti-Au contact. Sputter deposition and evaporation are each offering unique advantages for thin-film deposition. Sputter deposition involves bombarding a metal target with high-energy ions in a plasma, causing atoms from the target to be ejected and deposited onto a substrate. This method allows for precise control over film thickness and uniformity, making it ideal for depositing a wide range of materials from ceramics to metals. Through the high energetic plasma, the sputtered material reaches higher binding energies, resulting in better interlayer bonds and higher adhesion to the substrate compared to evaporation methods. Additionally, through the higher process pressure compared to evaporation, the molecules to be deposited also carry a moment perpendicular to the direction of the applied electric field. Thus effective sidewall coverage can be achieved without tilting and spinning the sample. Top contacts of laser waveguides serve not only to establish an electrical connection but also to dissipate the heat generated during device operation. Effective heat dissipation can be achieved by thoroughly covering the sidewalls of the ridges with metal.

Sputter target cleaning

Sputter target cleaning is an essential step to ensure proper deposition of the desired material onto the sample. Despite evacuating the sputter chamber to high vacuum, each sample transfer introduces oxygen atoms into the chamber. Most metals, except noble metals, tend to react with oxygen, forming thin oxide layers on the target surface. With every transfer, this oxide layer grows. If sputtering begins without prior cleaning, the oxide layer is deposited onto the sample, altering its expected electrical, thermal, and mechanical properties. Therefore, sputtering onto an empty target to remove the oxide layer before actual deposition is crucial, as neglecting this step can compromise the entire sample. On the other hand, evaporation involves heating a metal source in a high-vacuum environment until it vaporizes, with the vapor then condensing onto the substrate to form a thin film. This technique is often favored for its simplicity and ability to deposit high-purity films as the chamber is evacuated and no plasma is used. As the target materials are stored in carbon crucibles, deposited layers may exhibit minimal carbon contamination which can be disadvantageous for certain applications. Another property of evaporation is the high anisotropy of the method. As the chamber is under high vacuum ($\sim 10^{-7}$ mbar), the mean free path of molecules is in the range of hundreds of meters. The distance between the metal target and the sample approximately accounts to max. 50 cm, thus no collisions between metal vapor molecules and residual gas molecules are occurring. This leads to a nearly perfectly unidirectional deposition which is advantageous if for example deposition on the structure sidewalls should be avoided (e.g. on-chip laser/detector facets).

6.4.6 Electroplating of Au

Improper resist use and underplating

When the resist does not function properly, gaps or imperfections in the resist pattern enable plating ions to reach unintended areas, causing unwanted material buildup beneath or around the edges of the resist. This can result in non-uniform electroplating, with the material spreading into regions meant to remain unplated. To avoid underplating, it is essential to ensure high-quality resist application, proper curing, and sufficient resist thickness, as well as optimizing process conditions such as the electrolyte solution and plating parameters. Underplating occurred when using nLof2070 negative resist. Thus, this resist should not be used for electroplating lithographies. Figure 6.17 shows a mirror combiner structure after electroplating. In the red circles, Au deposits are visible. These areas were covered with nLof2070 resist during the electroplating process. Although the deposition rate in these regions is low, even small deposits can potentially short-circuit the uncovered laser facets. As a result, this device failed to function properly

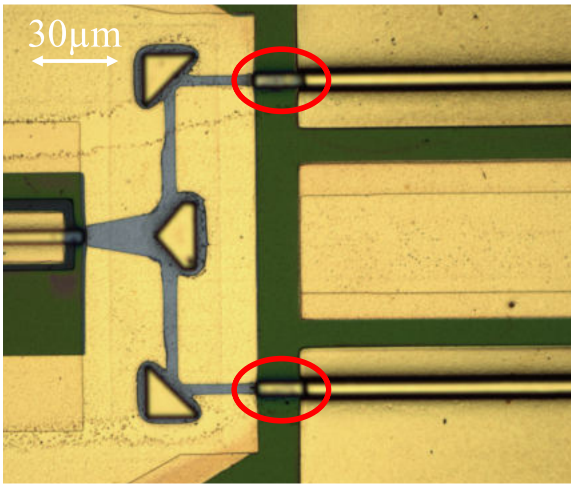

Figure 6.17: Gold deposition on areas that were covered with nLof2070 resist during electroplating (red circles).

Nonuniform deposition rates

While electroplating provides advantages such as high deposition rates and efficient resource use compared to e.g. thermal evaporation, achieving uniform deposition across devices can be challenging. One common issue is thickness non-uniformity, especially when devices exhibit varying electrical resistances, leading to different deposition rates across the substrate. This results in inconsistent deposition thickness and thus difficulties in further fabrication steps. A solution to this problem involves short-circuiting the devices by sputtering a thin Au layer, ensuring uniform current distribution and deposition rates during electroplating. This thin Au layer has to be removed after the electroplating. Figure 6.18 shows two makro-images of 1×1 cm samples where a) shows a sample with varying deposition thicknesses as the single devices were not on the same potential. b) shows a different sample after electroplating where the single ring-devices were kept on the same potential through a ~50 nm Au layer, deposited through sputtering. This layer can then be removed through a short KI/I_2 Au-etch dip.

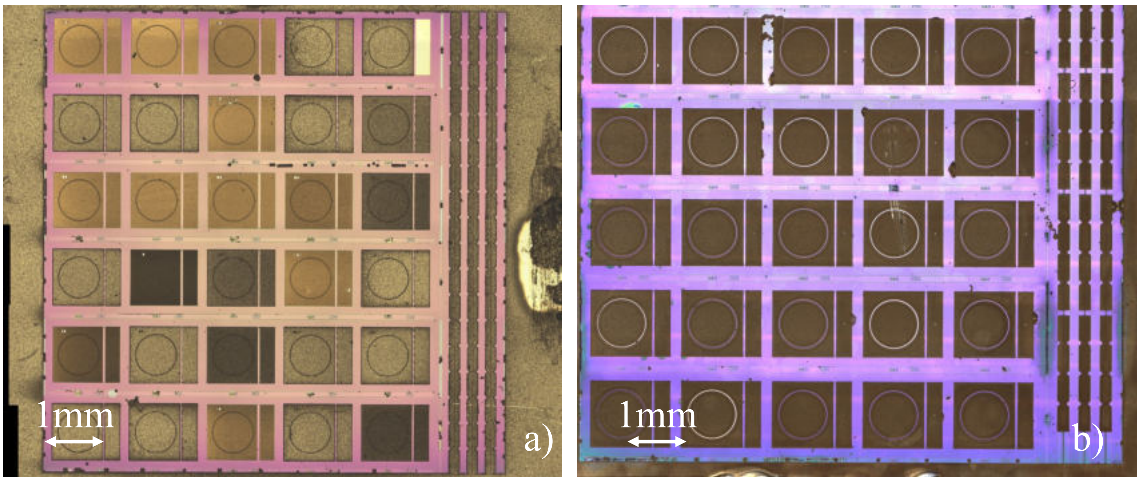

Figure 6.18: a) Different deposited thicknesses dependent on the resistance of the single devices. b) Uniformly deposited thickness after the single devices were shortcircuited with a thin Au-layer

Edge effects

Another significant challenge in Au electroplating is the "edge effect," where thicker layers accumulate at the edges of features, such as bonding pads. This non-uniform deposition can cause bonding surfaces to become uneven, making it difficult to achieve proper bonding between components. Addressing these edge effects requires careful control of the electroplating parameters or post-processing to ensure flat and

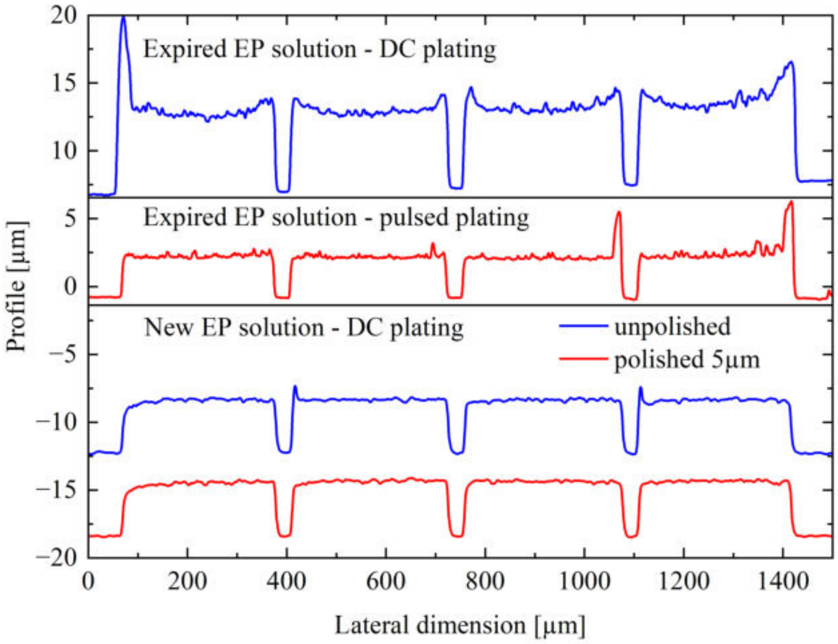

Figure 6.19: Comparison between different electroplating methods. Top: DC-plating with expired Au solution, Middle: AC-plating with expired Au solution, Bottom: DC-plating with fresh Au solution unpolished (blue) and polished (red)

consistent surfaces. Figure 6.19 presents the profiles of four electroplated submounts used for ring ICLs, as referenced in the publication in chapter 4. The quality of the electroplated layers appears to degrade with the aging of the electroplating solution. The top profile illustrates the deposition on four pads using an expired solution. Significant lateral edge effects are visible, extending nearly across the entire width of the pads, resulting in a bowl-shaped surface. Such a profile is unsuitable for bonding ring laser structures. In an attempt to improve the uniformity, AC-electroplating was tested, yielding generally more even profiles but exacerbating the edge spikes, as seen in the central profile.[229] However, these results were still inadequate for bonding. The experiment was then repeated using new electroplating solution, as shown in the two bottom profiles. DC-electroplating with fresh electrolyte produced smooth, even surfaces, with only minor edge spikes (blue line). To eliminate these residual spikes, the sample was manually polished using a 5 µm grit polishing paper, gently passing it over the paper—fixed on a glass plate for surface uniformity—two or three times. While other technologies taking use of planarizing the surface by diamond fly-cutting might provide better results,[230] the efficacy of our simple approach is also visible in Figure 6.20, where microscope pictures show the differences of the surface before and after the polishing.

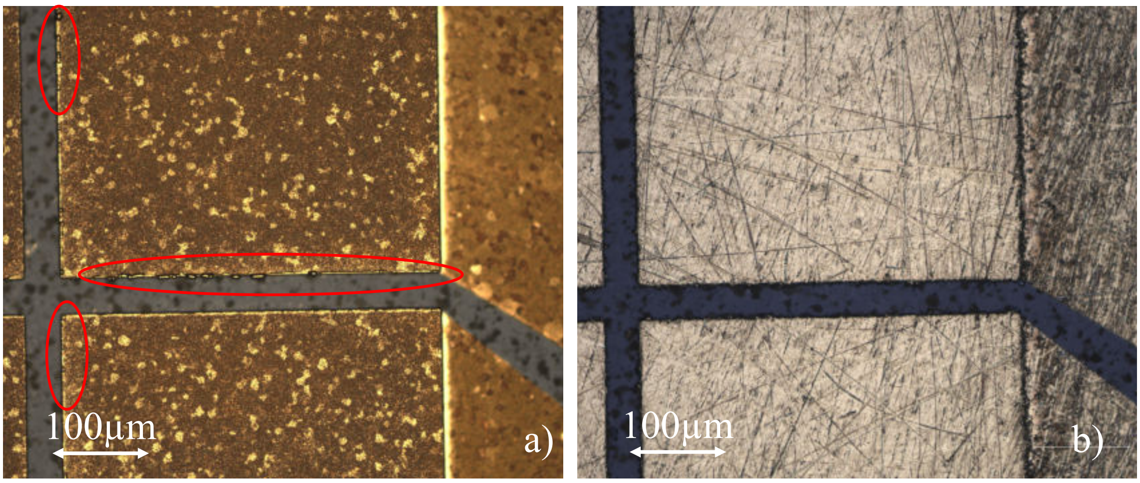

Figure 6.20: a) Edge spikes visible in the red marked areas before polishing. b) Sample after polishing with a 5 µm grit paper shows an even surface

APPENDIX A

APPENDIX

A.1 Fabrication Standard Recipes

A.1.1 Optical lithography Processes

The following list gives some standard parameters of resists used for processing in this thesis. If parameters were changed, the explicit numbers are given in the detailed description of the process. Keep in mind that the Standard Recipes only give a solid starting point, adjustments might have to be done at each processing step. The precise control of baking and exposure parameters is essential in achieving the desired patterns and features in photolithographic processes. Depending on the desired outcome, adjustments of the standard parameters are necessary. If for example the resist has to be removed from deep trenches, the exposure (time or dose) and/or development time might necessarily be larger compared to lithographic processes done on plane samples. Depending on the available structures, their size and heights, different resists can be used. Thicker resists allow proper vertical structure coverage while thinner resists are usually processed faster and allow smaller feature sizes. Some basic rules have to be applied when handling photoresists:

- Only open PR containers on the chemical bench with activated fume exhaust
- Store PRs according to the manufacturers declarations
- To inhibit water absorption, only open PR containers when they are at room temperature
- Only use fresh pipettes to dosage PR

- If PRs are expired, replace them with new ones as quality and reproducability are not given anymore

Substrate cleaning

Substrate cleaning shall be done before every lithography step in order to remove residuals and water from the sample surface. If the sample is not processed directly after cleaning, it can be stored on a hotplate at elevated temperatures to inhibit water adsorption.

- *Flush sample in Acetone for 15 s*
  - *If the sample is contaminated with residuals from cleaving, ultrasonic support with low power might be helpful*
- *Flush sample in Isopropanole for 15 s*
- *Blowdry sample with* N_2

Adhesion promotion with Ti-prime

The use of an adhesion promoter like Ti-prime is suggested if improper resist adhesion is observed. In most cases, there is no need for this step. Through experience it can be said that the outcome of lithographies may be influenced by air humidity, temperature, resist age and personal stress levels among others and sometimes adhesion promoters may offer a helpful possibility to tackle this.

- *Spinning 35 s @ 3000 rpm*
- *Soft Bake 90 s @ 120 °C*
- *Cool down sample to room temperature and continue with resist spinning immediately*

AZ5214JP Positive Process, Laserwriter, Recipe 1

- *Spinning 35 s @ 6000 rpm (thickness* $\sim 1.1\,\mu m$*)*
- *Soft Bake 60 s @ 100 °C*
- *Exposure with Heidelberg MLA* $140\,mJ/cm^2$*, defoc 0*
- *15 s development in* $AZ351B : H_2O$ *(1:4)*
- *15 s development stopping in* H_2O

AZ5214JP Positive Process, Laserwriter, Recipe 2, reduced speed

This recipe was developed by J. Fuchsberger and not tested in processes in this thesis. Through the reduced writing speed it shows improved reproducibility and high quality results even at very small feature sizes of around 1 µm.

- *Spinning 35 s @ 6000 rpm (thickness* $\sim$ *1.1 µm)*
- *Soft Bake 60 s @ 100 °C*
- *Exposure with Heidelberg MLA 300 mJ/cm*^{2}*, with reduced writing speed (10 mm/s), defoc 0*
- *15 s development in AZ351B :* H_2O *(1:4)*
- *15 s development stopping in* H_2O

AZ5214JP Image Reversal Process, Mask aligner, Recipe 1

- *Spinning 35 s @ 4500 rpm (thickness* $\sim$ *1.4 µm)*
- *Soft Bake 90 s @ 100 °C*
- *Edge removal exposure 15 s*
- *40 s development in AZ351B :* H_2O *(1:4)*
- *Structure exposure 0.7 s*
- *Hard Bake 60 s @ 120 °C*
- *Flood Exposure 12 s*
- *28-30 s development in AZ351B :* H_2O *(1:4)*
- *15 s development stopping in* H_2O

TI35 positive process, Mask aligner

- *Spinning 35 s @ 3000 rpm (thickness* $\sim$ *4 µm)*
- *Soft Bake 120 s @ 100 °C*
- *Edge removal exposure 2 x 60 s with 30 s break in between*
- *180 s development in AZ351B :* H_2O *(1:4)*
- *Structure exposure 40 s*
- *Wait 10 min for* N_2 *diffusion*
- *1 min development in AZ351B :* H_2O *(1:4)*
- *15 s development stopping in* H_2O

TI35 Image Reversal process, Mask aligner

- *Spinning 35 s @ 3000 rpm (thickness* $\sim$ *4 µm)*
- *Soft Bake 120 s @ 100 °C*
- *Edge removal exposure 2 x 60 s with 30 s break in between*
- *180 s development in AZ351B :* H_2O *(1:4)*
- *Structure exposure 3 s*
- *Wait 10 min for* N_2 *diffusion*

- *Cross Bake 120 s @ 120 °C*
- *Flood Exposure 70 s*
- *4-6 min development in AZ351B : H_2O (1:4)*
- *15 s development stopping in H_2O*

TI35 Image Reversal process, Laser Writer

- *Spinning 35 s @ 3000 rpm (thickness ∼ 4 µm)*
- *Soft Bake 120 s @ 100 °C*
- *Structure exposure with Heidelberg MLA 200 mJ/cm^2*
- *Wait 10 min for N_2 diffusion*
- *Cross Bake 120 s @ 120 °C*
- *Flood Exposure 70 s with mask aligner*
- *4-6 min development in AZ351B : H_2O (1:4)*
- *15 s development stopping in H_2O*

If after the development process resist residuals are still visible, the sample can be treated with oxygen plasma for 10 minutes with a power of 600 W.

MaP1275 Positive Resist, Mask aligner

- *Spinning 35 s @ 8000 rpm (thickness ∼ 6 µm)*
- *Soft Bake 300 s @ 100 °C*
- *Edge removal exposure 50 s*
- *30 s development in maD333*
- *Structure exposure 10 s*
- *6 s development in maD333*
- *15 s development stopping in H_2O*

MaP1275 Positive Resist, Laserwriter

- *Spinning 35 s @ 8000 rpm (thickness ∼ 6 µm)*
- *Soft Bake 300 s @ 100 °C*
- *Structure exposure with Heidelberg MLA 350 mJ/cm^2*
- *12 s development in maD333*
- *15 s development stopping in H_2O*

nLof2070 Negative Resist, Laserwriter

- *Spinning 35 s @ 8000 rpm (thickness ∼ 3 µm)*

- *Soft Bake 180 s @ 100 °C*
- *Structure exposure with Heidelberg MLA 300 mJ/cm*^{2}
- *Post Exposure Bake 65 s @ 110 °C*
- *90 s development in AZ726MIF*
- *15 s development stopping in* H_2O

Attention: nLof2070 is a resist that is not soluble in acetone after crosslinking. For lift-off processes and resist removal after crosslinking the remover mR-Rem700 has to be used. Best results were achieved when the remover was heated to 70 °C.

Resist Removal

Resist removal is an important step before conducting deep etch processes through reactive ion etching. Through the high process temperatures during the chlorine-based processes, the resist might start to evaporate and create micro-masking defects trough redeposition on the sample. The high temperatures are similar to a long hard-bake making subsequent resist removal extremely challenging.

- *5-10 minutes* O_2 *plasma ashing @ 600 W*
- *Flush sample in Acetone for 15 s (use mR-Rem700 @ 70 °C in case of nLof2070 resist)*
- *Flush sample in Isopropanole for 15 s*
- *Blowdry sample with* N_2

A.1.2 Electron beam lithography Processes

The following process description is valid for e-beam exposure with the Raith e-Line system at ZMNS. During writing of this thesis, a modern high performance e-beam lithography system (Raith Voyager) has been installed in the cleanroom facilities and the reader is encouraged to take use of this upgrade. Operating an e-beam lithography system requires good knowledge of a variety of system parameters and functions and this process description should only give a rough overview of the tasks involved.

AR-P 672.08 e-beam lithography

- *Spinning 35 s @ 4000 rpm*
- *Soft Bake min. 300 s @ 170 °C*
- *Load sample and reset coordinate system*
- *Column settings: 10 kV, aperture 30 µm, working distance 8 mm*

- *Measure beam current at Faraday Cup and calculate beam speeds to achieve the following dose values*
  - *Area dose: 133 μC/cm^2*
  - *Curved elements dose: 133 μC/cm^2*
  - *Line dose: 330 μC/cm*
  - *Dot dose: 0.143 μC*
- *Perform Aperture alignment and correct stigmator field of SEM*
- *Set origin and coordinate system on the sample (use predefined markers created during the deep-etch) and adjust the working distance at the 3-point alignment to create a virtual layer compensating the sample tilt*
- *Perform writefield alignment at a known marker-position (use a writefield size that adequatly fits the design size)*
- *Check if auto-marker alignment works properly (linescan)*
- *Exposure*
- *Unload sample*
- *20 s development in AR 600-55*
- *30 s development stopping in Isopropanole*

A.1.3 Plasma Enhanced Chemical Vapor Deposition (PECVD) of Silicon Nitride (SiN)

NH_3-free PECVD of SiN

- *Chamber Pressure: 600 mtorr*
- *Chamber Temperature: 280 °C*
- *SiH_4 flow: 80 sccm*
- *N_2 flow: 900 sccm*
- *CVD Power: 40 W*
- *Deposition Rate: 12.5 nm/min*

NH_3-based PECVD of SiN

- *Chamber Pressure: 600 mtorr*
- *Chamber Temperature: 280 °C*
- *SiH_4 flow: 875 sccm*
- *NH_3 flow: 20 sccm*
- *N_2 flow: 500 sccm*
- *CVD Power: 20 W*

- *Deposition Rate: 9.3 nm/min*

Reactive Sputtering of SiN

- *Chamber Pressure: 8e-3 mbar*
- *Si-Target Clean: 1 x 120 s @ 100 W*
- *N_2 flow: 10 sccm*
- *Ar flow: 30 sccm*
- *Deposition Rate: 0.129 nm/s @ 100 W*
- *Deposition Rate: 0.298 nm/s @ 200 W*

The deposition rates of the sputter process were measured as sputtered on a glass substrate with a Filmetrics thickness measurement system.

A.1.4 Reactive Ion Etching (RIE) of SiN, Ge and III-V Semiconductors

The following standard recipes for SiN etching are optimized for a Oxford PlasmaPro Cobra 180 RIE system. The name corresponds to the process name stored in the system at ZMNS.

Isotropic SF_6 etching of SiN (Name: SiN SF6 etch)

This process can also be used to etch TiO_2 with an etch rate of approximately 20 nm/min.

- *Chamber Pressure: 15 mTorr*
- *HF Power: 60 W*
- *ICP Power: 0 W*
- *SF_6 flow: 40 sccm*
- *Helium backing: 10 Torr*
- *Chamber Temperature: 20 °C*
- *Etch rate: 230 nm/min*
- *Carrier wafer: Soda Lime*

Anisotropic CHF_3 etching of SiN (Name: SiN RIE mode)

- *Chamber Pressure: 55 mTorr*
- *HF Power: 150 W*
- *ICP Power: 0 W*

- *CHF_3 flow: 50 sccm*
- *O_2 flow: 5 sccm*
- *Helium backing: 10 Torr*
- *Chamber Temperature: 20 °C*
- *Etch rate: 80 nm/min*
- *Carrier wafer: Si CHF_3*

SF_6-ICP etching of Germanium (Name: Ge-SF6 ICP etching Georg)

SF_6 Etching of Germanium was used to pattern waveguides. The fluorine radicals react with the germanium surface, forming volatile compounds like germanium fluoride (GeF_4), effectively etching the material. For waveguide fabrication sidewalls of high quality are necessary, which can be achieved through a ICP coupled plasma etch.[231]

- *Chamber Pressure: 10 mTorr*
- *HF Power: 100 W*
- *ICP Power: 100 W*
- *SF_6 flow: 10 sccm*
- *Helium backing: 10 Torr*
- *Chamber Temperature: 20 °C*
- *Etch rate: 300 nm/min*
- *Carrier wafer: Si*

All III-V semiconductor etches were conducted with Cl_2-Ar chemistry. The chlorine species react with the III-V material to form volatile chloride compounds, while the ion bombardment aids in removing these compounds from the surface.

Cl_2-Ar etch of InAs/AlSb/GaSb epistructures (ICL) (Name: ICL Cl2-Ar)

- *Chamber Pressure: 2 mTorr*
- *HF Power: 125 W*
- *ICP Power: 300 W*
- *Cl_2 flow: 1 sccm*
- *Ar flow: 24 sccm*
- *Helium backing: 10 Torr*
- *Chamber Temperature: 200 °C*
- *Etch rate: 210-230 nm/min*
- *Selectivity to SiN: 6:1*
- *Carrier wafer: Si-Cl_2*

Cl_2-Ar etch of InGaAs/InAlAs epistructures (QCL, QCD) (Name: InGaAs/InAlAs Cl2-Ar etch)

- *Chamber Pressure: 2 mTorr*
- *HF Power: 140 W*
- *ICP Power: 250 W*
- *Cl_2 flow: 4 sccm*
- *Ar flow: 18 sccm*
- *Helium backing: 10 Torr*
- *Chamber Temperature: 175 °C*
- *Etch rate: 1000-1200 nm/min*
- *Selectivity to SiN: 12:1*
- *Carrier wafer: Si-Cl_2*

A.1.5 Wet etch recipes

Handling acids and bases, used to etch semiconductor materials or metals, always requires full attention and safety precautions. Always wear adequate safety equipment like gloves, aprons and safety glasses. The preparation of the etchants and the handling of acids and bases must happen below an appropriate fume hood. Next to the desired etching solutions, which are prepared in adequate beakers of glass or plastic, always prepare two glasses filled with deionized water to rinse the sample after the wet-etch. Furthermore, paper wipes should be prepared to dry the sample.

Smoothing of ICL sidewalls

Different chemistries have been used to smoothen the sidewalls of ICL material after the RIE deep-etch. The effectivity of the approach still has to be experimentally proven, anyway sidewall profiles look better in the SEM after a wet-etch smoothening. Good results have been achieved in using only hydrochloric acid (HCl) for 15 s. Another way to smoothen the GaSb based material strucures is the following recipe. A mix of

- *0.1 g citric acid ($C_6H_8O_7$) in powder form dissolved in 10 ml H_2O*
- *0.67 g orthophosphoric acid (H_3PO_4)*
- *0.79 g hydrogen peroxide (H_2O_2)*

is prepared and used at a temperature of 30°C. The etch rate is approximately 80 nm/min.

Smoothening of QCL structures

To smoothen often ocurring "pillar-like" structures after the Cl−2-Ar RIE deep etch, a mixture of

- *1 part hydrochloric acid (HCl)*
- *1 part orthophosphoric acid* (H_3PO_4)
- *2 parts acetic acid* ($C_2H_4O_2$)

can be used. Etching times of 10 s should already visibly smoothen the surface. It is advised to supervise the etch progress with help of the SEM.

Wet etching of Au

Au layers were wet-etched with a commercially available, pre-mixed potassium iodide-iodine (KI-I_2) etchant. The etch rate of Au is at around 10 nm/s. As KI-I_2 also etches semiconductors like GaSb, sensitive areas of the semiconductor have to be covered by resist or SiN before the wet-etch.

A.1.6 Deposition of metals through sputtering and evaporation processes

Here the program names, powers and times are given. The program names are as they are implemented in the ZMNS Creavac Sputter System. The used sample holder was always water cooled (WC). If a photoresist structure is used to mask the sample, its advised to adjust the sputter time in multiples of 30 s to avoid extensive heating of the resist.

Top contact sputtering of Ti-Au

- *003-Vent Pump Loadlock - load sample*
- *004-Move Load to WC*
- *121-Etch Ti Au WC*
    - *Substrate Clean: 1 x 60 s @ 50 W*
    - *Ti-Target Clean: 1 x 60 s @ 100 W*
    - *Depostit ~ 10 nm Ti adhesion layer: 0.08 nm/s @ 30 W*
    - *Depostit ~ 300 nm Au contact: 0.55 nm/s @ 30 W*
- *005-Move WC to Load*
- *003-Vent Pump Loadlock - unload sample*

Top contact sputtering of Ti-Pt-Au (ICL processes)

- *003-Vent Pump Loadlock - load sample*
- *004-Move Load to WC*
- *160-Etch TiPtAu WC-holder*
    - *Substrate Clean: 1 x 60 s @ 50 W*
    - *Ti-Target Clean: 1 x 60 s @ 100 W*
    - *Depostit ∼ 10 nm Ti adhesion layer: 0.08 nm/s @ 30 W*
    - *Depostit ∼ 100 nm Pt diffusion barrier: 0.14 nm/s @ 30 W*
    - *Depostit ∼ 300 nm Au contact: 0.55 nm/s @ 30 W*
- *005-Move WC to Load*
- *003-Vent Pump Loadlock - unload sample*

Bottom contact sputtering of Ge-Au-Ni-Au for ohmic contacts on low doped GaSb substrates

The exact contact resistance of the deposited contact structure given here was never thoroughly evaluated during measurements in this thesis. The contact layer structure definitely works as such but might be improved by implementation of slightly different deposition routines as suggested in existing literature.[226, 227, 228]

- *003-Vent Pump Loadlock - load sample*
- *004-Move Load to WC*
- *161-Etch GeAuNiAu WC-holder*
    - *Substrate Clean: 1 x 60 s @ 50 W*
    - *Ge-Target Clean: 1 x 60 s @ 100 W*
    - *Depostit ∼ 15 nm Ge layer: 0.44 nm/s @ 30 W*
    - *Depostit ∼ 30 nm Au layer: 0.55 nm/s @ 30 W*
    - *Ni-Target Clean: 1 x 120 s @ 100 W*
    - *Depostit ∼ 15 nm Ni layer: 0.33 nm/s @ 60 W*
    - *Depostit ∼ 200 nm Au contact: 0.55 nm/s @ 30 W*
- *005-Move WC to Load*
- *003-Vent Pump Loadlock - unload sample*

Sputtering of Ge-layers

Ge is transparent in the MIR region up to wavelengths of around 10 µm and can be used for effective mode or plasmon confinement through its high refractive index.

- *003-Vent Pump Loadlock - load sample*
- *004-Move Load to WC*
- *162-Etch Ge WC-holder*
  - *Substrate Clean: 1 x 60 s @ 50 W*
  - *Ge-Target Clean: 1 x 60 s @ 100 W*
  - *Depostit $\sim$ 300 nm Ge layer: 0.44 nm/s @ 30 W*
- *005-Move WC to Load*
- *003-Vent Pump Loadlock - unload sample*

Evaporation of metal layers

Evaporation was conducted with a Plassys Evaporation system. Before the deposition of the first layer, the sample was etched with Ar-plasma with the included plasma gun.

- *Sample clean plasma etch explain*
  - *Shut down RGA and safe the recorded data*
  - *Shut down electron multiplier*
  - *Shut down filament*
  - *Disconnect COM6*
  - *Substrate holder tilt: Etch*
  - *Run Process: WS 2023 etch 6 mA 200 V*
  - *Etch rate: 0.5 nm/min for* SiO_2
- *Ti: Current 42 mA, deposition rate: 0.05 nm/s*
- *Pt: Current 55 mA, deposition rate: 0.1 nm/*
- *Au: Current 160 mA, deposition rate: 0.05 nm/*

The deposition of thick ($\sim$ 100 nm) Pt layers is not recommended as the high current comined with the low deposition rates can lead to substantial heating of the cryopump and worsening of the chamber pressure.

BIBLIOGRAPHY

[1] Z. Yang, T. Albrow-Owen, W. Cai, and T. Hasan, “Miniaturization of optical spectrometers,” *Science*, vol. 371, no. 6528, p. eabe0722, 2021. – cited on page 1.

[2] A. Delga, “Quantum cascade detectors: A review,” *Mid-infrared Optoelectronics*, pp. 337–377, 2020. – cited on pages 1 and 21.

[3] L. Gendron, M. Carras, A. Huynh, V. Ortiz, C. Koeniguer, and V. Berger, “Quantum cascade photodetector,” *Applied Physics Letters*, vol. 85, no. 14, pp. 2824–2826, 2004. – cited on page 2.

[4] S. Chakravarty, J. Midkiff, K. Yoo, A. Rostamian, and R. T. Chen, “Monolithic integration of quantum cascade laser, quantum cascade detector, and subwavelength waveguides for mid-infrared integrated gas sensing,” in *Quantum Sensing and Nano Electronics and Photonics XVI*, vol. 10926, pp. 204–211, SPIE, 2019. – cited on page 2.

[5] B. Schwarz, P. Reininger, D. Ristanić, H. Detz, A. M. Andrews, W. Schrenk, and G. Strasser, “Monolithically integrated mid-infrared lab-on-a-chip using plasmonics and quantum cascade structures,” *Nature Communications*, vol. 5, no. 1, p. 4085, 2014. – cited on pages 2, 34, and 47.

[6] A. Spott, J. Peters, M. L. Davenport, E. J. Stanton, C. D. Merritt, W. W. Bewley, I. Vurgaftman, C. S. Kim, J. R. Meyer, J. Kirch, *et al.*, “Quantum cascade laser on silicon,” *Optica*, vol. 3, no. 5, pp. 545–551, 2016. – cited on page 2.

[7] A. Hangauer, J. Chen, R. Strzoda, M. Ortsiefer, and M.-C. Amann, “Wavelength modulation spectroscopy with a widely tunable InP-based 2.3 µm

vertical-cavity surface-emitting laser," *Optics Letters*, vol. 33, no. 14, pp. 1566–1568, 2008. – cited on page 2.

[8] A. Einstein, "Über einen die Erzeugung und Verwandlung des Lichtes betreffenden heuristischen Gesichtspunkt," *Annalen der Physik*, vol. 322, no. 6, pp. 132–148, 1905. – cited on page 3.

[9] W. Herschel, "Xiv. Experiments on the refrangibility of the invisible rays of the sun," *Philosophical Transactions of the Royal Society of London*, no. 90, pp. 284–292, 1800. – cited on page 3.

[10] D. R. Lide, *CRC handbook of chemistry and physics*, vol. 85. CRC press, 2004. – cited on page 3.

[11] A. Krier, *Mid-infrared semiconductor optoelectronics*, vol. 118. Springer, 2007. – cited on page 4.

[12] C. R. Petersen, U. Møller, I. Kubat, B. Zhou, S. Dupont, J. Ramsay, T. Benson, S. Sujecki, N. Abdel-Moneim, Z. Tang, *et al.*, "Mid-infrared supercontinuum covering the 1.4–13.3 µm molecular fingerprint region using ultra-high NA chalcogenide step-index fibre," *Nature Photonics*, vol. 8, no. 11, pp. 830–834, 2014. – cited on page 4.

[13] B. H. Stuart, *Infrared spectroscopy: fundamentals and applications.* John Wiley & Sons, 2004. – cited on page 4.

[14] L. Flannigan, L. Yoell, and C.-Q. Xu, "Mid-wave and long-wave infrared transmitters and detectors for optical satellite communications—a review," *Journal of Optics*, vol. 24, p. 043002, mar 2022. – cited on pages 4 and 30.

[15] I. E. Gordon *et al.*, "The HITRAN2020 molecular spectroscopic database," vol. 277, p. 107949, Jan. 2022. – cited on page 5.

[16] A. Sommerfeld, "Zur Elektronentheorie der Metalle auf Grund der Fermischen Statistik: I. Teil: Allgemeines, Strömungs-und Austrittsvorgänge," *Zeitschrift für Physik*, vol. 47, pp. 1–32, 1928. – cited on page 4.

[17] P. Drude, "Zur Elektronentheorie der Metalle," *Annalen der Physik*, vol. 306, no. 3, pp. 566–613, 1900. – cited on page 5.

[18] E. Schrödinger, "An undulatory theory of the mechanics of atoms and molecules," *Physical Review*, vol. 28, no. 6, p. 1049, 1926. – cited on page 5.

[19] F. Bloch, "Über die Quantenmechanik der Elektronen in Kristallgittern," *Zeitschrift für Physik*, vol. 52, no. 7, pp. 555–600, 1929. – cited on page 6.

[20] H. Ibach and H. Lüth, *Festkörperphysik: Einführung in die Grundlagen*. Springer-Verlag, 2009. – cited on page 6.

[21] I. Vurgaftman, J. Meyer, and L. R. Ram-Mohan, "Band parameters for III-V compound semiconductors and their alloys," *Journal of Applied Physics*, vol. 89, no. 11, pp. 5815–5875, 2001. – cited on page 7.

[22] R. Dupuis, "Metalorganic chemical vapor deposition of III-V semiconductors," *Science*, vol. 226, no. 4675, pp. 623–629, 1984. – cited on page 7.

[23] L. L. Chang and K. Ploog, *Molecular beam epitaxy and heterostructures*, vol. 87. Springer Science & Business Media, 2012. – cited on page 7.

[24] G. A. Reider, *Photonik: eine Einführung in die Grundlagen*. Springer-Verlag, 2013. – cited on page 8.

[25] J. Faist, *Quantum Cascade Lasers*. EBSCO ebook academic collection, OUP Oxford, 2013. – cited on pages 9 and 15.

[26] R. Q. Yang, "Infrared laser based on intersubband transitions in quantum wells," *Superlattices and Microstructures*, vol. 17, no. 1, pp. 77–83, 1995. – cited on pages 9 and 17.

[27] J. Meyer, I. Vurgaftman, R. Yang, and L. Ram-Mohan, "Type-II and type-I interband cascade lasers," *Electronics Letters*, vol. 32, no. 1, pp. 45–46, 1996. – cited on pages 9 and 17.

[28] J. Meyer, C. Hoffman, F. Bartoli, and L. Ram-Mohan, "Type-II quantum-well lasers for the mid-wavelength infrared," *Applied Physics Letters*, vol. 67, no. 6, pp. 757–759, 1995. – cited on pages 9 and 18.

[29] I. Vurgaftman, W. W. Bewley, C. L. Canedy, C. S. Kim, M. Kim, J. R. Lindle, C. D. Merritt, J. Abell, and J. R. Meyer, "Mid-IR type-II interband cascade lasers," *IEEE Journal of Selected Topics in Quantum Electronics*, vol. 17, no. 5, pp. 1435–1444, 2011. – cited on page 10.

[30] M. Planck, *Über das gesetz der energieverteilung im normalspektrum*. Springer, 1978. – cited on page 11.

[31] M. Holzbauer, *Quantum cascade interband and intersubband ring lasers*. PhD thesis, Technische Universität Wien, 2018. – cited on pages 12, 15, and 28.

[32] M. A. Kats, R. Blanchard, S. Zhang, P. Genevet, C. Ko, S. Ramanathan, and F. Capasso, “Vanadium dioxide as a natural disordered metamaterial: Perfect thermal emission and large broadband negative differential thermal emittance,” *Phys. Rev. X*, vol. 3, p. 041004, Oct 2013. – cited on page 12.

[33] D. Jung, S. Bank, M. L. Lee, and D. Wasserman, “Next-generation mid-infrared sources,” *Journal of Optics*, vol. 19, no. 12, p. 123001, 2017. – cited on page 12.

[34] W. T. Silfvast, *Laser fundamentals*. Cambridge University Press, 2004. – cited on page 12.

[35] L. A. Coldren, S. W. Corzine, and M. L. Mashanovitch, *Diode lasers and photonic integrated circuits*, vol. 218. John Wiley & Sons, 2012. – cited on pages 13 and 69.

[36] R. N. Hall, G. E. Fenner, J. Kingsley, T. Soltys, and R. Carlson, “Coherent light emission from GaAs junctions,” *Physical Review Letters*, vol. 9, no. 9, p. 366, 1962. – cited on page 13.

[37] J. Faist, F. Capasso, D. L. Sivco, C. Sirtori, A. L. Hutchinson, and A. Y. Cho, “Quantum cascade laser,” *Science*, vol. 264, no. 5158, pp. 553–556, 1994. – cited on page 14.

[38] M. S. Vitiello, G. Scalari, B. Williams, and P. De Natale, “Quantum cascade lasers: 20 years of challenges,” *Optics Express*, vol. 23, no. 4, pp. 5167–5182, 2015. – cited on page 14.

[39] J. Faist, F. Capasso, C. Sirtori, D. L. Sivco, J. N. Baillargeon, A. L. Hutchinson, S.-N. G. Chu, and A. Y. Cho, “High power mid-infrared (λ 5 μm) quantum cascade lasers operating above room temperature,” *Applied Physics Letters*, vol. 68, no. 26, pp. 3680–3682, 1996. – cited on page 14.

[40] C. Gmachl, A. M. Sergent, A. Tredicucci, F. Capasso, A. L. Hutchinson, D. L. Sivco, J. N. Baillargeon, S. G. Chu, and A. Y. Cho, “Improved CW operation of quantum cascade lasers with epitaxial-side heat-sinking,” *IEEE Photonics Technology Letters*, vol. 11, no. 11, pp. 1369–1371, 1999. – cited on page 14.

[41] D. Hofstetter, M. Beck, T. Aellen, J. Faist, U. Oesterle, M. Ilegems, E. Gini, and H. Melchior, "Continuous wave operation of a 9.3 μm quantum cascade laser on a Peltier cooler," *Applied Physics Letters*, vol. 78, no. 14, pp. 1964–1966, 2001. – cited on page 14.

[42] M. Beck, D. Hofstetter, T. Aellen, J. Faist, U. Oesterle, M. Ilegems, E. Gini, and H. Melchior, "Continuous wave operation of a mid-infrared semiconductor laser at room temperature," *Science*, vol. 295, no. 5553, pp. 301–305, 2002. – cited on page 14.

[43] F. Wang, S. Slivken, D. Wu, and M. Razeghi, "Room temperature quantum cascade lasers with 22% wall plug efficiency in continuous-wave operation," *Optics Express*, vol. 28, no. 12, pp. 17532–17538, 2020. – cited on page 14.

[44] F. Wang, S. Slivken, D. Wu, and M. Razeghi, "Room temperature quantum cascade laser with 31% wall-plug efficiency," *AIP Advances*, vol. 10, no. 7, 2020. – cited on page 14.

[45] O. Cathabard, R. Teissier, J. Devenson, J. Moreno, and A. Baranov, "Quantum cascade lasers emitting near 2.6 μm," *Applied Physics Letters*, vol. 96, no. 14, 2010. – cited on page 14.

[46] Y. Yao, A. J. Hoffman, and C. F. Gmachl, "Mid-infrared quantum cascade lasers," *Nature Photonics*, vol. 6, no. 7, pp. 432–439, 2012. – cited on page 14.

[47] M. Wienold, B. Röben, X. Lü, G. Rozas, L. Schrottke, K. Biermann, and H. T. Grahn, "Frequency dependence of the maximum operating temperature for quantum-cascade lasers up to 5.4 Thz," *Applied Physics Letters*, vol. 107, no. 20, 2015. – cited on page 14.

[48] A. W. Lee, Q. Qin, S. Kumar, B. S. Williams, Q. Hu, and J. L. Reno, "Real-time terahertz imaging over a standoff distance ($>$ 25meters)," *Applied Physics Letters*, vol. 89, no. 14, 2006. – cited on page 14.

[49] G. Scalari, C. Walther, M. Fischer, R. Terazzi, H. Beere, D. Ritchie, and J. Faist, "THz and sub-THz quantum cascade lasers," *Laser & Photonics Reviews*, vol. 3, no. 1-2, pp. 45–66, 2009. – cited on page 14.

[50] K. Kinjalk, D. A. Díaz-Thomas, Z. Loghmari, M. Bahriz, R. Teissier, and A. N. Baranov, "Inas-based quantum cascade lasers with extremely low threshold," in *Photonics*, vol. 9, p. 747, MDPI, 2022. – cited on page 14.

[51] C. Gmachl, F. Capasso, D. L. Sivco, and A. Y. Cho, "Recent progress in quantum cascade lasers and applications," *Reports on Progress in Physics*, vol. 64, no. 11, p. 1533, 2001. – cited on page 15.

[52] Z. Liu, D. Wasserman, S. S. Howard, A. J. Hoffman, C. F. Gmachl, X. Wang, T. Tanbun-Ek, L. Cheng, and F.-S. Choa, "Room-temperature continuous-wave quantum cascade lasers grown by MOCVD without lateral regrowth," *IEEE Photonics Technology Letters*, vol. 18, no. 12, pp. 1347–1349, 2006. – cited on page 16.

[53] E. Mujagić, *Ring cavity surface emitting semiconductor lasers*. PhD thesis, Technische Universität Wien, 2010. – cited on pages 16, 58, and 70.

[54] S. Rudin and T. L. Reinecke, "Electron–LO-phonon scattering rates in semiconductor quantum wells," *Physical Review B*, vol. 41, pp. 7713–7717, Apr 1990. – cited on page 16.

[55] F. Capasso, "High-performance midinfrared quantum cascade lasers," *Optical Engineering*, vol. 49, no. 11, pp. 111102–111102, 2010. – cited on page 16.

[56] D. Burghart, W. Oberhausen, K. Zhang, A. Gardanow, J. Krakofsky, G. Boehm, and M. A. Belkin, "Mid-infrared quantum cascade lasers with 9 stages for regrowth-free low voltage continuous wave operation," in *2021 Conference on Lasers and Electro-Optics Europe European Quantum Electronics Conference (CLEO/Europe-EQEC)*, pp. 1–1, 2021. – cited on page 16.

[57] Lin, Yang, D. Zhang, S. Murry, S. Pei, A. Allerman, and S. Kurtz, "Type-II interband quantum cascade laser at 3.8 μm," *Electronics Letters*, vol. 33, no. 7, pp. 598–599, 1997. – cited on page 17.

[58] I. Vurgaftman, J. R. Meyer, and L. R. Ram-Mohan, "Mid-IR vertical-cavity surface-emitting lasers," *IEEE Journal of Quantum Electronics*, vol. 34, no. 1, pp. 147–156, 1998. – cited on page 17.

[59] R. Yang, J. Bruno, J. Bradshaw, J. Pham, and D. Wortman, "High-power interband cascade lasers with quantum efficiency> 450%," *Electronics Letters*, vol. 35, no. 15, pp. 1254–1255, 1999. – cited on page 17.

[60] R. Q. Yang, C. J. Hill, B. Yang, and J. K. Liu, "Room-temperature type-II interband cascade lasers near 4.1 μm," *Applied Physics Letters*, vol. 83, no. 11, pp. 2109–2111, 2003. – cited on page 17.

[61] M. Kim, C. Canedy, W. Bewley, C. Kim, J. Lindle, J. Abell, I. Vurgaftman, and J. Meyer, “Interband cascade laser emitting at $\lambda = 3.75\ \mu$m in continuous wave above room temperature,” *Applied Physics Letters*, vol. 92, no. 19, 2008. – cited on page 17.

[62] I. Vurgaftman, W. Bewley, C. Canedy, C. Kim, M. Kim, C. Merritt, J. Abell, J. Lindle, and J. Meyer, “Rebalancing of internally generated carriers for mid-infrared interband cascade lasers with very low power consumption,” *Nature Communications*, vol. 2, no. 1, p. 585, 2011. – cited on pages 17 and 19.

[63] R. Weih, M. Kamp, and S. Höfling, “Interband cascade lasers with room temperature threshold current densities below 100 A/cm2,” *Applied Physics Letters*, vol. 102, no. 23, 2013. – cited on pages 17 and 57.

[64] Y. Lin, Y. Ma, W. Zheng, K. Zhang, H. Lu, and R. Q. Yang, “Low threshold, high temperature operation of continuous wave interband cascade lasers near 5 μm,” *Applied Physics Letters*, vol. 125, no. 12, 2024. – cited on page 17.

[65] J. Scheuermann, R. Weih, M. von Edlinger, L. Nähle, M. Fischer, J. Koeth, M. Kamp, and S. Höfling, “Single-mode interband cascade lasers emitting below 2.8 μm,” *Applied Physics Letters*, vol. 106, no. 16, 2015. – cited on page 17.

[66] J. Nauschütz, H. Knötig, R. Weih, J. Scheuermann, J. Koeth, S. Höfling, and B. Schwarz, “Pushing the room temperature continuous-wave operation limit of GaSb-based interband cascade lasers beyond 6 μm,” *Laser & Photonics Reviews*, vol. 17, no. 4, p. 2200587, 2023. – cited on page 17.

[67] H. Knötig, J. Nauschütz, N. Opačak, S. Höfling, J. Koeth, R. Weih, and B. Schwarz, “Mitigating valence intersubband absorption in interband cascade lasers,” *Laser & Photonics Reviews*, vol. 16, no. 9, p. 2200156, 2022. – cited on page 17.

[68] J. A. Massengale, Y. Shen, R. Q. Yang, S. D. Hawkins, and J. F. Klem, “Long wavelength interband cascade lasers,” *Applied Physics Letters*, vol. 120, no. 9, 2022. – cited on page 17.

[69] M. Kim, W. W. Bewley, C. L. Canedy, C. S. Kim, C. D. Merritt, J. Abell, I. Vurgaftman, and J. R. Meyer, “High-power continuous-wave interband cascade lasers with 10 active stages,” *Optics Express*, vol. 23, no. 8, pp. 9664–9672, 2015. – cited on page 17.

[70] A. Windischhofer, N. Opačak, and B. Schwarz, "Charge transport in interband cascade lasers: An ab-initio self-consistent model," *Laser & Photonics Reviews*, p. 2400866, 2024. – cited on page 18.

[71] I. Vurgaftman, R. Weih, M. Kamp, J. Meyer, C. Canedy, C. Kim, M. Kim, W. Bewley, C. Merritt, J. Abell, *et al.*, "Interband cascade lasers," *Journal of Physics D: Applied Physics*, vol. 48, no. 12, p. 123001, 2015. – cited on page 18.

[72] A. Bauer, K. Rößner, T. Lehnhardt, M. Kamp, S. Höfling, L. Worschech, and A. Forchel, "Mid-infrared semiconductor heterostructure lasers for gas sensing applications," *Semiconductor Science and Technology*, vol. 26, no. 1, p. 014032, 2010. – cited on page 18.

[73] G. P. Agrawal and N. K. Dutta, *Long-wavelength semiconductor lasers*, vol. 1. Springer, 1986. – cited on page 19.

[74] C. L. Canedy, J. Abell, C. D. Merritt, W. W. Bewley, C. S. Kim, M. Kim, I. Vurgaftman, and J. R. Meyer, "Pulsed and CW performance of 7-stage interband cascade lasers," *Optics Express*, vol. 22, no. 7, pp. 7702–7710, 2014. – cited on page 19.

[75] C. J. Hill, B. Yang, and R. Q. Yang, "Low-threshold interband cascade lasers operating above room temperature," *Physica E: Low-dimensional Systems and Nanostructures*, vol. 20, no. 3-4, pp. 486–490, 2004. – cited on page 19.

[76] K. W. Busch and M. A. Busch, *Multielement detection systems for spectrochemical analysis*, vol. 106. John Wiley & Sons, 1991. – cited on page 19.

[77] S. P. Langley, "The bolometer and radiant energy," in *Proceedings of the American Academy of Arts and Sciences*, vol. 16, pp. 342–358, JSTOR, 1880. – cited on page 19.

[78] M. J. Golay, "Theoretical consideration in heat and infra-red detection, with particular reference to the pneumatic detector," *Review of Scientific Instruments*, vol. 18, no. 5, pp. 347–356, 1947. – cited on page 20.

[79] W. Schottky, "Zur Halbleitertheorie der Sperrschicht-und Spitzengleichrichter," *Zeitschrift für Physik*, vol. 113, pp. 367–414, 1939. – cited on page 20.

[80] W. Lawson, S. Nielsen, E. Putley, and A. Young, “Preparation and properties of HgTe and mixed crystals of HgTe-CdTe,” *Journal of Physics and Chemistry of Solids*, vol. 9, no. 3-4, pp. 325–329, 1959. – cited on page 20.

[81] P. Norton, “HgCdTe infrared detectors,” *Optoelectronics Review*, no. 3, pp. 159–174, 2002. – cited on page 20.

[82] T. Takahashi, T. Mitani, Y. Kobayashi, M. Kouda, G. Sato, S. Watanabe, K. Nakazawa, Y. Okada, M. Funaki, R. Ohno, *et al.*, “High-resolution Schottky CdTe diode detector,” *IEEE Transactions on Nuclear Science*, vol. 49, no. 3, pp. 1297–1303, 2002. – cited on page 20.

[83] R. Q. Yang, Z. Tian, Z. Cai, J. Klem, M. B. Johnson, and H. Liu, “Interband-cascade infrared photodetectors with superlattice absorbers,” *Journal of Applied Physics*, vol. 107, no. 5, 2010. – cited on page 20.

[84] J. V. Li, R. Q. Yang, C. J. Hill, and S. L. Chuang, “Interband cascade detectors with room temperature photovoltaic operation,” *Applied Physics Letters*, vol. 86, no. 10, 2005. – cited on page 20.

[85] N. Gautam, S. Myers, A. Barve, B. Klein, E. Smith, D. Rhiger, L. Dawson, and S. Krishna, “High operating temperature interband cascade midwave infrared detector based on type-II InAs/GaSb strained layer superlattice,” *Applied Physics Letters*, vol. 101, no. 2, 2012. – cited on page 21.

[86] P. Didier, H. Knötig, O. Spitz, L. Cerutti, A. Lardschneider, E. Awwad, D. Diaz-Thomas, A. Baranov, R. Weih, J. Koeth, *et al.*, “Interband cascade technology for energy-efficient mid-infrared free-space communication,” *Photonics Research*, vol. 11, no. 4, pp. 582–590, 2023. – cited on page 21.

[87] B. Levine, K. Choi, C. Bethea, J. Walker, and R. Malik, “A new 10 μm infrared detector using intersubband absorption in resonant tunneling GaAlAs superlattices,” in *Picosecond Electronics and Optoelectronics*, p. ThD6, Optica Publishing Group, 1987. – cited on page 21.

[88] D. Hofstetter, M. Beck, and J. Faist, “Quantum-cascade-laser structures as photodetectors,” *Applied Physics Letters*, vol. 81, no. 15, pp. 2683–2685, 2002. – cited on pages 21 and 33.

[89] G. Marschick, M. David, E. Arigliani, N. Opačak, B. Schwarz, M. Giparakis, A. Delga, M. Lagree, T. Poletti, V. Trinite, *et al.*, “High-responsivity opera-

tion of quantum cascade detectors at 9 µm," *Optics Express*, vol. 30, no. 22, pp. 40188–40195, 2022. – cited on page 21.

[90] B. Schwarz, P. Reininger, H. Detz, T. Zederbauer, A. Maxwell Andrews, S. Kalchmair, W. Schrenk, O. Baumgartner, H. Kosina, and G. Strasser, "A bi-functional quantum cascade device for same-frequency lasing and detection," *Applied Physics Letters*, vol. 101, no. 19, 2012. – cited on page 22.

[91] K. Shimoda, *Introduction to laser physics*, vol. 44. Springer, 2013. – cited on page 23.

[92] K. J. Ebeling, *Integrated optoelectronics: waveguide optics, photonics, semiconductors*. Springer Science & Business Media, 2012. – cited on page 23.

[93] J. Hillbrand, D. Auth, M. Piccardo, N. Opačak, E. Gornik, G. Strasser, F. Capasso, S. Breuer, and B. Schwarz, "In-phase and anti-phase synchronization in a laser frequency comb," *Physical Review Letters*, vol. 124, no. 2, p. 023901, 2020. – cited on page 24.

[94] N. Opačak, S. Dal Cin, J. Hillbrand, and B. Schwarz, "Frequency comb generation by Bloch gain induced giant Kerr nonlinearity," *Physical Review Letters*, vol. 127, no. 9, p. 093902, 2021. – cited on page 24.

[95] J. Hillbrand, N. Opačak, M. Piccardo, H. Schneider, G. Strasser, F. Capasso, and B. Schwarz, "Mode-locked short pulses from an 8 μm wavelength semiconductor laser," *Nature Communications*, vol. 11, no. 1, p. 5788, 2020. – cited on page 24.

[96] N. Opačak, B. Schneider, J. Faist, and B. Schwarz, "Impact of higher-order dispersion on frequency-modulated combs," *Optics Letters*, vol. 49, no. 4, pp. 794–797, 2024. – cited on page 24.

[97] J. Faist, C. Gmachl, M. Striccoli, C. Sirtori, F. Capasso, D. L. Sivco, and A. Y. Cho, "Quantum cascade disk lasers," *Applied Physics Letters*, vol. 69, no. 17, pp. 2456–2458, 1996. – cited on page 24.

[98] G. C. Righini, Y. Dumeige, P. Féron, M. Ferrari, G. Nunzi Conti, D. Ristic, and S. Soria, "Whispering gallery mode microresonators: fundamentals and applications," *La Rivista del Nuovo Cimento*, vol. 34, pp. 435–488, 2011. – cited on page 24.

[99] L. Rayleigh, “CXII. The problem of the whispering gallery,” *The London, Edinburgh, and Dublin Philosophical Magazine and Journal of Science*, vol. 20, no. 120, pp. 1001–1004, 1910. – cited on page 25.

[100] S. McCall, A. Levi, R. Slusher, S. Pearton, and R. Logan, “Whispering-gallery mode microdisk lasers,” *Applied Physics Letters*, vol. 60, no. 3, pp. 289–291, 1992. – cited on page 25.

[101] G. Marschick, S. Isceri, R. Szedlak, H. Moser, J. P. Waclawek, E. Arigliani, R. Weih, W. Schrenk, G. Strasser, B. Hinkov, *et al.*, “Compact vertical emitting ring interband cascade lasers for isotope-resolved CO_2 sensing,” *APL Photonics*, vol. 9, no. 10, 2024. – cited on page 25.

[102] R. Szedlak, M. Holzbauer, D. MacFarland, T. Zederbauer, H. Detz, A. M. Andrews, C. Schwarzer, W. Schrenk, and G. Strasser, “The influence of whispering gallery modes on the far field of ring lasers,” *Scientific Reports*, vol. 5, no. 1, p. 16668, 2015. – cited on page 25.

[103] M. Jaidl, N. Opačak, M. A. Kainz, S. Schönhuber, D. Theiner, B. Limbacher, M. Beiser, M. Giparakis, A. M. Andrews, G. Strasser, *et al.*, “Comb operation in terahertz quantum cascade ring lasers,” *Optica*, vol. 8, no. 6, pp. 780–787, 2021. – cited on page 25.

[104] H. Knötig, B. Hinkov, R. Weih, S. Höfling, J. Koeth, and G. Strasser, “Continuous-wave operation of vertically emitting ring interband cascade lasers at room temperature,” *Applied Physics Letters*, vol. 116, no. 13, 2020. – cited on pages 25, 58, and 70.

[105] N. Opačak, D. Kazakov, L. L. Columbo, M. Beiser, T. P. Letsou, F. Pilat, M. Brambilla, F. Prati, M. Piccardo, F. Capasso, *et al.*, “Nozaki–Bekki solitons in semiconductor lasers,” *Nature*, vol. 625, no. 7996, pp. 685–690, 2024. – cited on page 26.

[106] S. Schönhuber, M. Brandstetter, T. Hisch, C. Deutsch, M. Krall, H. Detz, A. M. Andrews, G. Strasser, S. Rotter, and K. Unterrainer, “Random lasers for broadband directional emission,” *Optica*, vol. 3, no. 10, pp. 1035–1038, 2016. – cited on page 26.

[107] M. Holzbauer, R. Szedlak, H. Detz, R. Weih, S. Höfling, W. Schrenk, J. Koeth, and G. Strasser, “Substrate-emitting ring interband cascade lasers,” *Applied Physics Letters*, vol. 111, no. 17, 2017. – cited on pages 26 and 58.

[108] R. Szedlak, J. Hayden, P. Martín-Mateos, M. Holzbauer, A. Harrer, B. Schwarz, B. Hinkov, D. MacFarland, T. Zederbauer, H. Detz, *et al.*, "Surface emitting ring quantum cascade lasers for chemical sensing," *Optical Engineering*, vol. 57, no. 1, pp. 011005–011005, 2018. – cited on pages 26 and 70.

[109] D. Stark, M. Beck, and J. Faist, "Microring quantum cascade surface emitting lasers," *arXiv preprint arXiv:2410.19584*, 2024. – cited on page 26.

[110] T.-P. Lee, C. Burrus, J. Copeland, A. Dentai, and D. Marcuse, "Short-cavity InGaAsP injection lasers: Dependence of mode spectra and single-longitudinal-mode power on cavity length," *IEEE Journal of Quantum Electronics*, vol. 18, no. 7, pp. 1101–1113, 1982. – cited on page 26.

[111] P. Fuchs, J. Seufert, J. Koeth, J. Semmel, S. Höfling, L. Worschech, and A. Forchel, "Widely tunable quantum cascade lasers with coupled cavities for gas detection," *Applied Physics Letters*, vol. 97, no. 18, 2010. – cited on page 26.

[112] A. Hugi, R. Maulini, and J. Faist, "External cavity quantum cascade laser," *Semiconductor Science and Technology*, vol. 25, no. 8, p. 083001, 2010. – cited on page 26.

[113] C. Gmachl, A. Straub, R. Colombelli, F. Capasso, D. L. Sivco, A. M. Sergent, and A. Y. Cho, "Single-mode, tunable distributed-feedback and multiple-wavelength quantum cascade lasers," *IEEE Journal of Quantum Electronics*, vol. 38, no. 6, pp. 569–581, 2002. – cited on page 26.

[114] H. Kogelnik and C. V. Shank, "Coupled-wave theory of distributed feedback lasers," *Journal of Applied Physics*, vol. 43, no. 5, pp. 2327–2335, 1972. – cited on page 27.

[115] E. Kapon, A. Hardy, and A. Katzir, "The effect of complex coupling coefficients on distributed feedback lasers," *IEEE Journal of Quantum Electronics*, vol. 18, no. 1, pp. 66–71, 1982. – cited on page 28.

[116] M. I. Amanti, M. Fischer, G. Scalari, M. Beck, and J. Faist, "Low-divergence single-mode terahertz quantum cascade laser," *Nature Photonics*, vol. 3, no. 10, pp. 586–590, 2009. – cited on page 28.

[117] D. F. Swinehart, "The Beer-Lambert law," *Journal of Chemical Education*, vol. 39, no. 7, p. 333, 1962. – cited on page 29.

[118] T. L. Hughes, C. M. Methven, T. G. Jones, S. E. Pelham, P. Fletcher, and C. Hall, "Determining cement composition by fourier transform infrared spectroscopy," *Advanced Cement Based Materials*, vol. 2, no. 3, pp. 91–104, 1995. – cited on page 29.

[119] L. Fernández-Carrasco, D. Torrens-Martín, L. Morales, and S. Martínez-Ramírez, "Infrared spectroscopy in the analysis of building and construction materials," in *Infrared Spectroscopy* (T. Theophanides, ed.), ch. 19, Rijeka: IntechOpen, 2012. – cited on page 29.

[120] H. Choudhary, A. Anupama, R. Kumar, M. Panzi, S. Matteppanavar, B. N. Sherikar, and B. Sahoo, "Observation of phase transformations in cement during hydration," *Construction and Building Materials*, vol. 101, pp. 122–129, 2015. – cited on page 29.

[121] L. Raphael, "Application of FTIR spectroscopy to agricultural soils analysis," *Fourier Transforms—New Analytical Approaches and FTIR Strategies*, pp. 385–404, 2011. – cited on page 29.

[122] A. Tinti, V. Tugnoli, S. Bonora, and O. Francioso, "Recent applications of vibrational mid-infrared (IR) spectroscopy for studying soil components: A review," *Journal of Central European Agriculture*, vol. 16, no. 1, pp. 1–22, 2015. – cited on page 29.

[123] S. T. Forrester, L. J. Janik, J. M. Soriano-Disla, S. Mason, L. Burkitt, P. Moody, C. J. Gourley, and M. J. McLaughlin, "Use of handheld mid-infrared spectroscopy and partial least-squares regression for the prediction of the phosphorus buffering index in australian soils," *Soil Research*, vol. 53, no. 1, pp. 67–80, 2015. – cited on page 29.

[124] H. G. Brittain, "Mid-infrared spectroscopy of pharmaceutical solids," *Profiles of Drug Substances, Excipients and Related Methodology*, vol. 43, pp. 321–358, 2018. – cited on page 29.

[125] F. Gabrieli, K. A. Dooley, M. Facini, and J. K. Delaney, "Near-UV to mid-IR reflectance imaging spectroscopy of paintings on the macroscale," *Science Advances*, vol. 5, no. 8, p. eaaw7794, 2019. – cited on page 29.

[126] S. Wartewig and R. H. Neubert, "Pharmaceutical applications of mid-IR and raman spectroscopy," *Advanced Drug Delivery Reviews*, vol. 57, no. 8, pp. 1144–1170, 2005. – cited on page 29.

[127] M. Brandstetter, L. Volgger, A. Genner, C. Jungbauer, and B. Lendl, "Direct determination of glucose, lactate and triglycerides in blood serum by a tunable quantum cascade laser-based mid-IR sensor," *Applied Physics B*, vol. 110, pp. 233–239, 2013. – cited on page 29.

[128] S. Rassel, C. Xu, S. Zhang, and D. Ban, "Noninvasive blood glucose detection using a quantum cascade laser," *Analyst*, vol. 145, no. 7, pp. 2441–2456, 2020. – cited on page 29.

[129] B. Hinkov, F. Pilat, L. Lux, P. L. Souza, M. David, A. Schwaighofer, D. Ristanić, B. Schwarz, H. Detz, A. M. Andrews, *et al.*, "A mid-infrared lab-on-a-chip for dynamic reaction monitoring," *Nature Communications*, vol. 13, no. 1, p. 4753, 2022. – cited on pages 29 and 47.

[130] A. Borin and R. J. Poppi, "Application of mid infrared spectroscopy and iPLS for the quantification of contaminants in lubricating oil," *Vibrational Spectroscopy*, vol. 37, no. 1, pp. 27–32, 2005. – cited on page 29.

[131] A. A. Gowen, R. Tsenkova, M. Bruen, and C. O'donnell, "Vibrational spectroscopy for analysis of water for human use and in aquatic ecosystems," *Critical Reviews in Environmental Science and Technology*, vol. 42, no. 23, pp. 2546–2573, 2012. – cited on page 29.

[132] A. S. Luna, A. P. da Silva, J. Ferré, and R. Boqué, "Classification of edible oils and modeling of their physico-chemical properties by chemometric methods using mid-IR spectroscopy," *Spectrochimica Acta Part A: Molecular and Biomolecular Spectroscopy*, vol. 100, pp. 109–114, 2013. – cited on page 30.

[133] A. Dabrowska, M. David, S. Freitag, A. M. Andrews, G. Strasser, B. Hinkov, A. Schwaighofer, and B. Lendl, "Broadband laser-based mid-infrared spectroscopy employing a quantum cascade detector for milk protein analysis," *Sensors and Actuators B: Chemical*, vol. 350, p. 130873, 2022. – cited on pages 30 and 34.

[134] A. Kosterev, G. Wysocki, Y. Bakhirkin, S. So, R. Lewicki, M. Fraser, F. Tittel, and R. Curl, "Application of quantum cascade lasers to trace gas analysis," *Applied Physics B*, vol. 90, pp. 165–176, 2008. – cited on page 30.

[135] G. Stewart, *Laser and fiber optic gas absorption spectroscopy*. Cambridge University Press, 2021. – cited on page 30.

[136] I. Galli, S. Bartalini, R. Ballerini, M. Barucci, P. Cancio, M. De Pas, G. Giusfredi, D. Mazzotti, N. Akikusa, and P. De Natale, “Spectroscopic detection of radiocarbon dioxide at parts-per-quadrillion sensitivity,” *Optica*, vol. 3, no. 4, pp. 385–388, 2016. – cited on page 30.

[137] G. Genoud, J. Lehmuskoski, S. Bell, V. Palonen, M. Oinonen, M.-L. Koskinen-Soivi, and M. Reinikainen, “Laser spectroscopy for monitoring of radiocarbon in atmospheric samples,” *Analytical Chemistry*, vol. 91, no. 19, pp. 12315–12320, 2019. PMID: 31500419. – cited on page 30.

[138] Q. Liang, Y.-C. Chan, P. B. Changala, D. J. Nesbitt, J. Ye, and J. Toscano, “Ultrasensitive multispecies spectroscopic breath analysis for real-time health monitoring and diagnostics,” *Proceedings of the National Academy of Sciences*, vol. 118, no. 40, p. e2105063118, 2021. – cited on page 30.

[139] R. Selvaraj, N. J. Vasa, S. M. S. Nagendra, and B. Mizaikoff, “Advances in mid-infrared spectroscopy-based sensing techniques for exhaled breath diagnostics,” *Molecules*, vol. 25, no. 9, 2020. – cited on page 30.

[140] C. R. Webster, P. R. Mahaffy, G. J. Flesch, P. B. Niles, J. H. Jones, L. A. Leshin, S. K. Atreya, J. C. Stern, L. E. Christensen, T. Owen, H. Franz, R. O. Pepin, A. Steele, and the MSL Science Team, “Isotope ratios of H, C, and O in CO_2 and H_2O of the martian atmosphere,” *Science*, vol. 341, no. 6143, pp. 260–263, 2013. – cited on page 30.

[141] J. C. Ricklin, S. M. Hammel, F. D. Eaton, and S. L. Lachinova, “Atmospheric channel effects on free-space laser communication,” *Journal of Optical and Fiber Communications Reports*, vol. 3, pp. 111–158, 2006. – cited on page 30.

[142] P. Didier, H. Dely, T. Bonazzi, O. Spitz, E. Awwad, E. Rodriguez, A. Vasanelli, C. Sirtori, and F. Grillot, “High-capacity free-space optical link in the mid-infrared thermal atmospheric windows using unipolar quantum devices,” *Advanced Photonics*, vol. 4, no. 5, pp. 056004–056004, 2022. – cited on page 30.

[143] A. K. Majumdar, J. C. Ricklin, D. Hutchinson, and R. Richards, “All-weather long-wavelength infrared free space optical communications,” *Free-Space Laser Communications: Principles and Advances*, pp. 407–417, 2008. – cited on page 30.

[144] P. Corrigan, R. Martini, E. Whittaker, and C. Gmachl, “Investigation of near and mid infrared (1.34, 1.55 and 8.1 µm) laser propagation through the New

York City metro area," in *Atmospheric Propagation IV* (C. Y. Young and G. C. Gilbreath, eds.), vol. 6551, p. 655107, International Society for Optics and Photonics, SPIE, 2007. – cited on page 31.

[145] H. Dely, T. Bonazzi, O. Spitz, E. Rodriguez, D. Gacemi, Y. Todorov, K. Pantzas, G. Beaudoin, I. Sagnes, L. Li, *et al.*, "10 Gbit s^{-1} free space data transmission at 9 µm wavelength with unipolar quantum optoelectronics," *Laser & Photonics Reviews*, vol. 16, no. 2, p. 2100414, 2022. – cited on pages 31 and 34.

[146] J. Faist, M. Beck, T. Aellen, and E. Gini, "Quantum-cascade lasers based on a bound-to-continuum transition," *Applied Physics Letters*, vol. 78, no. 2, pp. 147–149, 2001. – cited on page 33.

[147] M. Graf, N. Hoyler, M. Giovannini, J. Faist, and D. Hofstetter, "InP-based quantum cascade detectors in the mid-infrared," *Applied Physics Letters*, vol. 88, no. 24, 2006. – cited on page 33.

[148] M. Graf, G. Scalari, D. Hofstetter, J. Faist, H. Beere, E. Linfield, D. Ritchie, and G. Davies, "Terahertz range quantum well infrared photodetector," *Applied Physics Letters*, vol. 84, no. 4, pp. 475–477, 2004. – cited on page 33.

[149] Y. Su, W. Wang, X. Hu, H. Hu, X. Huang, Y. Wang, J. Si, X. Xie, B. Han, H. Feng, *et al.*, "10 Gbps DPSK transmission over free-space link in the mid-infrared," *Optics Express*, vol. 26, no. 26, pp. 34515–34528, 2018. – cited on page 33.

[150] K. Zou, K. Pang, H. Song, J. Fan, Z. Zhao, H. Song, R. Zhang, H. Zhou, A. Minoofar, C. Liu, *et al.*, "Demonstration of free-space 300-Gbit/s QPSK communications using both wavelength-and mode-division-multiplexing in the mid-IR," in *Optical Fiber Communication Conference*, pp. W7E–5, Optica Publishing Group, 2021. – cited on page 33.

[151] A. Bigioli, G. Armaroli, A. Vasanelli, D. Gacemi, Y. Todorov, D. Palaferri, L. Li, A. G. Davies, E. H. Linfield, and C. Sirtori, "Long-wavelength infrared photovoltaic heterodyne receivers using patch-antenna quantum cascade detectors," *Applied Physics Letters*, vol. 116, no. 16, 2020. – cited on page 34.

[152] M. Joharifar, H. Dely, X. Pang, R. Schatz, D. Gacemi, T. Salgals, A. Udalcovs, Y.-T. Sun, Y. Fan, L. Zhang, *et al.*, "High-speed 9.6 µm long-wave infrared free-space transmission with a directly-modulated QCL and a fully-passive

QCD," *Journal of Lightwave Technology*, vol. 41, no. 4, pp. 1087–1094, 2023. – cited on page 34.

[153] M. David, A. Dabrowska, M. Sistani, I. Doganlar, E. Hinkelmann, H. Detz, W. Weber, B. Lendl, G. Strasser, and B. Hinkov, "Octave-spanning low-loss mid-IR waveguides based on semiconductor-loaded plasmonics," *Optics Express*, vol. 29, no. 26, pp. 43567–43579, 2021. – cited on page 34.

[154] X. Pang, O. Ozolins, L. Zhang, R. Schatz, A. Udalcovs, X. Yu, G. Jacobsen, S. Popov, J. Chen, and S. Lourdudoss, "Free-space communications enabled by quantum cascade lasers," *Physica Status Solidi (A)*, vol. 218, no. 3, p. 2000407, 2021. – cited on page 34.

[155] B. Hinkov, A. Bismuto, Y. Bonetti, M. Beck, S. Blaser, and J. Faist, "Single-mode quantum cascade lasers with power dissipation below 1 W," *Electronics Letters*, vol. 48, no. 11, pp. 646–647, 2012. – cited on page 34.

[156] B. Hinkov, A. Hugi, M. Beck, and J. Faist, "RF-modulation of mid-infrared distributed feedback quantum cascade lasers," *Optics Express*, vol. 24, no. 4, pp. 3294–3312, 2016. – cited on page 34.

[157] T. Plank, E. Leitgeb, P. Pezzei, and Z. Ghassemlooy, "Wavelength-selection for high data rate free space optics (FSO) in next generation wireless communications," in *2012 17th European Conference on Networks and Optical Communications*, pp. 1–5, IEEE, 2012. – cited on page 34.

[158] F. Giorgetta, *Design, fabrication, and testing of intersubband infrared photodetectors operating at wavelengths between 2 μm and 17 μm.* PhD thesis, Universite de Neuchatel, 2007. – cited on page 34.

[159] B. Schwarz, P. Reininger, A. Harrer, D. MacFarland, H. Detz, A. M. Andrews, W. Schrenk, and G. Strasser, "The limit of quantum cascade detectors: A single period device," *Applied Physics Letters*, vol. 111, no. 6, 2017. – cited on page 35.

[160] M. Teich, "Infrared heterodyne detection," *Proceedings of the IEEE*, vol. 56, no. 1, pp. 37–46, 1968. – cited on page 35.

[161] R. Soref, "The past, present, and future of silicon photonics," *IEEE Journal of selected Topics in Quantum Electronics*, vol. 12, no. 6, pp. 1678–1687, 2006. – cited on page 45.

[162] H. Lin, Z. Luo, T. Gu, L. C. Kimerling, K. Wada, A. Agarwal, and J. Hu, "Mid-infrared integrated photonics on silicon: A perspective," *Nanophotonics*, vol. 7, no. 2, pp. 393–420, 2017. – cited on page 45.

[163] A. Yadav and A. M. Agarwal, "Integrated photonic materials for the mid-infrared," *International Journal of Applied Glass Science*, vol. 11, no. 3, pp. 491–510, 2020. – cited on page 45.

[164] P. T. Lin, V. Singh, J. Wang, H. Lin, J. Hu, K. Richardson, J. D. Musgraves, I. Luzinov, J. Hensley, L. C. Kimerling, *et al.*, "Si-CMOS compatible materials and devices for mid-IR microphotonics," *Optical Materials Express*, vol. 3, no. 9, pp. 1474–1487, 2013. – cited on page 45.

[165] A. Gutierrez-Arroyo, E. Baudet, L. Bodiou, J. Lemaitre, I. Hardy, F. Faijan, B. Bureau, V. Nazabal, and J. Charrier, "Optical characterization at 7.7 μm of an integrated platform based on chalcogenide waveguides for sensing applications in the mid-infrared," *Optics Express*, vol. 24, no. 20, pp. 23109–23117, 2016. – cited on page 45.

[166] P. Ma, D.-Y. Choi, Y. Yu, X. Gai, Z. Yang, S. Debbarma, S. Madden, and B. Luther-Davies, "Low-loss chalcogenide waveguides for chemical sensing in the mid-infrared," *Optics Express*, vol. 21, no. 24, pp. 29927–29937, 2013. – cited on page 45.

[167] C. Xin, H. Wu, Y. Xie, S. Yu, N. Zhou, Z. Shi, X. Guo, and L. Tong, "CdTe microwires as mid-infrared optical waveguides," *Optics Express*, vol. 26, no. 8, pp. 10944–10952, 2018. – cited on page 46.

[168] X. Wang, J. Antoszewski, G. Putrino, W. Lei, L. Faraone, and B. Mizaikoff, "Mercury–cadmium–telluride waveguides–a novel strategy for on-chip mid-infrared sensors," *Analytical Chemistry*, vol. 85, no. 22, pp. 10648–10652, 2013. – cited on page 46.

[169] A. Osman, M. Nedeljkovic, J. S. Penades, Y. Wu, Z. Qu, A. Khokhar, K. Debnath, and G. Mashanovich, "Suspended low-loss germanium waveguides for the longwave infrared," *Optics Letters*, vol. 43, no. 24, pp. 5997–6000, 2018. – cited on page 46.

[170] Y.-C. Chang, V. Paeder, L. Hvozdara, J.-M. Hartmann, and H. P. Herzig, "Low-loss germanium strip waveguides on silicon for the mid-infrared," *Optics Letters*, vol. 37, no. 14, pp. 2883–2886, 2012. – cited on page 46.

[171] J.-M. Fedeli and S. Nicoletti, “Mid-infrared (mid-IR) silicon-based photonics,” *Proceedings of the IEEE*, vol. 106, no. 12, pp. 2302–2312, 2018. – cited on pages 46 and 58.

[172] Y. Zou, S. Chakravarty, C.-J. Chung, X. Xu, and R. T. Chen, “Mid-infrared silicon photonic waveguides and devices,” *Photonics Research*, vol. 6, no. 4, pp. 254–276, 2018. – cited on page 46.

[173] J. S. Penadés, A. Sánchez-Postigo, M. Nedeljkovic, A. Ortega-Moñux, J. Wangüemert-Pérez, Y. Xu, R. Halir, Z. Qu, A. Khokhar, A. Osman, *et al.*, “Suspended silicon waveguides for long-wave infrared wavelengths,” *Optics Letters*, vol. 43, no. 4, pp. 795–798, 2018. – cited on page 46.

[174] R. A. Soref, S. J. Emelett, and W. R. Buchwald, “Silicon waveguided components for the long-wave infrared region,” *Journal of Optics A: Pure and Applied Optics*, vol. 8, no. 10, p. 840, 2006. – cited on page 46.

[175] T. Schädle and B. Mizaikoff, “Mid-infrared waveguides: A perspective,” *Applied Spectroscopy*, vol. 70, no. 10, pp. 1625–1638, 2016. – cited on page 46.

[176] J. Takahara, S. Yamagishi, H. Taki, A. Morimoto, and T. Kobayashi, “Guiding of a one-dimensional optical beam with nanometer diameter,” *Optics Letters*, vol. 22, no. 7, pp. 475–477, 1997. – cited on page 46.

[177] S. Sederberg, V. Van, and A. Elezzabi, “Monolithic integration of plasmonic waveguides into a complimentary metal-oxide-semiconductor-and photonic-compatible platform,” *Applied Physics Letters*, vol. 96, no. 12, 2010. – cited on page 46.

[178] A. L. Pyayt, B. Wiley, Y. Xia, A. Chen, and L. Dalton, “Integration of photonic and silver nanowire plasmonic waveguides,” *Nature Nanotechnology*, vol. 3, no. 11, pp. 660–665, 2008. – cited on page 46.

[179] C. Chen, D. A. Mohr, H.-K. Choi, D. Yoo, M. Li, and S.-H. Oh, “Waveguide-integrated compact plasmonic resonators for on-chip mid-infrared laser spectroscopy,” *Nano Letters*, vol. 18, no. 12, pp. 7601–7608, 2018. – cited on page 46.

[180] R. Soref, “Group IV photonics for the mid infrared,” in *Silicon Photonics VIII*, vol. 8629, pp. 11–25, SPIE, 2013. – cited on page 46.

[181] A. Krasavin and A. Zayats, "Passive photonic elements based on dielectric-loaded surface plasmon polariton waveguides," *Applied Physics Letters*, vol. 90, no. 21, 2007. – cited on page 46.

[182] J. Kischkat, S. Peters, B. Gruska, M. Semtsiv, M. Chashnikova, M. Klinkmüller, O. Fedosenko, S. Machulik, A. Aleksandrova, G. Monastyrskyi, *et al.*, "Mid-infrared optical properties of thin films of aluminum oxide, titanium dioxide, silicon dioxide, aluminum nitride, and silicon nitride," *Applied Optics*, vol. 51, no. 28, pp. 6789–6798, 2012. – cited on page 46.

[183] M. David, D. Disnan, E. Arigliani, A. Lardschneider, G. Marschick, H. T. Hoang, H. Detz, B. Lendl, U. Schmid, G. Strasser, *et al.*, "Advanced mid-infrared plasmonic waveguides for on-chip integrated photonics," *Photonics Research*, vol. 11, no. 10, pp. 1694–1702, 2023. – cited on page 46.

[184] D. R. Smith and E. V. Loewenstein, "Optical constants of far infrared materials. 3: plastics," *Applied Optics*, vol. 14, no. 6, pp. 1335–1341, 1975. – cited on page 46.

[185] M. David, D. Disnan, A. Lardschneider, D. Wacht, H. T. Hoang, G. Ramer, H. Detz, B. Lendl, U. Schmid, G. Strasser, *et al.*, "Structure and mid-infrared optical properties of spin-coated polyethylene films developed for integrated photonics applications," *Optical Materials Express*, vol. 12, no. 6, pp. 2168–2180, 2022. – cited on page 46.

[186] L. Markey, C. Vernoux, K. Hammani, J. Arocas, J.-C. Weeber, and A. Dereux, "A long-range plasmonic optical waveguide corner mirror chip," *Micro and Nano Engineering*, vol. 7, p. 100049, 2020. – cited on page 46.

[187] D. Marris-Morini, V. Vakarin, J. M. Ramirez, Q. Liu, A. Ballabio, J. Frigerio, M. Montesinos, C. Alonso-Ramos, X. Le Roux, S. Serna, *et al.*, "Germanium-based integrated photonics from near-to mid-infrared applications," *Nanophotonics*, vol. 7, no. 11, pp. 1781–1793, 2018. – cited on page 46.

[188] M. P. Fischer, A. Riede, K. Gallacher, J. Frigerio, G. Pellegrini, M. Ortolani, D. J. Paul, G. Isella, A. Leitenstorfer, P. Biagioni, *et al.*, "Plasmonic mid-infrared third harmonic generation in germanium nanoantennas," *Light: Science & Applications*, vol. 7, no. 1, p. 106, 2018. – cited on page 46.

[189] M. David, *Plasmonics for Mid-infrared Photonic Integrated Circuits*. PhD thesis, Technische Universität Wien, 2023. – cited on page 47.

[190] R. G. Beausoleil, “Large-scale integrated photonics for high-performance interconnects,” *ACM Journal on Emerging Technologies in Computing Systems (JETC)*, vol. 7, no. 2, pp. 1–54, 2011. – cited on page 47.

[191] I. Vurgaftman, W. W. Bewley, C. L. Canedy, C. S. Kim, M. Kim, C. D. Merritt, J. Abell, and J. R. Meyer, “Interband cascade lasers with low threshold powers and high output powers,” *IEEE Journal of Selected Topics in Quantum Electronics*, vol. 19, no. 4, pp. 1200210–1200210, 2013. – cited on page 57.

[192] L. Richard, I. Ventrillard, G. Chau, K. Jaulin, E. Kerstel, and D. Romanini, “Optical-feedback cavity-enhanced absorption spectroscopy with an interband cascade laser: application to SO_2 trace analysis,” *Applied Physics B*, vol. 122, no. 9, p. 247, 2016. – cited on page 57.

[193] M. Horstjann, Y. Bakhirkin, A. Kosterev, R. Curl, F. Tittel, C. Wong, C. Hill, and R. Yang, “Formaldehyde sensor using interband cascade laser based quartz-enhanced photoacoustic spectroscopy,” *Applied Physics B*, vol. 79, pp. 799–803, 2004. – cited on page 57.

[194] W. Ye, C. Li, C. Zheng, N. P. Sanchez, A. K. Gluszek, A. J. Hudzikowski, L. Dong, R. J. Griffin, and F. K. Tittel, “Mid-infrared dual-gas sensor for simultaneous detection of methane and ethane using a single continuous-wave interband cascade laser,” *Optics Express*, vol. 24, no. 15, pp. 16973–16985, 2016. – cited on page 57.

[195] J. J. Girard, R. M. Spearrin, C. S. Goldenstein, and R. K. Hanson, “Compact optical probe for flame temperature and carbon dioxide using interband cascade laser absorption near 4.2 μm,” *Combustion and Flame*, vol. 178, pp. 158–167, 2017. – cited on page 57.

[196] Z. Liu, C. Zheng, T. Zhang, Y. Li, Q. Ren, C. Chen, W. Ye, Y. Zhang, Y. Wang, and F. K. Tittel, “Midinfrared sensor system based on tunable laser absorption spectroscopy for dissolved carbon dioxide analysis in the south china sea: System-level integration and deployment,” *Analytical Chemistry*, vol. 92, no. 12, pp. 8178–8185, 2020. – cited on page 58.

[197] Z. Wang, Q. Wang, J. Y.-L. Ching, J. C.-Y. Wu, G. Zhang, and W. Ren, “A portable low-power QEPAS-based CO_2 isotope sensor using a fiber-coupled interband cascade laser,” *Sensors and Actuators B: Chemical*, vol. 246, pp. 710–715, 2017. – cited on page 58.

[198] A. Spott, E. J. Stanton, A. Torres, M. L. Davenport, C. L. Canedy, I. Vurgaftman, M. Kim, C. S. Kim, C. D. Merritt, W. W. Bewley, *et al.*, "Interband cascade laser on silicon," *Optica*, vol. 5, no. 8, pp. 996–1005, 2018. – cited on page 58.

[199] J. R. Meyer, C. S. Kim, M. Kim, C. L. Canedy, C. D. Merritt, W. W. Bewley, and I. Vurgaftman, "Interband cascade photonic integrated circuits on native III-V chip," *Sensors*, vol. 21, no. 2, p. 599, 2021. – cited on page 58.

[200] C. Schwarzer, E. Mujagić, S. I. Ahn, A. M. Andrews, W. Schrenk, W. Charles, C. Gmachl, and G. Strasser, "Grating duty-cycle induced enhancement of substrate emission from ring cavity quantum cascade lasers," *Applied Physics Letters*, vol. 100, no. 19, 2012. – cited on page 58.

[201] E. Mujagić, C. Schwarzer, Y. Yao, J. Chen, C. Gmachl, and G. Strasser, "Two-dimensional broadband distributed-feedback quantum cascade laser arrays," *Applied Physics Letters*, vol. 98, no. 14, 2011. – cited on page 58.

[202] G. Marschick, H. Knötig, R. Weih, J. Koeth, G. Strasser, and B. Hinkov, "Concentric double-ring interband cascade lasers for bi-color emission in continuous wave mode," in *Novel In-Plane Semiconductor Lasers XXII*, p. PC1244009, SPIE, 2023. – cited on page 58.

[203] I. Joindot, "Measurements of relative intensity noise (RIN) in semiconductor lasers," *Journal de Physique III*, vol. 2, no. 9, pp. 1591–1603, 1992. – cited on page 69.

[204] R. J. Fronen and L. K. Vandamme, "Low-frequency intensity noise in semiconductor lasers," *IEEE Journal of Quantum Electronics*, vol. 24, no. 5, pp. 724–736, 1988. – cited on page 69.

[205] B. J. Lawrie, P. D. Lett, A. M. Marino, and R. C. Pooser, "Quantum sensing with squeezed light," *ACS Photonics*, vol. 6, no. 6, pp. 1307–1318, 2019. – cited on page 70.

[206] J. Hodgkinson and R. P. Tatam, "Optical gas sensing: A review," *Measurement science and technology*, vol. 24, no. 1, p. 012004, 2012. – cited on page 70.

[207] N. J. Cerf, M. Levy, and G. Van Assche, "Quantum distribution of Gaussian keys using squeezed states," *Physical Review A*, vol. 63, no. 5, p. 052311, 2001. – cited on page 70.

[208] G. Frascella, S. Agne, F. Y. Khalili, and M. V. Chekhova, "Overcoming detection loss and noise in squeezing-based optical sensing," *NPJ Quantum Information*, vol. 7, no. 1, p. 72, 2021. – cited on page 70.

[209] S. Borri, M. Siciliani de Cumis, S. Viciani, F. D'Amato, and P. De Natale, "Unveiling quantum-limited operation of interband cascade lasers," *APL Photonics*, vol. 5, no. 3, 2020. – cited on page 70.

[210] S. Bartalini, S. Borri, I. Galli, G. Giusfredi, D. Mazzotti, T. Edamura, N. Akikusa, M. Yamanishi, and P. De Natale, "Measuring frequency noise and intrinsic linewidth of a room-temperature DFB quantum cascade laser," *Optics Express*, vol. 19, no. 19, pp. 17996–18003, 2011. – cited on page 70.

[211] Y. Deng, B.-B. Zhao, Y.-T. Gu, and C. Wang, "Relative intensity noise of a continuous-wave interband cascade laser at room temperature," *Optics Letters*, vol. 44, no. 6, pp. 1375–1378, 2019. – cited on page 70.

[212] P. A. Folkes, "Interband cascade laser photon noise," *Journal of Physics D: Applied Physics*, vol. 41, no. 24, p. 245109, 2008. – cited on page 70.

[213] P. Didier, O. Spitz, L. Cerutti, D. Diaz-Thomas, A. Baranov, M. Carras, and F. Grillot, "Relative intensity noise and intrinsic properties of RF mounted interband cascade laser," *Applied Physics Letters*, vol. 119, no. 17, 2021. – cited on page 70.

[214] H. Kim, P. Didier, S. Zaminga, D. A. Díaz-Thomas, A. Baranov, J.-B. Rodriguez, E. Tournié, H. Knötig, B. Schwarz, L. Cerutti, *et al.*, "Intensity noise and modulation dynamics of an epitaxial mid-infrared interband cascade laser on silicon," *APL Photonics*, vol. 9, no. 10, 2024. – cited on page 70.

[215] C. Koch and T. J. Rinke, *Fotolithografie: Grundlagen der Mikrostrukturierung*. MicroChemicals GmbH, 2017. – cited on page 92.

[216] S. Franssila and L. Sainiemi, *Reactive Ion Etching (RIE)*, pp. 1772–1781. Boston, MA: Springer US, 2008. – cited on page 97.

[217] M. K. Connors, J. J. Plant, K. G. Ray, and G. W. Turner, "Chamber conditioning process development for improved inductively coupled plasma reactive ion etching of GaAs/AlGaAs materials," *Journal of Vacuum Science & Technology B*, vol. 31, no. 2, 2013. – cited on page 98.

[218] C. Gatzert, A. Blakers, P. N. Deenapanray, D. Macdonald, and F. Auret, “Investigation of reactive ion etching of dielectrics and Si in CHF_3/ O_2 or CHF_3/ Ar for photovoltaic applications,” *Journal of Vacuum Science & Technology A*, vol. 24, no. 5, pp. 1857–1865, 2006. – cited on page 99.

[219] P. Kaspar, Y. Jeyaram, H. Jäckel, A. Foelske, R. Kötz, and S. Bellini, “Silicon nitride hardmask fabrication using a cyclic CHF_3-based reactive ion etching process for vertical profile nanostructures,” *Journal of Vacuum Science & Technology B*, vol. 28, no. 6, pp. 1179–1186, 2010. – cited on page 99.

[220] J. Ye and M. Zhou, “Carbon rich plasma-induced damage in silicon nitride etch,” *Journal of The Electrochemical Society*, vol. 147, no. 3, p. 1168, 2000. – cited on page 99.

[221] W.-H. Hung, J.-T. Hsieh, H.-L. Hwang, H.-Y. Hwang, and C.-C. Chang, “Surface etching of InP (100) by chlorine,” *Surface science*, vol. 418, no. 1, pp. 46–54, 1998. – cited on page 100.

[222] N. Siwak, X. Fan, and R. Ghodssi, “Fabrication challenges for indium phosphide microsystems,” *Journal of Micromechanics and Microengineering*, vol. 25, no. 4, p. 043001, 2015. – cited on page 100.

[223] A. Matsutani, H. Ohtsuki, S. Muta, F. Koyama, and K. Iga, “Mass effect of etching gases in vertical and smooth dry etching of InP,” *Japanese Journal of Applied Physics*, vol. 40, no. 3R, p. 1528, 2001. – cited on page 100.

[224] G. Beshkov, S. Lei, V. Lazarova, N. Nedev, and S. Georgiev, “IR and Raman absorption spectroscopic studies of APCVD, LPCVD and PECVD thin SiN films,” *Vacuum*, vol. 69, no. 1-3, pp. 301–305, 2002. – cited on page 104.

[225] A. Frigg, A. Boes, G. Ren, I. Abdo, D.-Y. Choi, S. Gees, and A. Mitchell, “Low loss CMOS-compatible silicon nitride photonics utilizing reactive sputtered thin films,” *Optics Express*, vol. 27, no. 26, pp. 37795–37805, 2019. – cited on page 104.

[226] N. Rahimi, A. A. Aragon, O. S. Romero, D. M. Shima, T. J. Rotter, S. D. Mukherjee, G. Balakrishnan, and L. F. Lester, “Electrical and microstructure analysis of nickel-based low-resistance ohmic contacts to n-GaSb,” *APL Materials*, vol. 1, no. 6, 2013. – cited on pages 105 and 121.

[227] K. Ikossi, M. Goldenberg, and J. Mittereder, “Metallization options and annealing temperatures for low contact resistance ohmic contacts to n-type

GaSb," *Solid-State Electronics*, vol. 46, no. 10, pp. 1627–1631, 2002. – cited on pages 105 and 121.

[228] J. Robinson and S. Mohney, "A low-resistance, thermally stable Ohmic contact to n-GaSb," *Journal of Applied Physics*, vol. 98, no. 3, 2005. – cited on pages 105 and 121.

[229] N. Mandich, "Pulse and pulse-reverse electroplating," *Metal Finishing*, vol. 97, no. 1, pp. 382–387, 1999. – cited on page 108.

[230] H. Hirano, K. Hikichi, and S. Tanaka, "The wafer-level vacuum sealing and electrical interconnection using electroplated gold bumps planarized by single-point diamond fly cutting," in *2015 Transducers-2015 18th International Conference on Solid-State Sensors, Actuators and Microsystems (TRANSDUCERS)*, pp. 1283–1286, IEEE, 2015. – cited on page 108.

[231] K. Shim, Y. Kil, H. Yang, B. Park, J. Yang, S. Kang, T. Jeong, and T. S. Kim, "Characteristics of germanium dry etching using inductively coupled SF_6 plasma," *Materials science in semiconductor processing*, vol. 15, no. 4, pp. 364–370, 2012. – cited on page 118.

ABBREVIATIONS

Abbreviations

DFB	distributed feedback
DTGS	deuterated triglycine sulfate
FSO	free space optical
FSR	free spectral range
FTIR	Fourier transform infrared spectrometer
ICD	interband cascade detector
ICL	interband cascade laser
ICIP	interband cascade infrared photodetector
ICP	inductively coupled plasma
INPSD	intensity noise power spectral density
LED	light emitting diode
LWIR	long-wave infrared
MBE	molecular beam epitaxy
MCT	mercury cadmium telluride
MIR	mid-infrared
MOCVD	metal-organic chemical vapor deposition
MWIR	mid-wave infrared
NEP	noise equivalent power
PE	polyethylene
PECVD	plasma enhanced chemical vapor deposition
PIC	photonic integrated circuit
QCD	quantum cascade detector
QCL	quantum cascade laser
QCLD	quantum cascade laser detector
QW	quantum well
RIE	reactive ion etching
RIN	relative intensity noise
SCL	separate-confinement layer
SEM	scanning electron microscope
SiN	silicon nitride
SMI	semimetallic interface

VOC	volatile organic compounds
WGM	whispering gallery modes